Electron power absorption in electronegative capacitively coupled discharges

Andrea Proto

Electron power absorption in electronegative capacitively coupled discharges

Andrea Proto

Dissertation submitted in partial fulfillment of a
Philosophiae Doctor degree in Physics

Advisor
Prof. Jón Tómas Guðmundsson

PhD Committee
Prof. Viðar Guðmundsson
Prof. Ágúst Valfells

Opponents
Prof. Pascal Chabert
Dr. Aranka Derzsi

Faculty of Physical Science
School of Engineering and Natural Sciences
University of Iceland
Reykjavik, June 2021

Electron power absorption in electronegative capacitively coupled discharges

Dissertation submitted in partial fulfillment of a *Philosophiae Doctor* degree in Physics

Abstract

The aim of this work is to explore the role of electronegativity and the electron power absorption mechanism in electronegative capacitively coupled oxygen and chlorine discharges. The fundamental mechanisms underlying the electron heating and the electron power absorption have been widely studied and discussed over the past decades. However, a fully consistent and general mathematical-physical explanation of the several physical mechanisms involved in the electron power transfer mechanism is still lacking. This is in particular true for electronegative capacitively coupled discharges. These difficulties are related to the overall complexity of these systems and to the behaviour of the plasma within the sheath regions. Since making analytical calculations is extremely complicated in this context, the main tool used for research on capacitive discharges is particle-in-cell Monte Carlo collision (PIC/MCC) simulations, which provide information on the various physical quantities such as the electron and ion densities, and their velocity and energy distributions, as well as phenomena such as electric field and electron power absorption. In the first part of the thesis the quenching probability of the singlet delta metastable molecule $O_2(a^1\Delta_g)$ on the electrodes is varied in the simulations, along with the secondary emission yield for ion impact and electron reflection for a capacitively coupled oxygen discharge, within the pressure range 0.13 – 6.66 Pa, in order to explore their influence on the electronegativity and the electron power absorption. In the second part, we explored the behaviour of both the electric field and the electron power absorption in a capacitively coupled oxygen discharge within the pressure range 1.33 – 13 Pa and in a capacitively coupled chlorine discharge within the pressure range 1 – 50 Pa, by comparing the physical quantities determined by the simulations to Boltzmann term analysis applied to the simulation outputs. This allows us to determine the processes that contribute to electron power absorption. In the oxygen discharge the electron power absorption mechanism depends on the discharge pressure. The electron power absorption is due to pressure heating and Ohmic heating. At low pressure (1.33 Pa) the electron temperature gradient term contributes to electron heating and the ambipolar term to electron cooling while the opposite is true at 13 Pa. The chlorine discharge is highly electronegative and at pressures > 10 Pa the Ohmic heating contribution to electron heating dominates. At lower pressure there is also a contribution from the electron temperature gradient term.

Útdráttur

Hér eru áhrif rafneikvæðni könnuð, sem og hver eru ráðandi ferli fyrir aflísog rafeinda í rafneikvæðum rýmdarafhleðslum, súrefni og klór. Grunnferlin að baki hitun rafeinda og aflísogs rafeinda hafa verið til skoðunnar í áratugi en þrátt fyrir það er ekki fyrir hendi sjálfsamkvæm og almenn stærðfræðileg lýsing á hinum ýmsu ferlum sem eiga í hlut. Þetta á sér í lagi við í tilfelli rafneikvæðra rýmdarafhleðsla. Þetta er vegna þess hve flókin þessi kerfi eru og vegna hegðunar rafgassins innan slíðursvæðanna. Þar sem aflfræðigreining þessa kerfis er verulega flókin, er megin tólið sem notað er til rannsókna á rýmdarafhleðslum particle-in-cell Monte Carlo árekstra (PIC/MCC) hermanir, sem gefa upplýsingar um hinar ýmsu eðlisstærðir eins og þéttleika rafeinda og jóna og dreifingu þeirra með hraða og orku, sem og eiginleika eins og rafsvið og aflísog. Í fyrri hlutanum eru áhrif þess á rafneikvæðni og aflísog rafeinda í súrefnis rýmdarafhleðslu, að kæfistuðull hálfstöðugu sameindarinnar $O_2(a^1\Delta_g)$ á rafskautunum sé látinn breytast, á þrýsingsbilinu 1.33 - 13 Pa, ásamt með framlagi refeindaútgeislunar vegna árekstra jóna við skautin og endurkasti rafeinda frá skautum, könnuð. Í síðari hlutanum er myndun rafsviðs, sem og aflísog, í rýmdarafhleðslu í súrefni, á þrýsingsbilinu 1.33 - 13 Pa, og í rýmdarafhleðslu í klór, á þrýstingsbilinu 1 - 50 P, skoðuð með því að bera saman ýmsar stærðir, sem ákvarðaðar eru með hermun, við þætti Boltzmann jöfnunnar, sem eru reiknaðir með því að nota niðurstöður hermunar, til að meta hvaða ferli leggja til aflísogs rafeinda. Í súrefnisafhleðslu ræðst hitun rafeindanna af gasþrýstingi. Aflísog rafeinda kemur til vegna þrýstingsþátta sem og Ohmskrar hitunar. Við lágan gasþrýsting (1.3 Pa) er það liðurinn sem stafar af stigli rafeindahitastigsins sem leggur mest til hitunar rafeindanna og ambipolar liðurinn leggur til kælingar rafeindanna, en hið gagnstæða er tilfellið við 13 Pa. Í klórafhleðslu er rafneikvæðnin há og fyrir gasþrýsting > 10 Pa er Ohmsk hitun ráðandi. Við lægri gasþrýsting er eitthvert framlag einnig frá stigli rafeindahitastigsins.

Contents

List of Original Papers

Paper 1: A. Proto and J. T. Gudmundsson, The role of surface quenching of the singlet delta molecule in a capacitively coupled oxygen discharge. *Plasma Sources Science and Technology*, **27**(7) (2018) 074002.

Paper 2: A. Proto and J. T. Gudmundsson, The influence of secondary electron emission and electron reflection on a capacitively coupled oxygen discharge. *Atoms*, **6**(4) (2018) 65.

Paper 3: J. T. Gudmundsson and A. Proto, Electron heating mode transitions in a low pressure capacitively coupled oxygen discharge. *Plasma Sources Science and Technology*, **28**(4) (2019) 045012.

Paper 4: A. Proto and J. T. Gudmundsson, Electron power absorption dynamics in a low pressure radio frequency driven capacitively coupled discharge in oxygen, *Journal of Applied Physics*, **128**(11) (2020) 113302.

Paper 5: A. Proto and J. T. Gudmundsson, Electron power absorption in radio frequency driven capacitively coupled chlorine discharge, *Plasma Sources Science and Technology*, accepted for publication.

Acknowledgments

1 Introduction

A capacitively coupled discharge consists of two parallel metallic electrodes, one driven by a rf voltage or current source while the other electrode is grounded (Chabert and Braithwaite, 2011; Lieberman and Lichtenberg, 2005). The electrodes typically have a radius of few tens of cm and they are separated by a few cm. By applying voltage of amplitude typically a few hundred volts, with the driving frequency in the range between hundreds of kHz and hundreds of MHz, a discharge is formed. Sometimes a capacitor is connected in series to the discharge. A schematic picture of a capacitively coupled oxygen discharge is shown in Figure 1.1. Typical voltages applied to the electrodes vary in the range 100 V – 5 kV, while the driving frequency is in the MHz or radio frequency (rf) range, where the most used fundamental frequency is $f = 13.56$ MHz. Capacitively coupled discharges are typically operated in the pressure range $0.1 - 100$ Pa and the charged particle density is $n \approx 10^{12} - 10^{16}$ m^{-3}. These discharges have been explored extensively over the past few decades. (Godyak, 1972; Godyak and Khanneh, 1986; Wood, 1991; Lieberman and Godyak, 1998; Mussenbrock and Brinkmann, 2006; Schulze et al., 2011a; Klick, 1996; Liu et al., 2016).

A plasma is usually defined as a collection of electrons and ions. If the electrons and the ions are in a quasi-neutral state, the plasma is labeled as thermal, otherwise it is called non-thermal. In contrast with inductive discharges, where the rf fields in the plasma are the result of a changing magnetic flux, in a capacitively coupled plasma electromagnetic phenomena are negligible. The neutral gas that provides the ions can be a noble gas such as argon and helium as well as molecular gases such as oxygen, nitrogen, tetrafluoromethane and chlorine, or mixtures of various gases. Each species within the discharge is described by a distribution function $f(r, v, t)$ in a six-dimensional phase space (r, v) of particle positions and velocities. The discharge electrons are typically in near-thermal equilibrium and are described by an equilibrium temperature T_e. Positive ions are almost never in thermal equilibrium and the neutral gas molecules may or may not be in thermal equilibrium. Moreover, the electron temperature T_e is typically a few eV, while the ion temperature is close to room temperature. In a plasma discharge the electrons feel the space-time rf field, while the ions feel the time averaged rf field only. The reason lies in the fact that, since $m_e \ll m_i$, where m_e is the electron mass and m_i is the ion mass, the ions experience a much bigger inertia. Consequently, it is the electrons that dissociate the feedstock gas molecules and therefore create the free radicals, the film forming species in deposition and etchant atoms that interact with substrates being processed. Furthermore, the electrons ionize the atoms and/or molecules to create the positive ions that then can bombard substrates. The low pressure rf driven capacitively coupled discharges have a wide range of applications, most notably in materials processing and in particular in integrated circuit manufacturing, where it

has been applied for a few decades.
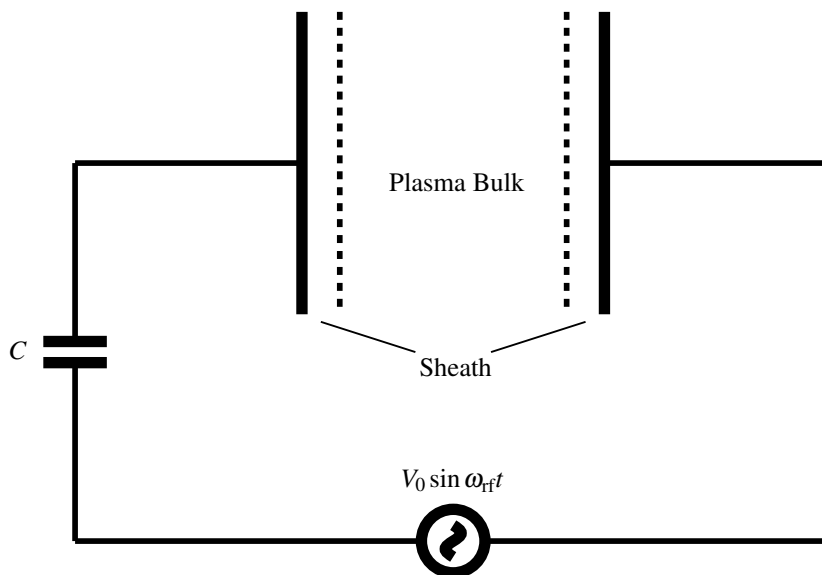
Figure 1.1. Schematic picture of a capacitively coupled discharge consisting of two parallel electrodes and driven by a sinusoidal voltage source.

The electron heating mechanism and the electron kinetics dictate the ionization and dissociation processes that maintain the discharge and create the radicals that are desired for materials processing. Although the fundamental mechanisms underlying these processes have been widely studied and discussed over the past decades, a fully consistent and general mathematical-physical explanation of the several physical mechanisms involved in the electron power transfer mechanism to the electrons is still lacking. This is in particular true for electronegative capacitively coupled discharges. These difficulties are related to the overall complexity of these systems and to the behaviour of the plasma within the sheath region. In fact the sheath represents the interface between the bulk plasma and the electrodes and it suffers from boundary effects, which are difficult to determine mathematically. Secondly, electrons and negative species are almost absent within the sheath region, making the use of the Boltzmann equation for electrons questionable. This is in particular true for electronegative capacitively coupled discharges.

Here, 1d-3v particle-in-cell Monte Carlo collision simulations are applied to study the contributions of the various mechanisms to the electric field and the electron power absorption within the electronegative core of a capacitively coupled electronegative discharge. This includes applying simplified Boltzmann term analysis of the discharge bulk, the study of the influence of surface processes on the electron power absorption mechanisms and the operating mode of the discharge. Chapter 2 gives a brief overview of the basic plasma parameters and relations used. Chapter 3 discusses the basics of the Boltzmann equation for the electrons and the most common paths to recover the

expressions for both the electric field and the electron power absorption. Chapter 4 discusses the electron power absorption mechanisms and operation modes that have been identified in capacitively coupled discharges. In Chapter 5 the basics of the particle-in-cell Monte Carlo collision method are discussed. In Chapter 6 the collision theory along with the chemical reactions included in the plasma discharge model for oxygen and chlorine are discussed. Chapter 7 summarizes the five journal papers that constitute the thesis and Chapter 8 gives the conclusions.

2 Fundamentals of plasma physics

A low pressure plasma discharge is typically not in thermal equilibrium. This non equilibrium character of a plasma discharge implies that the various species are not in thermal equilibrium among each other. In particular, the kinetic energy of the electrons may be much larger than that stored in the excitation of the heavy species within the discharge. To describe a low pressure discharge a number of parameters and processes need to be taken into account. Here some of the fundamentals of a low pressure plasma discharge are reviewed.

2.1 Debye shielding length

It is of significant importance to define a characteristic length scale in a plasma, i.e. the electron Debye length (Lieberman and Lichtenberg, 2005; Meichsner et al., 2013), which is the distance over which significant charge densities may exist. In order to estimate the Debye length, let us consider the Poisson equation

$$\frac{d^2\Phi}{dx^2} = -\frac{e}{\varepsilon_0}(n_i - n_e), \tag{2.1.0.1}$$

where we have considered a plasma that is made of electrons and positive ions only, where n_i is the ion density and n_e the electron density. At this point it can be useful to define the roman typeface symbol T for the voltage equivalent of the temperature, while the italic typeface symbol T refers to the temperature in Kelvins (Lieberman and Lichtenberg, 2005)

$$k_B T(\text{kelvins}) = e\text{T}(\text{volts}). \tag{2.1.0.2}$$

However, from now on, we will always refer to T for both the temperature units. Setting $n_e = n_0 \exp\left(\frac{\Phi}{T_e}\right)$, which is the Boltzmann relation for electrons, and taking $n_e = n_i = n_0$ one finds, after taking a Taylor expansion for $\Phi \ll T_e$, the following equation

$$\frac{d^2\Phi}{dx^2} = \frac{en_0}{\varepsilon_0}\frac{\Phi}{T_e}, \tag{2.1.0.3}$$

where T_e is the electron temperature and ε_0 is the vacuum permittivity. The solution of Eq. (2.1.0.3) reads

$$\Phi = \Phi_0 \exp\left(-\frac{|x|}{\lambda_{De}}\right) \quad \text{with} \quad \lambda_{De} = \left(\frac{\varepsilon_0 T_e}{en_0}\right)^{\frac{1}{2}}. \tag{2.1.0.4}$$

The quantity λ_{De} is known in the literature as Debye length and it is the smallest scale of a volume to confine a plasma (Lieberman and Lichtenberg, 2005; von Keudell and Schulz-von der Gathen, 2017). In capacitively coupled discharges, the Debye length is typically significantly smaller than the bulk gap length ($\lambda_{De} \ll d_{bulk}$) and it is larger or comparable to the sheath width ($\lambda_{De} \geq d_{sheath}$).

2.2 Quasineutrality

Now, let us consider the Poisson equation again. From Eq. (2.1.0.1) we know that (Lieberman and Lichtenberg, 2005; Meichsner et al., 2013)

$$\frac{d^2\Phi}{dx^2} \sim \frac{\Phi}{l^2} \sim \left| \frac{e}{\varepsilon_0} \left(Zn_i - n_e \right) \right|, \tag{2.2.0.1}$$

where Z stands for the ion charge and the condition $l \gg \lambda_{De}$ is supposed to hold, where l is the size of the system. Combining the expression for the Debye length shown in Eq. (2.1.0.4) with Eq. (2.2.0.1), one finds

$$\frac{|Zn_i - n_e|}{n_e} \leq \frac{\lambda_{De}^2}{l^2}. \tag{2.2.0.2}$$

Now, since the condition $l \gg \lambda_{De}$ holds, Eq. (2.2.0.2) is the same as requiring

$$Zn_i \approx n_e. \tag{2.2.0.3}$$

This expression is the so called quasineutrality condition.

2.3 Plasma frequency

In non-thermal plasmas the quasineutrality condition is rarely fulfilled, due to the oscillation of the electron ensamble caused by the rf field (Meichsner et al., 2013). The collective motion of the electrons leads to the formation of macroscopic space charges. In order to describe the collective oscillation of the plasma electrons the following relations have to be considered:

$$m_e \frac{d\vec{v}_e}{dt} = -e\vec{E} \tag{2.3.0.1}$$

$$\vec{\nabla}\vec{E} = \frac{\rho}{\varepsilon_0} \tag{2.3.0.2}$$

$$\frac{\partial \rho}{\partial t} = \vec{\nabla}\vec{J}_e \tag{2.3.0.3}$$

$$\vec{J}_e = -en_e\vec{v}_e, \tag{2.3.0.4}$$

where m_e is the electron mass, $\vec{v}_e$ is the electron velocity, $\vec{J}_e$ is the electron current density and ρ is the total charge density. Taking the divergence and the time derivative

of Eq. (2.3.0.1) and using Eq. (2.3.0.2), one finds

$$\vec{\nabla}\left(m_e \frac{d\vec{v}_e}{dt}\right) = -e\vec{\nabla}\vec{E} = -e\frac{\rho}{\varepsilon_0} \tag{2.3.0.5}$$

or

$$m_e \frac{\partial^2 \vec{\nabla}\vec{v}_e}{\partial t^2} = -\frac{e}{\varepsilon_0}\frac{\partial \rho}{\partial t} = \frac{e}{\varepsilon_0}\vec{\nabla}\vec{J}_e = -\frac{e^2 n_e \vec{\nabla}\vec{v}_e}{\varepsilon_0}. \tag{2.3.0.6}$$

By using the relation $\vec{\nabla}\vec{v}_e = \delta$ inside Eq. (2.3.0.6), one finds the equation

$$\frac{\partial^2 \delta}{\partial t^2} + \frac{e^2 n_e}{\varepsilon_0 m_e} = 0 \tag{2.3.0.7}$$

with the following solution

$$\delta(t) = \delta_0 \exp\left[-i\left(\omega_{pe}t + \phi_0\right)\right] \quad \text{with} \quad \omega_{pe}^2 = \frac{e^2 n_e}{\varepsilon_0 m_e}, \tag{2.3.0.8}$$

where $\delta(t)$ represents the collective shift of a free undamped harmonic oscillator and ω_{pe} stands for the *electron plasma frequency*. The same procedure can be applied for the ions, giving

$$\omega_{pi}^2 = \frac{e^2 Z^2 n_i}{\varepsilon_0 m_i} \tag{2.3.0.9}$$

which is known in the literature as *ion plasma frequency*. The quantities ω_{pe} and ω_{pi} describe the collective oscillation of the electrons and ions, respectively. The higher is the electron plasma frequency, the more rapidly the electrons follow the electric field oscillations. It is worth noting that alternative derivations exist and include the calculation of the electron plasma frequency starting from the assumption of a slab geometry (Lieberman and Lichtenberg, 2005). However, as it has been shown, such assumptions are restrictive and are not necessary. Finally, since $m_e \ll m_i$, we can state that the following inequality holds (Schulze, 2009)

$$\omega_{pi} \ll \omega_{RF} \ll \omega_{pe} \tag{2.3.0.10}$$

for most electrically driven partially ionized plasma discharges, where ω_{RF} is the frequency of the applied voltage.

2.4 Skin depth

An important quantity that has to be introduced is the plasma skin depth. The plasma skin depth, also known in the literature as collisionless skin depth, is the depth in a collisionless plasma to which low-frequency electromagnetic radiation can penetrate. It is defined by attenuation of the wave amplitude by a factor of $1/e$. In a traditional plasma the plasma skin depth δ_{es} reads

$$\delta_{es} = \frac{c}{\omega_{pe}}, \tag{2.4.0.1}$$

where c is the speed of light and ω_{pe} is the electron plasma frequency shown in Eq. (2.3.0.8). Analogously to what has been shown above, it is also possible to define the *ion inertial length* as

$$\delta_{is} = \frac{c}{\omega_{pi}}, \tag{2.4.0.2}$$

where ω_{pi} is the ion plasma frequency shown in Eq. (2.3.0.9). Finally, it is worth noting that

$$\delta_{es} \ll \delta_{is}, \tag{2.4.0.3}$$

since $\omega_{pe} \gg \omega_{pi}$ for most plasma discharges.

2.5 Plasma transport

In a plasma discharge, collisions lead to finite mean free path λ, which can be expressed as

$$\lambda = \frac{1}{n_g \sigma}, \tag{2.5.0.1}$$

where n_g is the density of the collision partners and σ is the collision cross section. In electrically driven partially ionized discharge the most frequent collisional partners are the neutral atoms or molecules of the feedstock gas. Therefore, $n_g \propto p$, where p is the pressure of the gas. Moreover, for a given velocity v of a species, it is possible to write the collision frequency v_c as

$$v_c = \frac{v}{\lambda}. \tag{2.5.0.2}$$

Since elastic collisions reduce the momentum of the species in one specific direction of a streaming plasma, they usually dominate the transport mechanism. Such a directionality has to be taken into account when the collision frequency v_c is derived, so that small angle collisions imply only a small momentum loss (von Keudell and Schulz-von der Gathen, 2017). In the literature plasma transport is separated into drift transport and diffusion transport. The drift transport is due to an external electric field, while the diffusion transport is due to a density gradient. The corresponding transport coefficients are the mobility μ and the diffusion coefficient D, which are defined as

$$\mu = \frac{q}{m v_c} \tag{2.5.0.3}$$

$$D = \frac{|q| T}{m v_c} \tag{2.5.0.4}$$

for a particle with charge q and mass m. Here the temperature T is expressed in Volts. The expressions above are linked between each other through the well known Einstein relation

$$D = \frac{q}{|q|} T \mu. \tag{2.5.0.5}$$

Now, we are able to rewrite Eq. (2.5.0.3) and Eq. (2.5.0.4) for the electrons as

$$\mu_e = \frac{-e}{m_e \nu_{ec}} \tag{2.5.0.6}$$

$$D_e = \frac{eT_e}{m_e \nu_{ec}}, \tag{2.5.0.7}$$

where ν_{ec} denotes the total collision frequency involving the electrons, and for the positive ions

$$\mu_i = \frac{e}{m_i \nu_{ic}} \tag{2.5.0.8}$$

$$D_i = \frac{eT_i}{m_i \nu_{ic}}, \tag{2.5.0.9}$$

where ν_{ic} denotes the total collision frequency involving the positive ions. Now, by defining the electron density flux Γ_e as

$$\vec{\Gamma}_e = \frac{\vec{J}_e}{e} \tag{2.5.0.10}$$

and the ion density flux as

$$\vec{\Gamma}_i = \frac{\vec{J}_i}{e}, \tag{2.5.0.11}$$

by simple dimensional considerations, it is possible to write down the flux density for the electrons

$$\vec{\Gamma}_e = \mu_e n_e \vec{E} - D_e \vec{\nabla} n_e \tag{2.5.0.12}$$

and for the positive ions

$$\vec{\Gamma}_i = \mu_i n_i \vec{E} - D_i \vec{\nabla} n_i. \tag{2.5.0.13}$$

Finally, by assuming the system to be in a steady state, it is possible to use the so called congruence assumption, i.e. that the electron and ion current density must be equal everywhere ($\Gamma = \Gamma_e = \Gamma_i$), along with the quasineutrality condition ($n = n_e \approx n_i$), we are allowed to write, by using Eqs. (2.5.0.12) and (2.5.0.13)

$$\Gamma = \mu_i n \vec{E} - D_i \vec{\nabla} n_i = -\mu_e n \vec{E} - D_e \vec{\nabla} n_e \tag{2.5.0.14}$$

which leads to the expression for the electric field

$$\vec{E} = \frac{D_i - D_e}{\mu_i + \mu_e} \frac{\vec{\nabla} n}{n}. \tag{2.5.0.15}$$

By plugging the expression above into Eq. (2.5.0.14) we find the expression

$$\vec{\Gamma} = -\frac{\mu_i D_e + \mu_e D_i}{\mu_i + \mu_e} \vec{\nabla} n \tag{2.5.0.16}$$

which defines the ambipolar diffusion coefficient D_a as

$$D_a = \frac{\mu_i D_e + \mu_e D_i}{\mu_i + \mu_e}. \tag{2.5.0.17}$$

So we arrive at the Fick's law $\vec{\Gamma} = -D_a \vec{\nabla} n$. In a weakly ionized discharge $\mu_e \gg \mu_i$ so that

$$D_a \Big|_{\frac{\mu_i}{\mu_e} \ll 1} \approx D_i + \frac{\mu_i}{\mu_e} D_e = D_i \left(1 + \frac{T_e}{T_i} \right), \tag{2.5.0.18}$$

where in the last step the Einstein relation, shown in Eq. (2.5.0.5), has been used. Moreover, in a weakly ionized plasma, i.e. for $T_e \gg T_i$, we find that

$$D_a \Big|_{\substack{\frac{\mu_i}{\mu_e} \ll 1 \\ \frac{T_i}{T_e} \ll 1}} \approx \mu_i T_e. \tag{2.5.0.19}$$

It is worth noting that considering the limits $\mu_i \ll \mu_e$ and $T_i \ll T_e$ simultaneously is like taking $D_i \ll D_e$ (Eq. (2.5.0.5)). In this limit, Eq. (2.5.0.16) reads

$$\Gamma \Big|_{\substack{\frac{\mu_i}{\mu_e} \ll 1 \\ \frac{T_i}{T_e} \ll 1}} \approx \mu_i T_e \vec{\nabla} n. \tag{2.5.0.20}$$

Finally, we observe that, by inspecting Eq. (2.5.0.15) in the same limit ($D_i \ll D_e$) we find

$$\vec{E} \Big|_{\substack{\frac{\mu_i}{\mu_e} \ll 1 \\ \frac{T_i}{T_e} \ll 1}} \approx -T_e \frac{\vec{\nabla} n}{n}. \tag{2.5.0.21}$$

By plugging Eq. (2.5.0.21) into Eq. (2.5.0.12) we find, with the help of the Einstein relation,

$$\vec{\Gamma}_e \Big|_{\substack{\frac{\mu_i}{\mu_e} \ll 1 \\ T_i \ll T_e}} \approx 0. \tag{2.5.0.22}$$

On the other hand, plugging Eqs. (2.5.0.20) and (2.5.0.21) into Eq. (2.5.0.13) leads to

$$\vec{\Gamma}_i \Big|_{\substack{\frac{\mu_i}{\mu_e} \ll 1 \\ T_i \ll T_e}} \approx -\mu_i n E. \tag{2.5.0.23}$$

Hence the ion motion is dominated by the mobility and electron motion is determined by a Boltzmann equilibrium (Lieberman and Lichtenberg, 2005).

2.6 Sheath and boundary effects

2.6.1 The sheath region

Usually plasma discharges, which are quasineutral within the bulk region in most cases, are joined to wall surfaces across positively charged layers called sheaths. Since the electron mass (temperature) is very much smaller (higher) than the ions mass (temperature), the electron thermal velocity is sharply higher than the ion thermal velocity. This also means that fast moving electrons are not confined within the bulk region and are free to hit the electrodes. This means that, on a very short time scale, the electrons get lost to the walls and a net positively charged region builds up, which is usually known in the literature as a sheath. The formation of sheaths is demonstrated in Figure 2.1. Using the Poisson equation along with that said above, we are allowed to say

$$\boxed{\text{Bulk Region}} \implies \rho = 0 \implies \vec{\nabla}\vec{E}(t,\vec{x}) = 0 \underbrace{\implies}_{1D} \frac{\partial E}{\partial x} = 0 \implies E = C \qquad (2.6.1.1)$$

$$\boxed{\text{Sheath Region}} \implies \rho \geq 0 \implies \vec{\nabla}\vec{E}(t,\vec{x}) \geq 0 \underbrace{\implies}_{1D} \frac{\partial E}{\partial x} \geq 0 \implies E = \frac{e}{\varepsilon_0} \int_{x_s}^{x} \rho \, dx, \qquad (2.6.1.2)$$

where x_s stands for the sheath location. Assuming the net charge density to be constant within the sheath region for simplicity, one finds

$$E = \frac{e}{\varepsilon_0} \rho (x - x_s) \text{ for } x \geq x_s \qquad (2.6.1.3)$$

$$E = \frac{e}{\varepsilon_0} \rho (x_s - x) \text{ for } x \leq -x_s. \qquad (2.6.1.4)$$

This means that, since the value of the electric field for both relations shown in Eq. (2.6.1.1) and Eq. (2.6.1.2) has to be the same on both sheath edges, one finds $E = C = 0$ (Eq. (2.6.1.1)). Consequently we have a constant potential within the bulk region. Moreover, since the potential has to be zero on both electrodes, we can conclude that it falls sharply to zero once both sheath edges are crossed. The electric field formulas shown in Eqs. (2.6.1.3) and (2.6.1.4) mean that the direction of the electric field is outward (toward the walls), while the electric force acting on the electrons, namely $-eE$, is directed inward (toward the bulk). In this way the potential acts as a potential valley that confines the electrons and the negative ions within the plasma bulk, reflecting the electrons travelling towards the walls back to the plasma bulk. As regards to the positive ions we have an opposite situation. In fact the positive ions are accelerated toward the walls once they have crossed both sheath edges, since they experience a net electric force, namely eE which is now directed outward (to the walls).

(a)

(b)
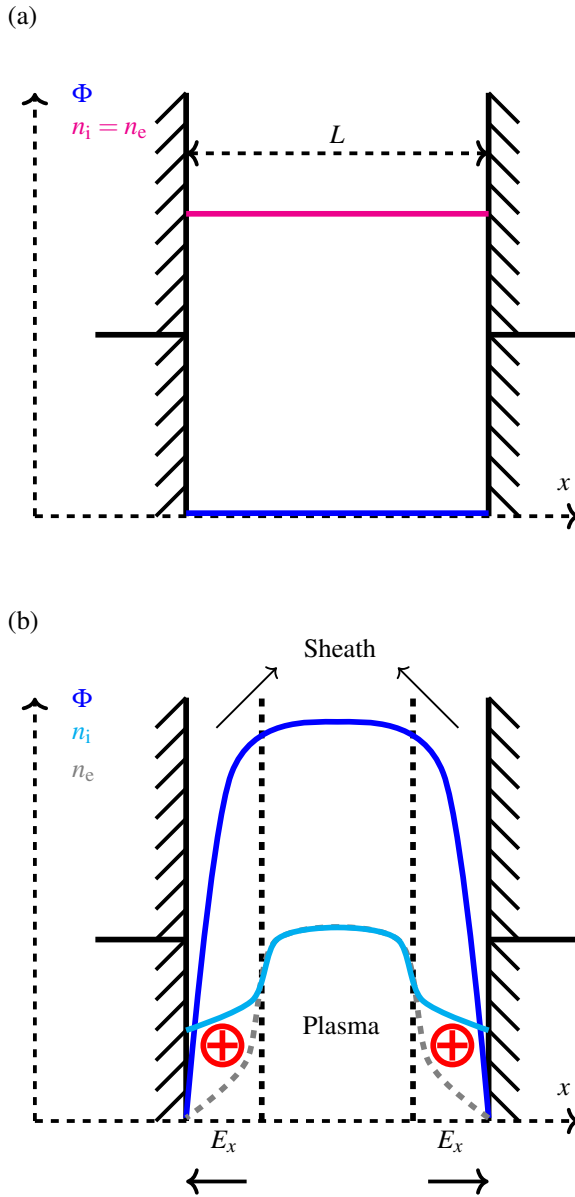
Figure 2.1. The formation of plasma sheaths: (a) initial ion and electron densities and potential; (b) ion density (solid light blue line), electron density (grey dashed line), and potential (solid dark blue) after sheaths have developed.

2.6.2 The matrix sheath

The matrix sheath (Lieberman and Lichtenberg, 2005) is the simplest model that has been developed to describe the behaviour of the potential within the sheath region. Assuming the quasi-neutrality to hold within the plasma bulk ($n_e = n_i$), the electron (ion) density to be zero (constant) within the sheath region, whose thickness is labeled by s, one finds, by using the Poisson equation and choosing $x = 0$ at the plasma sheath edge

$$\frac{\partial E(t,x)}{\partial x} = \frac{en_0}{\varepsilon_0}, \tag{2.6.2.1}$$

the equation above leads to

$$E = \frac{en_0[x - s_i(t)]}{\varepsilon_0}, \tag{2.6.2.2}$$

where s_i is the left (right) plasma sheath edge for $i = 1$ ($i = 2$). Moreover, in order to get Eq. (2.6.2.2), we have set the boundary condition $E(t, x = s_i) = 0$. Again, in terms of the potential Φ, Eq. (2.6.2.2) reads

$$\Phi_{s_i}(t) = \int_0^{s_i} E\, dx = -\frac{en_0 s_i^2}{2\varepsilon_0}. \tag{2.6.2.3}$$

By using Eq. (2.6.2.3) and setting $\Phi_s = -V_s = -V_{s_1} = -V_{s_2}$, where V_{s_1} and V_{s_2} are the voltage drops at the left and right sheath edge, respectively, we obtain the location of the sheath edge with respect to the discharge center

$$s_i = (-1)^i \left(\frac{2\varepsilon_0 V_s}{en_0} \right)^{\frac{1}{2}} \tag{2.6.2.4}$$

or, in terms of the Debye length (Eq. (2.1.0.4))

$$s_i = (-1)^i \lambda_{De} \left(\frac{2V_s}{T_e} \right)^{\frac{1}{2}}. \tag{2.6.2.5}$$

Moreover, since the instantaneous charge in the sheath region is

$$Q(t) = en_0 A s_i(t), \tag{2.6.2.6}$$

where A is the area of the electrode, we are allowed to write, by using Eq. (2.6.2.4)

$$V_{s_2} = \frac{Q^2(t)}{2\varepsilon_0 en_0} \propto Q^2(t). \tag{2.6.2.7}$$

Taking into account the spatial dependency of the ion density (Czarnetzki, 2013), the previous expression can be updated as follows

$$V_{s_2} \propto Q^2(t)(1 - aQ(t)), \tag{2.6.2.8}$$

where the quantity a dictates the cubic correction due to the already cited spatially dependent ion density. Finally, defining the rf current as $I = I_0 \sin \omega t$, one finds, using Eq. (2.6.2.6)

$$s_1(t) = s_0 (1 - \cos \omega t) - L \quad \text{with} \quad s_0 = \frac{I_0}{eA\omega n_0}, \tag{2.6.2.9}$$

where L is the distance from the left (right) electrode to the discharge center. We also observe that, defining the quantity $s_m \equiv L - 2s_0$, the maximum sheath left expansion s_{m_1} is equal to $-s_m$. In order to get Eq. (2.6.2.9), the boundary condition $s_2(t = 0) = -L$ has been employed. It is worth noting that, by defining the time averaged sheath width $\bar{s}$, the time average left sheath edge is placed at $\bar{s} \equiv \bar{s}_1 = s_0 - L$. Analogously for the right sheath location, one finds

$$s_2(t) = -s_0 (1 + \cos \omega t) + L, \tag{2.6.2.10}$$

where now the maximum right sheath expansion s_{m_2} is equal to s_m. In order to get Eq. (2.6.2.9), the boundary condition $s_2(t = \pi/\omega) = L$ has been employed. Moreover, the time average right sheath edge is placed at $\bar{s}_2 = -\bar{s}$. It is worth noting that

$$|s_1(t)| + |s_2(t)| = 2(s_0 - L) = 2\bar{s}. \tag{2.6.2.11}$$

Again, taking into account the spatial dependence of the ion distribution, Lieberman (1988) updated Eq. (2.6.2.9) as follows

$$s_m = \frac{5l_0^3}{12e(h_l n_0)^2 (\omega A)^3 \varepsilon_0 k_B T_e}, \tag{2.6.2.12}$$

where $h_l = n_s/n_0$ is the ratio of the density at the sheath edge to the density at the plasma center. Now, plugging Eq. (2.6.2.9) into Eq. (2.6.2.4), one finds the following expression for the voltage drop at the left sheath edge

$$V_{s_1} = \frac{en_0}{2\varepsilon_0} \left[\bar{s}^2 + \frac{s_0^2}{2} - 2\bar{s}s_0 \cos \omega t + \frac{s_0^2}{2} \cos 2\omega t \right]. \tag{2.6.2.13}$$

An analogous expression for the voltage drop on the left sheath edge can be found plugging Eq. (2.6.2.10) into Eq. (2.6.2.4)

$$V_{s_2} = \frac{en_0}{2\varepsilon_0} \left[\bar{s}^2 + \frac{s_0^2}{2} + 2\bar{s}s_0 \cos \omega t + \frac{s_0^2}{2} \cos 2\omega t \right]. \tag{2.6.2.14}$$

As we can see from both Eqs. (2.6.2.13) and (2.6.2.14), the voltage develops a non linear behaviour in presence of a linearly time dependent current. Finally, we observe that

$$\Delta V \equiv V_{s_2} - V_{s_1} = V_0 \cos \omega t \quad \text{with} \quad V_0 = \frac{2en_0\bar{s}s_0}{\varepsilon_0} \tag{2.6.2.15}$$

i.e. the voltage drop difference between the right and the left sheath edge is free of non linear terms. It is worth noting that we have neglected the voltage drop across the bulk,

since it is usually very small compared to the sheath region. It can be seen from Eqs. (2.6.2.13) and (2.6.2.14) that the time averaged potential drop at the sheath edges s_1 and s_2 is

$$\overline{V} \equiv \overline{V}_{s_1} = \overline{V}_{s_1} = V_0 \left[\frac{\overline{s}}{s_0} + \frac{s_0}{2\overline{s}} \right]. \tag{2.6.2.16}$$

Since the ions do not respond to the rf modulation, they are assumed to bombard the electrodes with average energy $\varepsilon_i = \overline{V}$ in a collisionless sheath. Finally, it is possible to define a sheath capacitance using the following relation

$$Q = C_s \Delta V \Longrightarrow I = C_s \frac{d\Delta V}{dt}, \tag{2.6.2.17}$$

where the capacitance C_s is assumed to be time independent. Using the definition $I = I_0 \sin \omega t$, along with Eq. (2.6.2.15) as well as the relations for both I_0 and V_0 shown in Eqs. (2.6.2.9) and (2.6.2.13) we find

$$C_s = \frac{\varepsilon_0 A}{\overline{s}}. \tag{2.6.2.18}$$

Finally, in most plasma discharges the following inequality holds (Schulze, 2009)

$$\lambda_{\mathrm{De}} \ll \overline{s} \ll L \ll \lambda_{\mathrm{es}}, \tag{2.6.2.19}$$

where λ_{De} is the Debye length defined in Eq. (2.1.0.4) and λ_{es} is the plasma skin depth defined in Eq. (2.4.0.1). If the plasma density (voltage) is low (high), i.e. at low gas pressure, the time averaged sheath width s may approach the bulk gap length.

2.6.3 The Child-Langmuir sheath

In the following we will set $x = 0$ at the plasma sheath edge and $x = s$ at the electrode (Lieberman and Lichtenberg, 2005). In the limit that the initial ion energy $\mathcal{E}_s$ is small compared to the potential, the ion energy reads

$$\frac{M_i u_i^2}{2} = -e\Phi(x), \tag{2.6.3.1}$$

where u_i is the ion velocity and M_i is the ion mass. On the other hand, the flux conservation reads

$$e n_i(x) u_i(x) = J_0, \tag{2.6.3.2}$$

where n_i is the ion density and J_0 is the constant ion current. Plugging the expression for u_i from Eq. (2.6.3.1) into Eq. (2.6.3.2), one finds

$$n_i(x) = \frac{J_0}{e} \left(-\frac{2e\Phi}{M_i} \right)^{\frac{1}{2}}. \tag{2.6.3.3}$$

15

Since there are no electrons within the sheath region, the previous expression can be rewritten by using the Poisson equation as follows

$$\frac{d^2\Phi}{dx^2} = -\frac{J_0}{e}\left(-\frac{2e\Phi}{M_i}\right)^{\frac{1}{2}}.$$

(2.6.3.4)

Multiplying the previous expression by $d\Phi/dx$, integrating from 0 to x, taking the square root and integrating again, one finds

$$-\Phi^{\frac{3}{4}} = \frac{3}{2}\left(\frac{J_0}{\varepsilon_0}\right)^{\frac{1}{2}}\left(\frac{2e}{M_i}\right)^{-\frac{1}{4}}x,$$

(2.6.3.5)

where the boundary conditions $\Phi = 0$ and $d\Phi/dx = 0$ at $x = 0$ have been chosen. Setting $\Phi(x = s) = -V_s$ we obtain

$$J_0 = \frac{4}{9}\varepsilon_0\left(\frac{2e}{M_i}\right)^{\frac{1}{2}}\frac{V_s^{\frac{3}{2}}}{s}$$

(2.6.3.6)

which is the Child law (Child, 1911). Plugging Eq. (2.6.3.6) into Eq. (2.6.3.7), one finds

$$\Phi = -V_s\left(\frac{x}{s}\right)^{\frac{4}{3}},$$

(2.6.3.7)

which leads to an expression for the electric field

$$E = \frac{4}{3}\frac{V_s}{s}\left(\frac{x}{s}\right)^{\frac{1}{3}}$$

(2.6.3.8)

and, using the Poisson equation, the expression for the ion density

$$n_i = \frac{4}{9}\frac{\varepsilon_0}{e}\frac{V_s}{s^2}\left(\frac{s}{x}\right)^{\frac{2}{3}}.$$

(2.6.3.9)

First of all we observe that another way to get Eq. (2.6.3.9) is to plug the expression for J_0 in Eq. (2.6.3.6) along with the expression for Φ in Eq. (2.6.3.7) into Eq. (2.6.3.3). Secondly, it is worth noting that if $x \to 0$ the expression above is singular. Such a problem can be avoided considering an extension of Eq. (2.6.3.2) where the ion energy at the sheath edge cannot be neglected, such that

$$\frac{M_i u_i^2}{2} + e\Phi = \frac{M_i u_s^2}{2}.$$

(2.6.3.10)

Plugging the expression for u_i into Eq. (2.6.3.2), we find

$$n_i = \frac{J_0}{e}\left[u_s^2 - \frac{2e\Phi}{M_i}\right]^{-\frac{1}{2}}$$

(2.6.3.11)

which is the natural extension of Eq. (2.6.3.3). Now, analogously to what has been said previously, plugging the expression for J_0 in Eq. (2.6.3.6) along with the expression for Φ into Eq. (2.6.3.11), we get

$$n_i = \frac{4}{9} \frac{\varepsilon_0}{e} \left(\frac{2e}{M_i} \right)^{\frac{1}{2}} \frac{V_0^{\frac{3}{2}}}{s^2} \left[u_s^2 + \frac{2e}{M_i} V_0 \left(\frac{x}{s} \right)^{\frac{4}{3}} \right]^{-\frac{1}{2}}. \qquad (2.6.3.12)$$

In the limit $x \to 0$ the expression above reduces to

$$n_{si} = \frac{4}{9} \frac{\varepsilon_0}{u_s e} \left(\frac{2e}{M_i} \right)^{\frac{1}{2}} \frac{V_0^{\frac{3}{2}}}{s^2}, \qquad (2.6.3.13)$$

where n_{si} labels the ion density at the sheath edge, i.e. for $x = 0$. Now, plugging the relation $J_0 = e n_{si} u_B$ into Eq. (2.6.3.6), where u_B is the Bohm velocity, one finds

$$s = \frac{\sqrt{2}}{3} \lambda_{De} \left(\frac{2V_0}{T_e} \right)^{\frac{3}{4}} \qquad (2.6.3.14)$$

which differs from the sheath thickness of the matrix sheath model shown in Eq. (2.6.2.5) by an overall factor and for the exponent. Finally, assuming a zero initial ion velocity and plugging Eq. (2.6.3.7) into Eq. (2.6.3.1), we get

$$\frac{dx}{dt} = v_0 \left(\frac{x}{s} \right)^{\frac{2}{3}} \quad \text{with} \quad v_0 = \left(\frac{2eV_0}{M_i} \right)^{\frac{1}{2}}, \qquad (2.6.3.15)$$

where v_0 is the characteristic ion velocity in the sheath. Integrating Eq. (2.6.3.15) one finds

$$\frac{x(t)}{s} = \left(\frac{v_0 t}{3s} \right)^3 \qquad (2.6.3.16)$$

which, after setting $x = s$, becomes

$$\tau_i = \frac{3s}{v_0} \qquad (2.6.3.17)$$

which is the ion transit time across the sheath (Lieberman and Lichtenberg, 2005).

2.6.4 The Brinkmann criterion

For a given set of positive ion and electron densities, the electron sheath edge s_e is formally defined as the point where the total electron charge on the left side of the left sheath edge is equal to the 'missing charge' on the right side of the left sheath edge (Brinkmann, 2007; Salabaş and Brinkmann, 2006; Brinkmann, 2015) :

$$\int_{-\infty}^{s_e} e n_e dx - \int_{s_e}^{\infty} e \left(n_{i_+} - n_e \right) = 0. \qquad (2.6.4.1)$$

The expression above is known in the literature as the Brinkmann criterion. It is worth noting that the previous expression can be recast as follows

$$\int_{-\infty}^{+\infty} e n_e dx = \int_{s_e}^{+\infty} e n_{i_+} \tag{2.6.4.2}$$

or, alternatively

$$\sigma = \int_{-\infty}^{s_e} e n_{i_+} dx, \tag{2.6.4.3}$$

where

$$\sigma \equiv \int_{-\infty}^{+\infty} e \left(n_{i_+} - n_e \right). \tag{2.6.4.4}$$

As we can see from Eq. (2.6.4.3), the Brinkmann criterion can also be fulfilled when the quasineutrality breaks down. It is not hard to see that the Brinkmann criterion can be applied to electropositive plasma discharges, where positive ions belong to a single species and are the only charged species in the plasma, along with the electrons.

2.6.5 The Brinkmann criterion extension

In this section we will explore the possibility of generalizing the Brinkmann criterion Brinkmann (2007) to an electronegative gas discharge, with a multiple number of positive and negative ion species. The easiest way to achieve this goal is to add directly the negative ion densities $\sum_{i_-} n_{i_-}$ with the plus (negative) sign on the l.h.s. (r.h.s.) of Eq. (2.6.4.1) and to add a sum on the positive ion density, averaged on the number of ion species. So the Brinkmann criterion extension reads

$$\int_{-\infty}^{s} \left(n_e + \frac{\sum_{i_-}^{N_-} n_{i_-}}{N_-} \right) dx = \int_{s}^{+\infty} \left(\frac{\sum_{i_+}^{N_+} n_{i_+}}{N_+} - n_e - \frac{\sum_{i_-}^{N_-} n_{i_-}}{N_-} \right) dx, \tag{2.6.5.1}$$

where N_+ (N_-) is the number of positive (negative) species. The expression above can also be recast in the following way

$$\int_{-\infty}^{+\infty} \left(n_e + \frac{\sum_{i_-}^{N_-} n_{i_-}}{N_-} \right) dx = \int_{s}^{+\infty} \left(\frac{\sum_{i_+}^{N_+} n_{i_+}}{N_+} \right) dx. \tag{2.6.5.2}$$

Recasting the expression above in the same manner as we have done when we have found Eq. (2.6.4.2), we find

$$\tilde{\sigma} = \int_{-\infty}^{s_e} e \sum_{i_+} n_{i_+} dx, \tag{2.6.5.3}$$

where

$$\tilde{\sigma} \equiv \int_{-\infty}^{+\infty} e \left(\frac{\sum_{i_+}^{N_+} n_{i_+}}{N_+} - \frac{\sum_{i_-}^{N_-} n_{i_-}}{N_-} - n_e \right). \tag{2.6.5.4}$$

Assuming

$$\int_{-\infty}^{s_e} \left(\frac{\Sigma_{i_+}^{N_+} n_{i_+}}{N_+} \right) dx \approx 0, \tag{2.6.5.5}$$

from Eq. (2.6.5.4) we get

$$\tilde{\sigma} = \int_{-\infty}^{+\infty} e \left(\frac{\Sigma_{i_+}^{N_+} n_{i_+}}{N_+} - \frac{\Sigma_{i_-}^{N_-} n_{i_-}}{N_-} - n_e \right) dx = 0. \tag{2.6.5.6}$$

Since some of the most used settings in PIC/MCC simulations involves two positive ion species and one negative ion species, we can set, for example, $N_+ = 2$ and $N_- = 1$, getting

$$\int_{-\infty}^{+\infty} e \left(\frac{n_{1_+} + n_{2_+}}{2} - n_- - n_e \right) = 0. \tag{2.6.5.7}$$

The equation above can be solved by the strict equality

$$\frac{n_{1_+}(t^*, x^*) + n_{2_+}(t^*, x^*)}{2} - n_-(t^*, x^*) - n_e(t^*, x^*) = 0, \tag{2.6.5.8}$$

where t^* is the time-step considered and x^* is expected to be close to the electron sheath edge s_e.

2.7 The Bohm sheath criterion in electropositive plasma discharge

In order for the transition from the quasi-neutral plasma to the space charge region of the sheath to occur (or in other words in order for the electron density to drop faster than the ion density in the sheath region so that quasi-neutrality is broken), it can be shown that a condition known as the Bohm criterion has to be satisfied. In the following we will assume electropositive gas, Maxwellian electrons, collisionless sheath ($\lambda_i \gg s$, where s is the sheath thickness), negative sign of the potential in the sheath region ($\phi(z > 0) < 0$), as well as the following boundary conditions at the sheath edge:

$$\phi(z) \bigg|_{z=0} = 0 \tag{2.7.0.1}$$

$$\frac{\partial \phi(z)}{\partial z} \bigg|_{z=0} = 0. \tag{2.7.0.2}$$

All the assumptions/constraints listed above are needed in order to build the Bohm criterion and will be relaxed later, when electronegative plasma discharges will be considered.

We will start from the equation of continuity of the ion flux and the conservation of the ion energy in the space charge sheath respectively

$$n_{i_+}(z)v_{i_+}(z) = n_{i_+}(0)v_{i_+}(0) + C$$

$$\frac{1}{2}m_{i_+}v_{i_+}^2(z) = \frac{1}{2}m_{i_+}v_{i_+}^2(0) - e\phi(z). \tag{2.7.0.3}$$

The combination of both equations gives

$$n_{i_+}(z) = \left(\frac{C}{v_{i_+}(0)} + n_{i_+}(0)\right)\left(1 - \frac{2e\phi(z)}{m_{i_+}v_{i_+}^2(0)}\right)^{-\frac{1}{2}}. \tag{2.7.0.4}$$

Using the assumption made in the previous subsection we are able to write the Poisson equation (2.1.0.1) in the following way

$$\frac{\partial^2 \phi(z)}{\partial z^2} = \frac{e}{\varepsilon_0}\left[n_e(z) - n_{i_+}(z)\right] = \frac{e}{\varepsilon_0}\left\{n(0)\exp\left(\frac{\phi(z)}{T_e}\right) - \left(\frac{C}{v_{i_+}(0)} + n(0)\right)\left(1 - \frac{2e\phi(z)}{m_{i_+}v_{i_+}^2(0)}\right)^{-\frac{1}{2}}\right\}. \tag{2.7.0.5}$$

Multiplying by $\frac{\partial \phi}{\partial z}$ and integrating over z we find

$$\frac{1}{2}\int_0^\phi \frac{\partial}{\partial z}\left(\frac{\partial \phi}{\partial z}\right)^2 dz =$$

$$\frac{e}{\varepsilon_0}\left\{n(0)\int_0^\phi \frac{\partial \phi}{\partial z}\exp\left(\frac{\phi(z)}{T_e}\right)dz - \left(\frac{C}{v_{i_+}(0)} + n(0)\right)\int_0^\phi \frac{\partial \phi}{\partial z}\left(1 - \frac{2e\phi(z)}{m_{i_+}v_{i_+}^2(0)}\right)^{-\frac{1}{2}}dz\right\}. \tag{2.7.0.6}$$

Now let us perform the integral. We find

$$\frac{1}{2}\left[\left(\frac{\partial \phi}{\partial z}\right)^2\right]_0^\phi =$$

$$\frac{e}{\varepsilon_0}\left\{n(0)\left[T_e\exp\left(\frac{\phi}{T_e}\right)\right]_0^\phi + \left(\frac{C}{v_{i_+}(0)} + n(0)\right)\left(\frac{m_{i_+}v_{i_+}^2(0)}{e}\right)\left[\sqrt{1 - \frac{2e\phi(z)}{m_{i_+}v_{i_+}^2(0)}} - 1\right]_0^\phi\right\}. \tag{2.7.0.7}$$

We can form a Taylor expansion on ϕ using the boundary conditions at the sheath edge shown in Eq. (2.7.0.1) which we will rewrite for completeness

$$\phi(z)\bigg|_{z=z_s} = 0 \quad \text{and} \quad \frac{\partial \phi(z)}{\partial z}\bigg|_{z=z_s} = 0. \tag{2.7.0.8}$$

The first term on the r.h.s. of Eq. (2.7.0.7), after the Taylor expansion, reads

$$\left[T_e\exp\left(\frac{\phi}{T_e}\right)\right]_0^\phi \approx T_e\left[\frac{1}{2}\frac{\phi^2}{T_e^2} + \sum_{k=3}\frac{1}{k!}\left(\frac{\phi}{T_e}\right)^k\right]. \tag{2.7.0.9}$$

As regards to the second term of the r.h.s. of Eq. (2.7.0.7), knowing that

$$\sqrt{1-y} = 1 - \frac{y}{2} - \frac{y^2}{8} - \sum_{k=3} y^k \frac{(2k-3)!}{k!(k-2)!2^{2k-2}}, \qquad (2.7.0.10)$$

we have

$$\left[\sqrt{1 - \frac{2e\phi(z)}{m_{i_+} v_{i_+}^2(0)}} - 1\right]_0^\phi \approx -\left\{ \frac{e^2\phi^2}{2m_{i_+}^2 v_{i_+}^4(0)} + \sum_{k=3} \frac{(2k-3)!}{k!(k-2)!2^{2k-2}} \left(\frac{e}{m_{i_+} v_{i_+}^2} \right)^k \phi^k \right\}. \qquad (2.7.0.11)$$

In this way, applying the 2nd condition of Eq. (2.7.0.8) to the l.h.s. of Eq. (2.7.0.7) and inserting the Taylor expansions of Eqs. (2.7.0.9) and (2.7.0.11) inside Eq. (2.7.0.7), we find

$$\frac{1}{2}\left(\frac{\partial \phi}{\partial z}\right)^2 = \frac{e}{\varepsilon_0}\left\{ \frac{\phi^2}{2}\left[\frac{n(0)}{T_e} - \left(\frac{C}{v_{i_+}(0)} + n(0)\right)\frac{e}{m_{i_+} v_{i_+}^2} \right] \right\}$$

$$+ \frac{e}{\varepsilon_0}\sum_{k=3} \phi^k \left[\frac{n(0)}{k!}\frac{1}{T_e^{k-1}} - \left(\frac{C}{v_{i_+}(0)} + n(0)\right)\frac{(2k-3)!}{k!(k-2)!2^{2k-2}}\left(\frac{e}{m_{i_+} v_{i_+}^2} \right)^{k-1} \right]. \qquad (2.7.0.12)$$

Now, since

$$\left(\frac{\partial \phi}{\partial z}\right)^2 \geq 0, \qquad (2.7.0.13)$$

we have

$$\frac{e}{\varepsilon_0}\left\{ \frac{\phi^2}{2}\left[\frac{n(0)}{T_e} - \left(\frac{C}{v_{i_+}(0)} + n(0)\right)\frac{e}{m_{i_+} v_{i_+}^2} \right] \right\}$$

$$+ \frac{e}{\varepsilon}\sum_{k=3} \phi^k \left[\frac{n(0)}{k!}\frac{1}{T_e^{k-1}} - \left(\frac{C}{v_{i_+}(0)} + n(0)\right)\frac{(2k-3)!}{k!(k-2)!2^{2k-2}}\left(\frac{e}{m_{i_+} v_{i_+}^2} \right)^{k-1} \right] \geq 0. \qquad (2.7.0.14)$$

Since ε is assumed to be positive in the sheath region, we have

$$\frac{\phi^2}{2}\left[\frac{n(0)}{T_e} - \left(\frac{C}{v_{i_+}(0)} + n(0)\right)\frac{e}{m_{i_+} v_{i_+}^2} \right]$$

$$+ \sum_{k=3} \phi^k \left[\frac{n(0)}{k!}\frac{1}{T_e^{k-1}} - \left(\frac{C}{v_{i_+}(0)} + n(0)\right)\frac{(2k-3)!}{k!(k-2)!2^{2k-2}}\left(\frac{e}{m_{i_+} v_{i_+}^2} \right)^{k-1} \right] \geq 0. \qquad (2.7.0.15)$$

Let us see what happens if we truncate the expression of Eq. (2.7.0.15) to the second order in k. We find

$$\left[\frac{n(0)}{T_e} - \left(\frac{C}{v_{i_+}(0)} + n(0) \right) \frac{e}{m_{i_+} v_{i_+}^2} \right] \geq 0. \tag{2.7.0.16}$$

For $C = 0$ Eq. (2.7.0.16) becomes

$$v_{i_+} \geq \sqrt{\frac{eT_e}{m_{i_+}}} \equiv u_B \tag{2.7.0.17}$$

which is the original Bohm criterion (Bohm, 1949). Instead, keeping $C \neq 0$, we find

$$v_{i_+}^2 \geq \frac{eT_e}{m_{i_+}} \left[\frac{C}{v_{i_+}(0)n(0)} + 1 \right]. \tag{2.7.0.18}$$

Furthermore, since $v_{i_+}^2 \geq 0$, we have to impose

$$C \geq -v_{i_+}(0)n(0) \tag{2.7.0.19}$$

2.8 The generalized Bohm sheath criterion

A generalized Bohm sheath criterion was derived (Riemann, 1991; Meichsner et al., 2013) for the limit $\lambda_{De} \rightarrow 0$ including electrons and negative ions. The expression is the following

$$\frac{1}{m_{i_+}} \int_0^{+\infty} \frac{1}{v_+^2} f(v_{i_+}) dv_{i_+} = \frac{1}{m_{i_+}} \left\langle \frac{1}{v_{i_+}^2} \right\rangle \leq \frac{1}{en_{i_+}(0)} \frac{d(n_e + n_-)}{d\phi_s} \bigg|_{\phi=0}. \tag{2.8.0.1}$$

Replacing the ion energy distribution function (IEDF) by the Dirac delta function as well as the Maxwellian EEDF, one finds

$$\frac{1}{m_{i_+}} \int_0^{+\infty} \frac{1}{v_{i_+}^2} f(v_+) dv_{i_+} = \frac{1}{m_{i_+} v_{i_+}^2(0)} \leq \frac{1}{e} \frac{d}{d\phi} \exp\left(\frac{e\phi}{k_B T_e} \right) \bigg|_{\phi=0} = \frac{1}{k_B T_e}, \tag{2.8.0.2}$$

which is the same expression found in Eq. (2.7.0.17). Moreover, in the literature the previous expression has been further generalized (Allen, 2009) in the following way

$$\frac{1}{m_{i_+}} \left\langle \frac{1}{v_{i_+}^2} \right\rangle \leq -\frac{1}{m_e} \int_{-\infty}^{+\infty} \frac{1}{v_e} \frac{df_e}{dv_e} dv_e. \tag{2.8.0.3}$$

Eq. (2.8.0.2) can be applied to electronegative discharges. Under the assumption of one positive and one negative species, Eq. (2.8.0.2) can be simplified considering cold ions and Maxwellian electrons. Therefore, setting $\gamma_{i_-} \equiv \frac{T_e}{T_{i_-}}$ and the electronegativity $\alpha \equiv \frac{n_{i_-}}{n_e}$, one can build the following relations

$$n_{i_+}(0) = (1 + \alpha_0) n_e(0) \tag{2.8.0.4}$$

$$n_e + n_{i_+} = n_e(0) \left[\exp\left(\frac{e\phi}{k_B T_e} \right) \right], \tag{2.8.0.5}$$

where α_0 is the center electronegativity. Moreover, in order to get the previous expressions, the quasineutrality condition at the sheath edge has been employed. Plugging Eq. (2.8.0.4) into Eq. (2.8.0.2), one finds the Bohm sheath criterion for an electronegative gas discharge

$$\frac{k_B T_e}{m_{i_+} v_{i_+}^2} \leq \frac{1 + \alpha_0 \gamma_-}{1 + \alpha_0}, \tag{2.8.0.6}$$

where monoenergetic ions at the sheath edge have been considered. Now, let us consider the Boltzmann relation for the electrons

$$n_e(0) = n_{e,pl} \exp\left(\frac{-e\phi_{pl}}{k_B T_e}\right), \tag{2.8.0.7}$$

where $n_{e,pl}$ and ϕ_{pl} are the bulk electron density and the voltage drop within the bulk, respectively. For the negative ions the following relation holds

$$n_-(0) = n_{-,pl} \exp\left(\frac{-e\phi_{pl}}{k_B T_{i_-}}\right) \tag{2.8.0.8}$$

in the presheath, where $n_{-,pl}$ is the bulk negative ion density. From Eqs. (2.8.0.7) and (2.8.0.8) follows

$$\alpha_0 = \alpha_{pl} \exp\left[e\left(1 - \gamma_{i_-}\right) \frac{\phi_{pl}}{k_B T_e}\right]. \tag{2.8.0.9}$$

Moreover, by using the energy conservation of negative ions, we obtain

$$\frac{e\phi_{pl}}{k_B T_e} = \frac{1}{2} \frac{1 + \alpha_0}{1 + \gamma_{i_-} \alpha_0}. \tag{2.8.0.10}$$

Plugging Eq. (2.8.0.10) into Eq. (2.8.0.9), we find

$$\alpha_{pl} = \alpha_0 \exp\left[\frac{(1 + \alpha_0)(\gamma - 1)}{2(1 + \gamma_{i_-} \alpha_0)}\right], \tag{2.8.0.11}$$

which is the expression for the bulk plasma electronegativity (Meichsner et al., 2013). We observe that, if the bulk plasma electronegativity α_{pl} is known, both the electronegativity at the sheath edge α_0 and $e\phi/k_B T_e$ can be calculated. Such numerical calculations have been performed by Boyd and Thompson (1959), who found that for $\alpha_{pl} < 2$ and $\gamma > 30$ the plasma sheath is similar to electropositive plasmas. Later, Braithwaite and Allen (1988) have shown the additional formation of double layer for $\gamma > \left(5 + 24^{1/2}\right)$.

Several authors (Allen, 2009; Lieberman and Lichtenberg, 2005) have proposed an expression for the Bohm sheath criterion in electropositive plasmas for multiple species. By using the Poisson's equation including multiple positive species only, along with the continuity equation for cold ions, we are allowed to write

$$\frac{dn_{i_+}}{d\Phi} = \frac{en_{i_+}}{m_{i_+} v_{i_+}^2}, \tag{2.8.0.12}$$

where we have also made use of the first momentum macroscopic Boltzmann equation (momentum conservation equation) (Lieberman and Lichtenberg, 2005; Meichsner et al., 2013). Using the Boltzmann relation for Maxwellian electrons ($n_e = n_0 \exp(\Phi\,T_e)$), we have

$$\frac{1}{n_e}\frac{dn_e}{d\Phi}\bigg|_s = \frac{1}{T_e}. \tag{2.8.0.13}$$

Moreover, using the Bohm criterion, we get

$$\sum_{i_+}\frac{dn_{i_+}}{d\Phi}\bigg|_s = \frac{dn_e}{d\Phi}\bigg|_s. \tag{2.8.0.14}$$

Plugging Eqs. (2.8.0.12) and (2.8.0.13) into Eq. (2.8.0.14), we get the final expression for the multispecies Bohm criterion in an electropositive plasma (Lieberman and Lichtenberg, 2005; Gozadinos, 2001)

$$\sum_{i_+}\frac{en_{i_+s}}{m_{i_+}u_{i_+s}^2} = \frac{n_{i_+s}}{T_e}. \tag{2.8.0.15}$$

Finally, it can be shown that the expression above does not define a unique Bohm velocity for each the positive ion species (Lieberman and Lichtenberg, 2005; Gozadinos, 2001).

2.9 Discharge currents

2.9.1 General principles

The total current density $J_T(t,x)$ flowing through the discharge can be decomposed as follows (Lieberman and Lichtenberg, 2005):

$$\bar{J}_T(t,x) = \bar{J}_{cond} + \bar{J}_{displ} + \bar{J}_P + \bar{J}_M + \bar{J}_{ion}, \tag{2.9.1.1}$$

where $\bar{J}_{cond}$ is the electron current density, $\bar{J}_{ion}$ is the ion current density, $\bar{J}_{displ}$ is the displacement current density, $\bar{J}_P$ is the polarization current density due to the motion of bound charges in a dielectric medium and $\bar{J}_M$ is due to magnetic moments in a magnetic material. Since we are dealing with a plasma in a vacuum we can state

$$\bar{\nabla}\cdot\left(\bar{\nabla}\times\bar{H}\right) = 0 = \bar{\nabla}\cdot\bar{J}_T = \bar{\nabla}\cdot\left(\bar{J}_{cond} + \bar{J}_{displ} + \bar{J}_{ion}\right) \tag{2.9.1.2}$$

or, in other words

$$J_{cond}(t,x) + J_{displ}(t,x) + J_{ion} = J_T(t), \tag{2.9.1.3}$$

where we have considered the one dimensional case for simplicity. Eq. (2.9.1.3) is extremely important because it states that the spatial behaviours of both the electron current density and the displacement current density must compensate somehow in order to sustain the discharge.

2.9.2 Time averaged current density

The time averaged analogous of Eq. (2.9.1.3) reads

$$\overline{J_{\text{cond}}} + \overline{J_{\text{displ}}} + \overline{J_{\text{ions}}} = \overline{J_{\text{T}}}. \tag{2.9.2.1}$$

Now let us focus on the quantity $\overline{J_{\text{displ}}}$. Since the electric field E is a function in t, we know that

$$\overline{J_{\text{displ}}} = \frac{1}{T} \int_0^T \varepsilon_0 \frac{\partial E}{\partial t} dt = 0. \tag{2.9.2.2}$$

Finally, let us consider the quantity $\overline{J_{\text{T}}}$. We know that J_{T} has to be a periodic function in T. In general, when $f(T)$ is a continuous periodic function with period T, the anti-derivatives of f are periodic if and only if

$$\int_0^T f(t)dt = 0. \tag{2.9.2.3}$$

This means that, defining $h(s)$ as

$$h(s) \equiv \int_0^s J_{\text{T}}(t)dt, \tag{2.9.2.4}$$

we can state, by using Eq. (2.9.2.1)

$$\text{If } h(s) \text{ is periodic} \implies \overline{J_{\text{cond}}} + \overline{J_{\text{ions}}} = 0 \tag{2.9.2.5}$$
$$\text{If } h(s) \text{ is not periodic} \implies \overline{J_{\text{cond}}} + \overline{J_{\text{ions}}} = \overline{J_{\text{T}}} \tag{2.9.2.6}$$

2.10 Frequency domain

2.10.1 The set up

Let us start by considering the first momentum macroscopic Boltzmann equation (Lieberman and Lichtenberg, 2005; Meichsner et al., 2013)

$$\frac{\partial (m_e n_e u_e)}{\partial t} + en_e E + m_e \nu_e n_e u_e = 0, \tag{2.10.1.1}$$

where the spatial gradients have been neglected. Setting for electrically driven discharge

$$E = \tilde{E} \exp(i\omega t) \tag{2.10.1.2}$$
$$u_e = \tilde{u}_e \exp(i\omega t), \tag{2.10.1.3}$$

where ω is the driving frequency, and considering n_e as time independent, Eq. (2.10.1.23) becomes

$$im_e \omega n_e \tilde{u}_e = -m_e \nu_e n_c \tilde{u}_e - en_e \tilde{E}, \tag{2.10.1.4}$$

after having neglected non linear terms. Eq. (2.10.1.4) leads directly to

$$\tilde{J}_e = \sigma\tilde{E} \quad \text{with} \quad \sigma = \frac{e^2 n_e}{m_e(i\omega + v_c)} = \frac{\varepsilon_0 \omega_{pe}^2}{(i\omega + v_c)}, \qquad (2.10.1.5)$$

where ω_{pe} is the electron plasma frequency and is given in Eq. (2.3.0.8). By using Eq. (2.9.1.3) and neglecting the ion current density we can write the total current density amplitude as

$$\tilde{J}_T = \tilde{J}_{cond} + \tilde{J}_{displ} = \sigma\tilde{E} + i\varepsilon_0\omega\tilde{E}. \qquad (2.10.1.6)$$

We can write the previous expression in two different forms

$$\tilde{J}_T = i\omega\varepsilon_0\varepsilon_p(\omega)\tilde{E} \qquad (2.10.1.7)$$

with

$$\varepsilon_p(\omega) = 1 - \frac{\omega_{pe}^2}{\omega(\omega - iv_c)} = 1 - \frac{i\sigma(\omega)}{\varepsilon_0\omega}, \qquad (2.10.1.8)$$

where ε_p is the relative dielectric constant, the composite quantity $\varepsilon \equiv \varepsilon_0\varepsilon_p$ is the plasma dielectric constant and

$$\tilde{J}_T = \sigma_p\tilde{E} \qquad \text{with} \quad \sigma_p = i\omega\varepsilon_0\varepsilon_p(\omega). \qquad (2.10.1.9)$$

Moreover, by defining the refractive index of the media as

$$n_{ref}^2 = \varepsilon_p(\omega) = \frac{k^2 c^2}{\omega^2}, \qquad (2.10.1.10)$$

we can state, making use of Eq. (2.10.1.7), that

$$\frac{k^2 c^2}{\omega^2} = 1 - \frac{\omega_{pe}^2}{\omega(\omega - iv_c)}, \qquad (2.10.1.11)$$

which is the dispersion relation or, alternatively

$$k = \frac{\omega}{c}\sqrt{1 - \frac{\omega_{pe}^2}{\omega(\omega - iv_c)}}. \qquad (2.10.1.12)$$

Moreover, recalling that $k = k_r - ik_i$, where the real part k_e determines the wavelength and the phase velocity of the wave while the imaginary part k_i defines the skin depth $\delta = k_i^{-1}$, we are allowed to write

$$k_r - i\delta^{-1} = \frac{\omega}{c}\sqrt{1 - \frac{\omega_{pe}^2}{\omega(\omega - iv_c)}}. \qquad (2.10.1.13)$$

Finally, it is worth noting that in RF plasmas $\omega \ll \omega_{pe}$. Now, we consider two important conditions.

Low pressure ($\nu_c < \omega$)

From Eqs. (2.10.1.6), (2.10.1.7), (2.10.1.9) and (2.10.1.11) we see that, in this case

$$\varepsilon_p(\omega) \approx 1 - \frac{\omega_{pe}^2}{\omega^2} \qquad (2.10.1.14)$$

$$\sigma_p \approx i\omega\varepsilon_0 \left(1 - \frac{\omega_{pe}^2}{\omega^2} \right) \qquad (2.10.1.15)$$

$$\sigma \approx -\frac{i\varepsilon_0\omega_{pe}^2}{\omega} \qquad (2.10.1.16)$$

$$k^2c^2 \approx \omega^2 - \omega_{pe}^2. \qquad (2.10.1.17)$$

From Eqs. (2.10.1.17) and (2.10.1.14) we see that for $\omega < \omega_{pe}$ there is no wave propagation and that $\varepsilon_p < 0$. So, for $\omega < \omega_{pe}$, the plasma behaves like a conductor such that the electromagnetic waves cannot penetrate into its interior. Finally, from Eq. (2.10.1.13), we get $\delta = c/\omega_{pe} = \delta_{es}$, which is the collisionless skin depth shown in Eq. (2.4.0.1). On the other hand, when $\omega > \omega_{pe}$, we observe that the electromagnetic waves are allowed to propagate (Eq. (2.10.1.17)) and that $0 < \varepsilon_p < 1$. In this case the plasma behaves as an ordinary dielectric medium.

High pressure ($\nu_c > \omega$)

From Eqs. (2.10.1.6), (2.10.1.7) and (2.10.1.9) we see that, in this case

$$\varepsilon_p \approx 1 - \frac{i\omega_{pe}^2}{\omega\nu_c} \qquad (2.10.1.18)$$

$$\sigma_p \approx i\omega\varepsilon_0 + \frac{\varepsilon_0\omega_{pe}^2}{\nu_c} \qquad (2.10.1.19)$$

$$\sigma \approx \frac{\varepsilon_0\omega_{pe}^2}{\nu_c} \qquad (2.10.1.20)$$

$$\frac{k^2c^2}{\omega^2} \approx 1 - \frac{i\omega_{pe}^2}{\omega\nu_c}. \qquad (2.10.1.21)$$

From the equations above we see that, when $\omega_{pe} \ll \omega$,

$$\varepsilon \approx 1 \qquad (2.10.1.22)$$

$$\frac{\omega^2}{k^2} = c^2, \qquad (2.10.1.23)$$

i.e. the plasma behaves as a perfect dielectric. Moreover, from Eq. (2.10.1.13), applying the conditions explained above, one finds

$$\delta = \frac{c}{\omega_{pe}} \sqrt{\frac{2\nu_e}{\omega}}, \qquad (2.10.1.24)$$

which is the expression for the collisionless skin depth in the high pressure limit. When $\nu_c \gg \omega_{pe}$, (collisional plasma) the skin depth is very large and the plasma behaves as a perfect dielectric.

3 The Boltzmann equation

3.1 Boltzmann equation for electrons

3.1.1 The history

During the past three decades several attempts to describe correctly the behaviour of the electron heating using the Boltzmann equation have been made. Surendra and Dalvie (1993) were the first to set up a mathematical model to describe the electron power absorption using the Boltzmann equations for both electrons and ions using PIC/MCC simulation results as input. They were able to isolate all the single terms contributing to both the electric field and the electron power absorbed. Moreover, they found the electron pressure term to be important for the collisionless heating and they observed, for a constant electron temperature, that the collisionless electron heating vanishes on time average. In the years that followed several authors used the formulation set forth by Surendra and Dalvie (1993) to develop similar models (Turner, 1995; Gozadinos et al., 2001; Lafleur et al., 2014a; Liu et al., 2018; Brinkmann, 2016; Grapperhaus and Kushner, 1997; Kaganovich et al., 1996). Among these, Brinkmann (2016) derived an unified description of electron power absorption in capacitively coupled discharges using a mathematical formulation where the electron density profile has been approximated by a smooth step function, finding that the total time averaged electron power absorption is the sum of four terms, each one corresponding to one of the heating mechanism known from separate previous theories, i.e. non linear electron resonance heating, stochastic heating (hard wall model), ambipolar/pressure heating and Ohmic heating. Brinkmann also demonstrated that a time dependent electron temperature is necessary to obtain a non zero time averaged electron power absorption. More recently, Schulze used a simplified moment analysis of the Boltzmann equation where the electron temperature gradient was both neglected and considered (Schulze et al., 2008a, 2018) in order to describe both the electric field and the electron power absorbed in an electropositive low pressure capacitively coupled argon discharge. They found that the time averaged ambipolar electron power absorption completely vanishes for a temporally independent electron temperature. In the following we will review the mathematical set up needed to address the physics behind the electric field and the electron power absorption in plasma discharges (Lieberman and Lichtenberg, 2005; Meichsner et al., 2013; Tong, 2012)

3.1.2 The Boltzmann equation environment

Our starting point will be the Boltzmann Equation

$$\frac{\partial f}{\partial t} + v_k \frac{\partial f}{\partial x_k} + \frac{F_k}{m} \frac{\partial f}{\partial v_k} = \left. \frac{\partial f}{\partial t} \right|_{\text{coll}} \equiv C(f). \tag{3.1.2.1}$$

In the literature one often finds the following definition

$$\boxed{\text{Streaming Operator}} \equiv \frac{\partial}{\partial t} + v_k \frac{\partial}{\partial x_k} + \frac{F_k}{m} \frac{\partial}{\partial v_k}, \tag{3.1.2.2}$$

which is commonly referred to as streaming term. The approach reflected by the Boltzmann equation approach assumes the following inequality

$$\boxed{\text{Time between collisions}} \equiv \tau \geq \tau_{\text{coll}} \equiv \boxed{\text{Collision Time}}. \tag{3.1.2.3}$$

3.1.3 The collision integral for elastic collisions

Now, let us build the collisional integral which is the term present on the r.h.s. of Eq. (3.1.2.1). To make this we will assume that a particle sits at $(\vec{x}_1, \vec{v}_1)$ and collides with another particle at $(\vec{x}_2, \vec{v}_2)$ in the phase space. In the following we assume the collisions to be local so that

$$\vec{x}_1 = \vec{x}_2 \ \text{ at the collision point.} \tag{3.1.3.1}$$

We will assume that these particles collide at velocity $\vec{v}_1$ and $\vec{v}_2$ and emerge with velocity $\vec{v}'_1$ and $\vec{v}'_2$. Then, we can define the rate at which the collision occurs as

$$\boxed{\text{Rate}} = \psi\left(\vec{p}_1, \vec{p}_2 | \vec{p}'_1, \vec{p}'_2\right) \times f\left(t, \vec{x}, \vec{p}_1, \vec{p}_2\right) d^3 p_2 d^3 p'_1 d^3 p'_2. \tag{3.1.3.2}$$

We remark that, at least in principle, it would be possible to calculate the ψ function from the two bodies potential $U(\vec{x})$, which is related to the differential cross section. Moreover, assuming elastic collisions, we also know the following relations to hold

$$\vec{p}_1 + \vec{p}_2 = \vec{p}'_1 + \vec{p}'_2 \tag{3.1.3.3}$$

$$\vec{p}_1^2 + \vec{p}_2^2 = \vec{p}'^2_1 + \vec{p}'^2_2, \tag{3.1.3.4}$$

where we have assumed

$$m_1 = m_2 \tag{3.1.3.5}$$

and

$$\nabla U_{\vec{x}} \approx 0 \ \text{ over microscopic scales.} \tag{3.1.3.6}$$

Now, since collisions can deflect particles out of a state with velocity $\vec{v}_1$ into a different velocity and vice versa, we are allowed to write

$$\left. \left(\frac{\partial f_1}{\partial t} \right) \right|_{\text{coll}} = + \int d^3 p_2 d^3 p'_1 d^3 p'_2 \left[\psi\left(\vec{p}'_1, \vec{p}'_2 | \vec{p}, \vec{p}_1\right) f_2\left(\vec{r}, \vec{r}, \vec{p}'_1, \vec{p}'_2\right) \right]$$

$$- \int d^3 p_2 d^3 p'_1 d^3 p'_2 \left[\psi\left(\vec{p}, \vec{p}_2 | \vec{p}'_1, \vec{p}'_2\right) f_2\left(\vec{r}, \vec{r}, \vec{p}, \vec{p}_2\right) \right], \tag{3.1.3.7}$$

where the first (second) term captures scattering into (out of) the state $\vec{p}$. It is important to say that the expression shown in Eq. (3.1.3.7) is non vanishing when the conditions shown in Eqs. (3.1.3.3) and (3.1.3.4) are fulfilled. Now, under time reversal, we know that $\vec{p} \to -\vec{p}$, so that

$$\psi\left(\vec{p}, \vec{p}_2 | \vec{p}_1', \vec{p}_2'\right) = \psi\left(-\vec{p}_1', -\vec{p}_2' | -\vec{p}, -\vec{p}_2\right) \qquad (3.1.3.8)$$

as well as, under parity $\vec{x} \to -\vec{x}$

$$\psi\left(\vec{p}, \vec{p}_2 | \vec{p}_1', \vec{p}_2'\right) = \psi\left(-\vec{p}, -\vec{p}_2 | -\vec{p}_1', -\vec{p}_2'\right). \qquad (3.1.3.9)$$

Plugging Eq. (3.1.3.8) into Eq. (3.1.3.9), we arrive at the final relation

$$\psi\left(\vec{p}, \vec{p}_2 | \vec{p}_1', \vec{p}_2'\right) = \psi\left(\vec{p}_1', \vec{p}_2' | \vec{p}, \vec{p}_2\right). \qquad (3.1.3.10)$$

If the particle velocities are uncorrelated before the collision, we can state

$$f_2\left(\vec{r}, \vec{r}, \vec{p}, \vec{p}_2\right) = f_1\left(\vec{r}, \vec{p}\right) f_1\left(\vec{r}, \vec{p}_2\right). \qquad (3.1.3.11)$$

Such a condition is usually known in the literature as molecular chaos assumption. Plugging Eq. (3.1.3.11) into Eq. (3.1.3.7), we get

$$\left(\frac{\partial f_1}{\partial t}\right)\bigg|_{\text{coll}} =$$
$$\int d^3 p_2 d^3 p_1' d^3 p_2' \psi\left(\vec{p}_1', \vec{p}_2' | \vec{p}, \vec{p}_2\right) \left[f_1\left(\vec{r}, \vec{p}_1'\right) f_1\left(\vec{r}, \vec{p}_2'\right) - f_1\left(\vec{r}, \vec{p}\right) f_1\left(\vec{r}, \vec{p}_2\right)\right].$$
$$(3.1.3.12)$$

Moreover, we observe that the r.h.s. of Eq. (3.1.3.12) vanishes if the condition

$$f_1^{\text{eq}}\left(\vec{r}, \vec{p}_1'\right) f_1^{\text{eq}}\left(\vec{r}, \vec{p}_2'\right) = f_1^{\text{eq}}\left(\vec{r}, \vec{p}\right) f_1^{\text{eq}}\left(\vec{r}, \vec{p}_2\right) \qquad (3.1.3.13)$$

is fulfilled. By using the momentum and energy conservation equations (Eqs. (3.1.3.3) and (3.1.3.3)) it can be shown that Eq. (3.1.3.13) is fulfilled if and only if

$$f_1^{\text{eq}} = n\left(\frac{\beta}{2\pi m}\right)^{\frac{3}{2}} \exp\left(-\beta m \left(\vec{v} - \vec{u}\right)^2 / 2\right), \qquad (3.1.3.14)$$

which is the Maxwell-Boltzmann distribution. In the picture above $\vec{v}$ is the microscopic velocity, $\vec{u}$ is the drift velocity, n is the particle density and β can be identified as the inverse temperature such that $\beta = (kT)^{-1}$.

3.1.4 The global equilibrium Maxwell-Boltzmann distribution

Now, let us consider the expression shown in Eq. (3.1.3.14), which is the so called global equilibrium Maxwell-Boltzmann distribution

$$f_1^{\text{eq glob}} = n\left(\frac{m}{2\pi eT}\right)^{\frac{3}{2}} \exp\left(-\frac{m\left(\vec{v} - \vec{u}\right)^2}{2eT}\right), \qquad (3.1.4.1)$$

where $\vec{u}$ is a constant vector, while n and T are the constant electron density and the electron temperature, respectively. Integrating directly expression (3.1.4.1) we see that

$$\int f_1^{\text{eq glob}} d^3 v = n \tag{3.1.4.2}$$

$$\int v_k f_1^{\text{eq glob}} d^3 v = n u_k. \tag{3.1.4.3}$$

Taking the Boltzmann equation shown in Eq. (3.1.2.1), knowing that the collision operator is zero for the global equilibrium Maxwell-Boltzmann distribution as stated above, and knowing that T, v and u are space-time independent quantities, we are left with

$$-\frac{F_k}{eT} (v_k - u_k) f_1^{\text{eq glob}} = 0, \tag{3.1.4.4}$$

which is satisfied under two different conditions

$$F_k = 0 \implies \forall v_k , \ \forall u_k \tag{3.1.4.5}$$

$$F_k \neq 0 \implies v_k = u_k. \tag{3.1.4.6}$$

3.1.5 The Master equation

The average of a quantity $\vec{A}$ is defined as follows

$$\langle A \rangle = \frac{\int d^3 v \, A(\vec{x}, \vec{v}, t) f(\vec{x}, \vec{v}, t)}{\int f(\vec{x}, \vec{v}, t)}, \tag{3.1.5.1}$$

where $f(\vec{x}, \vec{v}, t)$ is a generic distribution. Setting

$$n(\vec{x}, t) = \int d^3 v \, f(\vec{x}, \vec{v}, t), \tag{3.1.5.2}$$

Eq. (3.1.5.1) becomes

$$\langle A \rangle = \frac{1}{n(\vec{x}, \vec{v}), t} \int d^3 v \, A(\vec{x}, \vec{v}, t) f(\vec{x}, \vec{v}, t). \tag{3.1.5.3}$$

Since $n(\vec{x}, t)$ does not depend on the velocity $\vec{v}$, we are free to write

$$\langle n(\vec{x}, t) \, A \rangle = n(\vec{x}, t) \langle A \rangle = \int d^3 v \, A(\vec{x}, \vec{v}, t) f(\vec{x}, \vec{v}, t). \tag{3.1.5.4}$$

Moreover, we can also define the following quantities

$$\langle n(\vec{x}, t) \, v \rangle = n(\vec{x}, t) \, u(\vec{x}, t) = \int d^3 v \, v \, f(\vec{x}, \vec{v}, t). \tag{3.1.5.5}$$

Since we are ultimately interested in quantities which vary slowly, we are looking for functions A which make the collisional term vanish. So we will set

$$\int d^3 v \, A(\vec{x}, \vec{v}, t) \left(\frac{\partial f}{\partial t} \right)\Big|_{\text{coll}} = 0. \tag{3.1.5.6}$$

Now, let us consider Eq. (3.1.2.1). Because the collision term vanishes, we have

$$\int d^3v \, A(\vec{x},\vec{v},t) \left(\frac{\partial}{\partial t} + v_i \frac{\partial}{\partial x_i} + \frac{F_i}{m} \frac{\partial}{\partial v_i} \right) f(\vec{x},\vec{v},t) = 0. \qquad (3.1.5.7)$$

In the following we will assume the distribution function $f(\vec{x},\vec{v},t)$ to decrease steeply to zero. Now, let us consider Eq. (3.1.5.7) term by term. As regards to the last term involving F_i, assuming F_i not to depend on v_i, the we get

$$\frac{\partial}{\partial v_i} \int d^3v \, A \, F_i \, f = \int F_i \frac{\partial A}{\partial v_i} \, f + \int \frac{F_i}{m} \frac{\partial f}{\partial v_i} \, A = 0. \qquad (3.1.5.8)$$

As regards to the second term we find

$$\frac{\partial}{\partial x_i} \int d^3v \, A \, v_i \, f = \int d^3v \, \frac{\partial A}{\partial x_i} \, v_i \, f + \int d^3v \, A_i \, v_i \, \frac{\partial f}{\partial x_i}, \qquad (3.1.5.9)$$

and for the first term

$$\frac{\partial}{\partial t} \int d^3v \, A \, f = \int d^3v \, \frac{\partial A}{\partial t} \, f + \int d^3v \, A \, \frac{\partial f}{\partial t}. \qquad (3.1.5.10)$$

Substituting Eqs. (3.1.5.8), (3.1.5.9), (3.1.5.10) into Eq. (3.1.5.7), we find

$$\frac{\partial}{\partial t} \int d^3v \, A \, f - \int d^3v \, \frac{\partial A}{\partial t} \, f + \frac{\partial}{\partial x_i} \int d^3v \, A \, v_i \, f - \int d^3v \, \frac{\partial A}{\partial x_i} \, v_i \, f - \int \frac{F_i}{m} \frac{\partial A}{\partial v_i} \, f = 0. \tag{3.1.5.11}$$

Using the bracket notation, the previous equation can be recast in the following way

$$\frac{\partial}{\partial t} \langle n \, A \rangle - \left\langle n \frac{\partial A}{\partial t} \right\rangle + \frac{\partial}{\partial x_i} \langle n \, A \, v_i \rangle - \left\langle n \, v_i \frac{\partial A}{\partial x_i} \right\rangle - \left\langle n \frac{F_i}{m} \frac{\partial A}{\partial v_i} \right\rangle = 0. \qquad (3.1.5.12)$$

This is the so called master equation. Recalling that $n(\vec{x},t)$ is a velocity independent quantity, Eq. (3.1.5.12) can be written as follows

$$\frac{\partial}{\partial t} [n \langle A \rangle] - n \left\langle \frac{\partial A}{\partial t} \right\rangle + \frac{\partial}{\partial x_i} [n \, \langle A \, v_i \rangle] - n \left\langle v_i \frac{\partial A}{\partial x_i} \right\rangle - n \left\langle \frac{F_i}{m} \frac{\partial A}{\partial v_i} \right\rangle = 0, \tag{3.1.5.13}$$

which is again the so called master equation.

3.1.6 The continuity equation

Setting $A = 1$ in Eq. (3.1.5.12), we find

$$\frac{\partial n}{\partial t} + \frac{\partial}{\partial x_i} (n u_i) = 0, \qquad (3.1.6.1)$$

which is the 0-th momentum macroscopic Boltzmann equation, also known in the literature as continuity equation.

3.1.7 Momentum part I

Setting $A = v_j$ in Eq. (3.1.5.12), we find

$$\frac{\partial (mnu_j)}{\partial t} + \frac{\partial \langle mnv_i v_j \rangle}{\partial x_i} - nF_j = 0. \tag{3.1.7.1}$$

Defining the quantities

$$w_i = v_i - u_i \tag{3.1.7.2}$$
$$P_{ij} = mn \langle w_i w_j \rangle, \tag{3.1.7.3}$$

along with the relationship

$$\langle v_i v_j \rangle = \langle w_i w_j \rangle + u_i u_j, \tag{3.1.7.4}$$

we can recast the term in the middle of the l.h.s. of Eq. (3.1.7.1) as follows

$$\frac{\partial (mnu_j)}{\partial t} + \frac{\partial P_{ij}}{\partial x_i} + mu_i u_j \frac{\partial n}{\partial x_i} + mnu_j \frac{\partial u_i}{\partial x_i} + mnu_i \frac{\partial u_j}{\partial x_i} - nF_j = 0. \tag{3.1.7.5}$$

The expression above is the first momentum (in the velocity v_j) macroscopic Boltzmann equation, also known in the literature as momentum conservation equation. Now, using the continuity equation shown in Eq. (3.1.6.1), we find

$$mn \left(\frac{\partial}{\partial t} + u_i \frac{\partial}{\partial x_i} \right) u_j = nF_j - \frac{\partial P_{ij}}{\partial x_i}. \tag{3.1.7.6}$$

Defining the material derivative

$$D_t \equiv \frac{\partial}{\partial t} + u_i \frac{\partial}{\partial x_i}, \tag{3.1.7.7}$$

we can rewrite Eq. (3.1.7.6) as follows

$$mnD_t = nF_j - \frac{\partial P_{ij}}{\partial x_i}. \tag{3.1.7.8}$$

3.1.8 Momentum part II

Setting $A = w_j$ in Eq. (3.1.5.12), we find

$$mn \frac{\partial u_j}{\partial t} + \frac{\partial P_{ij}}{\partial x_i} + mnu_i \frac{\partial u_j}{\partial x_i} - nF_j = 0. \tag{3.1.8.1}$$

The previous equation can be recasted as follows:

$$mn \left(\frac{\partial}{\partial t} + u_i \frac{\partial}{\partial x_i} \right) u_j = nF_j - \frac{\partial P_{ij}}{\partial x_i}, \tag{3.1.8.2}$$

which is surprisingly exactly the same as Eq. (3.1.7.6).

3.1.9 Kinetic energy part I

Setting $A = \frac{v^2}{2}$ in Eq. (3.1.5.12), we find

$$\frac{\partial}{\partial t} \left\langle \frac{mnv^2}{2} \right\rangle + \frac{\partial}{\partial x_i} \left\langle \frac{mnv^2 v_i}{2} \right\rangle - n \left\langle F_i v_i \right\rangle = 0. \tag{3.1.9.1}$$

Now, since $v^2 = \delta_{ij} v_i v_j$ and using

$$\left\langle mnw^2 \right\rangle = \text{Tr P} \tag{3.1.9.2}$$

$$mn \left\langle v^2 v_i \right\rangle = mn \left\langle w^2 w_i \right\rangle + mnu^2 u_i + 2u_k P_{ki} + u_i \text{Tr P}, \tag{3.1.9.3}$$

along with Eqs. (3.1.7.3) and (3.1.7.4), one finds

$$\frac{1}{2} \frac{\partial}{\partial t} \left[mnu^2 \right] + \frac{1}{2} \frac{\partial \text{Tr P}}{\partial t} + \frac{\partial}{\partial x_i} \left[\frac{mn \left\langle w^2 w_i \right\rangle}{2} + \frac{mnu^2 u_i}{2} + u_k P_{ki} + \frac{u_i \text{Tr P}}{2} \right] - nF_i u_i = 0. \tag{3.1.9.4}$$

Defining a new quantity, the heat flux

$$H_i \equiv \frac{1}{2} \left\langle mnw^2 w_i \right\rangle, \tag{3.1.9.5}$$

Eq. (3.1.9.4) becomes

$$\frac{1}{2} \frac{\partial}{\partial t} \left[mnu^2 \right] + \frac{1}{2} \frac{\partial \text{Tr P}}{\partial t} + \frac{\partial}{\partial x_i} \left[H_i + \frac{mnu^2 u_i}{2} + u_k P_{ki} + \frac{u_i \text{Tr P}}{2} \right] - nF_i u_i = 0. \tag{3.1.9.6}$$

The expression above is the second momentum (in the velocity v_j) macroscopic Boltzmann equation, also known in the literature as energy conservation equation.

3.1.10 Kinetic energy part II

Setting $A = \frac{(v-u)^2}{2} = \frac{w^2}{2}$ in Eq. (3.1.5.12), we find

$$\frac{\partial}{\partial t} \left[\frac{mn \left\langle w^2 \right\rangle}{2} \right] - n \left\langle \frac{\partial}{\partial t} \left(\frac{mw^2}{2} \right) \right\rangle + \frac{\partial}{\partial x_i} \left[\frac{mn \left\langle w^2 v_i \right\rangle}{2} \right]$$

$$- \frac{nm}{2} \left\langle v_i \frac{\partial w^2}{\partial x_i} \right\rangle - \frac{nF_i}{2} \left\langle \frac{\partial w^2}{\partial v_i} \right\rangle = 0. \tag{3.1.10.1}$$

Now, since

$$\left\langle \frac{\partial w^2}{\partial t} \right\rangle = -\frac{\partial u_k}{\partial t} \left\langle 2w_k \right\rangle = 0 \tag{3.1.10.2}$$

$$\left\langle v_i \frac{\partial w^2}{\partial x_i} \right\rangle = -2 \frac{\partial u_k}{\partial x_i} \left\langle w_i w_k \right\rangle \tag{3.1.10.3}$$

$$\left\langle \frac{\partial w^2}{\partial v_i} \right\rangle = \left\langle 2w_i \right\rangle = 0, \tag{3.1.10.4}$$

Eq. (3.1.10.1) becomes

$$\frac{\partial}{\partial t}\left[\frac{mn\langle w^2\rangle}{2}\right] + \frac{\partial}{\partial x_i}\left[\frac{mn\langle w^2 w_i\rangle}{2}\right] + \frac{\partial}{\partial x_i}\left[\frac{mnu_i\langle w^2\rangle}{2}\right]$$

$$+ \frac{\partial u_k}{\partial x_i}\langle mnw_i w_k\rangle = 0. \tag{3.1.10.5}$$

By using Eqs. (3.1.9.5), (3.1.9.2) and (3.1.7.3), Eq. (3.1.10.5) becomes

$$\frac{1}{2}\frac{\partial}{\partial t}\text{Tr P} + \frac{\partial H_i}{\partial x_i} + \frac{1}{2}\frac{\partial (u_i\text{Tr P})}{\partial x_i} + \frac{\partial u_k}{\partial x_i}P_{ik} = 0. \tag{3.1.10.6}$$

3.1.11 The ideal fluid

The full equation set of the macroscopic Boltzmann Equations is therefore given by

$$\frac{\partial n}{\partial t} + \frac{\partial}{\partial x_i}(nu_i) = 0 \tag{3.1.11.1}$$

$$\frac{\partial (mnu_j)}{\partial t} + \frac{\partial P_{ij}}{\partial x_i} + mu_iu_j\frac{\partial n}{\partial x_i} + mnu_j\frac{\partial u_i}{\partial x_i} + mnu_i\frac{\partial u_j}{\partial x_i} - nF_j = 0 \tag{3.1.11.2}$$

$$mn\frac{\partial u_j}{\partial t} + \frac{\partial P_{ij}}{\partial x_i} + mnu_i\frac{\partial u_j}{\partial x_i} - nF_j = 0 \tag{3.1.11.3}$$

$$\frac{1}{2}\frac{\partial}{\partial t}\left[mnu^2\right] + \frac{1}{2}\frac{\partial\text{Tr P}}{\partial t} + \frac{\partial}{\partial x_i}\left[H_i + \frac{mnu^2u_i}{2} + u_kP_{ki} + \frac{u_i\text{Tr P}}{2}\right] - nF_iu_i = 0 \tag{3.1.11.4}$$

$$\frac{1}{2}\frac{\partial}{\partial t}\text{Tr P} + \frac{\partial H_i}{\partial x_i} + \frac{1}{2}\frac{\partial (u_i\text{Tr P})}{\partial x_i} + \frac{\partial u_k}{\partial x_i}P_{ik} = 0. \tag{3.1.11.5}$$

3.1.12 Time varying quantities

Now let us express the temporal gradient of n, u_i and T by using the equation system shown above. First of all we know that, from Eq. (3.1.11.1)

$$\frac{\partial n}{\partial t} = -u_i\frac{\partial n}{\partial x_i} - n\frac{\partial u_i}{\partial x_i}. \tag{3.1.12.1}$$

On the other hand, from Eq. (3.1.11.3), we have

$$\frac{\partial u_j}{\partial t} = -\frac{e}{mn}\frac{\partial (nT)}{\partial x_j} - u_i\frac{\partial u_j}{\partial x_i} - \frac{eE_j}{m}, \tag{3.1.12.2}$$

where the ideal gas law $p_{ij} = \delta_{ij}enT$ and the relation $F_j = -eE_j$ have been employed. Finally, let us consider Eq. (3.1.11.5). Employing the ideals gas law again and using Eq. (3.1.12.1), one finds

$$\frac{\partial T}{\partial t} = -\frac{2T}{3}\frac{\partial u_i}{\partial x_i} - u_i\frac{\partial T}{\partial x_i} - \frac{2}{3}\frac{1}{en}\frac{\partial H_i}{\partial x_i}, \tag{3.1.12.3}$$

where the relation $\text{Tr}p_{ij} = 3enT$ has been used.

3.1.13 Displacement current

From Eq. (3.1.12.2) it is not difficult to calculate the displacement current J_{displ}. By taking the time derivative of both the r.h.s. and the l.h.s. of Eq. (3.1.12.2) we find

$$J_{\text{displ,j}} = -\frac{m_e \varepsilon_0}{e} \frac{\partial^2 u_j}{\partial t^2} - \varepsilon_0 \frac{\partial}{\partial t} \left[\frac{1}{n} \frac{\partial (nT)}{\partial x_j} \right] - \frac{m \varepsilon_0}{e} \frac{\partial}{\partial t} \left(u_i \frac{\partial u_j}{\partial x_i} \right). \tag{3.1.13.1}$$

3.1.14 Relating positive ion density to negative ion density

By taking the spatial derivative of both the r.h.s. and the l.h.s. of Eq. (3.1.12.2) we find

$$\frac{e}{m} \frac{\partial E_j}{\partial x_k} = -\frac{e}{m} \frac{\partial}{\partial x_k} \left[\frac{1}{n} \frac{\partial (nT)}{\partial x_j} \right] - \frac{\partial}{\partial x_k} \left(u_i \frac{\partial u_j}{\partial x_i} \right) - \frac{\partial^2 u_j}{\partial t \partial x_k}. \tag{3.1.14.1}$$

Setting $j = k$ and using the Poisson equation, we finally get

$$\frac{e^2}{m \varepsilon_0} \left(\sum_{i_+} n_{i_+} - \sum_{i_-} n_{i_-} - n_e \right) = -\frac{e}{m} \frac{\partial}{\partial x_j} \left[\frac{1}{n} \frac{\partial (nT)}{\partial x_j} \right] - \frac{\partial}{\partial x_j} \left(u_i \frac{\partial u_j}{\partial x_i} \right) - \frac{\partial^2 u_j}{\partial t \partial x_j}. \tag{3.1.14.2}$$

3.1.15 Isotropy and anisotropy

Now, let us consider the pressure tensor

$$p_{e,ij} = \begin{pmatrix} p_{x,x} & p_{x,y} & p_{x,z} \\ p_{y,x} & p_{y,y} & p_{y,z} \\ p_{z,x} & p_{z,y} & p_{z,z} \end{pmatrix} \tag{3.1.15.1}$$

and the temperature tensor

$$T_{e,ij} = \begin{pmatrix} T_{x,x} & T_{x,y} & T_{x,z} \\ T_{y,x} & T_{y,y} & T_{y,z} \\ T_{z,x} & T_{z,y} & T_{z,z} \end{pmatrix} \tag{3.1.15.2}$$

Assuming the ideal gas law (off-diagonal terms equal to zero), we are allowed to write

$$p_{e,ij} = e n_e T_{e,ij} \tag{3.1.15.3}$$

such that

$$\text{Tr}\left(p_{e,ij}\right) = e n_e \text{Tr}\left(T_{e,ij}\right), \tag{3.1.15.4}$$

Moreover, it is worth noting that every single component of the electron temperature has been calculated as $T_{e,ii} = \frac{2}{e} \mathcal{E}_{e,ii} - \frac{m_e}{e} u_{e,i}^2$ where $\mathcal{E}_{e,ii}$ and $u_{e,ii}^2$, with $i = x, y, z$, are the mean electron energy density and the mean electron velocity respectively. Since $\mathcal{E}_{e,i} = \frac{m_e}{2} \langle v_{e,i}^2 \rangle$ by definition, the expression for the electron temperature given above is the same as the one shown by Wilczek et al. (2020), when the mean particle velocity

is not negligible. Assuming both the pressure and the temperature to be isotropic, i.e. $p_e \equiv p_{e,xx} = p_{e,yy} = p_{e,zz}$, along with $T_e \equiv T_{e,xx} = T_{e,yy} = T_{e,zz}$, one finds

$$p_e = p_{e,ii} = en_e T_{e,ii} = en_e T_e. \qquad (3.1.15.5)$$

On the other hand, assuming the pressure (temperature) to be (not isotropic), i.e. setting $p_e \equiv p_{e,xx} = p_{e,yy} = p_{e,zz}$ and $T_e \equiv T_{e,xx} \neq T_{e,yy} \neq T_{e,zz}$, we find, by using Eq. (3.1.15.4)

$$p_e = en_e T_e, \qquad (3.1.15.6)$$

where

$$T_e \equiv \frac{T_{e,xx} + T_{e,yy} + T_{e,zz}}{3}. \qquad (3.1.15.7)$$

3.1.16 The local equilibrium Maxwell-Boltzmann distribution

Now, let us consider a new class of distributions which satisfies the condition for the collision operator to vanish (Eq. (3.1.3.13)). This class of distribution is a natural extension of the global equilibrium Maxwell-Boltzmann distribution, where now T, n and u are to be intended as space-time dependent quantities. Due to the space-time dependency, this class of distributions is known in the literature as "local". The expression for the local equilibrium Maxwell distribution reads

$$f_1^{\text{eq loc}}(t,\vec{x},\vec{v}) = n(t,\vec{x}) \left(\frac{m}{2\pi eT(t,\vec{x})} \right)^{\frac{3}{2}} \exp\left(-\frac{m(\vec{v} - \vec{u}(t,\vec{x}))^2}{2eT(t,\vec{x})} \right), \qquad (3.1.16.1)$$

where $\vec{u}(t,\vec{x})$ is the electron distribution averaged velocity and $n(t,\vec{x})$, $T(t,\vec{x})$ are the space-time dependent electron density and electron temperature respectively. Integrating directly expression Eq. (3.1.16.1), we see that

$$\int f_1^{\text{eq loc}}(t,\vec{x},\vec{v}) d^3 v = n(t,\vec{x}) \qquad (3.1.16.2)$$

$$\int v_k f_1^{\text{eq loc}}(t,\vec{x},\vec{v}) d^3 v = u(t,\vec{x}). \qquad (3.1.16.3)$$

Now, we want to apply the streaming operator (Eq. (3.1.2.2)) to see what happens. Since

$$\frac{\partial f_1^{\text{eq loc}}}{\partial n} = \frac{f_1^{\text{eq loc}}}{n} \qquad (3.1.16.4)$$

$$\frac{\partial f_1^{\text{eq loc}}}{\partial T} = -\frac{3}{2}\frac{f}{T} + \frac{m}{2eT^2}(\vec{v} - \vec{u})^2 f_1^{\text{eq loc}} \qquad (3.1.16.5)$$

$$\frac{\partial f_1^{\text{eq loc}}}{\partial u_i} = \frac{m}{eT}(v_i - u_i) f_1^{\text{eq loc}} = -\frac{\partial f_1^{\text{eq loc}}}{\partial v_i} \qquad (3.1.16.6)$$

and, since

$$\frac{\partial f_1^{\text{eq loc}}}{\partial t} = \frac{\partial f_1^{\text{eq loc}}}{\partial n}\frac{\partial n}{\partial t} + \frac{\partial f_1^{\text{eq loc}}}{\partial T}\frac{\partial T}{\partial t} + \frac{\partial f_1^{\text{eq loc}}}{\partial u_i}\frac{\partial u_i}{\partial t} \qquad (3.1.16.7)$$

$$\frac{\partial f_1^{\text{eq loc}}}{\partial x_i} = \frac{\partial f_1^{\text{eq loc}}}{\partial n}\frac{\partial n}{\partial x_i} + \frac{\partial f_1^{\text{eq loc}}}{\partial T}\frac{\partial T}{\partial x_i} + \frac{\partial f_1^{\text{eq loc}}}{\partial u_j}\frac{\partial u_j}{\partial x_i}, \qquad (3.1.16.8)$$

we can write the streaming term applying the streaming operator (Eq. (3.1.2.2)) to the local equilibrium distribution, getting

$$
\boxed{\text{Streaming Term}} = f_1^{\text{eq loc}} \left\{ \frac{1}{n}\frac{\partial n}{\partial t} + \frac{\partial T}{\partial t}\left[\frac{m}{2eT^2}(\vec{v}-\vec{u})^2 - \frac{3}{2}\frac{1}{T}\right] + \frac{m}{eT}[v_i - u_i]\frac{\partial u_i}{\partial t} + \right.
$$
$$
\left. v_i\frac{\partial T}{\partial x_i}\left[\frac{m}{2eT^2}(\vec{v}-\vec{u})^2 - \frac{3}{2}\frac{1}{T}\right] + \frac{m}{eT}v_i(v_j - u_j)\frac{\partial u_j}{\partial x_i} + \frac{v_i}{n}\frac{\partial n}{\partial x_i} + \frac{E_i}{T}(v_i - u_i)\right\},
$$
$$(3.1.16.9)$$

where he have set $F_i = -eE_i$. Now, we need to remove the quantities $\frac{\partial n}{\partial t}$, $\frac{\partial u_i}{\partial t}$ and $\frac{\partial T}{\partial t}$. By using Eqs. (3.1.12.1), (3.1.12.2) and (3.1.12.3), we get

$$
\boxed{\text{Streaming Term}} = f_1^{\text{eq loc}} \left\{ \frac{1}{T}\frac{\partial T}{\partial x}w_i\left[\frac{m}{2eT}\vec{w}^2 - \frac{5}{2}\right] + \right.
$$
$$
\left. \frac{m}{eT}\left[w_i w_j\frac{\partial u_j}{\partial x_i} - \frac{1}{3}\vec{w}^2\frac{\partial u_i}{x_i}\right] - \frac{2}{3}\frac{1}{enT}\frac{\partial H_i}{\partial x_i}\left[\frac{m}{2eT}\vec{w}^2 - \frac{3}{2}\right] \right\}. \qquad (3.1.16.10)
$$

As we can see, the expression above cannot easily vanish. This means that the local equilibrium Maxwell-Boltzmann distribution function does not solve the Boltzmann equation. In order to deal with such a situation, it may be helpful to employ the following equality

$$
f_1 = f_1^{\text{eq local}} + \delta f_1 \qquad (3.1.16.11)
$$

along with the so called relaxation time approximation or Bhatnagar-Gross-Krook operator

$$
C(f_1^{\text{eq local}}) \equiv \left(\frac{\partial f_1^{\text{eq local}}}{\partial t}\right)_{\text{coll}} = -\frac{\delta f_1}{\tau_{\text{relax}}}, \qquad (3.1.16.12)
$$

where τ_{relax} is the relaxation time and dictates the rate change of f_1. Plugging Eqs. (3.1.16.11) and (3.1.16.12) into Eq. (3.1.2.1), we get

$$
\boxed{\text{Streaming Term}} = \frac{\partial f_1^{\text{eq local}}}{\partial t} + v_k\frac{\partial f_1^{\text{eq local}}}{\partial x_k} + \frac{F_k}{m}\frac{\partial f_1^{\text{eq local}}}{\partial v_k} = -\frac{\delta f_1}{\tau_{\text{relax}}}, \quad (3.1.16.13)
$$

where the time derivative, the space derivative and the velocity derivative in δf_1 have been neglected. Finally, recalling Eq. (3.1.16.10), we find

$$
\delta f_1 \approx -\tau_{\text{relax}}\left\{ \frac{1}{T}\frac{\partial T}{\partial x}w_i\left[\frac{m}{2eT}\vec{w}^2 - \frac{5}{2}\right] + \right.
$$
$$
\left. \frac{m}{eT}\left[w_i w_j\frac{\partial u_j}{\partial x_i} - \frac{1}{3}\vec{w}^2\frac{\partial u_i}{x_i}\right] - \frac{2}{3}\frac{1}{enT}\frac{\partial H_i}{\partial x_i}\left[\frac{m}{2eT}\vec{w}^2 - \frac{3}{2}\right] \right\}f_1^{\text{eq loc}}. \quad (3.1.16.14)
$$

The quantity δf_1, which is the correction to the distribution, can be employed to revisit some of the transport properties. For further insights the reader is referred to Tong (2012).

3.1.17 Final expression for the fluid equations

Since in the cases considered above the pressure is always taken as being isotropic, the various cases explored previously can be recast into a single equation writing

$$p_e = p_{e,xx} = p_{e,yy} = p_{e,zz} = en_e T_e, \tag{3.1.17.1}$$

where, for isotropic temperature

$$T_e \equiv T_{e,xx} = T_{e,yy} = T_{e,zz} \tag{3.1.17.2}$$

and, for non isotropic temperature

$$T_e \equiv \frac{T_{e,xx} + T_{e,yy} + T_{e,zz}}{3}. \tag{3.1.17.3}$$

In this way the equation set shown in subsection 3.1.11 becomes

$$\frac{\partial n}{\partial t} + \frac{\partial}{\partial x_i}(nu_i) = 0 \tag{3.1.17.4}$$

$$\frac{\partial (mnu_j)}{\partial t} + \frac{\partial (enT)}{\partial x_j} + mu_i u_j \frac{\partial n}{\partial x_i} + mnu_j \frac{\partial u_i}{\partial x_i} + mnu_i \frac{\partial u_j}{\partial x_i} - nF_j = 0 \tag{3.1.17.5}$$

$$mn\frac{\partial u_j}{\partial t} + \frac{\partial (enT)}{\partial x_j} + mnu_i \frac{\partial u_j}{\partial x_i} - nF_j = 0 \tag{3.1.17.6}$$

$$\frac{1}{2}\frac{\partial}{\partial t}\left[mnu^2\right] + \frac{3e}{2}\frac{\partial (nT)}{\partial t} + \frac{\partial}{\partial x_i}\left[H_i + \frac{mnu^2 u_i}{2} + \frac{5e}{2}u_i nT\right] - nF_i u_i = 0 \tag{3.1.17.7}$$

$$\frac{3}{2}\frac{\partial (nT)}{\partial t} + \frac{1}{e}\frac{\partial H_i}{\partial x_i} + \frac{3}{2}\frac{\partial}{\partial x_i}(u_i nT) + \frac{\partial u_k}{\partial x_k}nT = 0. \tag{3.1.17.8}$$

This is the fundamental equation set for the ideal fluid case. Now, we are ready for the work out in a plasma discharge environment.

3.1.18 The fluid model in 1D

Now, let us rewrite the equation set above in the case when the force is due to $F_j = -eE_j$.

$$\frac{\partial n}{\partial t} + \frac{\partial}{\partial x_i}(nu_i) = 0 \tag{3.1.18.1}$$

$$\frac{\partial (mnu_j)}{\partial t} + \frac{\partial (enT)}{\partial x_j} + mu_i u_j \frac{\partial n}{\partial x_i} + mnu_j \frac{\partial u_i}{\partial x_i} + mnu_i \frac{\partial u_j}{\partial x_i} + enE_j = 0 \tag{3.1.18.2}$$

$$mn\frac{\partial u_j}{\partial t} + \frac{\partial (enT)}{\partial x_j} + mnu_i \frac{\partial u_j}{\partial x_i} + enE_j = 0 \tag{3.1.18.3}$$

$$\frac{1}{2}\frac{\partial}{\partial t}\left[mnu^2\right] + \frac{3e}{2}\frac{\partial (nT)}{\partial t} + \frac{\partial}{\partial x_i}\left[H_i + \frac{mnu^2 u_i}{2} + \frac{5e}{2}u_i nT\right] + enE_i u_i = 0 \tag{3.1.18.4}$$

$$\frac{3}{2}\frac{\partial (nT)}{\partial t} + \frac{1}{e}\frac{\partial H_i}{\partial x_i} + \frac{3}{2}\frac{\partial}{\partial x_i}(u_i nT) + \frac{\partial u_k}{\partial x_k}nT = 0. \tag{3.1.18.5}$$

Projecting the equation set along the $x-$axis we find

$$\frac{\partial n}{\partial t} + \frac{\partial}{\partial x_i}(nu_i) = 0 \tag{3.1.18.6}$$

$$\frac{\partial (mnu_x)}{\partial t} + \frac{\partial (enT)}{\partial x} + mu_xu_x\frac{\partial n}{\partial x} + 2mnu_x\frac{\partial u_x}{\partial x} + enE = 0 \tag{3.1.18.7}$$

$$mn\frac{\partial u_x}{\partial t} + \frac{\partial (enT)}{\partial x} + mnu_x\frac{\partial u_x}{\partial x} + enE = 0 \tag{3.1.18.8}$$

$$\frac{1}{2}\frac{\partial}{\partial t}\left[mnu_x^2\right] + \frac{3e}{2}\frac{\partial (nT)}{\partial t} + \frac{\partial}{\partial x}\left[H_x + \frac{mnu_x^3}{2} + \frac{5e}{2}u_xnT\right] + enEu_x = 0 \tag{3.1.18.9}$$

$$\frac{3}{2}\frac{\partial (nT)}{\partial t} + \frac{1}{e}\frac{\partial H_x}{\partial x} + \frac{3}{2}\frac{\partial}{\partial x}(u_xnT) + \frac{\partial u_x}{\partial x}nT = 0, \tag{3.1.18.10}$$

where the electric field has been taken to exist along the $x-$axis only. In the following, we will write both the electric field and the electron power absorption formula coming from the equation system above.

3.1.19 The electric field

From the system of equations above we are able to write out the the main equation involving the electric field (Eq. (3.1.18.7))

$$E = -\frac{m}{e}\frac{u_x}{n}\frac{\partial n}{\partial t} - \frac{m}{e}\frac{\partial u_x}{\partial t} - \frac{T}{n}\frac{\partial n}{\partial x} - \frac{\partial T}{\partial x} - \frac{m}{e}\frac{u_x^2}{n}\frac{\partial n}{\partial x} - \frac{2m}{e}u_x\frac{\partial u_x}{\partial x}. \tag{3.1.19.1}$$

In the next subsections we will see that the equation above encounters several restrictions depending on the approximations used. Now, from the continuity equation (Eq. (3.1.18.1)), we know that

$$\frac{\partial u_i}{\partial x_i} = -\frac{1}{n}\frac{\partial n}{\partial t} - \frac{u_i}{n}\frac{\partial n}{\partial x_i}. \tag{3.1.19.2}$$

Plugging Eq. (3.1.19.2) into Eq. (3.1.19.1), one finds

$$E = \frac{m}{e}\frac{u_x}{n}\frac{\partial n}{\partial t} - \frac{m}{e}\frac{\partial u_x}{\partial t} + \frac{m}{e}\frac{u_x^2}{n}\frac{\partial n}{\partial x} - \frac{T}{n}\frac{\partial n}{\partial x} - \frac{\partial T}{\partial x}, \tag{3.1.19.3}$$

which is the final expression for the electric field in a 1D system. It is worth noting that this is the same expression as the one that would have been found by plugging Eq. (3.1.19.2) into Eq. (3.1.18.8).

3.1.20 The electron power absorption calculation using the I momentum Boltzmann equation

Let us define the electron power absorption as follows

$$\vec{J}\cdot\vec{E} = -en\vec{u}\vec{E}. \tag{3.1.20.1}$$

Since we are interested in a 1D system, the previous expression becomes

$$J_x \cdot E = -enu_x E. \tag{3.1.20.2}$$

By multiplying the equation for the electric field in 1D (Eq. (3.1.19.3)) by the quantity $(-enu_x)$ one finds

$$\vec{J} \cdot \vec{E} = J_x E = -mu_x^2 \frac{\partial n}{\partial t} + mnu_x \frac{\partial u_x}{\partial t} - mu_x^3 \frac{\partial n}{\partial x} + eTu_x \frac{\partial n}{\partial x} + enu_x \frac{\partial T}{\partial x}. \tag{3.1.20.3}$$

3.1.21 The electron power absorption calculation using the II momentum Boltzmann equation

Now, let us consider the II momentum Boltzmann equations. From Eqs. (3.1.18.9) and (3.1.18.10) we know that

$$\vec{J} \cdot \vec{E} = \frac{1}{2} \frac{\partial}{\partial t} \left[mnu^2 \right] + \frac{3e}{2} \frac{\partial (nT)}{\partial t} + \frac{\partial}{\partial x_i} \left[H_x + \frac{mnu_x^3}{2} + \frac{5e}{2} u_x nT \right] \tag{3.1.21.1}$$

$$\frac{\partial H_x}{\partial x} = -\frac{3}{2} \frac{\partial (enT)}{\partial t} - \frac{3}{2} \frac{\partial (eu_x nT)}{\partial x} - enT \frac{\partial u_x}{\partial x}, \tag{3.1.21.2}$$

where H_x is the $x-$projection of the heat flux defined in Eq. (3.1.9.5). Plugging the expression for the heat flux (Eq. (3.1.21.2)) into Eq. (3.1.21.1), we find the same expression for the electron power absorption as shown in Eq. (3.1.20.3), meaning that everything is consistent. Moreover, from Eq. (3.1.21.2), taking a constant heat flux and a Fourier heat flux, respectively (Surendra and Dalvie, 1993), we find, for constant heat flux ($H_x = \text{const}$)

$$\frac{3}{2} \frac{\partial (enT)}{\partial t} + \frac{3}{2} \frac{\partial (eu_x nT)}{\partial x} + enT \frac{\partial u_x}{\partial x} = 0 \tag{3.1.21.3}$$

and, for heat flux due to temperature gradient ($H_x^{\text{Fo}} = h_e \partial T / \partial x$)

$$\frac{\partial}{\partial x} \left(h_e \frac{\partial T}{\partial x} \right) = \frac{3}{2} \frac{\partial (enT)}{\partial t} + \frac{3}{2} \frac{\partial (eu_x nT)}{\partial x} + enT \frac{\partial u_x}{\partial x}, \tag{3.1.21.4}$$

where

$$h_e \sim \frac{k^2 n_e T_e}{m_e v_c} \tag{3.1.21.5}$$

is the thermal conductivity.

3.1.22 The Collisional operator and the electric field terms

In order to take collisions into account, the first step would be to consider the continuity equation (Eq. (3.1.7.1)) in presence of collisions

$$\frac{\partial n_e}{\partial t} + \frac{\partial}{\partial x} (u_e n_e) = G - L, \tag{3.1.22.1}$$

where G and L are the reaction rates involving the creation and the destruction of electrons, respectively. In order to make the equations simpler, usually the reactions involving the creation and destructions of particles (e.g., ionization, recombination) are neglected and only the reactions involving the neutral species, with a negligible velocity compared to the electrons, are considered. The second step lies in adding the quantity Π_c to the r.h.s. of Eq. (3.1.18.7). In this way we find

$$\frac{\partial}{\partial t}\left[m_e n_e u_e\right] + \frac{\partial}{\partial x}\left[m_e n_e u_e^2\right] + \frac{\partial}{\partial x}\left[e n_e T_e\right] + e n_e E + \Pi_c = 0. \qquad (3.1.22.2)$$

Now, according to Lieberman and Lichtenberg (2005), the momentum change term Π_c can be approximated by a Krook collisional operator as follows

$$\Pi_c = \sum_\beta m_e n_e \nu_{e\beta}\left(u_e - u_\beta\right) - m_e\left(u_e - u_G\right) G + m_e\left(u_e - u_L\right) L, \qquad (3.1.22.3)$$

where the summation is taken over all species, u_e and u_β are the mean velocities of the electrons and the species β, respectively, and $\nu_{e\beta}$ is the momentum transfer frequency for collisions between electrons and species β. Now, neglecting the reactions involving the creation and destructions of particles (e.g., ionization, recombination) and considering only the neutral species, with a negligible velocity compared to the electrons, the momentum change term becomes

$$\Pi_c = m_e \nu_e n_c u_e \qquad (3.1.22.4)$$

which, plugged into Eq. (3.1.22.2), returns the electric field

$$E = -\underbrace{\frac{m_e}{e}\frac{\partial u_e}{\partial t}}_{\text{I}} + \underbrace{\frac{m_e}{e}\frac{u_e^2}{n_e}\frac{\partial n_e}{\partial x}}_{\text{II}} + \underbrace{\frac{m_e}{e}\frac{u_e}{n_e}\frac{\partial n_e}{\partial t}}_{\text{III}} - \underbrace{\frac{T_e}{n_e}\frac{\partial n_e}{\partial x}}_{\text{IV}} - \underbrace{\frac{\partial T_e}{\partial x}}_{\text{V}} - \underbrace{\frac{m_e u_e \nu_c}{e}}_{\text{VI}}, \qquad (3.1.22.5)$$

where each term has been labeled and each electric field term in Eq. (3.1.22.5) has its own origin. The first and the third term (I and III) are electron inertia terms due to the temporal variation in the electron velocity and density, respectively. The second term (II) corresponds to an electric field due to the normalized electron density gradient. The fourth (IV) term corresponds to diffusion (ambipolar field) (Schulze et al., 2011a, 2008a). The fifth term (V) corresponds to the electron temperature gradient. Therefore, terms IV and V represent electron heating due to pressure effects which is referred to as a collisionless mechanism (Turner, 1995). The sixth term (VI) is due to electron collisions with atoms and molecules (drift field). It is worth noting that, by keeping the last three terms in Eq. (3.1.22.5), it is possible to recover Eq. (2.5.0.12).

3.1.23 The electron power absorption terms

Multiplying the electric field coming from Eq. (3.1.22.5) times the electron current density $J_e = -e n_e u_e$ it is possible to find the power absorbed by the electrons as

$$J_e \cdot E = \underbrace{m_e u_e n_e \frac{\partial u_e}{\partial t}}_{\text{I}} - \underbrace{m_e u_e^3 \frac{\partial n_e}{\partial x}}_{\text{II}} - \underbrace{m_e u_e^2 \frac{\partial n_e}{\partial t}}_{\text{III}} + \underbrace{e u_e T_e \frac{\partial n_e}{\partial x}}_{\text{IV}} + \underbrace{e n_e u_e \frac{\partial T_e}{\partial x}}_{\text{V}} + \underbrace{m_e n_e \nu_c u_e^2}_{\text{VI}},$$

$$(3.1.23.1)$$

where each electron power absorption term that constitutes Eq. (3.1.23.1) has its own origin which is strictly related to the electric field given by Eq. (3.1.22.5). The first and the third term (I and III) are electron inertia power absorption terms. The second term (II) corresponds to the power absorption term related to the electron density gradient. The fourth (IV) term is due to the ambipolar field orignating from the electron density gradient (Schulze et al., 2011a, 2008a). The fifth term (V) is related to the electron temperature gradient term for the electric field. The fourth and fifth terms are usually known in the literature as pressure heating terms (Schulze et al., 2018; Turner, 1995; Surendra and Dalvie, 1993). The sixth term (VI) is due to the collisions and represents Ohmic heating. It is worth noting that the electron power absorption formula shown in Eq. (3.1.23.1) can be split as follows (Surendra and Dalvie, 1993)

$$(J_e \cdot E) = (J_e \cdot E)_{\text{NonOhmic}} + (J_e \cdot E)_{\text{Ohmic}}, \qquad (3.1.23.2)$$

where

$$(J_e \cdot E)_{\text{NonOhmic}} = \text{Term I} + \text{Term II} + \text{Term III}$$
$$+ \text{Term IV} + \text{Term V} \qquad (3.1.23.3)$$
$$(J_e \cdot E)_{\text{Ohmic}} = \text{Term VI}. \qquad (3.1.23.4)$$

In turn the Non Ohmic contribution can be split up as follows (Lafleur et al., 2014a)

$$(J_e \cdot E)_{\text{NonOhmic}} = (J_e \cdot E)_{\text{Inertia}} + (J_e \cdot E)_{\text{Pressure}}, \qquad (3.1.23.5)$$

where

$$(J_e \cdot E)_{\text{Inertia}} = \text{Term I} + \text{Term II} + \text{Term III} \qquad (3.1.23.6)$$
$$(J_e \cdot E)_{\text{Pressure}} = \text{Term IV} + \text{Term V}. \qquad (3.1.23.7)$$

The same split applied to the electron power absorption can be applied to the electric field formula shown in Eq. (3.1.22.5). Moreover, it is worth noting that, rewriting the last term from Eq. (3.1.22.5), we find

$$J_{e,\text{Ohm}} = \sigma_{\text{dc}} E_{\text{VI}} \qquad (3.1.23.8)$$

with

$$\sigma_{\text{dc}} = \frac{\varepsilon_0 \omega_{\text{pe}}^2}{\nu_{\text{c}}}, \qquad (3.1.23.9)$$

where σ_{dc} is the dc plasma conductivity and ω_{pe} is the electron plasma frequency shown in Eq. (2.3.0.8). As we can see from Eq. (3.1.23.9), the higher is the collision frequency (electron plasma frequency), the lower (higher) is the conductivity and the more the plasma is resistive (conductive).

3.1.24 The adiabatic local change

First of all we see that combining Eq. (3.1.19.2) and (3.1.18.5) we get the following expression

$$\frac{3}{2} n \left[\frac{\partial}{\partial t} + u_i \frac{\partial}{\partial x_i} \right] T + \frac{1}{e} \frac{\partial H_i}{\partial x_i} + nT \frac{\partial u_i}{\partial x_i} = 0. \qquad (3.1.24.1)$$

Secondly, combining Eq. (3.1.24.1) and (3.1.12.2) (while setting the heat flux H_i to zero), we find the equation

$$\left(\frac{\partial}{\partial t} + u_i \frac{\partial}{\partial x_i}\right)\left(nT^{-\frac{3}{2}}\right) = 0 \tag{3.1.24.2}$$

which tells us that the quantity $nT^{-\frac{3}{2}}$ is constant along the streamlines or, in other words, that the motion along streamlines is adiabatic. Since n and T are functions of both space and time, we are talking about a local adiabatic change.

3.2 Boltzmann equation with Non-Maxwellian-EEDF

3.2.1 EEDF and EEPF

Now, we want to rewrite the previous conditions starting from the electron energy distribution function (EEDF). Let us define the a more general EEDF (Gudmundsson (2001)) as follows

$$f_{\mathrm{e}}(\mathscr{E}) = c_1 \mathscr{E}^{\frac{1}{2}} \exp\left(-c_2 \mathscr{E}^x\right), \tag{3.2.1.1}$$

where for $x = 1$ we have a Maxwellian EEDF, for $x = 2$ a Druyvesteyn distribution and so on. Setting the following conditions, analogous to Eq. (3.2.2.1) and Eq. (3.2.2.4), we find

$$\int_0^{+\infty} f_{\mathrm{e}}(\mathscr{E}) \, d\mathscr{E} = c_1 \int_0^{+\infty} \mathscr{E}^{\frac{1}{2}} \exp\left(-c_2 \mathscr{E}^x\right) = 1 \tag{3.2.1.2}$$

$$\int_0^{+\infty} \mathscr{E} f_{\mathrm{e}}(\mathscr{E}) \, d\mathscr{E} = c_1 \int_0^{+\infty} \mathscr{E}^{\frac{3}{2}} \exp\left(-c_2 \mathscr{E}^x\right) = \langle \mathscr{E} \rangle \equiv \frac{3}{2} e T_{\mathrm{e,eff}} \tag{3.2.1.3}$$

with the following values for c_1 and c_2

$$c_1 = \frac{x}{\langle \mathscr{E} \rangle^{\frac{3}{2}}} \frac{[\Gamma(\zeta_2)]^{\frac{3}{2}}}{[\Gamma(\zeta_1)]^{\frac{5}{2}}} \tag{3.2.1.4}$$

$$c_2 = \frac{1}{\langle \mathscr{E} \rangle^x} \left[\frac{\Gamma(\zeta_2)}{\Gamma(\zeta_1)}\right]^x, \tag{3.2.1.5}$$

where $\zeta_1 = 3/(2x)$ and $\zeta_2 = 5/(2x)$. In this way the complete expression for the electron nergy distribution function reads

$$f_{\mathrm{e}}(\mathscr{E}) = \frac{x \mathscr{E}^{\frac{1}{2}}}{\langle \mathscr{E} \rangle^{\frac{3}{2}}} \frac{[\Gamma(\zeta_2)]^{\frac{3}{2}}}{[\Gamma(\zeta_1)]^{\frac{5}{2}}} \exp\left(-\frac{\mathscr{E}^x}{\langle \mathscr{E} \rangle^x}\left[\frac{\Gamma(\zeta_2)}{\Gamma(\zeta_1)}\right]^x\right) \tag{3.2.1.6}$$

or, labelling $\tilde{f}_{\mathrm{e}}$ as the electron energy probability function (EEPF), along with the relation $f_{\mathrm{e}} = \mathscr{E}^{\frac{1}{2}} \tilde{f}_{\mathrm{e}}$

$$\tilde{f}_{\mathrm{e}}(\mathscr{E}) = \frac{x}{\langle \mathscr{E} \rangle^{\frac{3}{2}}} \frac{[\Gamma(\zeta_2)]^{\frac{3}{2}}}{[\Gamma(\zeta_1)]^{\frac{5}{2}}} \exp\left(-\frac{\mathscr{E}^x}{\langle \mathscr{E} \rangle^x}\left[\frac{\Gamma(\zeta_2)}{\Gamma(\zeta_1)}\right]^x\right). \tag{3.2.1.7}$$

Now, since

$$f_e(n_e, w_e, T_e)d^3w_e \equiv n_e f_e(\mathscr{E})d\mathscr{E} \qquad (3.2.1.8)$$

and assuming the electron velocity to be isotropic, along with the definition of the single electron energy as $\mathscr{E} = mw^2/2$, we can relate $f_e(n_e, w_e, T_e)$ to $f_e(\mathscr{E})$ as follows

$$f_e(n_e, w_e, T_e) = \frac{m_e n_e}{4\pi w_e} f_e(\mathscr{E}) \qquad (3.2.1.9)$$

for $w_e \neq 0$. By applying the expression above, it is not difficult to find the electron velocity distribution function for a Maxwellian distribution (Eq. (3.1.4.1)).

3.2.2 Constraints

Recalling Eqs. (3.1.16.2), (3.1.16.3), (3.1.7.3), (3.1.9.2) and (3.1.9.5), we are allowed to write the following compact equation set

$$\int f_e \, d^3v_e = \int f_e \, d^3w_e = n_e \qquad (3.2.2.1)$$

$$\int f_e \, w_{e,i} d^3w_e = 0 \qquad (3.2.2.2)$$

$$\int f_e \, w_{e,i} w_{e,j} \, d^3w_e = p_{e,ij} \qquad (3.2.2.3)$$

$$\int f_e \, w_e^2 \, d^3w_e = \mathrm{Tr} \, p_e \qquad (3.2.2.4)$$

$$\frac{m_e}{2} \int f_e \, w_e^2 \, w_{e,i} \, d^3w_e = H_i. \qquad (3.2.2.5)$$

In particular, the first three equations can be used as constraints in order to build a general electron energy distribution function.

3.2.3 The need for a Non-Maxwellian EEDF

Now, we want to figure out if it may be useful to rewrite the electric field and electron power absorption formula (Eqs. (3.1.22.5) and (3.1.23.1), respectively) for a non-Maxwellian EEDF. First of all we note that, independently of the electron velocity distribution function (EEVF) used, the constraints listed above must hold. This means that, by examining the electric field formula shown in Eq. (3.1.22.5), the only quantity which may really depend on the EEVF is the electron pressure p_e. So let us put the whole electron pressure term in Eq. (3.1.22.5) under examination. Let us suppose the electron pressure p_e to be very far from being equal to $en_e T_e$, as the ideal gas law states for a Maxwellian EEVF. This means that we have, more generally

$$p_e = p_e(n_e, T_e, E). \qquad (3.2.3.1)$$

At this point it is important to distinguish between the initial electron pressure and the final electron pressure. In the PIC/MCC model framework, the initial electron pressure is an input parameter and it is needed to make the PIC/MCC simulation start. On the

other hand, the final electron pressure is a simulation outcome and it is calculated using $T_{e,ii} = \frac{2}{e}\mathscr{E}_{e,ii} - \frac{m_e}{e}u_{e,i}^2$ where $\mathscr{E}_{e,ii}$ and $u_{e,ii}^2$, with $i = x, y, z$, are the mean electron energy density and the electron mean velocity respectively. Since $\mathscr{E}_{e,i} = \frac{m_e}{2}\langle v_{e,i}^2 \rangle$ by definition, this is equivalent to say $T_{e,ii} = \frac{m_e}{e}\langle v_{e,i} \rangle^2 - \frac{m_e}{e}u_{e,i}^2 = \frac{m_e}{e}\langle w_{e,i}^2 \rangle$. This electron temperature is actually an effective electron temperature. In fact, due to Eq. (3.1.7.3), we can state, in the 1D case

$$p_e \equiv e n_e T_{e,\text{eff}}. \tag{3.2.3.2}$$

That means that all the information about the EEVF is already stored in the electron pressure p_e. In this way there is no need to change the expression for the electron pressure p_e, in cases where the electron velocity distribution function is far from being Maxwellian.

4 Electron power absorption mechanisms

4.1 Electron heating and electron power absorption

The technological progress of capacitively coupled discharges requires a fundamental knowledge of the physical laws underlying the electron dynamics. Since the electrons create ions through ionization of neutral atoms and molecules, they need an energy above a certain threshold value to make this happen. In such a context it is necessary to understand both the electron power absorption and the electron power loss process in a capacitively coupled discharge (Schulze and Mussenbrock, 2016). Keep in mind that electron heating and electron power absorption are physically two different mechanisms (Wilczek et al., 2020). Heating occurs when the anisotropic distribution of the velocity components is redistributed in an isotropic manner by collisions with the neutral gas particles, which is called isotropization. In Figure 4.1 this difference is explained schematically. At the very beginning, i.e. before the electric field is applied, the electron ensemble is isotropic and is described by a temperature $T_{e,1}$. When the electric field is turned on, the electrons experience an acceleration and become anisotropic. During this acceleration in the electric field, the electrons gain energy and power absorption occurs due to the anisotropic increase of the velocity. Afterwards, due to the collisions, the electrons whose energy is lower than a certain cutoff ($T_{e,1}$) remain anisotropic, while the electrons whose energy is higher than $T_{e,1}$ become isotropic again. Electron heating occurs when the anisotropic distribution of the velocity components is redistributed isotropically by collisions with the neutral gas particles.

Therefore, isotropization is a necessary but not sufficient condition to have electron heating. It is not sufficient because, according to this picture, it is not possible to have electron heating without electron power absorption, while it is possible to have electron power absorption without electron heating (for example when the role of the collisions is negligible). This explains why it is possible to have electron heating in low pressure plasma discharge, i.e. when electrons transverse through the discharge without any collisions for a certain period (Wilczek et al., 2020) (negligible collisions). In this situation, an additional collisionless electron heating mechanism occurs, which is known in the literature as stochastic heating, which is based on the dynamics involving the electrons in a time and space varying electric field close to the space-time varying bulk-sheath interface (sheath edge). Finally, the full sequence of events starting from the initial isotropic electrons at $T_{e,1}$ ending with the isotropization at $T_{e,2} > T_{e,1}$ is known as heating mechanism, while the restricted sequence starting from the initial isotropic electrons at $T_{e,1}$ ending with the full anisotropization (before the collisions) is known as electron power absorption.
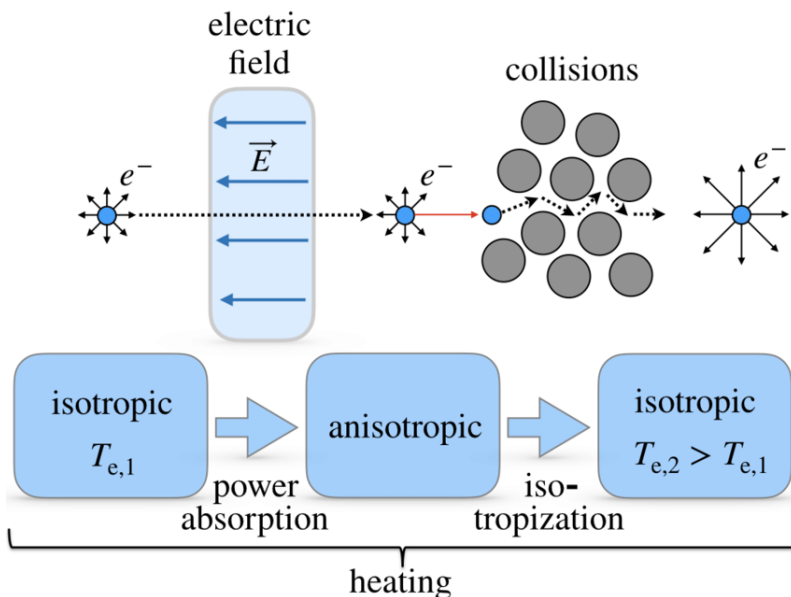
Figure 4.1. The electron heating process compared to the electron power absorption mechanism. Reprinted from Wilczek et al. (2020) with the permission of AIP Publishing.

The power transfer mechanism, which is commonly referred to as 'electron heating' or 'electron power absorption' in the literature, is still a topic rather poorly understood. A number of electron power absorption mechanisms have been identified in the capacitively coupled discharge. Historically, they were referred to as electron heating mechanisms, which remain in the discussion below. Although the electron heating mechanism is a topic widely studied and discussed over the past decades, a fully consistent and general mathematical-physical explanation of the several physical mechanisms involved in the power transfer mechanism is still lacking. It is widely accepted that the electron heating can be roughly divided into two main processes: the Ohmic heating (collisional heating) and the stochastic heating (collisionless heating). A few operating modes have been identified in the capacitively coupled discharge including the stochastic electron heating, due to the sheath motion (α-mode) (Lieberman and Godyak, 1998), secondary electron emission due to ion bombardment of the electrodes (γ-mode) (Godyak and Khanneh, 1986), the drift ambipolar (DA)-mode (Schulze et al., 2011a), the electron bounce resonance heating (BRH) (Wood, 1991), self-excited plasma series resonance (PSR oscillations) (Klick, 1996), non linear electron resonance heating (NERH) (Mussenbrock and Brinkmann, 2006), and the striation mode (Liu et al., 2016). Each of these operation modes are discussed below.

In particular, as discussed in section 2.6, space charge sheaths separate the plasma bulk from the electrodes. The energy transport mechanism and particle interactions in the plasma-surface interface region play a significant role in the capacitively coupled discharge. Furthermore, the electronegativity and the electron power absorption of the discharge are influenced by the recombination of atomic species and quenching

of metastable atoms and molecules on the electrode surfaces. Electrons, positive and negative ions are produced through electron impact ionization of neutral atoms and molecules, and electron impact dissociative attachment of molecules. These processes are dictated by the electron power absorption and the electron kinetics and are triggered by the high energy electrons which are generated by the electric field within the discharge.

4.2 Stochastic electron heating, α-mode electron heating mechanism

4.2.1 The history

At low pressure, where the electron mean free path is comparable to the typical plasma dimension, capacitively coupled discharges are maintained by collisionless heating of electrons in the strongly modulated sheaths adjacent to the electrodes. This collisionless electron heating mechanisms, usually known in the literature as stochastic heating, is widely accepted to be a type of Fermi acceleration (Fermi, 1949; Lieberman and Godyak, 1998). Godyak (1972) originally described a simplified version of the Fermi idea, known as hard wall model, in order to describe this sheath interaction as a collisionless heating in capacitive plasma discharges. In this model the reflected electrons during sheath expansion (collapse) are accelerated (decelerated) from the sheath into the plasma bulk. When a discharge is maintained by collisionless or stochastic heating it is said to be operating in α-mode. This mechanism has been investigated experimentally in single-frequency discharges (Tochikubo et al., 1990; Gans et al., 2004; Salabas et al., 2004; Mahony et al., 1997; Schulze et al., 2008b, 2007) and through both numerical and theoretical calculations (Belenguer and Boeuf, 1990; Vender, 1990b). Surendra and Graves (1991a) and Turner (1995) discussed the theoretical implications of this description. It is also worth to mention Wood (1991) who treated the stochastic heating in different regimes depending on the electron velocity with respect to the sheath velocity. On the other hand, Lieberman and Godyak (1998) approached the collisionless-stochastic electron heating in a systematic way by using the hard wall model. In recent years, the hard wall model has been subject to criticism by Gozadinos et al. (2001). In fact Gozadinos has shown that the hard wall description leads to zero time averaged electron power absorption when the current conservation is taken into account at the sheath edge. Also Lafleur et al. (2014a) has studied the theoretical origin of the collisionless heating considering the Boltzmann equations. He pointed out the problem arising from the equivalence between collisioness and stochastic heating. In fact Lafleur et al. (2014a), analysing the single terms coming from the Boltzmann equation and separating the Ohmic (collisional term) from the non Ohmic contributions (collisionless terms), identified the non Ohmic contributions as a sum over both the pressure and the inertia terms. In this picture the stochastic heating, which is responsible for the α-mode, is a subset of the collisionless heating mechanisms. Later on, the same authors (Lafleur and Chabert, 2015) have questioned the collisionless heating to be truly collisionless. They advanced the hypothesis that the non Ohmic heating is not

collisionless but rather due to non local collisions. Finally, it is worth noting that a higher number of high energy electrons increases the probability for threshold related electron impact processes. Since such processes are the most important ones in a low pressure capacitively coupled discharge, highly populated high energy levels ensure a significant Ohmic heating within the plasma bulk.

It is widely known that a mathematical approach to the stochastic heating exposes a lot of unsolved problems. The first problem lies in the fact that it is possible to evaluate the exact location of the sheath edge only heuristically (Brinkmann, 2007; Salabaş and Brinkmann, 2006). Secondly, while it is widely accepted that the displacement current carried by positive ions plays a major role in the expanded sheath regions, it is difficult to compute the space-time-resolved electric field in the fully expanded sheath region using the displacement current alone, since ions respond to time averaged fields only. However, the physics behind the electric field in the sheath region can sometimes be captured by ad hoc models (Brinkmann, 2007). Thirdly, the presence of different ion species influences the sheath dynamics in a highly non trivial way and different models are needed to estimate quantities such as the Bohm velocity (Baalrud et al., 2009; Baalrud and Hegna, 2011).

4.2.2 Field reversal

If the sheath collapses so fast that electrons cannot follow by diffusion, the electrons can be accelerated towards the electrode by a locally reversed electric field which is generated on the bulk-sheath interface in order to keep the current constant across the plasma discharge (Schulze et al., 2008a). Field reversal is one of the main features appearing in electronegative discharges, together with double layer structures (Tochikubo et al., 1990; Gottscho, 1987; Lieberman and Lichtenberg, 2005) and local maxima of the electrons in the sheath region (Gogolides et al., 1994; Denpoh and Nanbu, 1998; Mantzaris et al., 1995; Gogolides and Sawin, 1992), related to the sheath dynamics. In single-frequency discharges operated at high pressures the field reversal is usually explained through a collisional force acting on the electrons, irrespective of the gas considered (Mahony et al., 1997; Salabas et al., 2004; Belenguer and Boeuf, 1990), while at low pressures the field reversal effect is due to the electron inertia (Sato and Lieberman, 1990; Vender and Boswell, 1992; Schulze et al., 2008a).

4.2.3 The hard wall model

Godyak and Piejak (1990) have pointed out that an explanation for the electron heating involving the Ohmic component only is incomplete and several authors developed a new theory to describe the stochastic heating based on the hard wall model (Godyak, 1972; Lieberman, 1988; Lafleur et al., 2014b; Turner, 2009; Kaganovich et al., 2006). One of the main issues in the hard wall model is that it is not obtained from the Boltzmann equation so that, under this picture, collisional and collisionless heating are usually coming from two different separate models. Indeed, the hard wall model gives a stochastic contribution which has to be added to the Ohmic contribution in order to have the total absorbed power and the result agrees with the experiment only for specific and restricted cases that will not be discussed here. Although the hard wall model has been
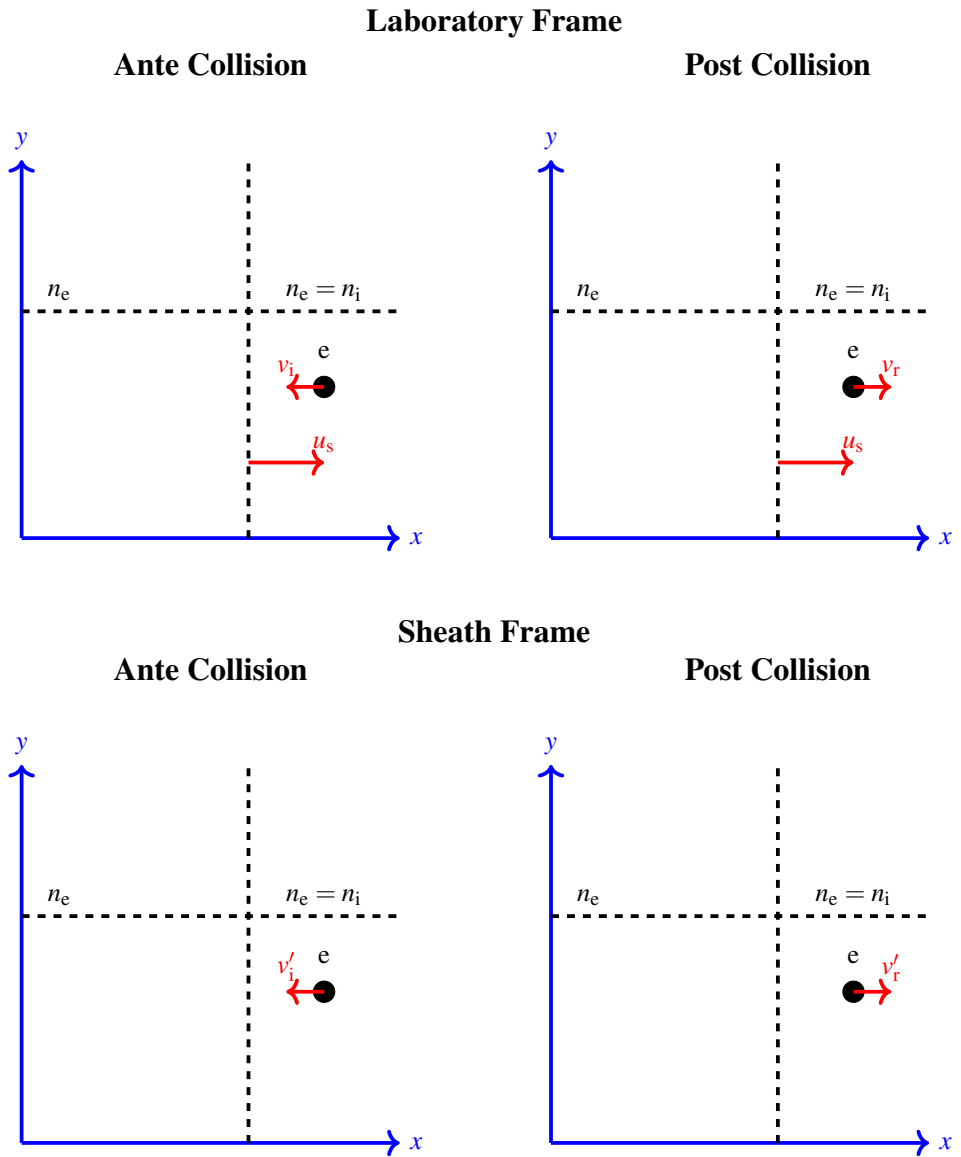
Figure 4.2. The hard wall model set up.

a significant improvement to the understanding of the stochastic collisionless heating, it cannot be considered a fully consistent description of the electron heating mechanism, especially in the electronegative capacitively coupled discharges. First of all the hard wall model returns the time averaged electron power absorption only. Secondly, this model assumes the electron reflecting from the large decelerating fields of a moving high-voltage sheath to be approximated by an elastic collision of a ball with a moving wall. The problem with this approximation is that the computation of both the distribution and time averaged integral requires the knowledge of the electron energy distribution function. This computation is highly not trivial and a Maxwellian distribution is often employed to make the calculation easier, although the electron energy distribution function is very far from being Maxwellian in most of the cases considered in the literature. Along this direction, Wood (1991) calculated analytically the time averaged electron heating for a low pressure argon plasma discharge using both a two temperature Maxwellian and a power law EEDF function getting a reasonable agreement with experiments. The analytical formulation of the electron heating mechanism which included a realistic EEDF is one of the most hard obstacles which prevents a full understanding of the stochastic heating using the hard wall model. Moreover, the hard wall model does not take into account physical phenomena discovered after its first introduction such as electron beams, which are responsible for the generation of a propagating ionization front (O'Connell et al., 2007) and for a not negligible amount of collisionless heating in asymmetric discharges (Schulze et al., 2008b,d), non linear electron resonance heating (NERH) (Mussenbrock and Brinkmann, 2006; Czarnetzki et al., 2006; Mussenbrock et al., 2008; Lieberman et al., 2008; Donkó et al., 2009), electron bounce resonance effect (Park et al., 2007; Liu et al., 2011), the generation of series resonance oscillations (Mussenbrock and Brinkmann, 2006; Mussenbrock et al., 2008), electron heating in dual and multi-frequency electrically asymmetric plasmas (Donkó et al., 2009; Turner and Chabert, 2006; Heil et al., 2008; Lafleur et al., 2012) and plasma-surface interactions such as secondary electrons emission and electron reflection (Derzsi et al., 2015a; Daksha et al., 2017; Roberto et al., 2006; Hannesdottir and Gudmundsson, 2016; Bojarov et al., 2010a; Lafleur et al., 2013; Korolov et al., 2013; Radmilović-Radjenović and Petrović, 2009; Bojarov et al., 2010b, 2014; Proto and Gudmundsson, 2018b,a). The hard wall model (Popov and Godyak, 1985; Lieberman and Godyak, 1998; Lieberman, 1988) was born as an attempt to describe the collisionless heating due to the Fermi acceleration, which plays a significant role in the formation of the electric field within the discharge. During sheath expansion (collapse) the reflected electrons are accelerated (decelerated) from the sheath into the plasma bulk. This mechanism has been investigated in single-frequency discharges both theoretically (Lieberman and Godyak, 1998; Surendra and Graves, 1991a; Turner, 1995; Gozadinos et al., 2001; Salabas et al., 2004; Vender, 1990b; Wood, 1991) and experimentally (Tochikubo et al., 1990; Gans et al., 2004; Mahony et al., 1997; Schulze et al., 2008b, 2007).

The idea is to consider a particle colliding against an infinitely massive moving wall in order to simulate the collision between the electrons and the moving sheaths. Usually, the starting point is to consider an incident electron with velocity $\bar{v}_i$ hitting an

expanding sheath. In the frame where the sheath is at rest, one finds

$$\vec{v}_i' = \vec{v}_i - \vec{u}_s,$$ (4.2.3.1)

where $\vec{v}_i'$ and $\vec{v}_i$ are the initial electron velocity in the sheath frame and in the laboratory frame, respectively, while $\vec{u}_s$ is the expanding sheath velocity in the laboratory frame (see Fig. 4.2). Consequently, after the collision, we have

$$\vec{v}_r' = \vec{v}_r - \vec{u}_s,$$ (4.2.3.2)

where $\vec{v}_r'$ and $\vec{v}_r$ are the final electron velocity in the sheath frame and in the laboratory frame, respectively. Now, since $\vec{v}_i' = -\vec{v}_r'$, we are allowed to write

$$\Delta\vec{v}' = \vec{v}_r' - \vec{v}_i' = 2\vec{v}_r' = 2\vec{v}_r - 2\vec{u}_s$$ (4.2.3.3)

so that

$$v_r = 2u_s - v_i.$$ (4.2.3.4)

Now, the number of electrons per unit area and per unit time can be written as follows

$$\frac{\text{Number of incident electrons}}{\text{Area} \times \text{time}} = (v_i - u_s) f_s (v_i, t) \, dv_i,$$ (4.2.3.5)

where $f_s (v_i, t)$ is the normalized electron velocity distribution function (EVDF) at the sheath edge. In this way we get

$$\int_{-\infty}^{+\infty} f_s (v_i, t) \, dv_i = n_i (s(t)) = n_s(t).$$ (4.2.3.6)

This means that the power transfer per unit area reads as follows

$$dS_{\text{stoch}} = \frac{m_e}{2} \left(v_r^2 - v_i^2 \right) (v_i - u_s) f_s (v_i, t) \, dv_i.$$ (4.2.3.7)

Using Eq. (4.2.3.4), we obtain

$$S_{\text{stoch}} = -2m_e \int_{u_s}^{\infty} u_s (v_i - u_s)^2 f_s (v_i, t) \, dv_i.$$ (4.2.3.8)

4.2.4 Hard wall model issues

As pointed out by several authors (Gozadinos et al., 2001), if a not drifting Maxwellian is considered at the sheath edge, there is no net time averaged heating localized at the sheath edge. To see how this happens let us consider the following set up

$$S_{\text{stoch}} = -2m_e \int_{u_s}^{\infty} u_s (v_i - u_s)^2 f_s (v_i, t) \, dv_i$$ (4.2.4.1)

$$v_i = u_{\text{drift}} + w_t$$ (4.2.4.2)

$$f_s (v_i, t) = g (w_t + u_{\text{drift}}),$$ (4.2.4.3)

where the incident electron velocity has been decomposed into a sum involving the drift velocity u_{drift} and the thermal velocity w_{t}. Furthermore, as clearly seen in Eq. (4.2.4.3), a non drifting Maxwellian has been considered at the sheath edge. Now, plugging both Eqs. (4.2.4.2) and (4.2.4.3) into Eq. (4.2.4.1), we get the following expression for the stochastic heating

$$
S_{\text{stoch}} = -2m_{\text{e}} \int_{u_{\text{s}} - u_{\text{drift}}}^{\infty} (u_{\text{s}} - u_{\text{drift}}) \left[u_{\text{drift}} + w_{\text{t}} - u_{\text{s}} \right]^2 g(w_{\text{t}}) dw_{\text{t}}
$$

$$
- 2m_{\text{e}} \int_{u_{\text{s}} - u_{\text{drift}}}^{\infty} u_{\text{drift}} \left[u_{\text{drift}} + w_{\text{t}} - u_{\text{s}} \right]^2 g(w_{\text{t}}) dw_{\text{t}}. \tag{4.2.4.4}
$$

Requiring the rf current continuity, i.e. setting $u_{\text{drift}} = u_{\text{s}}$, we are left with

$$
S_{\text{stoch}} = -2m_{\text{e}} u_{\text{drift}} \int_{u_{\text{s}} - u_{\text{drift}}}^{\infty} u_{\text{drift}} w_{\text{t}}^2 g(w_{\text{t}}) dw_{\text{t}}. \tag{4.2.4.5}
$$

Now, from Eq. (4.2.3.4) we can see that u_{i} and u_{r} share the same thermal velocity. Therefore, the thermal velocity w_{t} remains constant during the collision process. In other words, the thermal velocity is time independent. Consequently, the EVDF $g(w_{\text{t}} + u_{\text{drift}})$ is a stationary distribution and the whole expression shown in Eq. (4.2.4.5) is time independent. Since $\bar{u}_{\text{s}} = \bar{u}_{\text{drift}} = 0$, one deduces that $\bar{S}_{\text{stoch}} = 0$. The implications are twofold. Firstly, it has been argued that the hard wall model achieves a net time averaged heating at the sheath edges simply because it violates the rf current continuity somehow. However, such an explanation would be in contradiction (Gozadinos et al., 2001) with the match between the hard wall model and the kinetic fluid models (Turner, 2009; Chabert and Braithwaite, 2011), as well as between the hard wall model and PIC/MCC simulation results (Kawamura et al., 2006). On the other hand, it has been argued that the original distributions proposed by Godyak and Lieberman (Lieberman, 1988; Lieberman and Godyak, 1998; Godyak, 1972) cannot be taken into account, meaning that one should start considering drifting Maxwellian distributions.

4.2.5 The Lafleur proposal

More recently, Lafleur et al. (2014b) proposed a way to solve this problem. First of all they defined the total electron velocity distribution function f_{eT} as

$$
f_{\text{eT}} = \begin{cases} f_{\text{eI}}(v_{\text{i}}) & \text{for } u_{\text{s}} \leq v_{\text{i}} < \infty \\ f_{\text{eR}}(v_{\text{r}}) & \text{for } -\infty < v_{\text{r}} < u_{\text{s}} \end{cases} . \tag{4.2.5.1}
$$

Afterwards, they used the mapping shown in Eq. (4.2.3.4) in the following way

$$
f_{\text{eR}}(v_{\text{r}}) = f_{\text{eR}}(2u_{\text{s}} - v_{\text{i}}) \tag{4.2.5.2}
$$

so that Eq. (4.2.5.1) can be rewritten as follows

$$
f_{\text{eT}} = \begin{cases} f_{\text{eI}}(v) & \text{for } u_{\text{s}} \leq v < \infty \\ f_{\text{eR}}(2u_{\text{s}} - v) & \text{for } -\infty < v < u_{\text{s}} \end{cases} , \tag{4.2.5.3}
$$

where we have set $v \equiv v_i$ for simplicity. Taking the first and the second moment of the electron velocity distribution shown in Eq. (4.2.5.3), they found that

$$n_e = 2 \int_{u_s}^{\infty} f_{eI}(v) dv \qquad (4.2.5.4)$$

$$n_e u_e = n_e u_s. \qquad (4.2.5.5)$$

In particular, from Eq. (4.2.5.5), we see that, when $n_e \neq 0$, $u_e = u_s$. This means that the rf current continuity condition is satisfied for any EVDF. Moreover, since

$$p_e = 2 m_e \int_{u_{\text{drift}}}^{\infty} (v - u_{\text{drift}})^2 f_{eI} dv, \qquad (4.2.5.6)$$

the electron power transfer shown in Eq. (4.2.3.8) can be written as follows

$$S_{\text{stoch}} = -u_{\text{drift}} p_e. \qquad (4.2.5.7)$$

Now, using the ideal gas law $p_e = e n_e T_e$, Eq. (4.2.5.7), becomes

$$S_{\text{stoch}} = J_e T_e \qquad (4.2.5.8)$$

4.2.6 Hard wall model and beyond

Now, let us define the following quantities

$$\mathscr{E}_i = \frac{m_e v_i^2}{2} \quad , \quad \mathscr{E}_r = \frac{m_e v_r^2}{2} \quad , \quad p_i = m_e v_i \quad , \quad p_r = m_e v_r \qquad (4.2.6.1)$$

$$\tilde{\mathscr{E}}_i = \frac{m_e w_i^2}{2} \quad , \quad \tilde{\mathscr{E}}_r = \frac{m_e w_r^2}{2} \quad , \quad \tilde{p}_i = m_e w_i \quad , \quad \tilde{p}_r = m_e w_r, \qquad (4.2.6.2)$$

where we have set

$$w_i = v_i - u_i \quad , \quad w_r = v_r - u_r \qquad (4.2.6.3)$$

along with $f_{eR}(v_r) = f_{eR}(w_r)$. It is worth noting that, due to the mapping shown in Eq. (4.2.5.2), it is also true that

$$w_i = -w_r, \qquad (4.2.6.4)$$

Now, let us write the power density as

$$W_i = \frac{\partial}{\partial t} \int_{u_s}^{\infty} \tilde{p}_i w_i f_{eI} dv_i \quad , \quad W_r = \frac{\partial}{\partial t} \int_{-\infty}^{u_s} \tilde{p}_r w_r f_{eI} dv_r \qquad (4.2.6.5)$$

which has the dimensions of W/m^3. Plugging the expression for $\tilde{p}_i$ shown in Eq. (4.2.6.1) into the expression for W_i shown in Eq.(4.2.6.5), we find

$$W_i = m_e \frac{\partial}{\partial t} \int_{u_s}^{\infty} w_i^2 f_{eI} dv_i = 2 m_e \int_{u_s}^{\infty} w_i \frac{\partial w_i}{\partial t} f_{eI}(v_i) dv_i + m_e \int_{u_s}^{\infty} w_i^2 \frac{\partial f_{eI}(v_i)}{\partial t} dv_i.$$
$$(4.2.6.6)$$

By using the Boltzmann equation (Eq. (3.1.2.1)) and neglecting the collision term $C(f)$, the second term on the r.h.s. of Eq (4.2.6.6) becomes

$$m_e \int_{u_s}^{\infty} w_i^2 \frac{\partial f_{eI}(v_i)}{\partial t} dv_i = -m_e \int_{u_s}^{\infty} w_i^3 \frac{\partial f_{eI}(v_i)}{\partial x} dv_i - m_e u_i \int_{u_s}^{\infty} w_i^2 \frac{\partial f_{eI}(v_i)}{\partial x} dv_i$$

$$-m_e \int_{u_s}^{\infty} w_i^2 \frac{F}{m_e} \frac{\partial f_{eI}(v_i)}{\partial v_i} dv_i \qquad (4.2.6.7)$$

so that

$$W_i = 2m_e \int_{u_i}^{\infty} w_i \frac{\partial w_i}{\partial t} f_{eI}(v_i) dv_i - m_e \int_{u_i}^{\infty} w_i^3 \frac{\partial f_{eI}(v_i)}{\partial x} dv_i - m_e u_i \int_{u_i}^{\infty} w_i^2 \frac{\partial f_{eI}(v_i)}{\partial x} dv_i$$

$$-m_e \int_{u_i}^{\infty} w_i^2 \frac{F}{m_e} \frac{\partial f_{eI}(v_i)}{\partial v_i} dv_i \qquad (4.2.6.8)$$

or, alternatively

$$W_i = -2m_e \frac{\partial u_i}{\partial t} \int_0^{\infty} w_i f_{eI}(w_i) dw_i - m_e \int_0^{\infty} w_i^3 \frac{\partial f_{eI}(w_i)}{\partial x} dw_i - m_e u_i \int_0^{\infty} w_i^2 \frac{\partial f_{eI}(w_i)}{\partial x} dw_i$$

$$-m_e \int_0^{\infty} w_i^2 \frac{F}{m_e} \frac{\partial f_{eI}(w_i)}{\partial w_i} dw_i, \qquad (4.2.6.9)$$

where we have used Eq. (4.2.5.5). On the other hand, following the same steps, we get

$$W_r = 2m_e \int_{-\infty}^{u_s} w_r \frac{\partial w_r}{\partial t} f_{eR}(v_r) dv_r - m_e \int_{-\infty}^{u_s} w_r^3 \frac{\partial f_{eR}(v_r)}{\partial x} dv_r - m_e u_r \int_{-\infty}^{u_s} w_r^2 \frac{\partial f_{eR}(v_r)}{\partial x} dv_r$$

$$-m_e \int_{-\infty}^{u_s} w_r^2 \frac{F}{m_e} \frac{\partial f_{eR}(v_r)}{\partial v_r} dv_r. \qquad (4.2.6.10)$$

Recasting all the four terms on the r.h.s. of Eq. (4.2.6.10), one finds

$$2m_e \int_{-\infty}^{u_s} w_r \frac{\partial w_r}{\partial t} f_{eR}(v_r) dv_r = -2m_e \frac{\partial u_i}{\partial t} \int_{-\infty}^{0} w_i f_{eI}(w_i) dw_i \qquad (4.2.6.11)$$

$$-m_e \int_{-\infty}^{u_i} w_r^3 \frac{\partial f_{eR}(v_r)}{\partial x} dv_r = -m_e \int_{-\infty}^{0} w_i^3 \frac{\partial f_{eI}(w_i)}{\partial x} dw_i \qquad (4.2.6.12)$$

$$-m_e u_r \int_{-\infty}^{u_s} w_r^2 \frac{\partial f_{eR}(v_r)}{\partial x} dv_r = -m_e u_i \int_{-\infty}^{0} w_i^2 \frac{\partial f_{eI}(w_i)}{\partial x} dw_i \qquad (4.2.6.13)$$

$$-m_e \int_{-\infty}^{u_s} w_r^2 \frac{F}{m_e} \frac{\partial f_{eR}(v_r)}{\partial v_r} dv_r = -m_e \int_{-\infty}^{0} w_i^2 \frac{F}{m_e} \frac{\partial f_{eI}(w_i)}{\partial w_i} dw_i, \qquad (4.2.6.14)$$

getting, finally,

$$W_i = 2m_e \frac{\partial u_i}{\partial t} \int_0^{\infty} w_i f_{eI}(w_i) dw_i + m_e \int_0^{\infty} w_i^3 \frac{\partial f_{eI}(w_i)}{\partial x} dw_i - m_e u_i \int_0^{\infty} w_i^2 \frac{\partial f_{eI}(w_i)}{\partial x} dw_i$$

$$+ m_e \int_0^{\infty} w_i^2 \frac{F}{m_e} \frac{\partial f_{eI}(w_i)}{\partial w_i} dw_i. \qquad (4.2.6.15)$$

Defining the total power density $W_{\text{ToT}} \equiv W_{\text{i}} + W_{\text{r}}$ we find

$$W_{\text{ToT}} = -2m_{\text{e}} u_{\text{i}} \int_0^\infty w_{\text{i}}^2 \frac{\partial f_{\text{eI}}(w_{\text{i}})}{\partial x} dw_{\text{i}} = 2m_{\text{e}} u_{\text{i}} \frac{\partial}{\partial x} \int_0^\infty w_{\text{i}}^2 f_{\text{eI}}(w_{\text{i}}) dw_{\text{i}}. \qquad (4.2.6.16)$$

By making use of Eq. (4.2.5.6), after having set $u_{\text{drift}} = u_{\text{e}}$, Eq. (4.2.6.17) becomes

$$W_{\text{ToT}} = u_{\text{i}} \frac{\partial p_{\text{e}}}{\partial x}. \qquad (4.2.6.17)$$

Using the ideal gas law for Eq. (4.2.6.17), one finds

$$W_{\text{ToT}} = e n_{\text{e}} u_{\text{i}} \frac{\partial T_{\text{e}}}{\partial x} + e T_{\text{e}} u_{\text{i}} \frac{\partial n_{\text{e}}}{\partial x} \qquad (4.2.6.18)$$

which are the same electron power absorption pressure gradient terms (Term IV and Term V) as shown in Eq. (3.1.23.1).

4.3 The γ-mode electron heating mechanism

It is widely known that at high applied voltage and high pressures secondary electron emission can contribute significantly to the electron heating. Secondary electrons are emitted from the electrode surfaces due to impact of ions or neutral atoms, in particular due to metastable atoms. This electron power absorption mechanism is known in the literature as γ-mode electron heating. Early on, Godyak and Khanneh (1986) studied systematically the γ-mode electron heating in a rf driven capacitively coupled discharge from both the theoretical and the experimental point of view. In this type of discharge the ionization is driven by fast electrons generated at the electrode surfaces due to the ion bombardment and are accelerated across the sheath. They also noted that the transition into the γ-mode electron heating is accompanied by a decrease in electron temperature and an increase in the plasma density. Under the assumption of a constant mobility and a negligible recombination rate they found a good agreement between the theoretical calculations and the experiments. These results were later confirmed by Belenguer and Boeuf (1990) by a self consistent fluid model based on equations describing electron and ion transport coupled with Poisson's equation for the electric field. Later on, Godyak et al. (1992) studied experimentally the variation in the electron energy distribution function in low pressure helium and argon rf discharges during a transition from low voltage to high voltage mode. With increasing driving voltage, an increase of the electron density and a decrease in the electron temperature, caused by the secondary electron emission, is observed, along with a transition into a Maxwellian EEDF.

4.4 The DA-mode

In this subsection we will discuss the drift-ambipolar (DA)-mode. Firstly, we will consider the drift mode and the ambipolar mode separately, then we will go through the drift ambipolar-mode.

4.4.1 The drift mode (Ohmic mode or Ω-mode)

The drift mode, also known in the literature as Ohmic mode or Ω-mode, arises from electron neutral collisions described by $m_e n_e \nu_c u_e^2$, which is the VI term (drift/collisional term) of the electron power absorption (Eq. (3.1.23.1)). Under certain conditions, due to the low plasma conductivity caused by the high electron-neutral collision frequency (Eq. (3.1.23.9)) (Schulze et al., 2011a), the drift field accelerates electrons to high energies and dictates the ionization within the bulk region. Since in electropositive discharges the deposited power is distributed to a high number of electrons, the Ohmic heating does not cause a significant ionization. On the other hand, the Ohmic heating may cause a significant ionization in electronegative discharges, due to a lower number of electrons with respect to the electropositive discharges. The Ohmic mode has been observed in electronegative discharges (Denpoh and Nanbu, 2000, 1998; Proshina et al., 2010; Schulze et al., 2011b,a; Derzsi et al., 2013; Teichmann et al., 2013; Shibata et al., 1995; Liu et al., 2012, 2013; Yan et al., 2000) for various plasma discharge configurations and various electronegative gases. By using the expression for both E_{VI} and $J_e \cdot E$ shown in Eqs. (3.1.22.5) and (3.1.23.1), respectively, along with Eq. (3.1.23.9), we can state

$$(J_e \cdot E)_{VI} = \sigma_{dc} E_{VI}^2 = \frac{\varepsilon_0 \omega_{pe}^2}{\nu_c} E_{VI}^2 = \frac{e^2 n_e}{\nu_c m_e} E_{VI}^2 \qquad (4.4.1.1)$$

and

$$(J_e \cdot E)_{VI} = \frac{J_e^2}{\sigma_{dc}} = \frac{J_e^2 \nu_c}{\varepsilon_0 \omega_{pe}^2} = \frac{m_e \nu_c}{e^2 n_e} J_e^2. \qquad (4.4.1.2)$$

From Eq. (4.4.1.1) we see that, to have strong Ohmic heating, high values of σ_{dc} at fixed Ohmic electric field are required or, in other words, the Ohmic heating increases when the collision frequency (electron density) decreases (increases) when the Ohmic electric field is kept constant. On the other hand, since it is difficult to drive the Ohmic electric field in capacitively coupled discharges, it is better to change the point of view and to look at Eq. (4.4.1.2). In fact we see that, in order to have strong Ohmic heating, low values of σ_{dc} at fixed electron current density J_e are needed, or in other words, the Ohmic heating increases when the collision frequency (electron density) increases (decreases) at fixed electron current density. Finally, we observe that, when the negative ion density is kept fixed, a higher electronegativity means to have less free electrons and, consequently, a smaller conductivity. By looking at Eq. (4.4.1.2), we can state that in high (low) electronegative plasma a big (small) contribution of the drift mode to the overall electron heating has to be expected.

4.4.2 The ambipolar mode

In plasma discharges electrons (positive ions) are usually directed into the bulk (toward the electrodes). Such a mechanism creates an ambipolar field directed into the bulk which causes a force pushing the electrons towards the sheath edge. Then a local maximum of the electron density builds up at the sheath edge, causing a corresponding high value of $\partial n_e / \partial x$ on the bulk side of the sheath edge and, consequently, a peak in the electric field at the sheath edge (Schulze et al., 2011a). In such a context one should

expect Term IV from Eq. (3.1.23.1), as well as Term IV from Eq. (3.1.22.5), namely

$$(J_e \cdot E)_{\text{IV}} = e u_e T_e \frac{\partial n_e}{\partial x} \qquad (4.4.2.1)$$

to become relevant. When this situation occurs, it is said that we are in presence of the ambipolar mode. Furthermore, strong peaks in the electric field at the sheath edges have been observed in the electronegative CF_4 discharge (Georgieva et al., 2003). The observed peaks have been related to the corresponding local maxima of the electron density at the sheath edges which are caused by the ambipolar field built up by a net charge separation between the positive charges accelerated towards the electrode and the electrons, together with the negative ions, confined within the bulk region.

4.4.3 The DA-mode

The drift-ambipolar heating (DA-mode) (Schulze et al., 2011a; Derzsi et al., 2015b) is specific to electronegative discharges and refers to the simultaneous presence of both the Ohmic heating (Ω–mode) and the ambipolar heating (ambipolar mode). Being the DA-mode a combination between the drift-mode and of the ambipolar-mode, it arises from the contemporary strong presence of both Term IV and Term VI in Eq. (3.1.23.1). Schulze et al. (2011a) discussed a transition from DA-mode into the α-mode as the voltage was increased at fixed pressure and from α-mode into DA-mode demonstrated by increasing the pressure at fixed voltage in an electronegative CF_4 discharge in both simulations and experiments. The same result has been obtained for dual-frequency capacitively coupled discharges by Derzsi et al. (2015b) in the pressure range 10 - 80 Pa.

As regards to the capacitively coupled oxygen discharge, it has been demonstrated that the singlet metastable molecular states have a significant influence on the electron power absorption mechanism in the capacitively coupled oxygen discharge (Proto and Gudmundsson, 2018b; Gudmundsson and Lieberman, 2015; Gudmundsson and Ventéjou, 2015; Hannesdottir and Gudmundsson, 2016; Gudmundsson and Hannesdottir, 2017) as well as the ion energy distribution (Hannesdottir and Gudmundsson, 2017). At low (high) pressure, i.e. 1.3 Pa (6.6 – 66 Pa), the electron power absorption is mainly located within the plasma bulk (the sheath regions) (Gudmundsson and Ventéjou, 2015; Hannesdottir and Gudmundsson, 2016). Furthermore, when operating at low pressure, the time averaged electron heating within the discharge is due to a hybrid drift-ambipolar mode (DA-mode) and α-mode, while operating at higher pressures, the electron power absorption is due to stochastic heating and the discharge is operated in a pure α-mode (Gudmundsson and Snorrason, 2017; Gudmundsson et al., 2018). Moreover, detachment by singlet molecular metastable states is the process that has the most influence on the electron power absorption process in the higher pressure regime, while it has almost negligible influence at lower pressures (Hannesdottir and Gudmundsson, 2016; Gudmundsson and Ventéjou, 2015; Gudmundsson and Hannesdottir, 2017). However, this depends on the quenching of the singlet metastable states on the electrodes (Proto and Gudmundsson, 2018b).

It has also been demonstrated that the driving frequency plays a relevant role in determining the electron heating mode of an oxygen capacitively coupled discharge. At

low driving frequency and low operating pressure (5 and 10 mTorr), the time averaged electron heating within the discharge is observed to be a combination of stochastic (α-mode) and drift ambipolar (DA) heating in the bulk plasma (the electronegative core) and the time averaged power absorption is dominated by the DA-mode. As the driving frequency or pressure are increased, the electron power absorption is due to a pure α-mode, dominated by a stochastic heating within the bulk region (Gudmundsson et al., 2018). It is worth noting that electron power absorption transitions with increased pressure and driving frequency are only observed when the singlet metastable states are properly included in the discharge model. Conversely, when the singlet metastable states are excluded from the simulation, the electronegativity is high and a significant electron power absorbtion is observed within the bulk region (electronegative core) up to 100 mTorr. Moreover, it has been shown that the higher is the pressure, the higher (lower) is the population of low (high) energy electrons (Gudmundsson and Snorrason, 2017; Gudmundsson et al., 2018), causing a Druyvesteyn-like profile in the EEPF, which is commonly associated with the DA-mode or Ω-mode in the literature for capacitively coupled oxygen discharges. Finally, it is worth noting that a smaller number of high energy electrons decreases the probability for threshold related electron impact processes. Since such processes are the most important ones in a low pressure capacitively coupled oxygen discharge, low populated low energy levels ensure a negligible Ohmic heating within the plasma bulk.

4.5 Electron bounce resonance heating (BRH)

The electron bounce resonance heating (BRH) occurs when fast sheath expansion generates beamlike electrons, which are heated by the two sheaths coherently. Depending on the discharge parameters, such as geometry, pressure, voltage and electronegativity, the electron beams can propagate through the entire discharge and can be reflected at the opposing space-time moving sheath edge. The BSR heating is supposed to be an important constituent in the effective heating of electrons in capacitively coupled discharges when operated at low pressures, since it is closely related to stochastic heating. Moreover, the generation of electron beams can be enhanced by the PSR effect.

It was discovered by Wood et al. (Wood, 1991; Wood et al., 1995) that, in capacitively coupled discharges, fast electron beams can be created at low pressures by the expanding sheaths which can reach the opposite electrode and then collide with the expanding sheath, being reflected back after gaining substantial energy. It is clear that, in this subcategory of collisionless heating mechanisms, the electron motion must be coherent with the oscillation of the electric field. This type of heating mode, generally known in the literature as bounce resonance heating (BRH), was later studied in a theoretical framework by Kaganovich and others (Aliev et al., 1997; Kaganovich, 2002). They showed explicitly that at low pressures the BRH occurs when the time for an electron to traverse the bulk region τ is about half the rf period or its odd multiplets, i.e. $\tau = \frac{n\tau_{\mathrm{rf}}}{2}$. where τ_{rf} is one rf period and $n = 1,3,5,7...$ (Aliev et al., 1997). They predicted that for a fixed discharge frequency there exists a certain discharge gap at which the plasma resistance or equivalently the electron heating reaches the maximum

(Kaganovich, 2002).

Vender and Boswell (1992) pointed out a distortion in the electron velocity distribution in the sheath vicinity due to the electron-sheath interaction. This distortion had been explained through the existence of beam electrons which was supposed to exists independently of the secondary electrons emission. The BRH heating mechamisn was confirmed by Park et al. (2007) using PIC/MCC simulation, where a plateau in the electron energy probability function (EEPF) in the low energy regime has been observed. Later on, Wilczek et al. (2016), using PIC/MCC simulations of a symmetric low pressure single-frequency argon discharge, demonstrated that energetic beam electrons are accelerated by the expanding sheaths and are propagated into the plasma bulk. He also showed that this propagation leads to not negligible charge which form a local electric field in the discharge center. At the same time, the non-linear interaction of bulk electrons with the expanding sheath accelerates a second beam into the plasma bulk. This process is repeated until the sheath stops expanding and leads to the formation of multiple electron beams. Additionally, a local displacement current in the discharge center is present in order to compensate the local enhancement of the conduction current caused by the propagating beam electrons.

In capacitively coupled discharges, You et al. (2005) and several authors had observed electron bounce resonance heating among low energy electrons. However, the BRH heating does not affect the plasma properties. On the other hand, (Schulze et al., 2008c), using different gases such as neon and krypton in the low pressure regime, observed experimentally that electron beams are produced by a fast expanding sheath and reflected by the opposing one. The experiment was performed in an asymmetric single-frequency capacitively coupled radio-frequency discharges using phase resolved optical-emission spectroscopy. Unfortunately, in this experiment, the bouncing was not a resonant one. An experimental proof of the high energy electron BRH effect was presented by Liu et al. (2011), using a dual-frequency (DF) driven discharge with argon gas at low pressures. The proof of the existence of the high energy electrons BRH effect had been achieved by fine tuning some resonant conditions, involving the discharge geometry (full plasma length) and the value of the dual-frequency applied to the discharge.

4.6 Plasma series resonances (PSR) oscillations

Self-excited plasma series resonances (PSR) are high-frequency oscillations superimposed on the normal rf current. They arise from a periodic exchange between the kinetic electrons in the plasma bulk and the electric field in the plasma sheath. A plasma discharge can be often described by a zero-dimensional model consisting of two capacitors (the sheaths) and a lossy inductance (bulk). The effective inductance of the bulk is a consequence of the electron inertia and the Ohmic resistance due to electron-neutral collisions while the space charge in the sheaths provides a capacitive characteristic, although the charge voltage relation differs from a normal capacitor. For this reason, this phenomenon is usually known in the literature as plasma series resonance (PSR).

One of the first theoretical hints for the PSR effect came from the work by Klick

(1996). His work was focused on the relation between the sheath voltage and the displacement current for a low-pressure discharge. New theoretical insights about the PSR effect had been successively given by Ku et al. (1998a,b) in low pressure argon plasmas. Czarnetzki et al. (2006) was the first to study systematically the PSR effect in radio frequency discharges, considering a geometrically asymmetrical discharge where the area of the grounded electrode is much bigger than the area of the powered one, both numerically and theoretically. In fact he had shown that the nonlinearity of the sheath is essential for the excitation of the plasma series resonance oscillations by an rf frequency well below resonance. The choice of geometrically asymmetrical discharges was motivated by the fact that, as shown by Lieberman and Lichtenberg (2005), nonlinearity of the sheath cancels out in symmetrical plasma discharges. Also it is important to remember that most capacitive discharges used in industrial applications are geometrically asymmetric. Moreover, it has observed that the amplitude of high frequency oscillations grows with increased frequency and pressure. In recent times, Bora et al. (2012) has studied the PSR effect in dual-frequency geometrically symmetric plasmas finding a considerable variation in electron heating using electrical asymmetry effect (EAE). Later on, the same authors (Bora and Soto, 2014), using a non linear global model approach applied to a capacitively coupled radio frequency discharge, have studied the influence of finite geometrical asymmetry of the electrodes in terms of generation of dc self-bias and plasma heating.

One of the first experimental confirmations of the PSR mechanism was made by Taillet (1969). He considered radio-frequency plasmoids and resonance-sustained gas discharges. In recent times Godyak et al. (1994), considering an inductively coupled argon discharge at low pressure, showed the presence of non-local electron heating in the inhomogeneous RF field due to spatial dispersion of the plasma conductivity. This was later interpreted as a forerunner of the modern PSR effect. Later on Annaratone et al. (1995) discovered a PSR effect in radio frequency, parallel plate plasma reactors.

Later on Qiu et al. (2003) has confirmed the experiment results shown by Godyak et al. (1994) using PIC/MCC simulations. He discovered that the ion flux to the wall has a narrow angular spread about the normal and the ion bombarding energy distribution has a sharp peak at the plasma potential. This has been one of the first hints of the PSR effect using PIC/MCC simulations. Later on, the presence of the PSR effect has been confirmed experimentally in dual-frequency discharges by Semmler et al. (2007), and in low pressure geometrically symmetrical discharges if the driving voltage waveform makes the discharge electrically asymmetric by Donkó et al. (2009). In recent times, (Schüngel et al., 2015), using a combined approach involving both PIC/MCC simulations and a theoretical model based on an equivalent circuit, and making use of the EAE, which consists in varying the total number of harmonics and tuning the phase shifts between them, has demonstrated that the PSR effect occurs in geometrically symmetric capacitive discharges driven by either symmetric or asymmetric voltage waveforms (multiple consecutive waveforms) if the charge–voltage relation of the plasma sheaths deviates from a simple quadratic behavior and if the inductance of the plasma bulk exhibits a temporal modulation. Moreover, they found that the nonlinearity in the governing equation, which is required to self-excite high frequency PSR oscillations of the current, is found to be strongly affected by the temporal modulation of the bulk inductance and the cubic charge–voltage relation of the plasma sheaths.

Finally, (Schüngel et al., 2015) concluded that the additional heating due to the series resonance oscillations, which approximately doubles electron heating in the discharge half adjacent to the powered electrode, is the primary cause of the observed asymmetry of the electron heating.

4.7 From PSR to non linear electron resonance heating (NERH)

Mussenbrock and Brinkmann (2006) discussed the possibility of a new anomalous heating mechanism of capacitively driven plasmas when operated at low pressure. They proposed the enhanced Ohmic dissipation of a capacitively coupled plasma via the self-excitiation of the plasma series resonance by the nonlinearities of the boundary sheath. This new mechanism was named "non linear electron resonance heating" (NERH). Later on, the same authors (Mussenbrock et al., 2008) showed, by the mean of a nonlinear global model, that the self-excitation of the plasma series resonance in asymmetric capacitively coupled discharges affects both Ohmic heating and stochastic heating. Moreover, they observed that the series resonance effect sharply increases the dissipation. Inspired by the Mussenbrock et al. works, Ziegler et al. (2008) studied the high frequency behaviour of asymmetric dual-frequency capacitive discharges, from both the experimental and the theoretical point of view, finding a good quantitative correspondence. Later on, Yamazawa (2009) demonstrated a significant increase in electron density as the amplitude of the harmonics is increased along with the presence of the non-linear electron resonance heating in a capacitively coupled discharge. In recent times Wilczek et al. (2015) have studied the effect of changing the driving frequency on the plasma density and the electron dynamics in a capacitive radio-frequency argon plasma operated at low pressures using both PIC/MCC simulations and theoretical calculations. He found a step-like increase at a distinct driving frequency. This density jump was found to be caused by an electron heating mode transition from the classical α-mode into a low-density resonant heating mode characterized by the generation of two energetic electron beams at each electrode per sheath expansion phase.

4.8 The striaton mode

Goldstein et al. (1979) studied the striaton structures in an argon discharge from a theoretical point of view. Later on, Kolobov (2006) studied systematically the striaton structures in electropositive discharges in a theoretical way. In recent times, Denpoh (2012), using PIC/MCC simulations applied to an electropositive inductively coupled plasma discharge, has studied the striaton structures within the range pressure 10-200 mTorr finding a good agreement with the experiments. More in detail, the author revealed the electron density and the ionization rate to have a Lorentian-like profile within the striaton distribution as well as the electron temperature to be enhanced with respect to a normal inductively coupled plasma (ICP) with a consequent change in the electron heating mechanism. The first experimental confirmation of self-organized
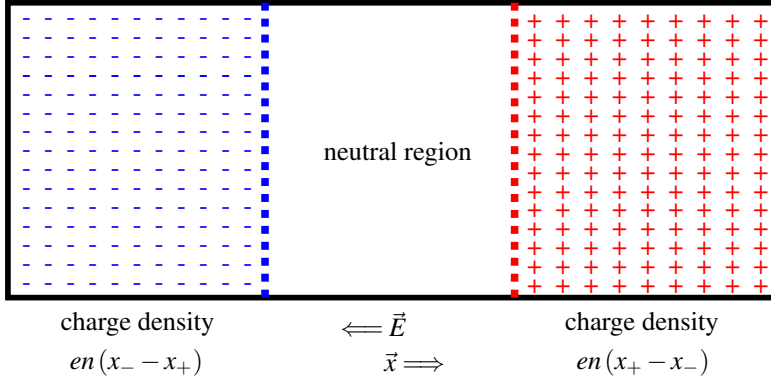
Figure 4.3. The positive and negative ion system immersed in a time-varying, spatially uniform electric field $\vec{E}$.

spatial structures in strong electronegative plasma is due to Liu et al. (2016). The experimental apparatus consisted of an ion-ion capacitive rf discharge of a strongly electronegative plasma (CF_4). By the help of particle-based kinetic simulations, the author has found that the resonance between the driving radio frequency and the eigenfrequency of the ion-ion plasma establishes a modulation of the electric field, the ion densities and the electron heating in the plasma, which leads to striaton structures. Later on, Liu et al. (2017) have extended the previous studies, observing the effects of the driving frequency on the striated structure. More precisely, they found the striations to result from the periodic generation of double layers due to the modulation of the densities of positive and negative ions responding to the externally applied rf potential. The same authors (Liu et al., 2017) also provided a theoretical framework to explain the appearance of striation structures. They analyzed the coupling between the motion of the positive and negative ions in an ion–ion plasma immersed in a time-varying and spatially uniform electric field, as shown in Figure 4.3. We follow Liu et al. (2017) starting from the momentum balance equation for ions

$$m_{i_\pm} n_{i_\pm} \left[\frac{\partial u_{i_\pm}}{\partial t} + u_{i_\pm} \frac{\partial u_{i_\pm}}{\partial x} \right] = \pm e n_{i_\pm} E - \frac{\partial p}{\partial x} - m_{i_\pm} n_{i_\pm} v_{i_\pm} u_{i_\pm} \qquad (4.8.0.1)$$

and neglecting the second term on l.h.s. as well as the pressure gradient term, due to the high pressure enviroment, one finds

$$\frac{\partial u_{i_\pm}}{\partial t} + v_{i_\pm} u_{i_\pm} = \frac{\pm e}{m_{i_\pm}} E. \qquad (4.8.0.2)$$

The positive ions (negative ions) with density n_+ (n_-) are expected to move a distance x_+ (x_-), the space charge is $e n_+ (x_+ - x_-)$ ($e n_- (x_- - x_+)$). In this way the total electric

field can be divided into an internal and external component respectively, so that

$$E = E_{\text{int}} + E_{\text{tot}} \tag{4.8.0.3}$$

$$E_{\text{int}} = \frac{\mp e n_{i_\pm}}{\varepsilon_0} (x_+ - x_-) \tag{4.8.0.4}$$

$$E_{\text{ext}} = E_0 \cos(\omega_{\text{rf}} t). \tag{4.8.0.5}$$

By using the condition $n_+ = n_-$ along with Eq. (4.8.0.3), Eq. (4.8.0.2) can be rewritten for positive and negative ions as follows

$$\frac{\partial u_{i_+}}{\partial t} + \nu_{i_+} u_{i_+} + \frac{e^n}{\varepsilon_0 m_{i_+}} (x_+ - x_-) = \frac{e}{m_+} \cos(\omega_{\text{rf}} t) \tag{4.8.0.6}$$

$$\frac{\partial u_{i_-}}{\partial t} + \nu_{i_-} u_{i_-} - \frac{e^2 n}{\varepsilon_0 m_{i_-}} (x_+ - x_-) = -\frac{e}{m_-} \cos(\omega_{\text{rf}} t). \tag{4.8.0.7}$$

Using the ion plasma frequency shown in Eq. (2.3.0.9), along with the definitions

$$u_{i_+} \equiv \dot{x}_+ \quad , \quad \frac{\partial u_{i_+}}{\partial t} = \ddot{x}_+ \quad , \quad u_{i_-} \equiv \dot{x}_- \quad , \quad \frac{\partial u_{i_-}}{\partial t} = \ddot{x}_-. \tag{4.8.0.8}$$

Eqs. (4.8.0.6) and (4.8.0.7) can be rewritten as follows

$$\ddot{x}_+ + \nu_+ \dot{x}_+ + \omega_+^2 (x_+ - x_-) = \frac{e}{m_+} \cos(\omega_{\text{rf}} t) \tag{4.8.0.9}$$

$$\ddot{x}_- + \nu_- \dot{x}_- - \omega_-^2 (x_+ - x_-) = -\frac{e}{m_-} \cos(\omega_{\text{rf}} t), \tag{4.8.0.10}$$

where $\nu_{i_\pm} = \nu_\pm$ has been set to make the notation homegeneous. By subtracting Eq. (4.8.0.9) from Eq. (4.8.0.10) and setting

$$x \equiv x_+ - x_- \quad , \quad \omega^2 \equiv \omega_+^2 - \omega_-^2 \equiv \frac{e^2 n}{\varepsilon_0 \mu} \quad , \quad \beta \equiv \frac{e E_0}{\mu} \quad \text{where } \mu \equiv \frac{m_+ m_-}{m_+ + m_-}, \tag{4.8.0.11}$$

we get the final equation to be solved

$$\ddot{x} + \nu \dot{x} + \omega^2 x = \beta \cos(\omega_{\text{rf}} t), \tag{4.8.0.12}$$

where the identity $\nu_+ = \nu_-$ has been set for simplicity. By assuming a constant ion collision frequency as well as an initial relative velocity $\dot{x}(0) = 0$ and an initial relative displacement $x(0) = 0$, the solution to Eq.(4.8.0.12) reads

$$x(t) = \frac{\beta}{\sqrt{\left(\omega_{\text{rf}}^2 - \omega^2\right)^2 + \omega_{\text{rf}}^2 \nu^2}} \left[\sin(\omega_{\text{rf}} t - \phi) - \frac{\omega}{\theta} \exp\left(-\frac{\nu t}{2}\right) \sin(\theta t - \psi) \right], \tag{4.8.0.13}$$

where

$$\cos\phi = \frac{\omega_{\rm rf}\nu}{\sqrt{\left(\omega_{\rm rf}^2 - \omega^2\right)^2 + \omega_{\rm rf}^2\nu^2}} \tag{4.8.0.14}$$

$$\cos\psi = \frac{\left[\frac{\nu}{\omega}\left(\omega^2 + \omega_{\rm rf}^2\right)\right]}{\sqrt{\left(\omega_{\rm rf}^2 - \omega^2\right)^2 + \omega_{\rm rf}^2\nu^2}} \tag{4.8.0.15}$$

$$\theta = \frac{1}{2}\sqrt{4\omega^2 - \nu^2} \quad \text{with} \quad 4\omega^2 - \nu^2 > 0. \tag{4.8.0.16}$$

Moreover, for a steady state

$$\lim_{t\to\infty} x(t) = A\sin\left(\omega_{\rm rf}t - \phi\right) \quad \text{with} \quad A = \frac{eE_0/\mu}{\sqrt{\left(\omega_{\rm rf}^2 - \omega^2\right)^2 + \omega_{\rm rf}^2\nu^2}}. \tag{4.8.0.17}$$

From Eq. (4.8.0.17) a resonance at $\omega = \omega_{\rm rf}$ is observed, so that

$$x_{\max}(t) = \left[\lim_{t\to\infty} x(t)\right]\bigg|_{\omega=\omega_{\rm rf}} = \frac{eE_0}{\mu\nu\omega_{\rm rf}}\sin\left(\omega_{\rm rf}t\right) = A_{\max}\sin\left(\omega_{\rm rf}t\right). \tag{4.8.0.18}$$

As shown in Eq. (4.8.0.18), for increasing ion collision frequency ν and/or driving frequency $\omega_{\rm rf}$, the amplitude $A_{\max}$ is suppressed. Moreover, it is worth noting that the ion collision frequency increases for increased pressure, so that the amplitude $A_{\max}$ decreases for increasing pressure. Finally, by using the resonance condition $\omega = \omega_{\rm rf}$, one finds the critical density, over which striations can be observed

$$n_{\rm critical} = \frac{\varepsilon_0\mu\omega_{\rm rf}^2}{e^2} \tag{4.8.0.19}$$

4.9 The equivalent circuit

In the following we will explore the analogy between a capacitively coupled plasma discharge and an equivalent circuit (Lieberman and Lichtenberg, 2005; Chabert et al., 2021). The equivalent circuit representation of a capacitive coupled discharge is shown in Figure 4.4 and consists of a resistor $R_{\rm p}$ in series with an inductor $L_{\rm p}$ for the plasma bulk, connected in series with a capacitor $C_{\rm s}$ and a resistor $R_{\rm s}$, which represent the total capacitance and resistance of the sheaths. Let us consider the electric field expression shown in Eq. (3.1.22.2). In order to build such an equivalence, let us split the equivalent circuit into a bulk and a sheath component, respectively, and let us consider the bulk region for starting. Neglecting the spatial gradients we are left with

$$\frac{\partial\left(m_{\rm e}n_{\rm e}u_{\rm e}\right)}{\partial t} + en_{\rm e}E + m_{\rm e}\nu_{\rm e}n_{\rm e}u_{\rm e} = 0, \tag{4.9.0.1}$$

$$R_{\text{s}} = 2R_{\text{i}} + 2R_{\text{stoc}} + 2R_{\text{Ohm,sh}} \qquad R_{\text{p}}$$

$$C_{\text{s}} \qquad L_{\text{p}}$$

$$V_0 \sin \omega_{\text{rf}} t$$
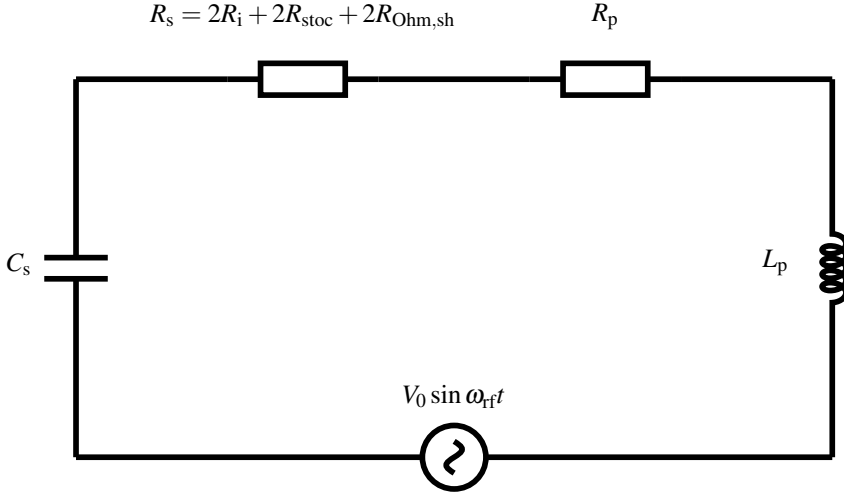
Figure 4.4. Equivalent circuit of a symmetrical capacitively coupled discharge driven by a single frequency.

where we have used the relation in Eq. (3.1.22.4) for Π_{c}. Using the definition for the electron current density $J_{\text{e}} = -en_e u_{\text{e}}$, Eq. (4.9.0.1) can be recast as follows

$$\frac{1}{\nu_{\text{e}}} \frac{\partial J_{\text{e}}}{\partial t} = \sigma_{\text{dc}} E - J_{\text{e}}, \qquad (4.9.0.2)$$

where σ_{dc} is the same dc plasma conductivity as defined in Eq. (3.1.23.9). Now, let us consider a homogeneous plasma slab of thickness d and area A. The total discharge current flowing through the slab is expected to be

$$I_{\text{e}} = A J_{\text{e}}. \qquad (4.9.0.3)$$

Assuming the electric field to be constant through the plasma slab, the voltage drop across the bulk is expected to be

$$\Delta V_{\text{p}} = Ed. \qquad (4.9.0.4)$$

Defining the bulk resistance as

$$R_{\text{p}} = \frac{d}{A \sigma_{\text{dc}}} \qquad (4.9.0.5)$$

and the bulk inductance as

$$L_{\text{p}} = \frac{R}{\nu_{\text{e}}}, \qquad (4.9.0.6)$$

we can rewrite the voltage drop across the plasma bulk, by using Eq. (4.9.0.2), as

$$\Delta V_{\text{p}} = R_{\text{p}} I_{\text{e}} + L_{\text{p}} \frac{\partial I_{\text{e}}}{\partial t}. \qquad (4.9.0.7)$$

Now, let us go through the sheath region by following Chabert et al. (2021). As discussed previously, it has been shown that it is possible to define a sheath capacitance as

$$C_{\mathrm{s}} = \frac{\varepsilon_0 A}{\bar{s}}. \qquad (2.6.2.18)$$

Moreover, the sheaths are also characterized by a total sheath resistance R_{s} which can be split into three different components as follows

$$R_{\mathrm{s}} = 2R_{\mathrm{i}} + 2R_{\mathrm{stoc}} + 2R_{\mathrm{Ohm,sh}}, \qquad (4.9.0.8)$$

where the presence of the factor 2 is due to the fact that we are dealing with two sheaths, one for each electrode. The first term on the r.h.s. of Eq. (4.9.0.8) is R_{i} and accounts for the power dissipation by the ion acceleration in the time-averaged potential of the sheath (Chabert et al., 2021). Knowing the power P_{i}, it is possible to write down the resistance R_{i} as

$$P_{\mathrm{i}} = \frac{1}{2} R_{\mathrm{i}} I_0^2 \qquad (4.9.0.9)$$

where the power may be given by the matrix sheath model or any other consistent model. The second term on the r.h.s. of Eq. (4.9.0.8) is R_{stoc} and accounts for the power dissipation in the sheath by the electrons through stochastic heating. Finally, the third term R_{Ohm} accounts for the power dissipation in the sheath by the electrons through Ohmic heating. Moreover, it is worth noting that power dissipation in the sheaths and in the bulk due to the Ohmic heating are quite similar (Chabert et al., 2021). The equivalent circuit shown in Figure 4.4, depending on the values of the circuit elements which are related to the amplitude and the voltage drop across them, is non linear and its elements all depend on the plasma parameters n_{e} (electron density), T_{e} (electron temperature) and s_{m} (sheath width). Finally, it is possible to write an equation system describing the equivalent circuit. The first equation is Eq. (2.6.2.12), which gives the sheath width and we rewrite

$$s_{\mathrm{m}} = \frac{5 l_0^3}{12 e (h_{\mathrm{l}} n_0)^2 (\omega A)^3 \varepsilon_0 k_{\mathrm{B}} T_{\mathrm{e}}}. \qquad (4.9.0.10)$$

The second equation is

$$n_0 n_{\mathrm{g}} K_{\mathrm{iz}}(T_{\mathrm{e}})(l - s_{\mathrm{m}}) = 2 h_{\mathrm{l}} n_0 u_{\mathrm{B}} \qquad (4.9.0.11)$$

and roughly states that the flux of the electron-ion pairs created in the bulk plasma volume $A(l - s_{\mathrm{m}})$ lost at the two electrodes is equal to the Bohm flux for each electrode. The third equation is

$$\frac{1}{2} \left(R_{\mathrm{p}} + 2R_{\mathrm{stoc}} + 2R_{\mathrm{Ohm,sh}} \right) I_0^2 = 2 e h_{\mathrm{l}} n_0 u_{\mathrm{B}} \mathscr{E}_{\mathrm{T}}(T_{\mathrm{e}}) A \qquad (4.9.0.12)$$

and it is a power balance equation. Eq. (4.9.0.12) states that the absorbed power calculated using the equivalent circuit on the r.h.s. is equal to the power loss on the r.h.s.,

which depends on the Bohm flux and on the energy loss per electron-ion pair created $\mathscr{E}_\mathrm{T}$. The physical quantity $\mathscr{E}_\mathrm{T}$ accounts for both energy loss internally by collisions and energy loss due to the particle flux to the electrodes. The equation system shown above can be solved numerically in order to calculate one quantity at a time, depending on the initial data.

4.10 Relating electron power absorption to ion power absorption

In the following we will show an expression which relates the electron power absorption to the ion power absorption. Let us start from the Poisson equation

$$\frac{\partial E}{\partial x} = \frac{e}{\varepsilon_0} \left(\sum_{i_+} n_{i_+} - \sum_{i_-} n_{i_-} - n_e \right). \qquad (4.10.0.1)$$

Multiplying Eq. (4.10.0.1) by the quantity $u_e E$, we get the following expression

$$u_e \frac{\varepsilon_0}{2} \frac{\partial E^2}{\partial x} = e u_e E \left(\sum_{i_+} n_{i_+} - \sum_{i_-} n_{i_-} \right) + J_e E \qquad (4.10.0.2)$$

or, more explicitely

$$u_e \frac{\varepsilon_0}{2} \frac{\partial E^2}{\partial x} = \sum_{i_+} \frac{u_e}{u_{i_+}} J_{i_+} E + \sum_{i_-} \frac{u_e}{u_{i_-}} J_{i_-} E + J_e E. \qquad (4.10.0.3)$$

The formula above relates the energy of the electrostatic field (l.h.s. of Eq. (4.10.0.3)) to both the electron and the ion power absorption.

5 PIC/MCC simulations

The particle-in-cell (PIC) method is based on a collisionless model and it is one of the most commonly used tools to numerically study the properties of a plasma discharge. The PIC scheme allows for a statistical representation of the general distribution functions in phase space. A plasma can be seen as a N-body problem and it is impossible to solve the Maxwell's equations along with the Boltzmann's equation for all the particles involved. Therefore, it was recognized that an alternative approach to analytical study of the plasma was needed and both numerical and seminumerical models were developed in the second half of 1950s.

The first self-consistent calculations were performed by Buneman (1959) and Dawson (1962), where the charged particles trajectories were computed in periodic systems. Later on, early models calculated Coulomb's law making N^2 operations for N particles. As the time went on, it was soon recognized that imposing a computational mesh could improve the scaling in N. These 1D schemes were successfully applied to basic plasma discharges in 1D without boundary, by using collective effects such as space charges and forces and were referred to as cloud-in-cell (CIC) or particle-in-cell (PIC), depending on the particle weighting considered. The technique has been further developed by Birdsal et al. (Birdsall, 1991; Birdsall and Langdon, 2004, 1991; Vahedi et al., 1993b,a), allowing for a more rigorous treatment of the boundaries, as well as the inclusion of charged-particle-neutral cross sections (Boswell and Morey, 1988) along with the adoption of more realistic differential cross sections (Vahedi and Surendra, 1995), and the extension to higher dimensions (Vahedi and DiPeso, 1997). Further steps in the improvement of the simultaneous solution involving both the external circuit and the plasma chamber have been made as described by Verboncoeur et al. (1993).

When the experiments cannot verify the assumptions made to develop the theory, the PIC simulations can provide insights on unexplored areas of plasma physics and can be thought of as an extension to experiments. On the other hand, when experiments are possible, they can be compared to PIC simulations in order to fine tune the experimental apparatus. The main upside in the PIC simulations is that they provide a self-consistent solution of the physical quantities involved in the plasma processes from first principles without the need for additional assumptions, excluding the eventual parameters to be set at the beginning of the simulation process. On the other hand, the main downside is that the PIC simulations may take a very long time before the results come out and this approach may be computationally expensive. Since time-scale length is proportional to the number of time-steps, large time-scales are difficult to calculate due to the computational cost. In fact in the PIC scheme the numerical fluctuations converge as $C \times N^{-\frac{1}{2}}$ for N particles, where the constant C can be fine tuned, depending on the model scheme. This difficulty has been overcome by using new faster microprocessors.

Finally, the tail of the distribution may be difficult to resolve, due to the poorer statistics (Verboncoeur, 2005).

The particle-in-cell (PIC) method, when combined with Monte Carlo (MC) treatment of collision processes, is currently the most frequently used numerical approach to investigate the properties and the operating modes of the low pressure capacitively coupled discharges. The combination of the particle-in-cell (PIC) method and Monte Carlo collision (MCC) treatment of collision processes is commonly referred to as PIC/MCC method. The basic idea of the PIC method is to allow typically a few hundred thousand computer-simulated particles (superparticles) to represent a significantly higher number of real particles (density in the range of 10^{14}-10^{18} m^{-3}) (Birdsall, 1991; Verboncoeur, 2005; Tskhakaya et al., 2007; Vahedi and Surendra, 1995). In a PIC simulation the position and the velocity of each particle are calculated through the simulation of the motion of these particles, as well as all the relevant micro-quantities. The spatio-temporal evolution of the various macro-quantities (plasma parameters) are evaluated using the field equations at points of a computational grid where each particle is located.

5.1 Global model

In order to determine the partial pressures of neutral species to be used as PIC/MCC inputs in the `oopd1` code as background densities, a global (volume averaged) is used, for both oxygen and chlorine discharges (Thorsteinsson and Gudmundsson, 2010b). In the global model a cylindrical chamber of radius R and length L is assumed. A steady flow Q of neutral species (Cl$_2$ or O$_2$) is introduced through the inlet. The content of the chamber is assumed to be spatially uniform and the power is deposited uniformly into the plasma bulk, except near the sheath edge where the density of positive ions drops significantly. An outlet-flow pressure, which partially controls the pumping of gas out of the chamber, is adjusted to establish the correct discharge pressure p, which is defined as the sum of all neutral species partial pressures in the discharge. Electrons are assumed to have a Maxwellian energy distribution function within the range 0.01–10 eV. The plasma chemistry is described by a set of non-linear equations

$$F(y,t) = dy/dt. \tag{5.1.0.1}$$

A particle balance equation for each of the species included in the discharge and one power balance equation describing the conservation of energy (Lee et al., 1994; Patel, 1998). In this study we assume steady state, namely

$$dy/dt = 0. \tag{5.1.0.2}$$

The equation system above is solved simultaneously by iteration with the MATLAB function `fsolve`, giving the particle densities and electron temperature at a given set of discharge conditions.

5.1.1 The global model reaction set for oxygen and chlorine

The reaction set included in the global model for capacitively coupled oxygen discharge is the same as the one discussed by Thorsteinsson and Gudmundsson (2010b) but with 32 additional reactions to improve the treatment of O_2^-, O_3 and $O_2(b^1\Sigma_g)$ (Proto and Gudmundsson, 2018b) and to make it more detailed as discussed by Toneli et al. (2015). Regarding the capacitively coupled chlorine discharge, the chlorine reaction set in the global model is rather comprehensive (Thorsteinsson and Gudmundsson, 2010b) (Thorsteinsson and Gudmundsson, 2010a). Finally, the global model accounts for boundary processes, such as ion loss at the walls, wall recombination of neutral atoms and wall quenching (Thorsteinsson and Gudmundsson, 2010b).

5.1.2 Particle balance

The particle balance for a species X is given by

$$\frac{dn^{(X)}}{dt} = \sum R_{\text{Generation},i}^{(X)} - \sum R_{\text{loss},i}^{(X)}, \tag{5.1.2.1}$$

where $R_{\text{Generation},i}^{(X)}$ and $R_{\text{loss},i}^{(X)}$ are the reaction rates of the various generation and loss processes of the species X, respectively (Thorsteinsson and Gudmundsson, 2010b). The reaction rate R for a given reaction is calculated as

$$R = k \times \prod_i n_{\text{r},i}, \tag{5.1.2.2}$$

where k is the rate coefficient of the reaction and $n_{\text{r},i}$ is the density of the i-th reactant. Since the discharge is assumed to be quasineutral

$$n_\text{e} = \sum_i n_{i+} - \sum_j n_{j-}, \tag{5.1.2.3}$$

an equation describing the particle balance of free electrons is not required.

5.1.3 Power balance

The power balance equation equates the absorbed power to power losses due to elastic and inelastic collisions and losses due to charged particle flow to the walls

$$\left[\frac{P_\text{abs}}{V} - en_\text{e} \sum_X n^{(X)} \mathscr{E}_\text{c}^{(X)} k_\text{iz}^{(X)} - eu_\text{B} n_\text{i} \frac{A_\text{eff}}{V} \left(\mathscr{E}_\text{i} + \mathscr{E}_\text{e} \right) \right] = \frac{d}{dt} \left(\frac{3}{2} en_\text{e} T_\text{e} \right) = \frac{d}{dt} \left(\frac{3}{2} p_\text{e} \right), \tag{5.1.3.1}$$

where P_abs is the absorbed power, p_e is the thermal electron energy density, u_B is the Bohm velocity shown in Eq. (2.7.0.17), V is the volume of the discharge chamber, $A_\text{eff} = 2\pi \left(R^2 h_\text{L} + RL h_\text{R} \right)$ is the effective surface area for ion loss, h_L and h_R are the axial and radial edge to center positive ion density ratios (Godyak, 1986; Thorsteinsson and Gudmundsson, 2010b, 2009; Lee and Lieberman, 1995), n_e is the electron density, n_i is the positive ion density, $\mathscr{E}_\text{c}$ is the electron collisional loss per electron-ion pair created and $\mathscr{E}_\text{e}$ is the mean kinetic energy per electron lost.

5.1.4 Surface Interactions

The surface interactions taken into account in the global model are the ion loss at the chamber walls, the wall recombination of neutral atoms and the wall quenching Thorsteinsson and Gudmundsson (2010b). The ion loss at the chamber walls process (Thorsteinsson and Gudmundsson, 2010b)

$$X^+ + \text{walls} \rightarrow X \qquad (5.1.4.1)$$

has a rate coefficient $k_{+,\text{wall}}$ equal to

$$k_{+,\text{wall}} = u_{\text{B}} \frac{A_{\text{eff}}}{V} \qquad (5.1.4.2)$$

where u_{B} is the Bohm velocity shown in Eq. (2.7.0.17), V and A_{eff} are the volume of the discharge chamber and the effective surface area for ion loss, respectively, already discussed in the previous section. The wall recombination of neutral atoms process (Thorsteinsson and Gudmundsson, 2010b)

$$X + \text{wall} \rightarrow \frac{1}{2} X_2 \qquad (5.1.4.3)$$

is generally considered to be the most important process for atomic loss in molecular discharges. The wall recombination coefficient γ_{rec} is considered to be one of the most important parameters in molecular discharge modelling (Thorsteinsson and Gudmundsson, 2010b). Finally, the wall quenching process

$$X^* + \text{wall} \rightarrow X \qquad (5.1.4.4)$$

$$(X^2)^* + \text{wall} \rightarrow X^2 \qquad (5.1.4.5)$$

can be important for the loss of excited species, in particular for the metastable species whose radiative lifetime is very long (Thorsteinsson and Gudmundsson, 2010b).

5.2 The PIC/MCC method

The particle-in-cell (PIC) simulations are realized using a certain number of particles. Usually, each computer particle, or superparticle, represents something like $10^6 - 10^9$ real particles. Therefore, the computer particles are actually a charge sheet which can move inside the simulation region (grid). Such a grid consists in N_c cells, resulting in a simulation region made of $N_c + 1$ points. In the 1d-3v PIC model every superparticle is assigned a position x and three velocity components, v_x, v_y and v_z. As shown in Figure 5.1, the computational cycle is made of a certain number of steps. Such a cycle allows to compute the physical quantities recursively. Every PIC/MCC cycle step will be reviewed in the following.

5.2.1 Weighting of the particles to the grid points

Given the continuous particle position, it is of paramount importance to calculate the charge density on the discrete grid points in order to determine the force at the particles
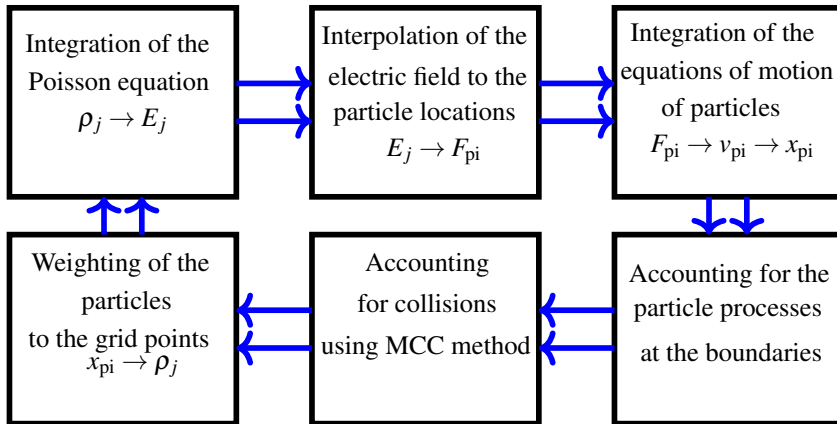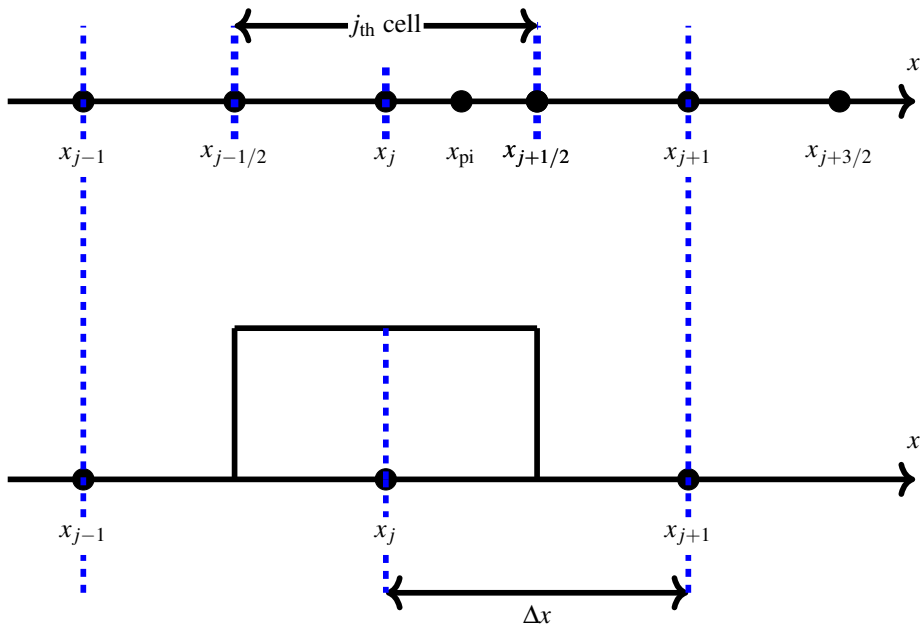
Figure 5.1. The PIC/MCC cycle.

Figure 5.2. The zero-order or NGP (nearest grid point) weighting.
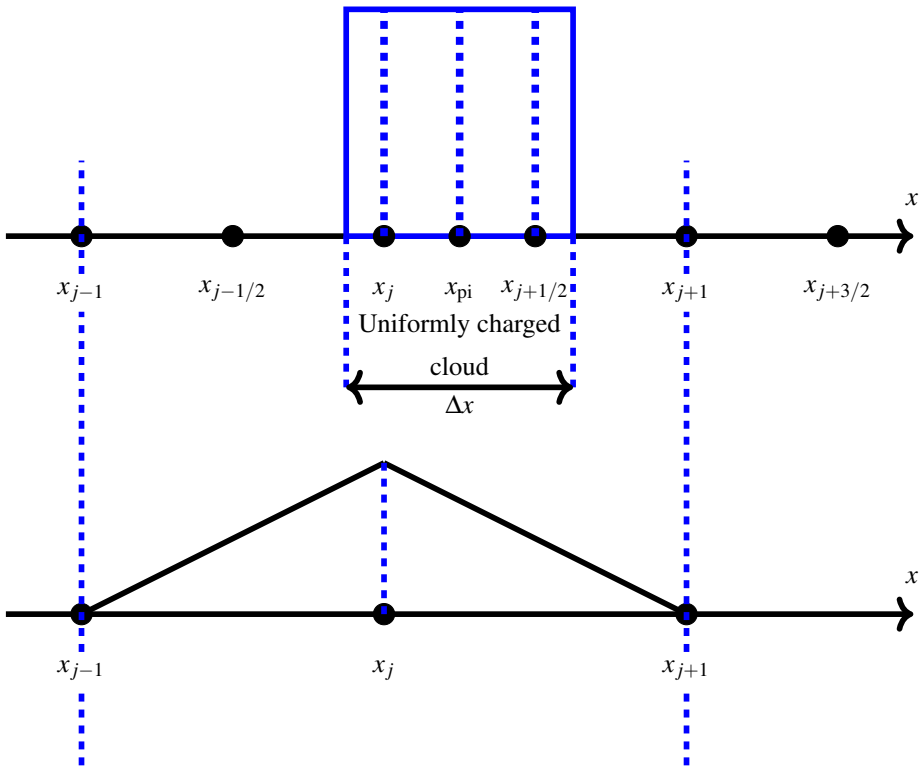
Figure 5.3. The first-order or CIC (cloud in cell) weighting.

from the fields on the grid points (Birdsall and Langdon, 1991). The charge density ρ_j at every grid point x_j is obtained by a weighting of the particles to the spatial grid. Such a procedure is also known in the literature as charge assignment. Such a procedure allows for a smoothing of the charge density in order to reduce the noise of the electric field due to the discrete calculations involved in the simulation (Birdsall, 1991; Langdon, 1970; Vender, 1990a). Therefore, the charge density is calculated on the discrete grid points x_j from the continuous particle position x_{pi}. The weighting function $W(x_j - x_{pi})$ can be zero order nearest-grid point (NGP), first order (CIC or PIC) or higher order (TSC and so on). In the weighting procedure the particles are considered as finite size rigid clouds and may pass freely through each other. The general expression for the charge assignment is (Birdsall, 1991; Langdon, 1970; Vender, 1990a)

$$\rho_j = \sum_{pi} q_{pi} W(x_j - x_{pi}), \qquad (5.2.1.1)$$

where x_j, x_{pi} and q_{pi} identify the discrete grid points, the continuous position and the charge of the ith particle, respectively (Birdsall, 1991; Langdon, 1970; Vender, 1990a; Georgieva, 2006).

In the zero-size-particle (ZSP) or nearest-grid-point (NGP) scheme (Figure 5.3), both the particle charge and mass are located at the nearest grid point and the force is evaluated consequently. The main upside in the ZSP-NGP weighting lies in the fact that the self-force is zero. Moreover, it is a fast process since, as we will see, only one grid look-up is needed. On the other hand, the main downside is that the force, between two particles within a gap range smaller than one-cell-width, vanishes. This makes the ZSP-NGP method inaccurate, although several ways have been suggested in order address this difficulty such as considering a higher number of particles in a Debye circle so that $N_{De} = 4\pi\lambda_{De}^2 \gg 1$ (Birdsall and Fuss, 1969). Moreover, both density and electric field jump at the boundaries, causing a manifest noise which can be intolerable in many plasma problems. In the ZSP scheme the density at every grid point, noted by the index j, is calculated counting the number of particles in the grid point surroundings with radius $\Delta x/2$ (where $\Delta x = x_{j+1} - x_j = x_{j+\frac{1}{2}} - x_{j-\frac{1}{2}}$) and dividing it by the volume of the surrounding. In one dimensional simulation this means counting particles in the interval $\left[x_{j-\frac{1}{2}}, x_{j+\frac{1}{2}} \right]$ and dividing it by Δx. The electric field used to determine the force is that at x_j for all particles in the j_{th} cell. Such a process is equivalent to consider a particle with finite-size rectangular shape with length Δx, as shown in Figure 5.3. Finally, we observe that we have a collection of finite-size particles so that the physics observed will be that of such particles rather than of point particles, as it can be clearly seen in Figure 5.3 (Birdsall and Langdon, 1991).

In the cloud-in-cell (CIC) or particle-in-cell (PIC) (Figure 5.3) scheme the particles are located at the center-of-mass-charge of charged clouds of finite size (Birdsall and Fuss, 1969; Birdsall, 1991). In the 1D models the assigned charge density is usually obtained by sharing the charges between the two-nearest-grid-points. It is worth saying that the cloud width can be different from the cell width. Moreover, the more the cloud width is increased, the more the force is smoothed out and the more the zero force region shrinks (Birdsall and Fuss, 1969; Birdsall, 1991). Naturally, as already said, taking a zero width cloud means dealing with the ZSP-NGP scheme. In principle, the cloud width could vary during the problem. Finally, in order to ensure the correct resolution of

the cloud density, the following condition has to be imposed (Birdsall and Fuss, 1969; Birdsall, 1991)

$$\Delta x \equiv \text{Cloud Width} > \text{Cell Width} \equiv \Delta x_c, \qquad (5.2.1.2)$$

where cell width stands for the size of each cell. Since the particles may be seen as objects extending over a cell width, the interpolation shown in Eq. (5.2.1.2) is commonly referred to as cloud-in-cell technique (CIC-PIC). If the particle or cloud has a uniform density with width equal to Δx and charge q_{pi}, the charge assigned to grid point j is

$$q_j = q_{pi} \left[\frac{\Delta x - (x_{pi} - x_j)}{\Delta x} \right] = q_{pi} \left[\frac{x_{j+1} - x_{pi}}{\Delta x} \right], \qquad (5.2.1.3)$$

while the charge assigned to grid point $j+1$ is

$$q_{j+1} = q_{pi} \left[\frac{\Delta x - (x_{j+1} - x_{pi})}{\Delta x} \right] = q_{pi} \left[\frac{x_{pi} - x_j}{\Delta x} \right], \qquad (5.2.1.4)$$

where we have used the definition $\Delta x \equiv x_{j+1} - x_j$. The previous expressions can be recast into a single one by writing for $|x_{pi} - x_j| \leq \Delta x$

$$W(x_j - x_{pi}) = 1 - \frac{|x_{pi} - x_j|}{\Delta x} \qquad (5.2.1.5)$$

and for $|x_{pi} - x_j| > \Delta x$

$$W(x_j - x_{pi}) = 0. \qquad (5.2.1.6)$$

Since the nearest left-hand grid point j is located first, the inequality $x_{pi} > x_j$ always holds. In this way the density and field fluctuations are smoothed and the noise is reduced. In fact, as a cloud moves through the grid, it contributes to density much more smoothly than with zero-order weight. As it is clearly seen from Figure 5.3, the net effect is to produce a triangular shape, with an amplitude equal to Δx (Figure 5.3) (Birdsall and Langdon, 1991). On the other hand, the first-order weighting has a higher computational cost compared to the zero-order weighting. Moreover, the PIC and the CIC scheme are equivalent in cartesian coordinates but differ in cylindrical and spherical coordinates (Birdsall, 1991). Finally, we underline that the first order weighting discussed above is the same as applying zero-order weighting to each nearest grid point (Birdsall and Langdon, 1991).

In the higher order weighting (area weighting, splines) the roughness in particle shape is reduced, as well as the density and field noise. However, this is much more computationally expensive than the second order weighting (Birdsall and Langdon, 1991).

5.2.2 Integration of the Poisson equation

At this point it is fundamental to calculate the potential by using the discretized version of the Poisson equation (Eq. (2.1.0.1)). In order to achieve this goal the finite-difference

scheme has to be employed. In this scheme three different types of first derivatives are available: the forward difference

$$f_i' = \frac{f_{i+1} - f_i}{\Delta x} + O(\Delta x), \tag{5.2.2.1}$$

the backward difference

$$f_i' = \frac{f_i - f_{i-1}}{\Delta x} O(\Delta x), \tag{5.2.2.2}$$

and the central difference

$$f_i' = \frac{f_{i+1} - f_{i-1}}{\Delta x} O(\Delta x^2), \tag{5.2.2.3}$$

as well as for the second derivatives. In fact we have the forward difference

$$f_i'' = \frac{f_{i+2} - 2f_{i+1} + f_i}{\Delta x} + O(\Delta x), \tag{5.2.2.4}$$

the backward difference

$$f_i'' = \frac{f_i - 2f_{i-1} + f_{i-2}}{\Delta x} O(\Delta x), \tag{5.2.2.5}$$

and the central difference

$$f_i'' = \frac{f_{i+1} - 2f_i + f_{i-1}}{\Delta x} O(\Delta x^2). \tag{5.2.2.6}$$

As we can see from the relations shown above, the central difference returns the best approximation. However, it is worth noting that the central difference approach could be troublesome when f is a highly oscillating function such that $f_{i+1} = f_{i-1}$, yielding $f_i' = 0$. Since this is not the case, we will assume a central difference in the following. So we are ready to calculate the potential as (Birdsall, 1991; Georgieva, 2006; Gozadinos, 2001)

$$\Phi_{j+1} = -\frac{(\Delta x)^2 \rho_j}{\varepsilon_0} + 2\Phi_j - \Phi_{j-1}. \tag{5.2.2.7}$$

Then the potential is used to calculate the electric field via the discretized version of the relation between the static potential and the electric field. This can be done by using the central difference scheme again (Birdsall, 1991; Georgieva, 2006; Gozadinos, 2001), as shown in Eq. (5.2.2.3)

$$E_j = \frac{\Phi_{j-1} - \Phi_{j+1}}{\Delta x} \tag{5.2.2.8}$$

in the electrostatic case. As we can see from Eq. (5.2.2.8) there is no loss of resolution.
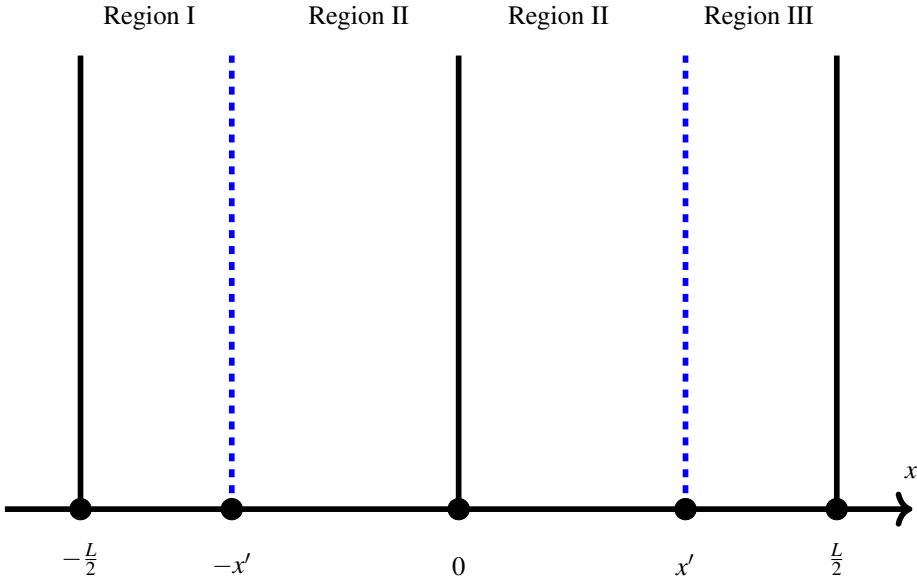
Figure 5.4. Two particles located at $x = \pm x'$, respectively, embedded in a grid with width equal to L.

5.2.3 Interpolation of the electric field

Since the electric field is evaluated midway between grid points, an interpolation procedure must be used to estimate the field at the particle positions as well as the forces acting on them. Such an interpolation can be the same as used for the density. Using the same interpolation kernel for both the density and the electric field allows us to avoid problems due to particle self forces (Birdsall, 1991; Vender, 1990a; Hockney and Eastwood, 1988), which are related to gravitation-like instabilities. The electric field at the particle position is

$$E(x_{\mathrm{pi}}) = \left[\frac{x_{j+1} - x_{\mathrm{pi}}}{\Delta x}\right] E_j + \left[\frac{x_{\mathrm{pi}} - x_j}{\Delta x}\right] E_{j+1}. \qquad (5.2.3.1)$$

The electric field is weighted using $W(x_j - x_{\mathrm{pi}})$ so that the electrostatic force reads as

$$F_{\mathrm{pi}} = q_{pi} \sum_j E_j W(x_j - x_{pi}). \qquad (5.2.3.2)$$

Now, let us consider two charges embedded in a d-dimensional system. It is widely known that

$$\vec{E} \propto \frac{1}{|\vec{r}|^{d-1}} \quad \text{where} \quad \vec{r} \equiv \vec{x}_2 - \vec{x}_1. \qquad (5.2.3.3)$$

This has two important consequences. Firstly, the force depends on the charge separation only and it is independent on the average particle location $\vec{r}_{\mathrm{CM}} \equiv (\vec{x}_1 + \vec{x}_2)/2$. Secondly,

in a one dimensional system, the electric field, and so the electrostatic force, is not even dependent of the separation between the two charges $\vec{r}$. In this case the force behaves like a step function, i.e. it is zero when $\vec{x}_1 = \vec{x}_2$ and changes sign when the particles cross each other. However, when a spatial grid is added to the system, the Coulomb law is modified at short range. It can be shown that, in a one dimensional system, the interaction force in the presence of a grid is given by (Birdsall, 1991; Langdon, 1970)

$$F(x_1, x_2) = F\left(\bar{x} - \frac{\tilde{x}}{2}, \bar{x} + \frac{\tilde{x}}{2}\right), \qquad (5.2.3.4)$$

where $\tilde{x} \equiv x_2 - x_1$ is the charge separation and $\bar{x} = (x_1 + x_2)/2$ is the mean charge position on the grid. In order to see how the presence of a grid can modify the behaviour of the force in a one dimensional system, let us consider a simple periodic system containing two equal and opposite charges (Hockney and Eastwood, 1988), as shown in Figure 5.4

$$\frac{d^2 \Phi}{dx^2} = -\frac{q}{\varepsilon_0} \left[\delta\left(x - x'\right) - \delta\left(x + x'\right)\right] \qquad (5.2.3.5)$$

along with the condition on the periodic potential

$$\Phi(x + L) = \Phi(x), \qquad (5.2.3.6)$$

where we have set $x_2 = -x_1 = x'$ for simplicity, so that, from now on, $\bar{x} = 0$ and $\tilde{x} = 2x'$. Solving Eq. (5.2.3.5) and Eq. (5.2.3.6), we will show that the force F will be a function of $\tilde{x}$ (x') only. In order to achieve this goal, let us decompose the space into three distinct spatial regions as shown in Figure 5.4, so that in Region I

$$\Phi_{\mathrm{I}} = A_{\mathrm{I}} x + B_{\mathrm{I}}, \qquad (5.2.3.7)$$

in Region II

$$\Phi_{\mathrm{II}} = A_{\mathrm{II}} x + B_{\mathrm{II}}, \qquad (5.2.3.8)$$

and in Region III

$$\Phi_{\mathrm{III}} = A_{\mathrm{III}} x + B_{\mathrm{III}}. \qquad (5.2.3.9)$$

Now, let us apply the continuity condition on the potential and on the first derivative of the potential at $x = |L/2|$

$$\Phi_{\mathrm{I}}\left(-\frac{L}{2}\right) = \Phi_{\mathrm{III}}\left(\frac{L}{2}\right) \implies -\frac{L}{2} A_{\mathrm{I}} + B_{\mathrm{I}} = \frac{L}{2} A_{\mathrm{III}} + B_{\mathrm{III}} \qquad (5.2.3.10)$$

$$\left.\frac{d\Phi_{\mathrm{I}}}{dx}\right|_{x=-\frac{L}{2}} = \left.\frac{d\Phi_{\mathrm{III}}}{dx}\right|_{x=\frac{L}{2}} \implies A_{\mathrm{I}} = A_{\mathrm{III}}. \qquad (5.2.3.11)$$

Then, we apply the boundary conditions on the layers dividing Region III from Region II and Region II from Region I getting, respectively

$$\Phi_{\mathrm{II}}\left(x'\right) = \Phi_{\mathrm{III}}\left(x'\right) \implies A_{\mathrm{II}} x' + B_{\mathrm{II}} = A_{\mathrm{III}} x' + B_{\mathrm{III}} \qquad (5.2.3.12)$$

$$\Phi_{\mathrm{II}}\left(-x'\right) = \Phi_{\mathrm{I}}\left(-x'\right) \implies -A_{\mathrm{II}} x' + B_{\mathrm{II}} = -A_{\mathrm{I}} x' + B_{\mathrm{I}}. \qquad (5.2.3.13)$$

Finally, integrating Eq. (5.2.3.5) between $x' + \varepsilon$ and $x' - \varepsilon$ and taking the limit for $\varepsilon \to 0$, one finds

$$\frac{d\Phi_{\text{III}}}{dx}\bigg|_{x=x'+\varepsilon} - \frac{d\Phi_{\text{II}}}{dx}\bigg|_{x=x'-\varepsilon} = -\frac{q}{\varepsilon_0} \implies A_{\text{III}} - A_{\text{II}} = -\frac{q}{\varepsilon_0} \tag{5.2.3.14}$$

$$\frac{d\Phi_{\text{II}}}{dx}\bigg|_{x=x'+\varepsilon} - \frac{d\Phi_{\text{I}}}{dx}\bigg|_{x=x'-\varepsilon} = \frac{q}{\varepsilon_0} \implies A_{\text{II}} - A_{\text{I}} = \frac{q}{\varepsilon_0}. \tag{5.2.3.15}$$

Gathering all the relations shown above leads to the following equation system

$$-\frac{L}{2}A_{\text{I}} + B_{\text{I}} = \frac{L}{2}A_{\text{III}} + B_{\text{III}} \tag{5.2.3.16}$$

$$A_{\text{I}} = A_{\text{III}} \tag{5.2.3.17}$$

$$A_{\text{II}}x' + B_{\text{II}} = A_{\text{III}}x' + B_{\text{III}} \tag{5.2.3.18}$$

$$-A_{\text{II}}x' + B_{\text{II}} = -A_{\text{I}}x' + B_{\text{I}} \tag{5.2.3.19}$$

$$A_{\text{III}} = A_{\text{II}} - \frac{q}{\varepsilon_0} \tag{5.2.3.20}$$

$$A_{\text{II}} = A_{\text{I}} + \frac{q}{\varepsilon_0}. \tag{5.2.3.21}$$

Moreover, since $d^2\Phi/dx^2$ is odd in x (Eq. (5.2.3.3)), we can set an additional condition

$$\Phi(x) + \Phi(-x) = 0 \tag{5.2.3.22}$$

which, applied to Region II, leads to

$$B_{\text{II}} = 0. \tag{5.2.3.23}$$

At this point we are able to solve the system, getting

$$A_{\text{I}} = -\frac{2x'}{L}\frac{q}{\varepsilon_0} \tag{5.2.3.24}$$

$$A_{\text{II}} = \frac{q}{\varepsilon_0}\left[1 - \frac{2x'}{L}\right] \tag{5.2.3.25}$$

$$A_{\text{III}} = -\frac{2x'}{L}\frac{q}{\varepsilon_0} \tag{5.2.3.26}$$

$$B_{\text{I}} = -\frac{qx'}{\varepsilon_0} \tag{5.2.3.27}$$

$$B_{\text{II}} = 0 \tag{5.2.3.28}$$

$$B_{\text{III}} = \frac{qx'}{\varepsilon_0} \tag{5.2.3.29}$$

so that, the potential evaluated in the three regions reads

$$\Phi_{\text{I}} = \frac{q}{\varepsilon_0 L}\left[-L-2x\right]x' \tag{5.2.3.30}$$

$$\Phi_{\text{II}} = \frac{q}{\varepsilon_0 L}\left[L-2x'\right]x \tag{5.2.3.31}$$

$$\Phi_{\text{III}} = \frac{q}{\varepsilon_0 L}\left[L-2x\right]x'. \tag{5.2.3.32}$$

Now, we are ready to calculate the electric field at $|x| = x'$, for $x \neq 0$ and $x \neq |L/2|$, as

$$E\Big|_{x=+x'} = -\frac{\frac{d\Phi_{\text{III}}}{dx}\Big|_{x=x'} + \frac{d\Phi_{\text{II}}}{dx}\Big|_{x=x'}}{2} = -\frac{q}{2\varepsilon_0 L}\left[L-4x'\right] \tag{5.2.3.33}$$

$$E\Big|_{x=-x'} = -\frac{\frac{d\Phi_{\text{I}}}{dx}\Big|_{x=x'} + \frac{d\Phi_{\text{II}}}{dx}\Big|_{x=x'}}{2} = -\frac{q}{2\varepsilon_0 L}\left[L-4x'\right] \tag{5.2.3.34}$$

so that (Hockney and Eastwood, 1988)

$$E\Big|_{|x|=x'} = -\frac{q}{2\varepsilon_0 L}\left[L-4x'\right] \quad \text{for} \quad x \neq 0 \quad \text{and} \quad x \neq |L/2|. \tag{5.2.3.35}$$

On the other hand, for $x = 0$ and $x = |L/2|$, we find, respectively (Hockney and Eastwood, 1988)

$$E\Big|_{x=0} = 0 \tag{5.2.3.36}$$

$$E\Big|_{x=|L/2|} = 0. \tag{5.2.3.37}$$

That means that, in a one dimensional system, two opposite charges embedded in one dimensional grid, equipped with a periodic potential, the electrostatic force depends on the charge separation (and on the period L), contrary to the situation when the grid absent, leading to a charge separation independent force. We remind that the mean charge separation is absent in Eq. (5.2.3.35), since it has been set equal to zero at the beginning. It is worth noting that, taking the separation average of the force defined in Eq. (5.2.3.4) as

$$\overline{F}(x_1, x_2) = \frac{1}{\Delta x}\int_{\Delta x} F\left[\bar{x}-\frac{x}{2},\bar{x}+\frac{x}{2}\right]d\bar{x} = \overline{F}(x_1-x_2), \tag{5.2.3.38}$$

we can define the quantity

$$\delta F = F - \overline{F} \tag{5.2.3.39}$$

which is a non-physical grid force. Such a quantity can be important since allows to employ different approximations when $\delta F \ll 1$ (Birdsall, 1991). Finally, for an infinite system, the force shown in Eq. (5.2.2.4) can be expanded as a Fourier series (Birdsall, 1991)

$$F\left(\bar{x}-\frac{\tilde{x}}{2},\bar{x}+\frac{\tilde{x}}{2}\right) = \int_{-\infty}^{+\infty}\frac{dk}{2\pi}\exp\left(ikx\right)\sum_{p=-\infty}^{p=+\infty}\exp\left(ipk_{\text{g}}\bar{x}\right)F_p\left(k\right) \quad \text{with} \quad k_{\text{g}} = \frac{2\pi}{L}, \tag{5.2.3.40}$$

where k_g is the grid wave number and

$$F_p(x) = \int_{-\frac{L}{2}}^{\frac{L}{2}} d\bar{x} \exp\left(-ipk_g\bar{x}\right) F\left(\bar{x} - \frac{\tilde{x}}{2}, \bar{x} + \frac{\tilde{x}}{2}\right) \quad \text{with} \quad k_g = \frac{2\pi}{\Delta x} \qquad (5.2.3.41)$$

$$F_p(k) = \int_{-\infty}^{+\infty} dx F_p(x) \exp\left(-ikx\right). \qquad (5.2.3.42)$$

Now, let us consider a particle density $n(x)$. Thr force $F(x)$ acting on a particle x is

$$F(x) = \int dx^* F(x^*, x) n(x^*) \qquad (5.2.3.43)$$

which, after the Fourier transform shown in Eq. (5.2.3.40), becomes

$$F(k) = \sum_{-\infty}^{+\infty} F_p\left(k - \frac{pk_g}{2}\right) n(k_p) \quad \text{where} \quad k_p = k - pk_g. \qquad (5.2.3.44)$$

That means that δF ($p \neq 0$ terms) couples density perturbations and forces at wave numbers which are different from the grid wave number k_g. The k_p values are said to be aliases of one another.

5.2.4 Integration of the equations of motion of particles

At every simulation step all particle positions and velocities are initially updated and the equations of motion are employed in order to obtain the particles new positions and velocities (Buneman, 1967; Boris, 1970; Birdsall, 1991). The integration scheme used is the leap-frog method illustrated in Figure 5.5. Since the particle's position and velocity are not known at the same time, the equations of motion are used to advance the particles to new positions and velocities. In this scheme a particle's position is known at time t, whereas its velocity is known at time $t - \Delta t$. So it is possible to replace the first order differential equations in the continuum

$$F = m\frac{dv}{dt} \qquad (5.2.4.1)$$

$$v = \frac{dx}{dt} \qquad (5.2.4.2)$$

by their discretized versions

$$F_t = m\left(\frac{v_{t+\frac{\Delta t}{2}} - v_{t-\frac{\Delta t}{2}}}{\Delta t}\right) \qquad (5.2.4.3)$$

and

$$\frac{x_{t+\Delta t} - x_t}{\Delta t} = v_{t+\frac{\Delta t}{2}}, \qquad (5.2.4.4)$$

respectively. The particle's position and velocity advance is shown in Figure 5.5. Finally, it is worth noting that the initial set up has to be chosen carefully in order to have the initial particle position equal to zero at $t = 0$. By looking at Figure 5.5, this means that $v(0)$ has to be pushed back to $v(-\Delta t/2)$ (Georgieva, 2006).
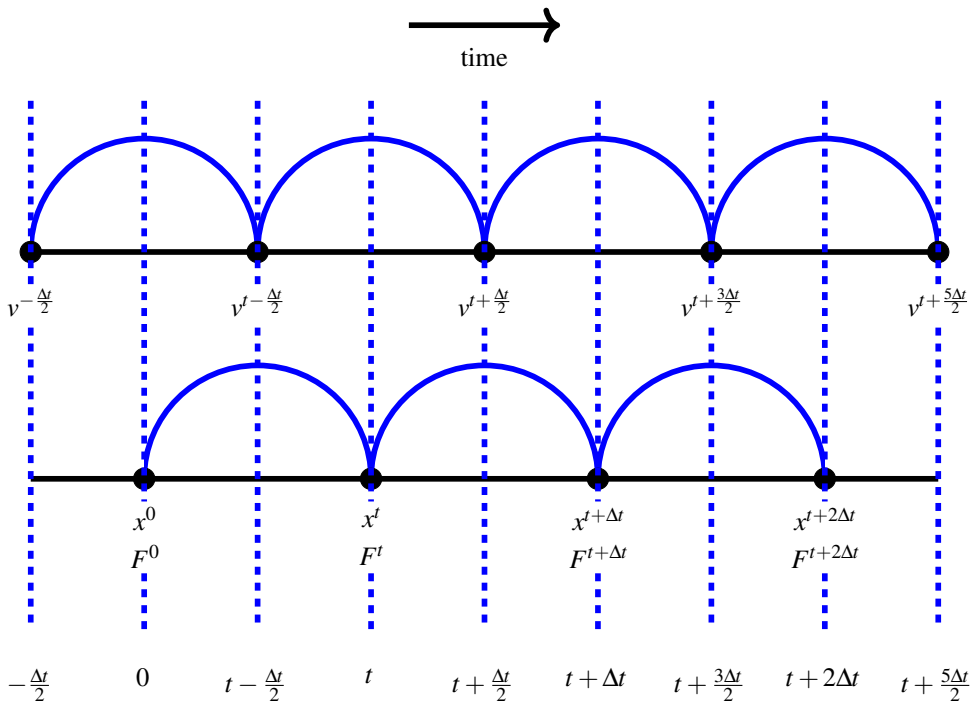
Figure 5.5. The leap-frog integration method.

5.2.5 Accounting for the processes at the boundaries

Since an external circuit current interacts with the plasma current via the electrode surface charge, a simultaneous solution for the potential and circuit equations is needed (Birdsall, 1991; Verboncoeur, 2005). The plasma discharge potential is usually given by the distribution of the space charge within the plasma, the electrode surface charge and the external circuit current. In order to join the charges at the boundaries with the external circuit, the first step is to consider the Gauss law applied to both the electrodes

$$\int_S \vec{E} d\vec{S} = \int_V \frac{\rho}{\varepsilon_0} dV + \frac{A_0 \sigma_0 + A_N \sigma_N}{\varepsilon_0} = 0, \tag{5.2.5.1}$$

where the surface $\vec{S}$ encloses the plasma and electrodes, A_0, σ_0, σ_N and A_N are the surface areas and charges of the bottom and top electrodes, respectively. The boundary conditions for the 1D system are

$$\Phi_T = 0 \tag{5.2.5.2}$$

and

$$E_0 = \frac{\sigma_0}{\varepsilon_0}. \tag{5.2.5.3}$$

Applying the Gauss law to each grid point one finds

$$\frac{\Phi_{j-1} - 2\Phi_j + \Phi_{j+1}}{(\Delta z)^2} = -\frac{\rho_j}{\varepsilon_0}. \tag{5.2.5.4}$$

Now, writing Eq. (5.2.5.3) at one half grid cell from the boundary along with the central difference applied to the definition of potential, one finds

$$E_{1/2} = \frac{\Phi_1 - \Phi_0}{\Delta z} = \frac{1}{\varepsilon_0} \left[\sigma_B + \rho_B \frac{\Delta z}{2} \right]. \tag{5.2.5.5}$$

Eq. (5.2.5.4), along with the boundary conditions shown in Eqs. (5.2.5.2) and (5.2.5.3), can be written in a general matrix form

$$
\begin{vmatrix}
b_0 & c_0 & 0 & \cdots & \cdots & \cdots & \cdots \\
a_1 & b_1 & c_1 & 0 & \cdots & \cdots & \cdots \\
0 & a_2 & b_2 & c_2 & 0 & \cdots & \cdots \\
\cdots & \cdots & \cdots & \cdots & \cdots & \cdots & \cdots \\
\cdots & \cdots & \cdots & \cdots & \cdots & \cdots & \cdots \\
\cdots & \cdots & \cdots & 0 & a_{N-2} & b_{N-2} & c_{N-2} \\
\cdots & \cdots & \cdots & \cdots & 0 & a_{N-1} & b_{N-1}
\end{vmatrix}
\times
\begin{vmatrix}
\Phi_0 \\
\Phi_1 \\
\Phi_2 \\
\cdots \\
\cdots \\
\Phi_{N-2} \\
\Phi_{N-1}
\end{vmatrix}
= -\frac{(\Delta z)^2}{\varepsilon_0}
\begin{vmatrix}
d_0 \\
d_1 \\
d_2 \\
\cdots \\
\cdots \\
d_{N-2} \\
d_{N-1}
\end{vmatrix},
\tag{5.2.5.6}
$$

where

$$a_j = 1 , \quad j = 1, 2, ..., N-1 \tag{5.2.5.7}$$

$$b_0 = -1 , \quad b_j = -2, \quad j = 1, 2, ..., N-1 \tag{5.2.5.8}$$

$$c_j = 1, \quad j = 0, 1, 2, ..., N-2 \tag{5.2.5.9}$$

$$d_0 = \frac{\sigma_0^t}{\Delta z} + \frac{\rho_0^t}{2} , \quad d_j = \rho_j^t \, j = 1, 2, ..., N-1. \tag{5.2.5.10}$$

The conservation charge at each wall reads

$$A\Delta\sigma = Q_{\text{conv}} + \Delta Q, \tag{5.2.5.11}$$

where Q_{conv} and ΔQ are the charges deposited related to the convection and external circuit current over a time interval, respectively. Eq. (5.2.5.11) can be directly applied to the bottom electrode, giving

$$\sigma_0^t = \sigma_0^{t-\Delta t} + \frac{Q_{\text{conv}}^t + Q^t - Q^{t-\Delta t}}{A_0} \tag{5.2.5.12}$$

The conservation charge law for the top electrode can be calculated knowing the charge deposited on the bottom electrode by using Eq. (5.2.5.12) along with the general relation shown in Eq. (5.2.5.1). Moreover, knowing the capacitance C, we are able to write the charge deposited on the capacitor at time t as follows

$$Q^t = C\left(V(t) + \Phi_N^t - \Phi_0^t\right). \tag{5.2.5.13}$$

It is possible to include both the conditions Eq. (5.2.5.13) and Eq. (5.2.5.12) within the system shown in Eq. (5.2.5.6), updating the definitions for b_0 and d_0 in Eq. (5.2.5.8) and Eq. (5.2.5.11) as follows

$$b_0 = -1 - \frac{C\Delta z}{\varepsilon_0 A_0} \tag{5.2.5.14}$$

$$d_0 = \frac{\rho_0^t}{2} + \frac{\sigma_0^{t-\Delta t}}{\Delta z} + \frac{1}{A_0 \Delta z}\left[Q_{\text{conv}}^t - Q^{t-\Delta t} + CV(t)\right]. \tag{5.2.5.15}$$

Such a system of non linear equations has non zero elements only on the diagonal plus and minus column.

5.2.6 Surface interactions for both oxygen and chlorine

For the wall recombination reaction (reaction (5.1.4.3)), it has been assumed that when an oxygen atom $O(^3P)$ or $O(^1D)$ hits the electrode, it returns as a thermal oxygen atom $O(^3P)$ with 50% probability or it recombines and forms a thermal O_2 molecule with 50% probability. The same applies for chlorine, where only the Cl atom is involved.

Regarding the wall quenching process (reaction (5.1.4.4)), Derzsi et al. (2016) demonstrated, using a PIC/MCC simulation, that the $O_2(a^1\Delta_g)$ density decreases exponentially with increasing quenching coefficient γ_{wqa} in the range $10^{-4} \leq \gamma_{\text{wqa}} \leq 5 \times 10^{-2}$. In these PIC/MCC simulation studies Derzsi et al. (2016, 2017) the $O_2(a^1\Delta_g)$ density is taken as a fraction of the ground state oxygen molecule $O_2(X^3)$. Similarly, using a 1D fluid model, Greb et al. (2015) demonstrated that the electronegativity depends strongly on the $O_2(a^1\Delta_g)$ surface quenching coefficient and argued that increased quenching coefficient leads to decreased $O_2(a^1\Delta_g)$ density, decreased detachment by the $O_2(a^1\Delta_g)$ state, and thus higher negative ion density. Less is known about the role of $O_2(b^1\Sigma_g)$ quenching at the electrodes. Conversely, for chlorine discharge, no wall quenching process has been implemented due to the lack of metastable species in the `oopd1` code (Huang and Gudmundsson, 2013).

In capacitively coupled oxygen discharge, ion-induced secondary electron emission and electron reflection play a very important role and have been implemented into the `oopd1` code by assuming it to be a constant (Gudmundsson et al., 2013; Gudmundsson and Lieberman, 2015; Gudmundsson and Ventéjou, 2015). More recently, Derzsi et al. (2015a) explored the effects of including an energy-dependent ion and neutral-secondary electron emission yield in an argon discharge, finding a significant change in the discharge characteristics. For the energy dependent secondary electron emission yield, they used fits developed by Phelps and Petrović (1999) and Phelps et al. (1999). For the capacitive oxygen discharge a similar approach was taken and a fit developed for the secondary electron emission yiled due to O^+ and O_2^+ ions bombarding metal electrodes as a function of energy (Hannesdottir and Gudmundsson, 2016).

In capacitively coupled chlorine discharge, both the electron reflection and the secondary electron emission yield at the electrodes are very rarely taken into account in the literature, although the former is know to be able to affect the discharge (Huang and Gudmundsson, 2013). Less is known about electron reflection.

5.3 Accounting for collisions using the MCC method

Charged-particle-neutral collisions were first implemented into the PIC scheme by Boswell and Morey (1988), using step probabilities, and later by Vahedi and Surendra (1995), using energy dependent cross sections.

5.3.1 The standard method

Collisions can be included by coupling the PIC method with a Monte Carlo (MC) method (Verboncoeur, 2005). When only few colliding particles per time-step are considered, the MC method is known in the literature as Monte Carlo collision (MCC) model. The MCC model (Birdsall, 1991; Vahedi and Surendra, 1995) calculates the time between collisions by a random number. Such a procedure is not compatible with the PIC method in itself. By defining the collision frequency ν_c

$$\nu_c = n_t(x_i)\sigma_{\mathrm{T}}(E_i)\Delta v_i, \qquad (5.3.1.1)$$

where $n_t(x_i)$ is the target particle local density at the position of the i-th bullet particle, σ_{T} is the total cross section summed over all the processes ($\sigma_{\mathrm{T}} = \sum_{\mathrm{p}}^{P} \sigma_p$), $E_i = \frac{mv_i^2}{2}$ is the incoming particle kinetic energy and $\Delta v_i = |v_i - v_t|$ is the difference in absolute value between the target particle velocity (v_t) and the bullet particle velocity (v_i). It is worth noting that for electron-neutral collisions, the neutrals can be considered as stationary so that $\Delta v_i \approx v_i$. For ion-neutral collisions this approximation is not valid any more, since ions and neutrals share almost the same velocity. In fact, in this case, after a collision, the ion velocity must be transformed from the ion frame back to the lab frame. Knowing that the collision probability P_i for the i-th particle can be calculated as

follows (Birdsall, 1991)

$$P_i = 1 - \exp\left(-\nu_c \Delta t\right), \tag{5.3.1.2}$$

a method to determine if a particle is subjected to a collision or not is needed. Such a method consists of taking a random real number R within the interval $[0, 1]$ and setting

$$P_i > R \implies \text{Collision} \tag{5.3.1.3}$$

$$P_i < R \implies \text{No Collision.} \tag{5.3.1.4}$$

Since the MCC scheme allows for only one collision for particle to occur at each time-step, it is possible to deduce that the error r, due to all the collisions neglected at the same time-step, is given by

$$r \approx \sum_{n=2}^{\infty} P_i^n = \frac{P_i^2}{1 - P_i}. \tag{5.3.1.5}$$

Since computing the collision probability for each time-step for each particle may be computationally very expensive, the MCC standard method shown above is not applied nowadays. Instead of it, the so called null-collision method is widely used.

5.3.2 The null collision method

Since calculating all the different P_i^n may have a high computational cost, it is useful to define the following quantity (Skullerud, 1968; Verboncoeur, 2005)

$$\nu_{\text{Tmax}} = \max\left(n_i(\vec{x})\right) \max\left(\sigma_{\text{T}}(E)\left(\frac{2E}{m_{\text{p}}}\right)^{\frac{1}{2}}\right), \tag{5.3.2.1}$$

where m_{p} is the charged particle mass. ν_{Tmax} returns a constant collision frequency in both $\vec{x}$ and E and it is calculated at the beginning of the simulation and used in the calculations in place of ν_c. That is like saying that another collision process, i.e. null-collision, is introduced in a manner that

$$\nu_c = \nu_{\text{Tmax}} + \nu_{\text{null}}. \tag{5.3.2.2}$$

Now, since

$$P_{\text{null}} \equiv P_{\text{Tmax}} = 1 - \exp\left(-\nu_{\text{Tmax}}\right), \tag{5.3.2.3}$$

the number of particles N_{coll} which experience a collision is

$$N_{\text{coll}} = N P_{\text{null}}, \tag{5.3.2.4}$$

where N is the number of particles, so that $N_{\text{coll}} \ll N$. Contrary to the standard method shown in Eq. (5.3.1.3), the particles are subject to a collision of the type k if

$$\frac{\sum_{k=0}^{l} \nu_{c,k}}{\nu_{\text{Tmax}}} \leq R \leq \frac{\sum_{k=1}^{l+1} \nu_{c,k}}{\nu_{\text{Tmax}}}, \tag{5.3.2.5}$$

while are subject to null collisions when

$$\frac{\sum_{k=1}^{N} \nu_{c,k}}{\nu_{\text{Tmax}}} \leq R. \tag{5.3.2.6}$$

5.4 The preliminary scaling

In order to make the calculations less computationally expensive, it is usually possible to rescale all the physical quantities involved before starting the PIC simulations in order to produce dimensionless quantities. Such a goal can be achieved by a normalization through the characteristic lengths of the system such as the cell size Δx, the time integration step Δt and the weighting function W_s. These quantities have to be balanced correctly in order to find an equilibrium between the accuracy and the computational time. The fundamental quantities can be rescaled as (Gozadinos, 2001)

$$\tilde{t} = \frac{t}{\Delta t} \ , \ \tilde{x} = \frac{x}{\Delta x} \ , \ \tilde{u} = \frac{u\Delta t}{\Delta x} \ , \ \tilde{n}_s = \frac{n_s \Delta x}{W} \ , \ \tilde{q} = \frac{q}{|q_e|} \ , \ \tilde{\rho}_s = \sum_s \frac{n_s \Delta x}{W_s} \ , \ \tilde{m} = \frac{m}{m_{ee}},$$

$$(5.4.0.1)$$

where s is the index referring to the sth type of species, while $\tilde{n}_s$ and $\tilde{\rho}$ are the rescaled particle density and the particle charge density respectively. In the following we will adopt the non-rescaled quantities for clearness.

5.5 Stability and accuracy of the PIC/MCC model

The PIC model simulates a finite number of particles. In order to minimize the discrete particle noise, the following condition has to be fulfilled

$$\frac{N_{SP}}{N_c} > 1, \tag{5.5.0.1}$$

where N_{SP} stands for the number of super-particles, while N_c stands for the number of grid cells. Moreover, the number of superparticles N_{SP} cannot be too large in order to minimize the computational time.

The easiest way to speed up simulations lies in increasing both the time-step Δt and the grid spacing Δx. However, in order to maintain stability and accuracy, both Δt and Δx must obey certain constraints. Of course, the closer are both the time-steps and the grid spacing to these limits, the higher is the performance. In order to explore the stability and accuracy of the leap-frog scheme (section 5.2.4), let us consider the simple harmonic oscillator (Birdsall and Langdon, 1991; Birdsall, 1991)

$$\frac{d^2 x}{dt^2} = -\omega_0^2 \tag{5.5.0.2}$$

with solution

$$x(t, t_0) = A(t_0) \cos \omega_0 t + B(t_0) \sin \omega_0 t. \tag{5.5.0.3}$$

By applying the leap-frog scheme, Eq. (5.5.0.2) becomes

$$\frac{x^{t+\Delta t} - 2x^t + x^{t-\Delta t}}{\Delta t^2} = -\omega_0^2 x^t. \tag{5.5.0.4}$$

Assuming a solution of the form

$$x^t = A \exp\left(-i\omega t\right), \tag{5.5.0.5}$$

it is not hard to find

$$\sin\left(\frac{\omega \Delta t}{2}\right) \approx \pm \frac{\omega_0 \Delta t}{2}. \tag{5.5.0.6}$$

For $\omega_0 \Delta t \ll 1$ we have

$$\frac{\omega}{\omega_0} = 1 + \mathscr{O}\left(\omega_0 \Delta t\right)^2, \tag{5.5.0.7}$$

showing a quadratic phase error. Tipically, the accuracy criterion is

$$\omega_0 \Delta t \leq 0.2 \tag{5.5.0.8}$$

or, for a plasma discharge with plasma frequency ω_{pe} (Birdsall and Langdon, 1991; Birdsall, 1991)

$$\omega_{\text{pe}} \Delta t \leq 0.2. \tag{5.5.0.9}$$

The condition above ensures that the time scale is properly resolved. In the same manner, in order to make the space scale properly resolved and to avoid numerical instabilities (Birdsall and Langdon, 1991; Birdsall, 1991) , the following condition needs to be fulfilled

$$\frac{\Delta x}{\lambda_{\text{De}}} < 0.5, \tag{5.5.0.10}$$

where λ_{De} is the electron Debye length shown in Eq. (2.1.0.4). The last condition which must always be satisfied is (Georgieva, 2006)

$$\frac{v_{\text{max,s}} \Delta t}{\Delta x} < 1, \tag{5.5.0.11}$$

where $v_{\text{max,s}}$ is the maximum particle velocity of a particle of species s and Δt_{s} is the corresponding time-step. Such a condition ensures that most particles will not travel more than one cell per time-step and will sample the electric fields properly. Such a criterion has been extended to different species involving different time steps (Courant et al., 1928; Kawamura et al., 2000). However, It is clear that if the accuracy conditions shown in Eqs. (5.5.0.9) and (5.5.0.10) are satisfied, also Eq. (5.5.0.11) is satisfied.

6 Plasma chemistry

The kinetics of capacitively coupled discharges has been studied using the PIC/MCC method for over three decades starting with studies of glow discharges in helium (Surendra and Graves, 1991b) followed by the study of the argon discharge (Vahedi et al., 1993a). Afterwards, Vahedi and Surendra (1995) used the 1D `xpdp1` code to explore argon and oxygen discharges. Since then, a few PIC/MCC studies have been reported on oxygen and Ar/O$_2$ discharges using the `xpdp1` series of codes, in both symmetrical and asymmetrical geometry, performed over a range of pressures and compared to experimental findings (Lee et al., 2006) and to analytical density profiles (Lichtenberg et al., 1994). These investigations showed good agreement when exploring the formation of the ion density distribution function in an Ar/O$_2$ mixture in an asymmetric capacitively coupled discharge, the influence of the secondary electron emission on the density profiles and the electron energy distribution function (EEDF) (Babaeva et al., 2005).

Capacitively coupled radio frequency discharges are of paramount importance for plasma processing applications ranging from microchip and solar cell manufacturing to the creation of biocompatible surfaces. Capacitive discharges of varying chemistries are used in a wide range of applications and they are indispensable for deposition, etching, and sputtering, which are all vital processes in microelectronics and solar cell fabrication. Oxygen discharges have been applied in material processing applications for over five decades. Among of the first applications of the capacitively coupled oxygen discharges was ashing of photoresist (Irving, 1968; Tolliver, 1984; Hartney et al., 1989), later came surface modification of polymer films (Chashmejahanbin et al., 2014; Vesel and Mozetic, 2017) and oxidation or anodization of silicon (Kawai et al., 1994; Hess, 1999). The chlorine discharge is widely used for etching, including both semiconductors and metals (Donnelly and Kornblit, 2013).

6.1 Collision theory

6.1.1 Classification of collisions

When a collision occurs both the momentum and the total energy of the system are fully conserved, namely

$$E_{\text{ToT before coll.}} = E'_{\text{ToT after coll.}}. \tag{6.1.1.1}$$

Now, let us consider a two particle system. Since the total energy before and after the collision of the system is the sum of the kinetic and the potential energy,

$$E_{\text{ToT before coll.}} = E_{1 \text{ before coll.}} + E_{2 \text{ before coll.}} \tag{6.1.1.2}$$

$$E'_{\text{ToT after coll.}} = E'_{1 \text{ after coll.}} + E'_{2 \text{ after coll.}}, \tag{6.1.1.3}$$

where

$$E_{1 \text{ before coll.}} \equiv E_{1 \text{ Kin before coll.}} + E_{1 \text{ Pot before coll.}} \tag{6.1.1.4}$$

$$E_{2 \text{ before coll.}} \equiv E_{2 \text{ Kin before coll.}} + E_{2 \text{ Pot before coll.}} \tag{6.1.1.5}$$

$$E'_{1 \text{ after coll.}} \equiv E'_{1 \text{ Kin after coll.}} + E'_{1 \text{ Pot after coll.}} \tag{6.1.1.6}$$

$$E'_{2 \text{ after coll.}} \equiv E'_{2 \text{ Kin after coll.}} + E'_{2 \text{ Pot after coll.}} \tag{6.1.1.7}$$

In this picture, we can distinguish three cases

$$E_{1 \text{ Kin before coll.}} + E_{2 \text{ Kin before coll.}} = E'_{1 \text{ Kin after coll.}} + E'_{2 \text{ Kin after coll.}} \tag{6.1.1.8}$$

$$\Longrightarrow \text{Elastic Collision} \tag{6.1.1.9}$$

$$E_{1 \text{ Kin before coll.}} + E_{2 \text{ Kin before coll.}} > E'_{1 \text{ Kin after coll.}} + E'_{2 \text{ Kin after coll.}} \tag{6.1.1.10}$$

$$\Longrightarrow \text{Inelastic Collision} \tag{6.1.1.11}$$

$$E_{1 \text{ Kin before coll.}} + E_{2 \text{ Kin before coll.}} < E'_{1 \text{ Kin after coll.}} + E'_{2 \text{ Kin after coll.}} \tag{6.1.1.12}$$

$$\Longrightarrow \text{Superelastic Collision.} \tag{6.1.1.13}$$

In an elastic collision kinetic and potential energy are conserved separately. In an inelastic collision usually an excitation or an ionization occurs. Finally, in a superelastic collision, an atom is usually de-excited, decreasing its internal energy. It is worth noting that, in this context, the potential energy includes the internal energy of the particle. Now, defining v_1 and v_2 ($\vec{v'_1}$ and $\vec{v'_2}$) as the velocities of the incoming and target particle respectively before (after) the collision and setting

$$v_2 = 0. \tag{6.1.1.14}$$

We can write the momentum and energy conservation equations for both elastic and inelastic collisions as follows (Meichsner et al., 2013)

$$\vec{p_1} = \vec{p'_1} + \vec{p'_2} \tag{6.1.1.15}$$

$$\frac{(\vec{p_1})^2}{2m_1} = K \frac{(\vec{p'_1})^2}{2m_1} + \frac{(\vec{p'_2})^2}{2m_2}, \tag{6.1.1.16}$$

where

$$K_{\min} < K < 1 \quad \text{inelastic collision} \tag{6.1.1.17}$$

$$K = 1 \quad \text{elastic collision} \tag{6.1.1.18}$$

$$K > 1 \quad \text{collision.} \tag{6.1.1.19}$$

Combining Eq. (6.1.1.15) with Eq. (6.1.1.16), one finds

$$E'_{2 \text{ Kin}} = E_{1 \text{ Kin}} \left(\frac{m_1 m_2}{(m_1 + m_2)^2} \right) \left[1 + \sqrt{1 + (k-1)\left(1 + \frac{m_1}{m_2}\right)} \right]^2, \tag{6.1.1.20}$$

where

$$E'_{2\,\text{Kin}} \equiv \frac{\vec{p'_2}}{2m_2} \qquad (6.1.1.21)$$

$$E_{1\,\text{Kin}} \equiv \frac{\vec{p'_1}}{2m_1} \qquad (6.1.1.22)$$

$$K_{\text{min}} = \frac{m_1}{m_1 + m_2}. \qquad (6.1.1.23)$$

Moreover, for specific values of K, we get

$$\text{for } K = K_{\text{min}} \Longrightarrow E'_{2\,\text{Kin}} = E_{1\,\text{Kin}} \left[\frac{m_1 m_2}{(m_1 + m_2)^2} \right] \qquad (6.1.1.24)$$

$$\text{for } K = 1 \Longrightarrow E'_{2\,\text{Kin}} = E_{1\,\text{Kin}} \left[\frac{4m_1 m_2}{(m_1 + m_2)^2} \right]. \qquad (6.1.1.25)$$

The results above hold for collinear momenta. If we consider non collinear momenta, the energy gain of the target particle after the collision can be calculated writing explicitly the angular dependency in the momentum conservation equation (Eq. (6.1.1.15))

$$m_1 v_1 = m_1 v'_1 \cos\theta_1 + m_2 v'_2 \cos\theta_2 \qquad (6.1.1.26)$$

$$0 = m_1 v'_1 \sin\theta_1 - m_2 v'_2 \sin\theta_2 \qquad (6.1.1.27)$$

$$\frac{m_1 v_1^2}{2} = \frac{m_1 v'^2_1}{2} + \frac{m_2 v'^2_2}{2}. \qquad (6.1.1.28)$$

Solving the equation system above it is not difficult to find

$$\frac{m_2 v'^2_2}{2} = \frac{m_1 v_1^2}{2} - \frac{m_1 v'^2_1}{2} = \frac{m_1 v_1^2}{2} \left[\frac{4m_1 m_2 \cos^2\theta_2}{(m_1 + m_2)^2} \right]. \qquad (6.1.1.29)$$

If $m_1 = m_2$ the previous expression becomes

$$\frac{m v'^2_2}{2} = \frac{m v_1^2 \cos^2\theta_2}{2}. \qquad (6.1.1.30)$$

6.1.2 Collision frequency

From the literature it is very well know that the number of incident particles per unit volume that undergo an interaction with target particles within a differential distance dx is

$$dn = -\sigma n n_g dx, \qquad (6.1.2.1)$$

where n_g and n are the target and the incident particle density, respectively, and σ is the cross section of the collision process. Moreover, setting the beam velocity as a time constant and defining the beam flux as $\Gamma = nv$, we can rewrite Eq. (6.1.2.1) as follows

$$d\Gamma = -\sigma \Gamma n_g dx \qquad (6.1.2.2)$$

so that the fraction of incident particles that collide within the distance dx is

$$\frac{d\Gamma}{\Gamma} = \frac{dn}{n} = -n_g \sigma dx. \tag{6.1.2.3}$$

Solving the equation above, one finds

$$\Gamma(x) = \Gamma_0 \left(1 - \exp\left(-\frac{x}{\lambda} \right) \right), \tag{6.1.2.4}$$

where λ is the mean free path defined in Eq. (2.5.0.1). From Eq. (2.5.0.2) we are able to define the mean free time between interactions as

$$\tau = \frac{\lambda}{v} \tag{6.1.2.5}$$

so that the collision frequency v_c reads

$$v_c = \tau^{-1} = n_g \sigma v \tag{6.1.2.6}$$

or, defining the rate coefficient as $k \equiv \langle \sigma v \rangle$

$$v_c = \tau^{-1} = n_g k. \tag{6.1.2.7}$$

6.1.3 Differential cross section

Let us consider a particle incident at a distance b off-center from the target particle that is scattered through an angle θ. The quantity b is the impact parameter and θ is the scattering angle. Due to flux conservation (Lieberman and Lichtenberg, 2005)

$$2\pi b db \Gamma = -2\pi \sin\theta d\theta \Gamma I(v, \theta). \tag{6.1.3.1}$$

Solving for $I(v, \theta)$, one finds

$$I(v, \theta) = \frac{b}{\sin\theta} \left| \frac{db}{d\theta} \right|, \tag{6.1.3.2}$$

where the quantity $\left| \frac{db}{d\theta} \right|$ can be calculated through the scattering force. By using Eq. (6.1.3.2), it is possible to define two fundamental quantities

$$\sigma_{\text{ToT}} = 2\pi \int_0^\pi I(v, \theta) \sin\theta d\theta \tag{6.1.3.3}$$

$$\sigma_m = 2\pi \int_0^\pi (1 - \cos\theta) I(v, \theta) \sin\theta d\theta, \tag{6.1.3.4}$$

where σ_{ToT} and σ_m are the total scattering cross section and the momentum transfer cross section, respectively.

Figure 6.1. The collision between two particles of mass m_1 and m_2 of initial and final velocity equal to v_1, $v_2 = 0$ and v'_1, v'_2, respectively, in the laboratory frame

Fixed Center

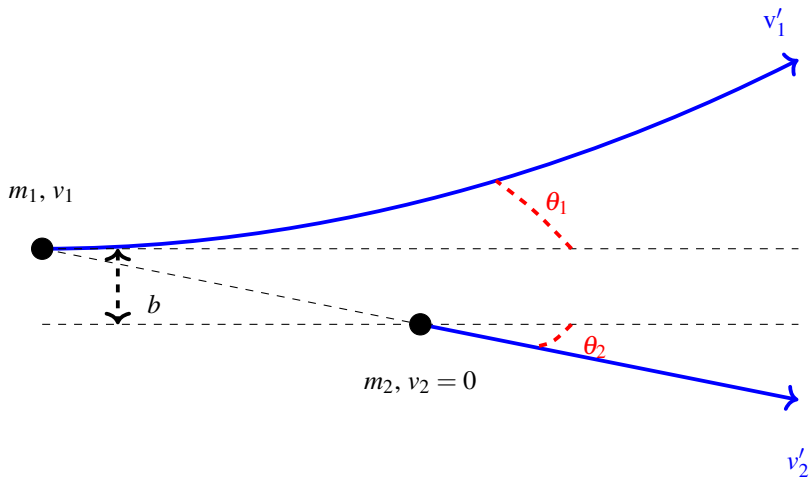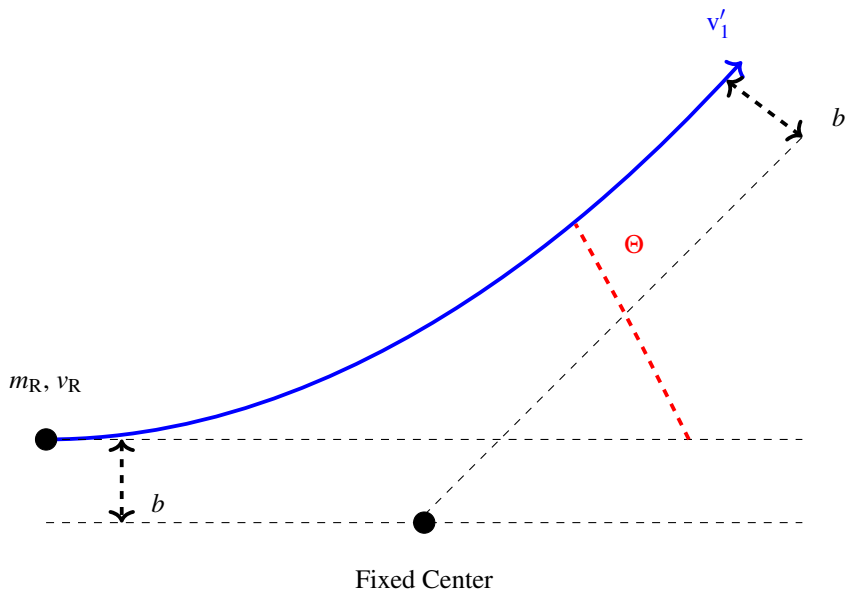*Figure 6.2. The collision between two particles of mass m_1 and m_2 of initial and final velocity equal to v_1, $v_2 = 0$ and v'_1, v'_2, respectively, in the center-of-mass frame*

6.1.4 Center of mass (CM) and laboratory frame

In the following, we will list some important relations involving the center-of-mass frame and the laboratory frame (Lieberman and Lichtenberg, 2005). First of all the

relations involving both the CM coordinates and the particle velocities are

$$\vec{R} = \frac{m_1 \vec{r}_1 + m_2 \vec{r}_2}{m_1 + m_2} \quad \text{where} \quad \vec{r} = \vec{r}_1 - \vec{r}_2 \tag{6.1.4.1}$$

$$\vec{V} = \frac{m_1 \vec{v}_1 + m_2 \vec{v}_2}{m_1 + m_2} \quad \text{where} \quad \vec{v}_R = \vec{v}_1 - \vec{v}_2. \tag{6.1.4.2}$$

Regarding the forces we have

$$m_1 \frac{d\vec{v}_1}{dt} = \vec{F}_{12}(r) \tag{6.1.4.3}$$

$$m_2 \frac{d\vec{v}_2}{dt} = \vec{F}_{21}(r) \tag{6.1.4.4}$$

$$m_R \frac{d\vec{v}_R}{dt} = \vec{F}_{12}(r). \tag{6.1.4.5}$$

For the angles, we have

$$\tan\theta_1 = \frac{\sin\Theta}{\left(\frac{m_1}{m_2}\right)\left(\frac{v_R}{v_R'}\right) + \cos\Theta} \tag{6.1.4.6}$$

$$\tan\theta_2 = \frac{\sin\Theta}{\left(\frac{v_R}{v_R'}\right) - \cos\Theta} \tag{6.1.4.7}$$

$$\theta_2 = \frac{(\pi - \Theta)}{2} \quad \text{for elastic collisions,} \tag{6.1.4.8}$$

where Θ is the scattering angle in the center-of-mass rest frame as shown in Figure 6.2. Moreover, for the differential cross section, the following relation holds

$$d\sigma = 2\pi I(v_R, \Theta) \sin\Theta d\Theta = 2\pi I(v_R, \theta_1) \sin\theta_1 d\theta_1. \tag{6.1.4.9}$$

Finally, the relation shown in Eq. (6.1.1.29), by using Eq. (6.1.4.8), can be rewritten in the following way

$$\frac{m_2 v_2'^2}{2} = \frac{m_1 v_1^2}{2} - \frac{m_1 v_1'^2}{2} = \frac{m_1 v_1^2}{2}\left[\frac{2m_1 m_2 (1 - \cos\Theta)}{(m_1 + m_2)^2}\right]. \tag{6.1.4.10}$$

For $m_1 = m_2$ the equation above reads

$$\frac{m v_2'^2}{2} = \frac{m v_1^2}{2}(1 - \cos\Theta). \tag{6.1.4.11}$$

6.1.5 Small angle scattering

Let us consider a small angle ($\Theta \ll 1$) scattering (Figure 6.3). In this case, it is possible to show that (Lieberman and Lichtenberg, 2005)

$$r^2 = b^2 + v_R^2 t^2 \tag{6.1.5.1}$$

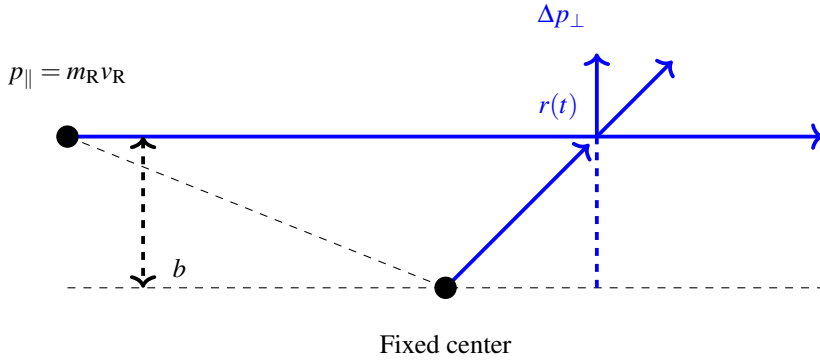$$\Delta p_\perp = \int_{-\infty}^{+\infty} \frac{b}{r}\left|\frac{dU}{dr}\right| dt, \tag{6.1.5.2}$$

Figure 6.3. The small angle differential cross section scattering in the center-of-mass frame.

where $p_\perp$ is the momentum impulse perpendicular to the trajectory (straight line). Assuming a central force

$$U(r) = \frac{C}{r^i}, \tag{6.1.5.3}$$

where C is an arbitrary constant, differentiating Eq. (6.1.5.1) and plugging the expression for dt into Eq. (6.1.5.2), one finds, after dividing the whole expression by the parallel momentum $p_\parallel = m_R v_R$

$$\Theta = \frac{\Delta p_\perp}{p_\parallel} = \frac{2b}{m_R v_R^2} \int_b^\infty \left| \frac{dU}{dr} \right| \frac{dr}{\sqrt{r^2 - b^2}}, \tag{6.1.5.4}$$

where v_R is given by Eq. (6.1.4.2), m_R is the reduced mass

$$m_R = \frac{m_1 m_2}{m_1 + m_2} \tag{6.1.5.5}$$

and b is the impact parameter shown in Figure 6.3. The calculation of the integral above returns

$$\Theta = \frac{A}{W_R b^i} \quad \text{where} \quad W_R = \frac{m_R v_R^2}{2} \quad \text{and} \quad A = \frac{C \sqrt{\pi} \Gamma \left[\frac{(i+1)}{2} \right]}{2 \Gamma \left[\frac{(i+2)}{2} \right]}. \tag{6.1.5.6}$$

Differentiating the expression above with respect to Θ and replacing the expressions for both b and db into Eq. (6.1.3.2), one finds for $\Theta \ll 1$

$$I(v_R, \Theta) = \frac{1}{i} \left(\frac{A}{2W_R} \right)^{\frac{2}{i}} \frac{1}{\Theta^{2 + \frac{2}{i}}}. \tag{6.1.5.7}$$

It can be shown that for

$$\text{Coulomb collision} \Longrightarrow U(r) \sim \frac{1}{r} \Longrightarrow \sigma \sim \frac{1}{v_R^4} \tag{6.1.5.8}$$

$$\text{Permanent dipole collision} \Longrightarrow U(r) \sim \frac{1}{r^2} \Longrightarrow \sigma \sim \frac{1}{v_R^2} \tag{6.1.5.9}$$

$$\text{Induced dipole} \Longrightarrow U(r) \sim \frac{1}{r^4} \Longrightarrow \sigma \sim \frac{1}{v_R}. \tag{6.1.5.10}$$

Therefore, for a Coulomb collision ($i = 1$), the differential cross section for small angles is given by

$$I(v_R, \Theta) = \left(\frac{b_0}{\Theta^2}\right)^2 \quad \text{where} \quad b_0 = \frac{q_1 q_2}{4\pi\varepsilon_0 W_R}. \tag{6.1.5.11}$$

Finally, for $\Theta \ll 1$ Eq. (6.1.4.11) becomes

$$\frac{m v_2'^2}{2} = \frac{m v_1^2}{2} \frac{\Theta^2}{4}. \tag{6.1.5.12}$$

6.1.6 Hard sphere collision

Let us consider the hard sphere collision case. Since $b = a_{12} \sin\chi$, we have

$$b\,db = \frac{a_{12}^2}{2} \sin 2\chi\, d\chi = -\frac{a_{12}^2}{4} \sin\theta\, d\theta, \tag{6.1.6.1}$$

where a_{12} is the segment joining the center of the hard sphere with the collision point, while χ is the angle given by the encounter between a_{12} and the horizontal axis passing through the hard sphere center. Moreover, θ and χ are related through the relation $\theta = \pi - 2\chi$ (Lieberman and Lichtenberg, 2005). By using Eq. (6.1.3.2), one finds

$$I(v, \theta) = \frac{a_{12}^2}{4} \tag{6.1.6.2}$$

so that, plugging Eq. (6.1.6.2) into Eq. (6.1.3.3) and Eq. (6.1.3.4), we get

$$\sigma_{\text{ToT}} = \sigma_m = \pi a_{12}^2 \tag{6.1.6.3}$$

6.2 Collision types

6.2.1 Coulomb collision

The interaction between two charged particles may be described by the classical Coulomb scattering. Starting from both the energy and angular momentum conservation equations (Meichsner et al., 2013)

$$\mathscr{E} = \frac{m v_0^2}{2} = \frac{m}{2}\left[\left(\frac{dr}{dt}\right)^2 + r^2\left(\frac{d\phi}{dt}\right)^2\right] + \mathscr{E}_{\text{Coul}}(r) \tag{6.2.1.1}$$

$$m v_0 b = m r^2 \frac{d\phi}{dt}, \tag{6.2.1.2}$$

where

$$\mathscr{E}_{\text{Coul}}(r) \equiv \frac{q_1 q_2}{4\pi\varepsilon_0 r}. \tag{6.2.1.3}$$

Plugging the expression for $\frac{d\phi}{dt}$ derived from Eq. (6.2.1.2) into Eq. (6.2.1.1), one finds the following relation

$$\frac{\frac{d\phi}{dt}}{\frac{dr}{dt}} = \frac{d\phi}{dr} = \frac{\frac{v_0 b}{r^2}}{\sqrt{v_0^2 - \frac{v_0^2 b^2}{r^2} - \frac{2\mathscr{E}_{\text{Coul}}(r)}{mv_0^2}}}. \tag{6.2.1.4}$$

Replacing the mass and the velocity in the laboratory system by the reduced mass and the relative velocity in the center of mass of the system and integrating, we get

$$\int_0^{\phi_0} d\phi = \int_{r_0}^{\infty} \frac{b\,dr}{r^2 \sqrt{\left(1 - \frac{b^2}{r^2} - 2\frac{\mathscr{E}_{\text{Coul}}}{m_R v_r^2}\right)}}. \tag{6.2.1.5}$$

By integrating Eq. (6.2.1.5) and since $\theta = \pi - 2\phi_0$ (Lieberman and Lichtenberg, 2005), it is possible to write

$$b_{\text{Coul}} = \frac{q_1 q_2}{4\pi\varepsilon_0 m_R v_r^2} \cot\frac{\theta}{2} \tag{6.2.1.6}$$

and, by using Eq. (6.1.3.2)

$$I(v,\theta) = \left(\frac{q_1 q_2}{8\pi\varepsilon_0 m_R v_r^2}\right)^2 \frac{1}{\sin^4\frac{\theta}{2}} \sim \frac{1}{v_r^4}. \tag{6.2.1.7}$$

Finally, by using Eq. (6.1.3.3), the total Coulomb cross section reads

$$\sigma_{\text{total}}^{\text{Coul}} = 2\pi \int_{\theta_{\min}}^{\theta_{\max}} I(v,\theta)\sin\theta\, d\theta = \frac{(q_1 q_2)^2}{4\pi\varepsilon_0^2} \frac{\log\left(\frac{\lambda_D}{l_L}\right)}{m_R^2 v_r^4}. \tag{6.2.1.8}$$

6.2.2 Polarization collision

At low relative translational energy the elementary collision process between a charged particle and a neutral particle is determined by short-range polarization scattering, while at higher energies for beams the collision time is shorter and no polarization occurs, giving a Coulomb-like scattering with maximum impact parameter in the order of the atomic radius (Lieberman and Lichtenberg, 2005; Meichsner et al., 2013). If a permanent dipole moment is neglected, an induced dipole moment $\vec{p}_{\text{ind}}$ of a neutral particle embedded in an electric field is defined as follows

$$\vec{p}_{\text{ind}} = \alpha_p \cdot \vec{E}, \tag{6.2.2.1}$$

where α_p is the atomic or molecular polarizability. Since the polarization force is

$$\vec{F}_{\text{pol}} = (\vec{p}_{\text{ind}} \cdot \vec{\nabla})\vec{E}, \tag{6.2.2.2}$$

one finds

$$\vec{F}_{\mathrm{pol}} = (\alpha_{\mathrm{p}} \cdot \vec{E} \vec{\nabla}) \vec{E}. \tag{6.2.2.3}$$

In this way, the polarization potential $U(\vec{r})$ reads (Meichsner et al., 2013)

$$U(\vec{r}) = -\int \vec{F}_{\mathrm{pol}}(\vec{r}) \cdot d\vec{r} = -\frac{\alpha_{\mathrm{p}} e^2}{2(4\pi\varepsilon_0)^2 r^4}, \tag{6.2.2.4}$$

where we have used the electric field for a point charge along with the definition for the polarization force.

The conservation of the mechanical energy and the angular momentum gives

$$\mathcal{E} = \frac{mv_0^2}{2} = \frac{m}{2}\left[\left(\frac{dr}{dt}\right)^2 + r^2\left(\frac{d\phi}{dt}\right)^2\right] - U(r) \tag{6.2.2.5}$$

$$mv_0 b = mr^2 \frac{d\phi}{dt}. \tag{6.2.2.6}$$

Solving (6.2.2.6) with respect to $\frac{d\phi}{dt}$ and plugging the result into (6.2.2.5), one finds, after having set $\left(\frac{dr}{dt}\right)\big|_{r=r_0} = 0$,

$$(r_0^2)^2 - b^2 r_0^2 + \frac{\alpha e^2}{mv_0^2(4\pi\varepsilon_0)^2} = 0 \tag{6.2.2.7}$$

and, consequently, the condition

$$\frac{b^4}{4} - \frac{\alpha e^2}{mv_0^2(4\pi\varepsilon_0)^2} = 0 \tag{6.2.2.8}$$

which, solved for $b_{\min} = b_1$, allows us to write the Langevin capture cross section σ_{L} as follows

$$\sigma_{\mathrm{L}} = \pi b_{\mathrm{L}}^2 = \left(\frac{\alpha e^2}{\varepsilon_0^2 m_R v_{\mathrm{r}}^2}\right)^{\frac{1}{2}} \sim \frac{1}{v_{\mathrm{r}}}, \tag{6.2.2.9}$$

where $v_{\mathrm{r}} = |\vec{v}_1 - \vec{v}_2|$ and $m_{\mathrm{R}} = \frac{m_1 m_2}{(m_1 + m_2)}$.

6.2.3 Neutral-neutral collision

When a collision between two neutral particles occurs, there is not any potential that has to be taken into account. This means that the target angular momentum equation can be written as follows (Lieberman and Lichtenberg, 2005; Meichsner et al., 2013)

$$v_{\mathrm{th}} b = v_\phi b_{\mathrm{eff}}. \tag{6.2.3.1}$$

If a threshold energy is required to make the reaction occur, the conservation energy equation reads

$$\mathcal{E} = \frac{mv_{\mathrm{th}}^2}{2} = \frac{mv_\phi^2}{2} + \mathcal{E}_{\mathrm{threshold}}. \tag{6.2.3.2}$$

Plugging Eq. (6.2.3.1) into (6.2.3.2), we find

$$\mathscr{E} = \mathscr{E}\left(\frac{\sigma}{\sigma_{\text{eff}}}\right) + \mathscr{E}_{\text{threshold}}, \tag{6.2.3.3}$$

where $\sigma = \pi b^2$ and $\sigma_{\text{eff}} = \pi b_{\text{eff}}^2$. For $\mathscr{E} > \mathscr{E}_{\text{threshold}}$ we get

$$\sigma = \sigma_{\text{eff}}\left(1 - \frac{\mathscr{E}_{\text{threshold}}}{\mathscr{E}}\right) \tag{6.2.3.4}$$

6.2.4 Excitation and de-excitation

In the classical framework, the electron describes a circular orbit around the nucleus. The orbit radius a is usually given by the balance between the inward electrostatic force and the outward centrifugal force, so that (Lieberman and Lichtenberg, 2005)

$$\frac{e^2}{4\pi\varepsilon_0 a^2} = \frac{mv^2}{a}. \tag{6.2.4.1}$$

Taking into account the quantum mechanical description which dictates the angular momentum to be an integral multiple of $\hbar$

$$mva = n\hbar, \tag{6.2.4.2}$$

one finds the quantized radii formula and the analogous expression for the velocity

$$a_n = n^2 a_0 \ \text{ with } \ a_0 = \frac{4\pi\varepsilon_0\hbar^2}{me^2} \tag{6.2.4.3}$$

$$v_n = \frac{v_{\text{at}}}{n} \ \text{ with } \ v_{\text{at}} = \frac{e^2}{4\pi\varepsilon_0\hbar}, \tag{6.2.4.4}$$

where a_0 is the Bohr radius and v_{at} is the electron velocity in the first Bohr orbit. Eqs. (6.2.4.3) and (6.2.4.4) allow us to define the characteristic atomic time-scale as follows

$$t_{\text{at}} = \frac{a_0}{v_{\text{at}}} \approx 2.42 \times 10^{-17}\text{s}. \tag{6.2.4.5}$$

Moreover, defining $W_n \equiv e\mathscr{E}_n$, where W_n is given by

$$W_n = \frac{mv_n^2}{2} - \frac{e^2}{4\pi\varepsilon_0 a_n}, \tag{6.2.4.6}$$

we obtain

$$\mathscr{E}_n = -\frac{\mathscr{E}_{\text{at}}}{n^2} \ \text{ with } \ \mathscr{E}_{\text{at}} = \frac{m}{2e}\left(\frac{e^2}{4\pi\varepsilon_0\hbar}\right)^2 = 13.61 \text{ V}, \tag{6.2.4.7}$$

where $\mathscr{E}_{\text{at}}$ is the ionization potential of the hydrogen atom in its lower energy state. Generally speaking, an atom in the ground state can be excited by collisions or radiation

to higher energy levels. Such an excitation, as well as the successive de-excitation, mainly involves the valence electrons

$$e + A \rightarrow e + A^* \rightarrow e + A + \gamma. \tag{6.2.4.8}$$
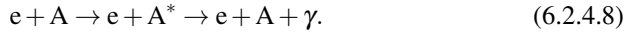
It can be useful to estimate the time-scale for electron-dipole radiation. Since

$$P_{\text{rad}} = \frac{\omega^4 p_{d0}^2}{12\pi\varepsilon_0 c^3} \quad \text{with} \quad p_d(t) = p_{d0}\cos\omega t, \tag{6.2.4.9}$$

we find

$$t_{\text{rad}} = \frac{12\pi\varepsilon_0\hbar^3}{\omega^3 p_{d0}^2} \tag{6.2.4.10}$$

so that $t_{\text{rad}} \approx 1.5 \times 10^{-9}$s for $p_{d0} = ea_0$ and $\omega = \frac{e\mathscr{E}_{\text{at}}}{\hbar}$. However, these is not the only characteristic time that can be built. In fact, the characteristic time between collisions is

$$\tau_{cc,e} \sim \left(n_{\text{g}}\pi a_0^2 \bar{v}\right)^{-1} \tag{6.2.4.11}$$

so that $\tau_{\text{cc,e}} \sim 10^{-7}$s for $T_{\text{e}} \sim 3$ V and $n_{\text{g}} \sim 10^{14}$ cm^{-3}. So, we can state that

$$t_{\text{at}} \ll t_{\text{rad}} \ll t_{\text{cc,e}}. \tag{6.2.4.12}$$

6.2.5 Heavy particle collisions

Usually, the heavy particle velocities are much smaller than the orbital electron velocity in an atom/molecule. The collision time t_{c} between two heavy particles can be approximated as

$$t_{\text{c}} \approx \frac{2a_0}{v_i} \sim \begin{cases} \text{for slow moving particles} \Longrightarrow 10^{-13} \text{ s} \\ \text{for fast moving particles} \Longrightarrow 10^{-14} \text{ s} \end{cases}. \tag{6.2.5.1}$$

From Eq. (6.2.4.5), Eq. (6.2.4.10) and Eq. (6.2.5.1) we can state

$$t_{\text{at}} \ll t_{\text{c}} \sim \tau_{\text{vib}} \ll \tau_{\text{rad}} \ll \tau_{\text{c}}. \tag{6.2.5.2}$$

6.2.6 Electron ionzation cross section

In the following we will determine the condition for an incident electron to ionize a valence electron. From Eq. (6.1.5.11), setting $q_1 = q_2 = -e$ and $m_1 = m_2 = m$, one finds

$$I(v,\Theta) = \left(\frac{e^2}{4\pi\varepsilon_0}\right)^2 \frac{1}{W_R^2} \frac{1}{\Theta^4} \quad \text{where} \quad W_R = \frac{m_R v^2}{2} \quad \text{and} \quad m_R = \frac{m}{2} \tag{6.2.6.1}$$

in the CM frame. Moving to the Laboratory frame by using Eq. (6.1.4.9), after setting

$$m_R = \frac{m}{2} \quad , \quad \theta = \frac{\Theta}{2} \quad , \quad W = \frac{mv^2}{2}, \tag{6.2.6.2}$$

one finds the following relation

$$I(v, \theta) = \left[\frac{e^2}{4\pi\varepsilon_0} \right]^2 \frac{1}{\Theta^4 W^2}. \tag{6.2.6.3}$$

Labelling $W_{\text{L}} \equiv \frac{mv_2'^2}{2}$ and $W \equiv \frac{mv_1'^2}{2}$, Eq. (6.1.5.12) reads as follows

$$W_{\text{L}} = \frac{\Theta^2}{4} W = \theta^2 W. \tag{6.2.6.4}$$

It is possible to remove the θ dependency in Eq. (6.2.6.3) replacing W by W_{L} by using Eq. (6.2.6.4), getting

$$I(v, \theta) = \left[\frac{e^2}{4\pi\varepsilon_0} \right]^2 \frac{1}{W_{\text{L}}^2}. \tag{6.2.6.5}$$

So, the total differential cross section is

$$d\sigma = \pi \left(\frac{e^2}{4\pi\varepsilon_0} \right)^2 \frac{1}{W} \frac{dW_{\text{L}}}{W_{\text{L}}^2}. \tag{6.2.6.6}$$

Integrating the previous expression between U_{iz} and W and employing the voltage units $W = e\mathscr{E}$ and $U_{\text{iz}} = e\mathscr{E}_{\text{iz}}$ we finally get

$$\sigma_{\text{iz}} = \pi \left(\frac{e^2}{4\pi\varepsilon_0} \right)^2 \frac{1}{\mathscr{E}} \left(\frac{1}{\mathscr{E}_{\text{iz}}} - \frac{1}{\mathscr{E}} \right) \quad \text{for} \quad \mathscr{E} > \mathscr{E}_{\text{iz}} \tag{6.2.6.7}$$

$$\sigma_{\text{iz}} = 0 \quad \text{for} \quad \mathscr{E} < \mathscr{E}_{\text{iz}}, \tag{6.2.6.8}$$
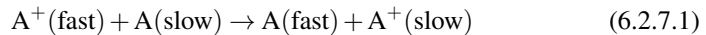
where σ_{iz} is the Thomson cross section (Thomson, 1912). Moreover,

$$\sigma_{\text{iz,max}} = \sigma_{iz}|_{\mathscr{E}=\mathscr{E}_{\text{iz}}} = \frac{\pi}{4} \left(\frac{e}{4\pi\varepsilon_0} \right)^2 \frac{1}{\mathscr{E}_{\text{iz}}^2} \tag{6.2.6.9}$$

$$\sigma_{\text{iz}} \sim \frac{1}{\mathscr{E}} \quad \text{for} \quad \mathscr{E} \gg \mathscr{E}_{\text{iz}}. \tag{6.2.6.10}$$

6.2.7 Ion-Atom Charge Transfer

The ion-atom charge transfer reaction (Lieberman and Lichtenberg, 2005)

$$\text{A}^+(\text{fast}) + \text{A}(\text{slow}) \rightarrow \text{A}(\text{fast}) + \text{A}^+(\text{slow}) \tag{6.2.7.1}$$

may happen in two different ways. Labelling as W_{rel} the energy of the level from which the electron is released and W_{capt} the energy of the level into which the electron is captured and defining the quantity $\Delta W \equiv W_{\text{rel}} - W_{\text{capt}}$, which is commonly known in the literature as energy defect, the process shown in Eq. (6.2.7.1) is said to be resonant when $\Delta W = 0$. Usually, the resonant ion-atom charge transfer is important in weakly

ionized plasmas, since the cross section for such a process is large at low collision energies. Now, let us consider the following reaction

$$A^+ + B \text{ (at rest)} \rightarrow A + B^+ \text{ (at rest)}, \tag{6.2.7.2}$$
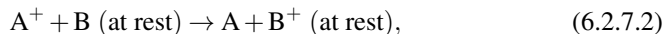
where an electron in the level n of B is captured from A. Now, since the potential energy of the electron in the n-th level of B is

$$W = -\frac{U_{izB}}{n^2} - \frac{e^2}{4\pi\varepsilon_0 a_{12}}, \tag{6.2.7.3}$$

where a_{12} is the center-to-center separation of A^+ and B and since the potential energy of an electron in the Coulomb fields of A^+ and B^+ ions is

$$U(z) = -\frac{e^2}{4\pi\varepsilon_0 z} - \frac{e^2}{4\pi\varepsilon_0 |a_{12} - z|}. \tag{6.2.7.4}$$

The condition for release from B can be found from the following equality

$$W = U_{max} = U\big|_{z=\frac{a_{12}}{2}} = -\frac{e^2}{\pi\varepsilon_0 a_{12}} \tag{6.2.7.5}$$

which returns

$$a_{12} = \frac{3e^2 n^2}{4\pi\varepsilon_0 U_{izB}}. \tag{6.2.7.6}$$

Finally, the process is possible if the following condition is fulfilled

$$\frac{m_{A+} v_{A+}^2}{2} \geq \Delta W_{AB} \approx \frac{U_{izB}}{n^2} - \frac{U_{izA}}{n^2} \tag{6.2.7.7}$$

so that, the cross section can be estimated as follows

$$\text{for} \quad \frac{m_{A+} v_{A+}^2}{2} < \Delta W_{AB} \Longrightarrow \sigma_{cx} = 0 \tag{6.2.7.8}$$

$$\text{for} \quad \frac{m_{A+} v_{A+}^2}{2} \geq \Delta W_{AB} \Longrightarrow \sigma_{cx} = \pi a_{12}^2 \tag{6.2.7.9}$$

$$\text{for} \quad \frac{m_{A+} v_{A+}^2}{2} \geq \Delta W_{AB} \quad \text{and} \quad A = B \Longrightarrow \sigma_{cx} = \frac{9\pi}{16} \left(\frac{e^2}{\pi\varepsilon_0 U_{iz}} \right)^2. \tag{6.2.7.10}$$

Since $v_{A+} \ll v_{at}$ and, consequently

$$t_{cx} \sim \frac{a_{12}}{v_{A+}} \gg t_{at}, \tag{6.2.7.11}$$

the ion-atom charge transfer reaction has a high probability to occur in a weakly ionized discharge. However, this is not the full story. Due to the tunnel effect, the ion-atom charge transfer reaction may occur for lower energy values. By solving the Schrödinger equation

$$-\frac{\hbar^2}{2m} \frac{\partial^2 \psi}{\partial x^2} = i\hbar \frac{\partial \psi}{\partial t} \quad \text{with} \quad \psi(t,x) = \psi(x) \exp(i\omega t), \tag{6.2.7.12}$$

where $\omega = \frac{2\pi}{\tau}$ and $\tau = \frac{h}{e\mathscr{E}_{iz}}$ (τ is the valence electron oscillation period in the B Coulomb field), one finds

$$P = \left| \frac{\psi(b_0)}{\psi(0)} \right|^2 = \exp(-2\alpha b_0) \quad \text{with} \quad \alpha = \left(\frac{2em\mathscr{E}_{iz}}{\hbar^2} \right)^{\frac{1}{2}}. \qquad (6.2.7.13)$$

Equating the tunnelling time to the collision time as follows

$$t_{tun} \equiv \tau P = \frac{b_0}{v_{A+}} \equiv t_{coll}, \qquad (6.2.7.14)$$

where t_{tun} and t_{coll} are the tunnelling and the collision time, respectively, we obtain

$$\sigma_{cx} \approx \pi b_0^2 \quad \text{with} \quad b_0 = \frac{1}{2\alpha} \log \left(\frac{\tau}{t_{coll}} \right). \qquad (6.2.7.15)$$

More detailed calculations and experiments show that σ_{cx} reads (Rapp and Francis, 1962; Lieberman and Lichtenberg, 2005)

$$\sigma_{cx} \approx \frac{1}{\mathscr{E}_{iz}} \left(C_1 - C_2 \log v_{A+} \right), \qquad (6.2.7.16)$$

where v_{A+} is in the range from 10^5 to 10^8 cm/s, $C_1 \approx 1.58 \times 10^{-7}$ and $C_2 \approx 7.24 \times 10^{-8}$. A further estimate returns (Lieberman and Lichtenberg, 2005)

$$\sigma_{cx} \approx \frac{\sigma_L}{2} \qquad (6.2.7.17)$$

for low collision energies.

6.3 PIC/MCC model for oxygen discharges

Several 1D PIC/MCC codes have been developed to explore the oxygen discharge in the course of time. The Monte Carlo collision (MCC) model for the oxygen discharge was described Vahedi and Surendra (1995) and applied to explore the density profiles of charged particles in an oxygen discharge and to compare the simulation outcomes to theoretical predictions (Lichtenberg et al., 1994). Afterwards, 1D PIC/MCC simulations have been applied to both symmetrical/asymmetrical Ar/O$_2$ discharges over a range of pressure by using the `xpdx1` series (Lee et al., 2006), showing a good agreement with the experiments. On the same route, Babaeva et al. (2005) explored the formation of the IEDF in an Ar/O$_2$ mixture in an asymmetric capacitively coupled discharge by using a 1D cylindrical model (`xpdc1`). Roberto et al. (2006) used the `xpdp1` code to investigate the influence of the secondary electron emission on the density profiles and the EEDF. Afterwards, other 1D PIC/MCC codes have been developed to study the oxygen discharge properties. A 1D PIC/MCC code developed in Greifswald that includes the metastable oxygen molecule O$_2(a^1\Delta_g)$ as a fraction of the ground state molecule, was applied to determine the ion energy distribution function (IEDF) in capacitive oxygen discharges (Bronold et al., 2007; Matyash et al., 2007). Furthermore,

by comparison with experiments, they determined that one sixth of the oxygen molecules are in the metastable singlet delta state. An hybrid PIC/MCC model has been applied to explore the electron power absorption and the influence of pressure on the particle densities in a low pressure capacitively coupled oxygen discharge (Bera et al., 2011a,b). Afterwards, a 1D PIC/MCC code developed in Dalian (Schüngel et al., 2011; Zhang et al., 2011b) was applied to explore the electrical asymmetry effect in a capacitively coupled oxygen discharge. Similar to Bronold et al. (2007) they assume the density for the singlet metastable molecule $O_2(a^1\Delta_g)$ to be constant. More recently, a 1D PIC/MCC code that was developed in Budapest has been used to explore the power absorption mechanism in a capacitively coupled oxygen discharge driven by tailored waveforms (composed of N harmonics in addition to a fundamental frequency f_1) (Derzsi et al., 2016, 2017). In all of these works none of the metastable molecules nor atoms were treated kinetically as opposed to the positive ion O_2^+ and the negative ion O^-, while the positive ion O^+ is neglected.

The one-dimensional-object-oriented plasma device one (oopd1) code allows us to simulate particles of different weights so that both charged and neutral particles can be tracked in the simulation. The basic reaction set for the oxygen discharge in oopd1 was benchmarked to the xpdp1 code (Gudmundsson et al., 2013). There are several important differences between the oopd1 and the xpdp1 code. Firstly, in the oopd1 code a relativistic treatment of electrons is implemented, while in the xpdp1 code the treatment of electrons is non-relativistic. Secondly, in the oopd1 code the particles can have different weights, where the particle weight is the number of real particles each superparticle represents, i.e. the ratio of the number of physical particles to computational particles, while in the xpdp1 code all the particles share the same particle weight. Since it is not possible to track all the neutrals due to the computational cost, only neutral species above a certain threshold are tracked kinetically, while neutral species below the threshold are assumed to be uniformly distributed in space as well as to have a Maxwellian velocity distribution at the gas temperature ($T_n = 26$ mV. Moreover, a sub-cycling of factor 16 for heavy particle has been chosen, as well as a parabolic initial density profile (Kawamura et al., 2000). The collisions of particles having different weights were implemented in oopd1 by Nguyen (2006) following the method suggested by Miller and Combi (1994). Another difference is that oopd1 and xpdp1 use different algorithms for the scattering of the incident and ejected electrons. In particular xpdp1 (oopd1) uses a non-relativistic (Vahedi and Surendra, 1995) (relativistic (Lim, 2007)) algorithm for electron scattering and electron-impact excitation and ionization. Additionally, oopd1 (xpdp1) does (does not) transform electron collisions into the rest frame of the neutral.

In recent years the oxygen reaction set in the one-dimensional object-oriented plasma device one (oopd1) code has been improved significantly (Gudmundsson et al., 2013; Gudmundsson and Lieberman, 2015; Hannesdottir and Gudmundsson, 2016). Recently, the oopd1 code has been applied to explore the electron power absorption in the capacitively coupled oxygen discharge while varying the various external parameters and operating conditions such as discharge pressure (Gudmundsson and Ventéjou, 2015; Hannesdottir and Gudmundsson, 2016; Gudmundsson and Hannesdottir, 2017), driving voltage amplitude (Gudmundsson and Snorrason, 2017), driving frequency (Gudmundsson et al., 2018), the secondary electron emission (Hannesdottir and Gudmundsson,

2016; Proto and Gudmundsson, 2018a), the surface quenching of the metastable states (Proto and Gudmundsson, 2018b) and the electrode gap distance (Gudmundsson and Proto, 2019).

The oxygen reaction set currently included in the `oopd1` code is rather extensive and nine different species are considered: electrons, the ground state neutrals $O(^3P)$ and $O_2(X^3\Sigma_g^-)$, the negative ions O^-, the positive ions O^+ and O_2^+, and the metastables $O(^1D)$, $O_2(a^1\Delta_g)$ and $O_2(b^1\Sigma_g^+)$. The standard reaction set included $O_2(X^3\Sigma_g^-)$, O_2^+ and O^- and it has been discussed in Gudmundsson et al. (2013), along with the adjoint of oxygen atoms in the ground state $O(^3P)$ and ions of the oxygen atom O^+ to the `oopd1` code. Finally, the singlet metastable molecule $O_2(a^1\Delta_g)$ and the metastable oxygen atom $O(^1D)$ were added (Gudmundsson and Lieberman, 2015), as well as the singlet metastable molecule $O_2(b^1\Sigma_g^+)$ (Hannesdottir and Gudmundsson, 2016).

6.4 The standard oxygen reaction set

The standard oxygen reaction set used in the `oopd1` code has been discussed by Gudmundsson et al. (2013). In the following we will briefly review the standard oxygen reaction set, reaction by reaction, which is shown in Table 6.1.

6.4.1 Electron impact O_2 elastic scattering

The cross section for the electron scattering reaction

$$e + O_2 \rightarrow e + O_2 \tag{6.4.1.1}$$

was taken from Itikawa (2009).

6.4.2 Electron impact O_2 rotational and vibrational excitation

The rotational and vibrational excitations are included to serve as an additional energy loss mechanism for electrons. Rotational excitation has been found to be relatively unimportant while vibrational excitations are found to considerably influence the shape of the EEDF (Vahedi and Surendra, 1995). These reactions have been included into the reaction set

$$e + O_2(r = 0) \rightarrow e + O_2(r > 0) \tag{6.4.2.1}$$
$$e + O_2(v = 0) \rightarrow e + O_2(v > 0) \tag{6.4.2.2}$$
$$\tag{6.4.2.3}$$
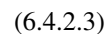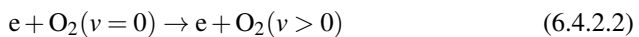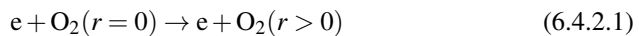
and their cross sections were taken from the Phelps (1985) collection.

111

Table 6.1. The chemical reaction, the process label and the related references for the standard oxygen reaction set as discussed in Gudmundsson et al. (2013).

Nr	Reaction	Process	Ref.
	Electron impact $O_2(X^3\Sigma_g^-)$		(Gudmundsson et al., 2013)
1	e+ $O_2 \rightarrow$ e+ O_2	Elastic scattering	Itikawa (2009)
2	e+ O_2 ($r=0$) $\rightarrow$ e+ O_2 ($r>0$)	Rotational excitation	Phelps (1985)
3	e+ O_2 ($v=0$) $\rightarrow$ e+ O_2 ($v>0$)	Vibrational Excitation	Phelps (1985)
4	e+ $O_2 \rightarrow$ e+ $O_2(a^1\Delta_g)$	Metastable excitation (0.98 eV)	Phelps (1985)
5	e+ $O_2 \rightarrow$ e+ $O_2(b^1\Sigma_g^+)$	Metastable excitation (1.63 eV)	Phelps (1985)
6	e+ $O_2 \rightarrow$ e+ $O_2(A^3\Sigma_u^+, A'^3\Delta_u, c^1\Sigma_u^-)$	Metastable excitation (4.05 eV)	Itikawa (2009); Shyn and Sweeney (2000); Green et al. (2001)
7	e+ $O_2 \rightarrow O(^3P) + O(^3P) + e$	Dissociation (6.12V eV)	Phelps (1985)
8	e+ $O_2 \rightarrow O(^3P) + O(^1D) + e$	Dissociation (8.4 eV)	Phelps (1985)
9	e+ $O_2 \rightarrow O(^1D) + O(^1D) + e$	Dissociation (9.97 eV)	Phelps (1985)
10	e+ $O_2 \rightarrow O_2^+ + 2e$	Electron-impact ionization (12.06 eV)	Krishnakumar and Srivastava (1992)
11	e+ $O_2 \rightarrow e + O + O(3p^3 P)$	Dissociative excitation (14.7 eV)	Phelps (1985)
12	e+ $O_2 \rightarrow O + O^-$	Dissociative attachment	Rapp and Briglia (1965)
13	e+ $O_2 \rightarrow O^+ + O^- + e$	Polar dissociation	Rapp and Briglia (1965)
14	e+ $O_2 \rightarrow O^+ + O + 2e$	Dissociative ionization	Krishnakumar and Srivastava (1992)
	Electron impact O		Gudmundsson et al. (2013)
15	e+ $O \rightarrow e + O$	Elastic scattering	Thomas and Nesbet (1975); Itikawa and Ichimura (1990)
16	e+ $O(^3P) \rightarrow e + O(^1D)$	Excitation to ^{1}D (1.96 eV)	Laher and Gilmore (1990)
17	e+ $O(^3P) \rightarrow e + O(^1S)$	Excitation to ^{1}S (4.18 eV)	Laher and Gilmore (1990)
18	e+ $O(^3P) \rightarrow e + O(^3P^0)$	Excitation to $^3P^0$ (15.65 eV)	Laher and Gilmore (1990)
19	e+ $O(^3P) \rightarrow e + O(^5S^0)$	Excitation to $^5S^0$ (9.14 eV)	Laher and Gilmore (1990)
20	e+ $O(^3P) \rightarrow e + O(^3S^0)$	Excitation to $^3S^0$ (9.51 eV)	Laher and Gilmore (1990)
21	e+ $O \rightarrow O^+ + 2e$	Ionization (13.62 eV)	Kim and Desclaux (2002)
	Detachment		Gudmundsson et al. (2013)
22	e + $O^- \rightarrow O + 2e$	Electron-impact detachment	Vejby-Christensen et al. (1996)
23	$O^- + O_2 \rightarrow O + O_2 + e$	Detachment by oxygen molecule	Comer and Schulz (1974)
24	$O^- + O \rightarrow O_2 + e$	Detachment by oxygen atom	Belostotsky et al. (2005)
	Recombination		(Gudmundsson et al., 2013)
25	$O^- + O \rightarrow O(^3P) + O(^1D)$	Dissociative recombination	Mul and McGowan (1979); Peverall et al. (2001)
26	$O^- + O_2^+ \rightarrow O + O_2$	Mutual neutralization	Padgett and Peart (1998); Olson (1972)
27	$O^-(^3P) \rightarrow O + O$	Mutual neutralization	Hayton and Peart (1993); Olson (1972)
	Charge exchange		Gudmundsson et al. (2013)
28	$O_2^+ + O_2 \rightarrow O_2 + O_2^+$	Charge exchange	Ellis et al. (1976); Baer et al. (1978); Wilcox and Moran (1981)
29	$O^+ + O_2 \rightarrow O + O_2^+$	Charge exchange	Lindsay and Stebbings (2005)
30	$O^+ + O \rightarrow O + O^+$	Charge exchange	Stebbings et al. (1964)
31	$O_2^+ + O \rightarrow O_2 + O^+$	Charge exchange (1.56 eV)	Stebbings et al. (1963); Stebbings (1966)
32	$O_2^+ + O_2 \rightarrow O + O_2 + O^+$	Fragmentation by energetic O_2^+	Gudmundsson et al. (2013)

6.4.3 Electron impact O_2 metastable excitation

The cross section for the reactions

$$e + O_2 \rightarrow e + O_2(a^1\Delta_g) \tag{6.4.3.1}$$

$$e + O_2 \rightarrow e + O_2(b^1\Sigma_g^+) \tag{6.4.3.2}$$
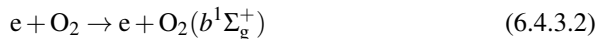
have been taken from the Phelps collection (Lawton and Phelps, 1978; Phelps, 1985). The cross section for the reaction

$$e + O_2 \rightarrow e + O_2(A^3\Sigma_u^+, A'^3\Delta_u, c^1\Sigma_u^-) \tag{6.4.3.3}$$
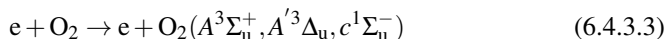
is taken from Shyn and Sweeney (2000).

6.4.4 Electron impact O_2 dissociation

The dissociation of the oxygen molecule is treated as an excitation of the oxygen molecule, which subsequently breaks into fragments. The dissociation products share an amount of energy equal to $\mathcal{E}_{\text{thres}} - \mathcal{E}_{\text{diss}}$, where $\mathcal{E}_{\text{thres}}$ is the threshold energy and $\mathcal{E}_{\text{diss}}$ is the binding energy of the original composite molecule (Lieberman and Lichtenberg, 2005). The process of electron impact excitation of a molecule is similar to the dissociation of the oxygen atom, the differential cross section shown in Eq. (6.2.6.6) can be employed, imposing that an electron with energy W transfers an energy W_L which obeys the following condition

$$U_1 < W < U_2, \tag{6.4.4.1}$$

where U_1 is the energy of the starting level and U_2 is the energy of the next higher final level. In this way, using the voltage units, one finds

$$\text{for} \quad \mathcal{E} < \mathcal{E}_1 \Longrightarrow \sigma_{\text{diss}} = \sigma_0 \frac{\mathcal{E} - \mathcal{E}_1}{\mathcal{E}_1} \tag{6.4.4.2}$$

$$\text{for} \quad \mathcal{E}_1 < \mathcal{E} < \mathcal{E}_2 \Longrightarrow \sigma_{\text{diss}} = \sigma_0 \frac{\mathcal{E}_2 - \mathcal{E}_1}{\mathcal{E}}, \tag{6.4.4.3}$$

where

$$\sigma_0 = \pi \left(\frac{e}{4\pi\varepsilon_0\mathcal{E}_1} \right)^2. \tag{6.4.4.4}$$

The electron transition is assumed to be rapid on a nuclear time-scale. The excitation to the 6.12 eV level leads to dissociation into $O(^3P) + O(^3P)$,

$$e + O_2 \rightarrow O(^3P) + O(^3P) + e \tag{6.4.4.5}$$
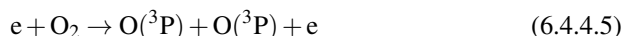
with a released energy for the pair $O(^3P) + O(^3P)$ equal to 1.03 eV. On the other hand, the excitation to the 8.4 eV level leads to dissociation into $O(^3P) + O(^1D)$,

$$e + O_2 \rightarrow O(^3P) + O(^1D) + e \tag{6.4.4.6}$$
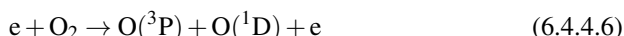
with a released energy for the pair O(^{3}P) + O(^{1}D) equal to 1.27 eV. Finally, the excitation to the 9.97 eV level leads to dissociation into O(^{1}D) + O(^{1}D),

$$e + O_2 \rightarrow O(^1D) + O(^1D) + e \tag{6.4.4.7}$$
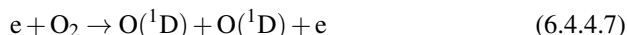
with a released energy for the pair O(^{3}P) + O(^{1}D) equal to 0.88 eV.

6.4.5 Electron impact O$_2$ ionization

The cross section for the electron impact ionization of the oxygen molecule in ground state

$$e + O_2 \rightarrow O_2^+ + 2e \tag{6.4.5.1}$$

was measured by Krishnakumar and Srivastava (1992) and the ionization potential is equal to 12.06 V.

6.4.6 Dissociative electron attachment

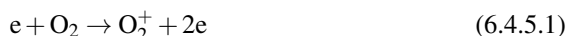The dissociative electron attachment reaction is important in discharges where the atoms have positive affinities because the threshold energy for production of negative ion fragments is lower than for pure dissociation processes. The dissociative electron attachment reaction usually produces a repulsive unbound intermediate state, which subsequently autodetaches or dissociates (Lieberman and Lichtenberg, 2005). The cross section is usually calculated balancing these two processes and it is generally smaller than the hard-sphere cross section of the molecule. Moreover, since the electron is captured, the process is resonant and becomes important only between a narrow energy interval (Lieberman and Lichtenberg, 2005). In the reaction

$$e + O_2 \rightarrow O + O^- \tag{6.4.6.1}$$

the electron transition is assumed to be rapid on a nuclear time-scale, and the energy of the ejected fragments can be calculated applying the Frank-Condon principle. The cross section is taken from Rapp and Briglia (1965). The threshold energy is equal to 4.2 eV and the incident electron loses its energy which is absorbed by the oxygen molecule to form O$_2^-$, which subsequently dissociates to form the fragments O and O$^-$. The potential energy for the O + O$^-$ pair is 3.63 eV above the ground state potential for O$_2$. The remaining incident electron energy is divided between the fragments.

6.4.7 Polar O$_2$ dissociation

The polar dissociation process

$$e + O_2 \rightarrow O^+ + O^- + e \tag{6.4.7.1}$$

proceeds by excitation of a polar state O$^+$ and O$^-$ of O$_2$. The cross section for the reaction above is taken from the measurements of Rapp and Briglia (1965).

6.4.8 Dissociative O$_2$ ionization

The dissociative ionization reactions usually require a threshold energy $\mathscr{E}_{\text{diz}}$ to occur. These cross sections have a similar form of the Thompson ionization cross section for atoms (Eq. (6.2.6.9)) (Lieberman and Lichtenberg, 2005). The cross section for the reaction

$$e + O_2 \rightarrow O^+ + O + 2e \qquad (6.4.8.1)$$

is taken from the measurement made by Krishnakumar and Srivastava (1992), while the ionization potential for dissociative ionization is equal to 18.73 V (Locht and Schopman, 1974).

6.4.9 Electron impact O elastic scattering

The cross section for electron elastic scattering from the oxygen atom

$$e + O \rightarrow e + O \qquad (6.4.9.1)$$

is taken from Thomas and Nesbet (1975) for $\mathscr{E} < 2$ eV and from Itikawa and Ichimura (1990) for $\mathscr{E} > 2$ eV.

6.4.10 Electron impact O excitation

The cross section for the electron impact excitation reactions

$$e + O(^3P) \rightarrow O(^1D) + e \qquad (6.4.10.1)$$
$$e + O(^3P) \rightarrow O(^1S) + e \qquad (6.4.10.2)$$
$$e + O(^3P) \rightarrow O(^3P^0) + e \qquad (6.4.10.3)$$
$$e + O(^3P) \rightarrow O(^5S^0) + e \qquad (6.4.10.4)$$
$$e + O(^3P) \rightarrow O(^3S^0) + e \qquad (6.4.10.5)$$

are taken from the review by Laher and Gilmore (1990) and have a threshold equal to 1.96, 4.18, 15.65, 9.14, 9.51 and 13.62 eV, respectively.

6.4.11 Electron impact O ionization

The electron impact ionization of the oxygen atom in the ground state reaction

$$e + O \rightarrow O^+ + 2e \qquad (6.4.11.1)$$

has a threshold equal to 13.62 eV and the cross section is taken from the theoretical work of Kim and Desclaux (2002).

6.4.12 Detachment

In the electron impact detachment reaction

$$e + O^- \rightarrow O + 2e \qquad (6.4.12.1)$$

the electron affinity $\mathscr{E}_{\text{aff}}$ of O atom plays the role of the ionization potential. Moreover, the repulsive Coulomb force between e and O^- lowers the cross section of approximatively a few dozen $\mathscr{E}_{\text{aff}}$ (Lieberman and Lichtenberg, 2005). The cross section for the reaction shown (6.4.12.1) is taken from the measurement of Vejby-Christensen et al. (1996), with a threshold energy equal to 1.46 eV. The cross section for the detachment from the negative oxygen ion by the oxygen molecule

$$O^- + O_2 \rightarrow O + O_2 + e \qquad (6.4.12.2)$$
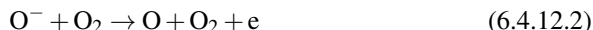
was taken from Comer and Schulz (1974), while the cross section for the negative oxygen ion by the oxygen atom

$$O^- + O \rightarrow O_2 + e \qquad (6.4.12.3)$$

was calculated from the rate coefficient at room temperature by (Belostotsky et al., 2005) and it is structured as follows
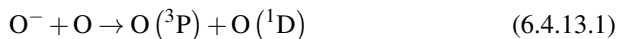
$$\text{for } \mathscr{E} \geq \mathscr{E}_* \implies \sigma = \sigma_0 \qquad (6.4.12.4)$$

$$\text{for } \mathscr{E} < \mathscr{E}_* \implies \sigma \sim \frac{1}{\sqrt{\mathscr{E}}}, \qquad (6.4.12.5)$$

where $\mathscr{E}_* = 184$ meV and $\sigma_0 = 1.09 \times 10^{-19}$ m^2.

6.4.13 Recombination

The dissociative recombination reaction

$$O^- + O \rightarrow O\left(^3P\right) + O\left(^1D\right) \qquad (6.4.13.1)$$

is assumed to create $O(^3P)$ and $O(^1D)$ in equal amounts and the respective cross section has been taken combining the measurements from Mul and McGowan (1979) and Peverall et al. (2001). The cross section for mutual neutralization

$$O^- + O_2^+ \rightarrow O + O_2 \qquad (6.4.13.2)$$

is taken from the measurements made by Padgett and Peart (1998) and Olson (1972), scaled by a factor of 5. Finally, the cross section for the reaction

$$O^- + O^+ \rightarrow O + O \qquad (6.4.13.3)$$

was taken from a measurement by Olson (1972) and scaled by a factor 6.4 in order to fit the measurement of Hayton and Peart (1993).

6.4.14 Charge exchange

The reaction

$$O_2^+ + O_2 \rightarrow O_2^+ + O_2 \qquad (6.4.14.1)$$

is usually interpreted as near-resonant and its cross section has been taken from Ellis et al. (1976) within the energy range $25.9 - 350$ meV, from Baer et al. (1978) within the energy range $1 - 40$ eV, and from Wilcox and Moran (1981) within the energy range $0.8 - 3$ keV. The reaction

$$O^+ + O_2 \rightarrow O_2^+ + O \tag{6.4.14.2}$$

does not have a threshold and its cross section is taken from Lindsay and Stebbings (2005). The charge exchange process

$$O^+ + O \rightarrow O + O^+ \tag{6.4.14.3}$$

is very likely at both small and large separations, leading to a cross section of the type shown in process of Eq. (6.2.7.16). In this work the cross section is taken from Stebbings et al. (1964). On the other hand, the charge exchange process

$$O_2^+ + O \rightarrow O_2 + O^+ \tag{6.4.14.4}$$

is very unlikely for collisions between thermal particles since it has a threshold energy equal to 1.56 eV. The cross section has been taken from the measurement by Stebbings et al. (1963) within the energy range $80 - 6000$ eV. The data have been extrapolated using the formula

$$\sigma = \sigma_0 \left(1 - \frac{\mathscr{E}_{\text{thre}}}{\mathscr{E}} \right) \tag{6.4.14.5}$$

along with $\mathscr{E}_{\text{thre}} = 1.56$ eV. The charge transfer reaction

$$O_2 + O^- \rightarrow O_2^- + O \tag{6.4.14.6}$$

has a threshold energy equal to 1.0 eV, which is much higher than the thermal energy of the heavy-particles, so that such a process has been neglected. Finally, the fragmentation reaction

$$O_2 + O_2 \rightarrow O + O_2 + O^+ \tag{6.4.14.7}$$

has the cross section shown in Eq. (6.4.14.5), where $\sigma_0 = 4.9 \times 10^{-19}$ m^2 is the gas kinetic cross section for O_2 (Lieberman and Lichtenberg, 2005). The potential energy required to form the $O^+ + O$ pair is 6.9 eV and we assume this process to have threshold energy that is twice this value, i.e. 13.8 eV. The remaining energy difference is split between the fragments.

6.5 The adjoint oxygen reaction set

Additional reactions have been included, as discussed in Gudmundsson and Lieberman (2015). The reactions are listed in Table 6.2.

Table 6.2. The chemical reaction, the process label and the related references for the adjoint oxygen reaction set as discussed in (Gudmundsson and Lieberman, 2015).

| Nr	Reaction	Process	Ref.
	Scattering		Gudmundsson et al. (2013)
33	$O^- + O_2 \rightarrow O^- + O_2$	Scattering	Muschlitz (1959)
34	$O + O_2 \rightarrow O + O_2$	Scattering	Brunetti et al. (1981)
35	$O_2^+ + O_2 \rightarrow O_2^+ + O_2$	Scattering	Gudmundsson et al. (2013)
36	$O^+ + O_2 \rightarrow O^+ + O_2$	Scattering	Gudmundsson et al. (2013)
37	$O_2 + O_2 \rightarrow O_2 + O_2$	Scattering	Brunetti et al. (1981)
38	$O + O \rightarrow O + O$	Scattering	Gudmundsson et al. (2013)
	Reactions involving $O(^1D)$		Gudmundsson and Lieberman (2015)
39	$e + O(^1D) \rightarrow O_+ + e + e$	Ionization	Kim and Desclaux (2002) (Threshold reduced)
40	$e + O(^1D) \rightarrow O(^3P) + e$	De-excitation	Laher and Gilmore (1990) (Detailed balancing)
	Reactions involving $O_2(a^1\Delta_g)$		Gudmundsson and Lieberman (2015)
41	$e + O_2(a^1\Delta_g) \rightarrow O_2^+ + e + e$	Ionization	Jaffke et al. (1992)
42	$e + O_2(a^1\Delta_g) \rightarrow O(^3P) + O^-$	Dissociative attachment	Jaffke et al. (1992) (Detailed balancing)
43	$e + O_2(a^1\Delta_g) \rightarrow O_2(X^3\Sigma_g^-) + e$	De-excitation	Laher and Gilmore (1990) (Threshold reduced)
44	$e + O_2(a^1\Delta_g) \rightarrow O_2(A^3\Sigma_u^+, A^3\Delta_u, c^1\Sigma_u^-) + e$	Metastable excitation (3.07 eV)	Itikawa (2009); Shyn and Sweeney (2000); Green et al. (2001) (Threshold reduced)
45	$e + O_2(a^1\Delta_g) \rightarrow O(^3P) + O(^3P) + e$	Dissociation (5.14 eV)	Phelps (1985) (Threshold reduced)
46	$e + O_2(a^1\Delta_g) \rightarrow O(^3P) + O(^1D) + e$	Dissociation (7.42 eV)	Phelps (1985) (Threshold reduced)
47	$e + O_2(a^1\Delta_g) \rightarrow O(^1D) + O(^1D) + e$	Dissociation (8.99 eV)	Phelps (1985) (Threshold reduced)
48	$e + O_2(a^1\Delta_g) \rightarrow O(^3P) + O^+ + 2e$	Dissociative ionization	Krishnakumar and Srivastava (1992) (Threshold reduced)
49	$O^- + O_2(a^1\Delta_g) \rightarrow$ Products	Detachment	Gudmundsson and Lieberman (2015)
50	$O_2(X^3\Sigma_g^-) + O_2(a^1\Delta_g) \rightarrow O_2(X^3\Sigma_g^-) + O_2(a^1\Delta_g)$	Scattering	Brunetti et al. (1981)
51	$O(^1D) + O_2(X^3\Sigma_g^-) \rightarrow O(^1D) + O_2(X^3\Sigma_g^-)$	Scattering	Brunetti et al. (1981)
52	$O_2^+ + O_2(a^1\Delta_g) \rightarrow O_2^+ + O_2(X^3\Sigma_g^-)$	Charge exchange	Ellis et al. (1976); Baer et al. (1978); Wilcox and Moran (1981)
53	$O^+ + O_2(a^1\Delta_g) \rightarrow O_2^+ + O(^3P)$	Charge exchange	Lindsay and Stebbings (2005)
	Reactions involving $O_2(b^1\Sigma_g^+)$		Hannesdottir and Gudmundsson (2016)
54	$e + O_2(b^1\Sigma_g^+) \rightarrow O_2^+ + e + e$	Ionization	Jaffke et al. (1992) (Threshold reduced)
55	$e + O_2(b^1\Sigma_g^+) \rightarrow O(^3P) + O^-$	Dissociative attachment	Jaffke et al. (1992) (Threshold reduced)
56	$e + O_2(b^1\Sigma_g^+) \rightarrow O_2(X^3\Sigma_g^-) + e$	De-excitation	Laher and Gilmore (1990) (Detailed balancing)
57	$e + O_2(b^1\Sigma_g^+) \rightarrow O_2(A^3\Sigma_u^+, A^3\Delta_u, c^1\Sigma_u^-) + e$	Metastable excitation (2.42 eV)	Itikawa (2009); Shyn and Sweeney (2000); Green et al. (2001) (Threshold reduced)
58	$e + O_2(b^1\Sigma_g^+) \rightarrow O(^3P) + O(^3P) + e$	Dissociation (4.49 eV)	Phelps (1985) (Threshold reduced)
59	$e + O_2(b^1\Sigma_g^+) \rightarrow O(^1D) + O(^3P) + e$	Dissociation (6.77 eV)	Phelps (1985) (Threshold reduced)
60	$e + O_2(b^1\Sigma_g^+) \rightarrow O(^1D) + O(^1D) + e$	Dissociation (8.34 eV)	Phelps (1985) (Threshold reduced)
61	$e + O_2(b^1\Sigma_g^+) \rightarrow O(^3P) + O^+ + 2e$	Dissociative ionization	Krishnakumar and Srivastava (1992) (Threshold reduced)
62	$O^- + O_2(b^1\Sigma_g^+) \rightarrow O(^3P) + O_2(X^3\Sigma_g^-) + e$	Detachment	Aleksandrov (1978)
63	$O(^1D) + O_2(X^3\Sigma_g^-) \rightarrow O(^3P) + O_2(b^1\Sigma_g^+)$	Energy Transfer	Baulch et al. (1982)
64	$O_2(X^3\Sigma_g^-) + O_2(b^1\Sigma_g^+) \rightarrow O_2(X^3\Sigma_g^-) + O_2(X^3\Sigma_g^-)$	Quenching	Baulch et al. (1982)
65	$O_2(X^3\Sigma_g^-) + O_2(b^1\Sigma_g^+) \rightarrow O_2(X^3\Sigma_g^-) + O_2(b^1\Sigma_g^+)$	Scattering	Brunetti et al. (1981)
66	$O_2^+ + O_2(b^1\Sigma_g^+) \rightarrow O_2(X^3\Sigma_g^-) + O_2^+$	Charge exchange	Ellis et al. (1976); Baer et al. (1978); Wilcox and Moran (1981)
67	$O^+ + O_2(b^1\Sigma_g^+) \rightarrow O_2^+ + O(^3P)$	Charge exchange	Lindsay and Stebbings (2005)

6.5.1 Elastic scattering of heavy particles

The elastic scattering of heavy particles are not included in the standard oxygen reaction set shown in Table 6.1. They are shown in Table 6.2 as reactions of the adjoint reaction set. The cross section for the elastic scattering involving O_2^+ and O_2, namely

$$O_2^+ + O_2 \rightarrow O_2^+ + O_2 \tag{6.5.1.1}$$

is taken to be half of the respective charge exchange reaction (process (6.4.14.1)). The cross section for the elastic scattering involving O and O_2, namely

$$O + O_2 \rightarrow O + O_2 \tag{6.5.1.2}$$

is taken from Brunetti et al. (1981). The cross section for the elastic scattering involving O^+ and O_2, namely

$$O^+ + O_2 \rightarrow O^+ + O_2 \tag{6.5.1.3}$$
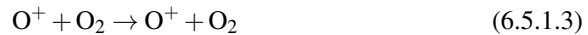
is assumed to be half of the cross section for the analogous charge exchange process shown in Eq. (6.4.14.2). The cross section of the process

$$O^- + O_2 \rightarrow O^- + O_2 \tag{6.5.1.4}$$

has been taken by the measurements of Muschlitz (1959). The cross section for the oxygen molecule scattering by an oxygen molecule

$$O_2 + O_2 \rightarrow O_2 + O_2 \tag{6.5.1.5}$$
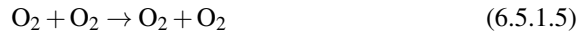
was taken from Brunetti et al. (1981), while the cross section for the oxygen atom scattering by an oxygen atom

$$O + O \rightarrow O + O \tag{6.5.1.6}$$

was taken from Gudmundsson et al. (2013).

6.5.2 Reactions involving O(^{1}D)

The reaction set involving the metastable oxygen atom O(^{1}D) has been discussed in Gudmundsson and Lieberman (2015). The cross section for electron impact ionization, namely
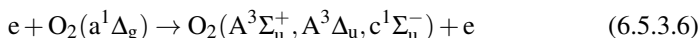
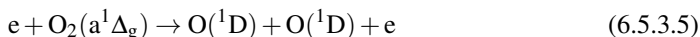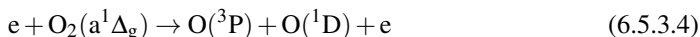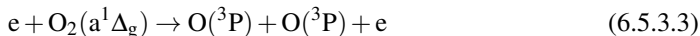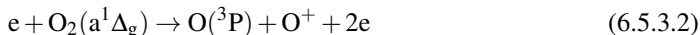$$e + O(^1D) \rightarrow O^+ + e + e \tag{6.5.2.1}$$

was taken from the calculations of Kim and Desclaux (2002) with a reduced threshold equal to 1.96 eV. The cross section for the electron impact de-excitation, namely

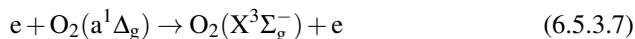$$e + O(^1D) \rightarrow O(^3P) + e \tag{6.5.2.2}$$

was estimated using the detailed balancing principle for the excitation cross section (Laher and Gilmore, 1990).

6.5.3 Reactions involving $O_2(a^1\Delta_g)$

The cross section for electron impact ionization, dissociative ionization, dissociation, excitation and de-excitation

$$e + O_2(a^1\Delta_g) \rightarrow O_2^+ + e + e \qquad (6.5.3.1)$$

$$e + O_2(a^1\Delta_g) \rightarrow O(^3P) + O^+ + 2e \qquad (6.5.3.2)$$

$$e + O_2(a^1\Delta_g) \rightarrow O(^3P) + O(^3P) + e \qquad (6.5.3.3)$$

$$e + O_2(a^1\Delta_g) \rightarrow O(^3P) + O(^1D) + e \qquad (6.5.3.4)$$

$$e + O_2(a^1\Delta_g) \rightarrow O(^1D) + O(^1D) + e \qquad (6.5.3.5)$$

$$e + O_2(a^1\Delta_g) \rightarrow O_2(A^3\Sigma_u^+, A^3\Delta_u, c^1\Sigma_u^-) + e \qquad (6.5.3.6)$$

are assumed to be the same as the respective ground state processes but with a reduced threshold. For example the electron impact ionization reaction (6.5.3.1) and the electron impact dissociative ionization reaction (6.5.3.2) have a reduced threshold equal to 0.98 eV. The de-excitation reaction

$$e + O_2(a^1\Delta_g) \rightarrow O_2(X^3\Sigma_g^-) + e \qquad (6.5.3.7)$$

was estimated using the detailed balancing principle for the excitation cross section (Laher and Gilmore, 1990). On the other hand, the reaction

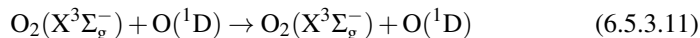$$e + O_2 \rightarrow O(^3P) + O(^3P) + O^- \qquad (6.5.3.8)$$
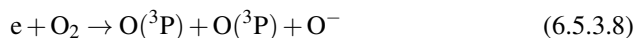
has a cross section that is roughly 3.5 times higher than the respective ground state process (Jaffke et al., 1992; Burrow, 1973). The cross section for the reaction

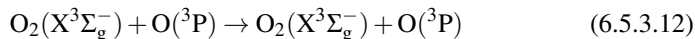$$O_2^+ + O_2 \rightarrow O + O^+ + O_2 \qquad (6.5.3.9)$$

has been updated with respect to a previous work (Gudmundsson et al., 2013) according to the cross section measured by Moran and Roberts (1968), with a threshold energy equal to 12.8 eV. The cross section for the reaction

$$O_2(X^3\Sigma_g^-) + O_2(a^1\Delta_g) \rightarrow O_2(X^3\Sigma_g^-) + O_2(a^1\Delta_g) \qquad (6.5.3.10)$$
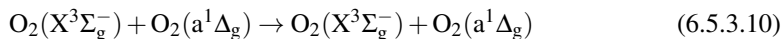
is assumed to be the same as for ground state molecules and it has been taken from Brunetti et al. (1981) and then extrapolated to higher and lower energy assuming a constant cross section. The cross section for the reaction

$$O_2(X^3\Sigma_g^-) + O(^1D) \rightarrow O_2(X^3\Sigma_g^-) + O(^1D) \qquad (6.5.3.11)$$

is assumed to be the same as

$$O_2(X^3\Sigma_g^-) + O(^3P) \rightarrow O_2(X^3\Sigma_g^-) + O(^3P) \qquad (6.5.3.12)$$

and it has been taken from Brunetti et al. (1981) and further discussed by Gudmundsson et al. (2013). The cross section for the reactions

$$O_2^+ + O_2(a^1\Delta_g) \rightarrow O_2(X^3\Sigma_g^-) + O_2^+ \qquad (6.5.3.13)$$

$$O^+ + O_2(a^1\Delta_g) \rightarrow O_2^+ + O(^3P) \qquad (6.5.3.14)$$
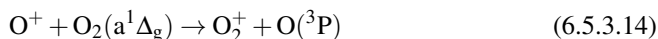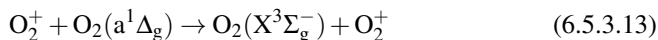
are assumed to be the same as for the respective ground state reactions and have been taken from literature (Ellis et al., 1976; Baer et al., 1978; Wilcox and Moran, 1981; Lindsay and Stebbings, 2005) and further discussed by Gudmundsson et al. (2013).

It is worth to mention the important role of the singlet metastable oxygen molecule $O_2(a^1\Delta_g)$ (Proto and Gudmundsson, 2018b) in the discharge. At low pressures the dissociative attachment from the metastable oxygen molecule $O_2(a^1\Delta_g)$ can be the most important source of O^- ions in the discharge and O^- is the dominant negative ion in the discharge, created through processes

$$e + O_2(a^1\Delta_g) \longrightarrow \begin{cases} O(^3P) + O^- \\ O(^1D) + O^- \end{cases} \qquad . \qquad (6.5.3.15)$$
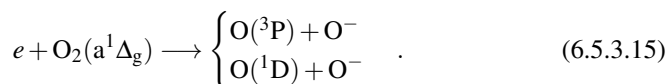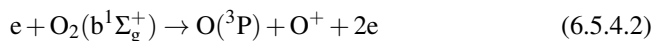
Conversely the the negative ion O^- ion losses are dominated by the following detachment process

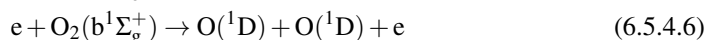$$O^- + O_2(a^1\Delta_g) \longrightarrow \text{Products}, \qquad (6.5.3.16)$$
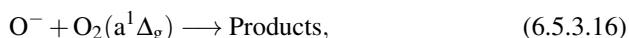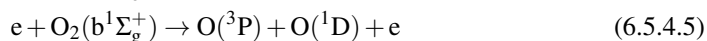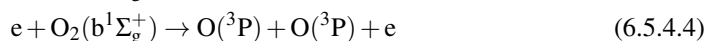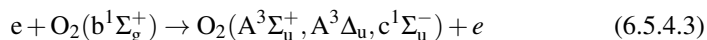
while detachment by the oxygen molecule in the ground state and ion-ion recombination are negligible. The reaction rate of the dissociative attachment (detachment) increases with decreasing (increasing) discharge pressure and higher (lower) effective electron temperature. At low pressure dissociative attachment dominates over detachment and the amount of electrons (O^-) decreases (increases) within the plasma discharge, i.e. the electronegativity is high.

6.5.4 Reactions involving $O_2(b^1\Sigma_g)$

Due to the lack of measurements and/or calculations of the cross sections for the electron impact ionization and electron impact dissociative ionization from the metastable $O_2(b^1\Sigma_g)$ molecule, namely

$$e + O_2(b^1\Sigma_g^+) \rightarrow O_2^+ + e + e \qquad (6.5.4.1)$$

$$e + O_2(b^1\Sigma_g^+) \rightarrow O(^3P) + O^+ + 2e \qquad (6.5.4.2)$$

are assumed to be the same as for the ground state molecule (Krishnakumar and Srivastava, 1992) but with a reduced threshold equal to 1.627 eV. Similarly, the cross sections for electron impact excitation and dissociation, namely

$$e + O_2(b^1\Sigma_g^+) \rightarrow O_2(A^3\Sigma_u^+, A^3\Delta_u, c^1\Sigma_u^-) + e \qquad (6.5.4.3)$$

$$e + O_2(b^1\Sigma_g^+) \rightarrow O(^3P) + O(^3P) + e \qquad (6.5.4.4)$$

$$e + O_2(b^1\Sigma_g^+) \rightarrow O(^3P) + O(^1D) + e \qquad (6.5.4.5)$$

$$e + O_2(b^1\Sigma_g^+) \rightarrow O(^1D) + O(^1D) + e \qquad (6.5.4.6)$$

are assumed to be the same as for the ground state molecule but with a reduced threshold equal to 1.63 eV. The cross section for the electron impact dissociative attachment

$$e + O_2(b^1\Sigma_g^+) \rightarrow O(^3P) + O^- \qquad (6.5.4.7)$$
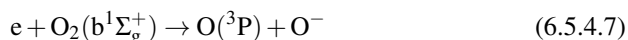
is assumed to be the same as the cross section for the electron impact dissociative attachment from $O_2(a^1\Delta_g)$ (Jaffke et al., 1992) but with a threshold reduced by 0.62 eV. On the other hand, the process

$$O(^1D) + O_2(X^3\Sigma_g^-) \to O(^3P) + O_2(b^1\Sigma_g^+) \tag{6.5.4.8}$$
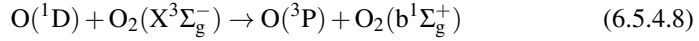
has the following cross section

$$\begin{cases} \text{for } 0 < \mathscr{E} < 184 \text{ meV} \implies \sigma \sim \frac{1}{\sqrt{\mathscr{E}}} \\ \text{for } \mathscr{E} > 184 \text{ meV} \implies \sigma = 2.56 \times 10^{-17} \exp\left(\frac{67}{T_n}\right) \end{cases}, \tag{6.5.4.9}$$

where T_n is the neutral background gas temperature, $\mathscr{E}$ is the energy of the metastable $O^1(D)$ in the $O_2(X^3\Sigma_g^-)$ rest frame. Moreover, the reaction above has been found to be dominant for the formation of $O_2(b^1\Sigma_g^+)$ in the oxygen discharge (Toneli et al., 2015) and is known to be an efficient quencher of the $O(^1D)$ state (Young and Black, 1967). The cross section for the detachment

$$O^- + O_2(b^1\Sigma_g^+) \to O(^3P) + O_2(X^3\Sigma_g^-) + e \tag{6.5.4.10}$$
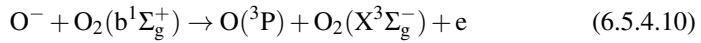
is

$$\begin{cases} \text{for } 0 < \mathscr{E} < 184 \text{ meV} \implies \sigma \sim \frac{1}{\sqrt{\mathscr{E}}} \\ \text{for } \mathscr{E} > 184 \text{ meV} \implies \sigma = \text{constant} \end{cases} \tag{6.5.4.11}$$

and it has been estimated by using the rate coefficient equal to 6.9×10^{-16} m^3 s^{-1} at 300 K (Aleksandrov, 1978). On the other hand, for the process

$$O_2(X^3\Sigma_g^-) + O_2(b^1\Sigma_g^+) \to O_2(X^3\Sigma_g^-) + O_2(X^3\Sigma_g^-) \tag{6.5.4.12}$$
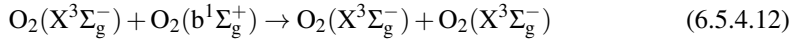
the following cross section has been employed

$$\begin{cases} \text{for } 0 < \mathscr{E} < 184 \text{ meV} \implies \sigma \sim \frac{1}{\sqrt{\mathscr{E}}} \\ \text{for } \mathscr{E} > 184 \text{ meV} \implies \sigma = \text{constant} \end{cases} \tag{6.5.4.13}$$

based on the rate constant equal to 4×10^{-23} m^3 s^{-1}, measured by Martin et al. (1976); Lawton et al. (1977) and recommended by Baulch et al. (1982). The cross section for the scattering and the charge exchange reactions

$$O_2(X^3\Sigma_g^-) + O_2(b^1\Sigma_g^+) \to O_2(X^3\Sigma_g^-) + O_2(b^1\Sigma_g^+) \tag{6.5.4.14}$$

$$O_2^+ + O_2(b^1\Sigma_g^+) \to O_2(X^3\Sigma_g^-) + O_2^+ \tag{6.5.4.15}$$

$$O^+ + O_2(b^1\Sigma_g^+) \to O_2^+ + O \tag{6.5.4.16}$$
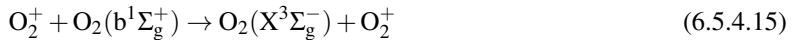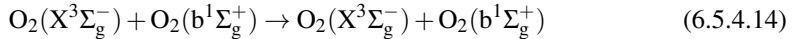
are assumed to be the same as for the ground state and taken from various sources (Brunetti et al., 1981), (Ellis et al., 1976; Baer et al., 1978; Wilcox and Moran, 1981) and (Lindsay and Stebbings, 2005), respectively. Finally, the cross section for the de-excitation reaction

$$e + O_2(b^1\Sigma_g^+) \to O_2(X^3\Sigma_g^-) + e \tag{6.5.4.17}$$
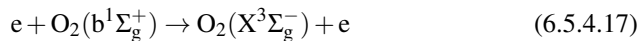
has been estimated using the detailed balancing principle for the excitation cross section (Laher and Gilmore, 1990).

6.6 PIC/MCC model for chlorine discharges

In the past years the PIC/MCC simulations were applied to chlorine discharge in order to achieve multiple tasks. In the beginning, PIC/MCC simulation were used to simulate a capacitively coupled chlorine discharge and the temporal behaviour of the plasma parameters (Nanbu et al., 1999a), to simulate the etching of a silicon wafer and investigate the flow of radicals and the generation of etch products (Nanbu et al., 1999b). Other PIC/MCC simulations have been applied to explore the dependence of the plasma structure on the discharge parameters (Kawano et al., 2000), as well as to study the spatio-temporal electron dynamics (Lymberopoulos and Economou, 1995). All these simulations neglected the Cl^+ ions as well as the Cl^+ involved reactions and electron impact dissociation processes. More recently, PIC/MCC simulations were applied to explore the influence of discharge pressure on a voltage driven single-frequency capacitively coupled chlorine discharge (Huang and Gudmundsson, 2013). Later on, the same authors explored the role of the driving frequency and secondary electron emission on a current driven single-frequency capacitively coupled chlorine discharge (Huang and Gudmundsson, 2014a). Furthermore, the PIC/MCC simulations have been applied to explore a current driven dual-frequency capacitively coupled chlorine discharge (Huang and Gudmundsson, 2014b,a) where both the higher and lower frequency sources were varied independently (Huang and Gudmundsson, 2015). As the driving higher frequency was increased, the average sheath potential and the higher frequency component of the voltage decrease dramatically as the plasma impedance for the higher frequency component decreases. However, as the driving lower frequency was increased, the electron power absorption, the ion flux, and the average sheath potential remained almost invariant. More recently, the electron power absorption and independent control of ion energy and ion flux onto the electrodes have been explored (Skarphedinsson and Gudmundsson, 2020).

The chlorine reaction set included in the `oopd1` code is rather extensive and includes five species: Cl_2 molecules, Cl atoms in the ground state and the ions Cl^-, Cl^+ and Cl_2^+ (Huang and Gudmundsson, 2013).

6.7 The chlorine reaction set

The chlorine reaction set included in the `oopd1` code is rather extensive and includes five heavy species in addition to electrons: the ground state neutrals $Cl(^3P)$ and $Cl_2(X^3\Sigma_g^-)$, the negative ions Cl^- and the positive ions Cl^+ and Cl_2^+. The reactions are shown in Table 6.3. The Cl atom has the highest electron affinity of all elements (3.61 eV) (Gottscho and Gaebe, 1986) and has a nearly zero threshold energy for dissociative attachment along with a low dissociation energy (2.48 eV) and a high electron affinity (Christophorou and Olthoff, 1999). Consequently, all electronic excitations of Cl_2 molecule appear to be dissociative and metastable states can hardly exist, so metastable states are neglected in our code due to their small significance in the discharge. In the chlorine discharge, the number of Cl atoms is much larger than the number of charged species.

Table 6.3. The chemical reaction, the process label and the related references for the standard chlorine reaction set as discussed in Huang and Gudmundsson (2013).

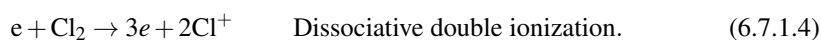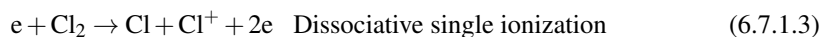| Nr	Reaction	Process	Ref.
	Electron impact Cl_2		Huang and Gudmundsson (2013)
1	$e + Cl_2 \rightarrow e + Cl_2$	Elastic scattering	Gregório and Pitchford (2012)
2	$e + Cl_2 \rightarrow Cl_2^+ + 2e$	Ionization (11.47 eV)	Basner and Becker (2004)
3	$e + Cl_2 \rightarrow Cl + Cl^+ + 2e$	Dissociative single ionization (15.7 ± 0.3 eV)	Basner and Becker (2004); Calandra et al. (2000)
4	$e + Cl_2 \rightarrow 2Cl^+ + 3e$	Dissociative double ionization ($31.13V$)	Basner and Becker (2004); Calandra et al. (2000)
5	$e + Cl_2 \rightarrow Cl + Cl^-$	Dissociative attachment	Kurepa and Belić (1978); Ruf et al. (2004)
6	$e + Cl_2 \rightarrow Cl^+ + Cl^- + e$	Polar dissociation (11.9 ± 0.2) V	Golovitskii (2000)
7	$e + Cl_2 \rightarrow Cl_2^* + e$	Excitation	Huang and Gudmundsson (2013)
	Electron impact Cl		Huang and Gudmundsson (2013)
8	$e + Cl \rightarrow e + Cl$	Elastic scattering	Wang et al. (2013)
9	$e + Cl \rightarrow Cl^+ + 2e$	Ionization (12.99 eV)	Hayes et al. (1987); Ali and Kim (2005)
10	$e + Cl \rightarrow e + Cl^*$	Excitation	Huang and Gudmundsson (2013)
	Electron detachment from Cl^-		(Huang and Gudmundsson, 2013)
11	$e + Cl^- \rightarrow Cl + 2e$	Electron-impact detachment (3.4 eV)	Fritioff et al. (2003)
12	$e + Cl^- \rightarrow Cl^+ + 3e$	Electron-impact detachment (28.6 eV)	Fritioff et al. (2003)
13	$Cl^- + Cl_2 \rightarrow Cl + Cl_2 + e$	Detachment by chlorine molecule (3.61 eV)	Huq et al. (1984)
14	$Cl^- + Cl \rightarrow Cl_2 + e$	Detachment by chlorine atom (1.13 eV)	Huang and Gudmundsson (2013)
	Recombination		(Huang and Gudmundsson, 2013)
15	$e + Cl_2^+ \rightarrow 2Cl$	Dissociative recombination	Zhang et al. (2011a)
16	$Cl_2^+ + Cl^- \rightarrow 3\,Cl$	Mutual neutralization	Church and Smith (1978)
17	$Cl^+ + Cl^- \rightarrow 2\,Cl$	Mutual neutralization	Church and Smith (1978)
	Charge exchange		(Huang and Gudmundsson, 2013)
18	$Cl^+ + Cl \rightarrow Cl + Cl^+$	Charge exchange	Subramonium (2003)
19	$Cl_2^+ + Cl_2 \rightarrow Cl_2 + Cl_2^+$	Charge exchange	Subramonium (2003)
20	$Cl^+ + Cl_2 \rightarrow Cl_2 + Cl^+$	Charge exchange	Španěl et al. (1993)
21	$Cl^- + Cl \rightarrow Cl + Cl^-$	Charge exchange	Karmohapatro (1965)
22	$Cl_2^+ + Cl \rightarrow Cl + Cl_2^+$	Charge exchange (1.52 eV)	Huang and Gudmundsson (2013)
	Fragmentation		Huang and Gudmundsson (2013)
23	$Cl_2^+ + Cl_2 \rightarrow Cl_2 + Cl + Cl^+$	Fragmentation (3.52 eV)	Huang and Gudmundsson (2013)
	Scattering		Huang and Gudmundsson (2013)
24	$Cl_2 + Cl_2 \rightarrow Cl_2 + Cl_2$	Scattering	Huang and Gudmundsson (2013)
25	$Cl + Cl_2 \rightarrow Cl_2 + Cl$	Scattering	Huang and Gudmundsson (2013)
26	$Cl + Cl \rightarrow Cl + Cl$	Scattering	Huang and Gudmundsson (2013)
27	$Cl_2^+ + Cl_2 \rightarrow Cl_2^+ + Cl_2$	Scattering	Huang and Gudmundsson (2013)
28	$Cl^+ + Cl_2 \rightarrow Cl_2 + Cl^+$	Scattering	Huang and Gudmundsson (2013)
29	$Cl^- + Cl_2 \rightarrow Cl_2 + Cl^-$	Scattering	Huang and Gudmundsson (2013)

6.7.1 Electron impact Cl_2 reactions

The dominant process involving the electrons is the elastic scattering with Cl_2 molecule in the ground state. In the reaction

$$e + Cl_2 \rightarrow e + Cl_2, \qquad (6.7.1.1)$$

a change in the electron momentum occurs. The cross section has been comprehensively reviewed in the literature (Christophorou and Olthoff, 1999; Gregório and Pitchford, 2012; Rescigno, 1994) . Ionization of the Cl_2 molecule may occur in three different ways

$$e + Cl_2 \rightarrow 2e + Cl_2^+ \qquad \text{Ionization} \qquad (6.7.1.2)$$

$$e + Cl_2 \rightarrow Cl + Cl^+ + 2e \quad \text{Dissociative single ionization} \qquad (6.7.1.3)$$

$$e + Cl_2 \rightarrow 3e + 2Cl^+ \qquad \text{Dissociative double ionization.} \qquad (6.7.1.4)$$

These three ionization cross sections have a similar behaviour as the Thomson ionization cross section for atoms so that (Lieberman and Lichtenberg, 2005)

$$\sigma_{\text{Ion}} \sim \sigma_{\text{Diss.singl.ion}} \sim \sigma_{\text{Diss.double.ion}} \sim \mathscr{E}^{-1}. \qquad (6.7.1.5)$$

Among these three ionization processes, non-dissociative ionization of Cl_2 to form Cl_2^+ is the dominant process in the entire range of energies (Basner and Becker, 2004). For the dissociative attachment reaction

$$e + Cl_2 \rightarrow Cl + Cl^- \qquad (6.7.1.6)$$

the threshold energy is close to zero. The incoming electron hits the Cl_2 molecule forming Cl_2^- ions, which dissociate to form both Cl atoms and Cl^- ions. Such a transition is assumed to be rapid on a nuclear timescale, and the energy of the ejected fragments can be calculated by applying the Franck–Condon principle. The potential energy for the Cl-Cl^- pair is assumed to be the difference between the dissociation energy of Cl_2 and the electron affinity of Cl, which is 1.13 eV below the ground state potential for Cl_2. This energy difference plus the incident electron energy, $\mathscr{E}_{\text{inc}}$ + 1.13 eV, is divided between the fragments. The cross section has been calculated in the following way: for energies above 0.2 eV the experimental cross section measured by Kurepa and Belić (1978), after enhancing its absolute value by 30% to be in agreement with electron swarm data (Christophorou and Olthoff, 1999), has been used. On the other hand, the cross section measured by Ruf et al. (2004) has been employed below 0.2 eV.

6.7.2 Electron impact excitation

All electronic excitations for the Cl_2 molecule appear to be dissociative, so the dissociation of the Cl_2 molecule is treated as an excitation of the Cl_2 molecule, which subsequently breaks into fragments, so that
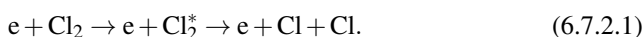
$$e + Cl_2 \rightarrow e + Cl_2^* \rightarrow e + Cl + Cl. \qquad (6.7.2.1)$$

Table 6.4. Electron impact electronic, rotational and vibrational excitations of a Cl₂ molecule with threshold energies, released energies and references for the cross sections as discussed in Huang and Gudmundsson (2013).

Excited State	Thresh. (eV)	Released (eV)	Ref.
$J > 0$	0.01	$--$	Christophorou and Olthoff (1999)
$v = 1$	0.07	$--$	Kolorenč and Horáček (2006)
$v = 2$	0.14	$--$	Kolorenč and Horáček (2006)
$v = 3$	0.21	$--$	Kolorenč and Horáček (2006)
$1^3\Pi_u$	3.24	0.76	Rescigno (1994)
$1^1\Pi_u$	4.04	1.56	Rescigno (1994)
$1^3\Pi_g$	6.23	3.75	Rescigno (1994)
$1^1\Pi_g$	6.86	4.38	Rescigno (1994)
$1^3\Sigma_u^+$	6.80	4.32	Rescigno (1994)
$2^1\Pi_u$	9.22	6.74	Rescigno (1994)
$1^1\Sigma_u^+$	9.32	6.84	Rescigno (1994)

Again, the electron transition is assumed to be rapid on a nuclear timescale and the cross sections for the electronic excitations of Cl₂ are taken from the theoretical work of Rescigno (1994). In Table 6.4 the threshold energies, the released energies and the references for the cross section for eletron impact electronic, rotational and vibrational excitation of a Cl₂ molecule are shown. The released energy for each pair of heavy fragments has been calculated as the difference between the threshold energy of the excitation and the potential of the ground state Cl + Cl (2.48 eV).

The vibrational and rotational excitations provide energy loss mechanism. Both rotationally and the vibrationally excitations are assumed to return instantaneously to the ground state. Moreover, the former are found to have no influence on the plasma discharge physics, while the latter may have a significant influence on the shape of the EEDF, as has been demostrated in oxygen discharges (Vahedi and Surendra, 1995). The cross section for rotational excitation from 0.01 up to 2 eV has been taken from the calculations made by Kutz and Meyer (1995), while the cross section from 2 eV up to 100 eV has been taken from the experimental measurements made by Gote and Ehrhardt (1995), and then extrapolated to 10^4 eV, assuming the dependence to be $\mathscr{E}^{-1}$ (Lieberman and Lichtenberg, 2005). The cross sections for the electronic excitations of Cl₂ ($1^3\Pi_u, 1^1\Pi_u, 1^3\Pi_g, 1^1\Pi_g, 1^3\Sigma_u^+, 2^1\Pi_u, 1^1\Sigma_u^+$) are taken from the theoretical work of Rescigno (1994) and all the excitations lead to dissociation into the ground state Cl + Cl (Peyerimhoff and Buenker, 1981).

Table 6.5. Electron impact excitations of a Cl atom with threshold energies and references for the cross sections. as discussed in Huang and Gudmundsson (2013).

Excited State	Threesh. (eV)	Ref.
4s	9.1	(Ganas, 1988)
5s	11.4	(Ganas, 1988)
6s	12.1	(Ganas, 1988)
4p	10.5	(Ganas, 1988)
5p	11.8	(Ganas, 1988)
3d	11.2	(Ganas, 1988)
4d	12.0	(Ganas, 1988)
5d	12.4	(Ganas, 1988)

6.7.3 Electron impact Cl reactions

The cross section for the elastic scattering reaction

$$e + Cl \rightarrow e + Cl \tag{6.7.3.1}$$

has been taken from Wang et al. (2013) and extrapolated up to 10^4 eV. On the other hand the cross section for the ionization

$$e + Cl \rightarrow Cl^+ + 2e \tag{6.7.3.2}$$

is taken from Hayes et al. (1987), with a threshold energy of 12.99 eV (Wise et al., 1995) and then extrapolated to higher energies using the cross section calculated by Ali and Kim (2005). At 200 eV that is the same cross section as measured by Hayes et al. (1987). Such a cross section is a typical Thomson cross section so that

$$\text{for } \mathscr{E} = 2\mathscr{E}_{\text{threshold}} \rightarrow \sigma = \sigma_{\text{minimum}} \tag{6.7.3.3}$$

$$\text{for } \mathscr{E} \gg \mathscr{E}_{\text{threshold}} \rightarrow \sigma \sim \mathscr{E}^{-1}. \tag{6.7.3.4}$$

Table 6.5 shows the electron impact excitations of a Cl atom with threshold energies and references for the cross sections, as discussed by Huang and Gudmundsson (2013). Since none of the lowest excited states of the Cl atom are metastable, electron impact excitations of the Cl atom are incorporated to only account for collisional energy loss and these excited states are assumed to return instantaneously to the ground state Cl (Huang and Gudmundsson, 2013).

6.7.4 Electron detachment from Cl⁻

The cross sections for the reactions

$$e + Cl^- \rightarrow Cl + 2e \tag{6.7.4.1}$$

$$e + Cl^- \rightarrow Cl^+ + 3e \tag{6.7.4.2}$$

are taken from Fritioff et al. (2003), with threshold energies equal to 3.4 eV (Chanson et al., 2012) and 28.6 eV (Fritioff et al., 2003), respectively. For detachment by the Cl_2 molecule

$$Cl_2 + Cl^- \rightarrow Cl + Cl_2 + e, \qquad (6.7.4.3)$$

the cross section measured by Huq et al. (1984) has been used, along with threshold of this reaction equal to the electron affinity of Cl, i.e. 3.61 eV. The calculation for the detachment by Cl atom

$$Cl^- + Cl \rightarrow Cl_2 + e \qquad (6.7.4.4)$$

is a little bit more involved. Since such a reactions is the inverse of the dissociative attachment, we assume the threshold of the process shown in (6.7.4.4) to have a threshold energy corresponding to the potential difference between the ground state Cl_2 and the Cl-Cl^+ pair, which is equal to 1.13 eV. The cross section for the detachment by Cl atom is assumed to be

$$\sigma = \sigma_0 \left(1 - \frac{\mathscr{E}_{\text{thr}}}{\mathscr{E}} \right), \qquad (6.7.4.5)$$

where $\sigma_0 = 1.09 \times 10^{-19}$ m^2, which is the same cross section as the detachment by O atom (reaction (6.4.12.3)) for the ion energy above 0.184 eV (Gudmundsson et al., 2013).

6.7.5 Recombination

For the dissociative recombination reaction

$$e + Cl^+ \rightarrow 2Cl, \qquad (6.7.5.1)$$

the cross section is taken from Zhang et al. (2011a). The cross section for ion-ion mutual neutralization has been obtained from the rate coefficients using the formula

$$\sigma = \frac{k}{\left(\frac{2e\mathscr{E}}{m} \right)^{\frac{1}{2}}}, \qquad (6.7.5.2)$$

where k is the rate coefficient of the reaction and m is the reduced mass of the reactants (Lieberman and Lichtenberg, 2005). The rate constant for the reaction

$$Cl_2^+ + Cl^- \rightarrow 3Cl \qquad (6.7.5.3)$$

is assumed to be 5×10^{-14} m^3 s^{-1} at 300 K (Church and Smith, 1978) and it has been modified in the following way

$$k = 5 \times 10^{-14} \left(\frac{300}{T_{\text{g}}} \right)^{\frac{1}{2}}. \qquad (6.7.5.4)$$
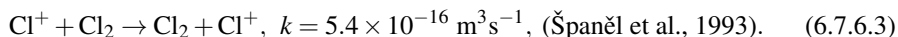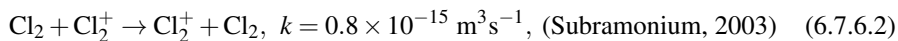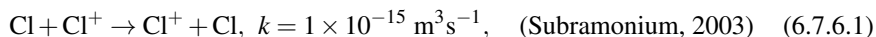
Regarding the reaction

$$Cl^+ + Cl^- \rightarrow 2Cl, \qquad (6.7.5.5)$$

it has been assumed to have the same rate constant as the $Cl_2^+ + Cl^-$ mutual neutralization (Rogoff et al., 1986; Thorsteinsson and Gudmundsson, 2010a; Lee and Lieberman, 1995; Kim et al., 2005).

6.7.6 Charge exchange

In the following the first three charge exchange reactions shown in Table 6.3 will be listed along with their rate constant:

$$Cl + Cl^+ \rightarrow Cl^+ + Cl, \ k = 1 \times 10^{-15} \ m^3 s^{-1}, \quad \text{(Subramonium, 2003)} \quad (6.7.6.1)$$

$$Cl_2 + Cl_2^+ \rightarrow Cl_2^+ + Cl_2, \ k = 0.8 \times 10^{-15} \ m^3 s^{-1}, \text{(Subramonium, 2003)} \quad (6.7.6.2)$$

$$Cl^+ + Cl_2 \rightarrow Cl_2 + Cl^+, \ k = 5.4 \times 10^{-16} \ m^3 s^{-1}, \text{(Španěl et al., 1993)}. \quad (6.7.6.3)$$

For the charge exchange between Cl atom and Cl^- ion

$$Cl + Cl^- \rightarrow Cl^- + Cl \quad (6.7.6.4)$$

a fit to the cross section calculated by Karmohapatro (1965) has been made. For the reaction

$$Cl_2^+ + Cl \rightarrow Cl + Cl_2^+, \quad (6.7.6.5)$$

the same cross section (Stebbings et al., 1963) as for the (6.4.14.4) oxygen reaction has been assumed, with a modified threshold energy equal to 1.52 eV, which is the difference between the ionization threshold between Cl and Cl_2.

6.7.7 Fragmentation

The cross section for the fragmentation reaction

$$Cl_2^+ + Cl_2 \rightarrow Cl + Cl_2 + Cl^+ \quad (6.7.7.1)$$
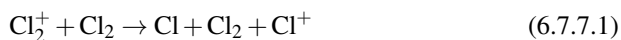
has been assumed to be the same as for the (6.5.3.9) reaction in oxygen (Moran and Roberts, 1968), where the threshold is assumed to be the potential energy required to form the Cl + Cl^+ pair, which is equal to 3.52 eV.

6.7.8 Heavy particle scattering

With regards to chlorine heavy-particles, their scattering has been treated analogous to oxygen. The scattering between Cl_2 molecules

$$Cl_2 + Cl_2 \rightarrow Cl_2 + Cl_2 \quad (6.7.8.1)$$

has been treated as the respective oxygen reaction

$$O_2 + O_2 \rightarrow O_2 + O_2 \quad (6.7.8.2)$$

and the cross section for oxygen measured by Brunetti et al. (1981) has been employed in the calculations. The same applies for the scattering of Cl atoms by Cl_2 molecules

$$Cl + Cl_2 \rightarrow Cl + Cl_2, \quad (6.7.8.3)$$

where the same cross section (Brunetti et al., 1981) as for the oxygen reaction (6.5.1.2) has been used for calculations. The following reaction

$$Cl^- + Cl_2 \rightarrow Cl^- + Cl_2 \qquad (6.7.8.4)$$

is assumed to share the same cross section as the oxygen reaction (6.5.1.4). The remaining three heavy-particle reactions, namely

$$Cl + Cl \rightarrow Cl + Cl \qquad (6.7.8.5)$$

$$Cl_2^+ + Cl_2 \rightarrow Cl_2^+ + Cl_2 \qquad (6.7.8.6)$$

$$Cl^+ + Cl_2 \rightarrow Cl^+ + Cl_2 \qquad (6.7.8.7)$$
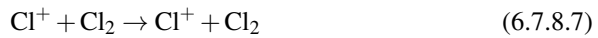
are assumed to have half the cross section of the respective oxygen reactions (Brunetti et al., 1981; Muschlitz, 1959).

7 Summary of papers

Paper I: The role of surface quenching of the singlet delta molecule in a capacitively coupled oxygen discharge

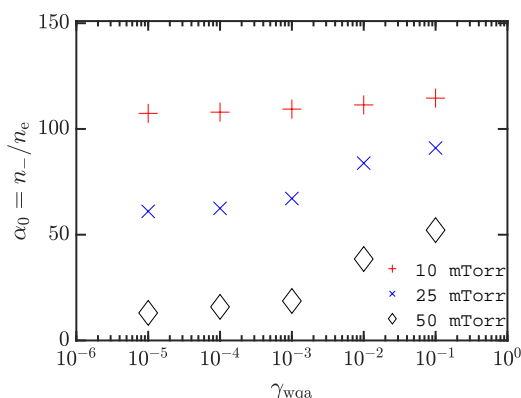*Figure 7.1. The electronegativity in the discharge center as a function of the quenching coefficient of the singlet metastable molecule $O_2(a^1\Delta_g)$ for a parallel plate capacitively coupled oxygen discharge with a gap separation of 4.5 cm driven by a 222 V voltage source at driving frequency of 13.56 MHz.*

The one-dimensional object-oriented particle-in-cell Monte Carlo collision code `oopd1` was applied to explore the evolution of the electron heating mechanism and the EEPF in a capacitively coupled oxygen discharge while the wall quenching probability of the singlet delta metastable molecule $O_2(a^1\Delta_g)$ was varied. It was demonstrated that at low pressure (10 mTorr) the surface quenching coefficient has no influence on the electron heating mechanism. Moreover, at 10 mTorr the electron heating is dominated by drift-ambipolar heating in the plasma bulk and electron cooling is observed in the sheath region. At 25 mTorr the electron heating exhibits a combination of DA-mode and α-mode. Furthermore, the higher is the quenching coefficient, the larger is the contribution of the DA-mode to the electron heating. At 50 mTorr, the discharge operates in α-mode and only for the highest quenching coefficients there is some electron power absorption in the bulk region. Figure 7.1 shows that the surface quenching coefficient of the singlet metastable molecule $O_2(a^1\Delta_g)$ dictates the electronegativity within the discharge and therefore the electron heating mechanism, except at very low operating

131

pressure (10 mTorr). At the higher pressures the higher the surface quenching, the higher is the electronegativity.

Paper II: The influence of secondary electron emission and electron reflection on a capacitively coupled oxygen discharge
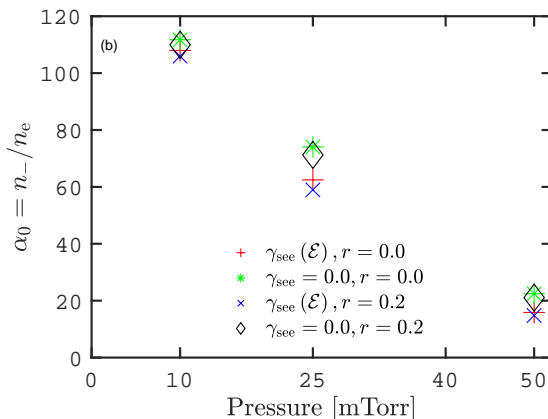

Figure 7.2. The electronegativity in the discharge center as a function of pressure for a parallel plate capacitively coupled oxygen discharge with a surface quenching coefficient for the singlet metastable molecule $O_2(a^1\Delta_g)$ as $\gamma_{wqa} = 0.0001$ and a gap separation of 4.5 cm driven by a 222 V voltage source at a driving frequency of 13.56 MHz

The one-dimensional object-oriented PIC/MCC code `oopd1` was applied to explore the evolution of the EEPF and of the electron heating mechanism in a capacitively coupled oxygen discharge while including and excluding the ion-induced secondary electron emission and electron reflection into the model. We have demonstrated that adding secondary electron emission enhances the EEPF with a high energy tail for all the pressures. At 10 mTorr the EEPF curves outward and no significant difference in the electron heating mechanism is observed including and excluding secondary electron emission from the electrodes due to ion bombardment. At 25 mTorr, the EEPF starts to develop an inward curving behaviour and a hybrid DA- and α-mode heating is observed. At 50 mTorr the EEPF is bi-Maxwellian, while no electron heating is observed in the plasma bulk. Figure 7.2 shows the electronegativity in the discharge center as a function of pressure for all cases studied. We see that at 10 mTorr all four cases are very close to each other, while at 25 mTorr, when secondary electron emission is included, excluding the electron reflection enhances the electronegativity. The same occurred when secondary electron emission was not included. At 50 mTorr the electronegativity is lowest when secondary electron emission is included in the simulation and that electron reflection did not play an important role. On the other hand, the electronegativity is

highest when secondary electron emission and electron reflection is excluded from the simulation.

Paper III: Electron heating mode transitions in a low pressure capacitively coupled oxygen discharge
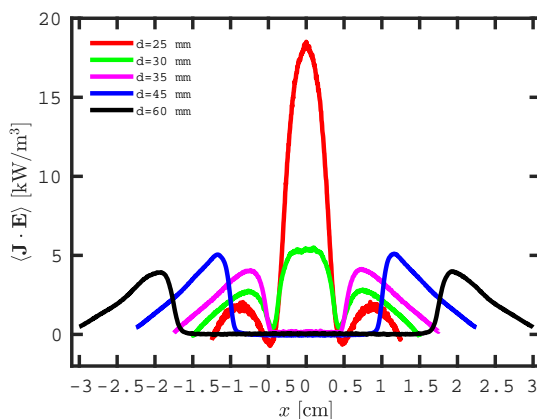

Figure 7.3. The time averaged electron power absorption for a parallel plate capacitively coupled oxygen discharge at 50 mTorr driven by a 400 V voltage source at driving frequency of 13.56 MHz *as the gap separation is varied.*

The one-dimensional object-oriented particle-in-cell Monte Carlo collision code oopd1 was applied to explore the evolution of the electron heating mechanism in a capacitively coupled oxygen discharge, while the pressure and the gap distance are varied. At fixed pressure, while varying the gap distance, we find that at 30 mm the electron heating in the sheath region dominates over the bulk. At 25 mm the electron heating occurs both within the bulk and in the sheath region. For larger gap separation (35, 45 and 60 mm) no heating is observed in the bulk and the discharge operates in pure α-mode. The smaller the discharge gap, the higher the relative contribution of surface quenching of the singlet metastable molecules, which results in lower singlet metastable molecule density and thus lower reaction rate for detachment and therefore higher electronegativity. Figure 7.3 shows the time averaged electron power absorption for different gap distances. At 25 mm the electron heating is almost entirely within the plasma bulk and the discharge is operated in the DA-mode. When the electrode separation is 30 mm a combination of the time averaged electron heating in the plasma bulk and in the sheath region is observed and the discharge operates in both DA-mode and α-mode. For electrode separation 35–60 mm the electron heating is almost solely in the sheath region and the discharge is operated in pure α-mode.

Paper IV: Electron power absorption dynamics in a low pressure radio frequency driven capacitively coupled discharge in oxygen
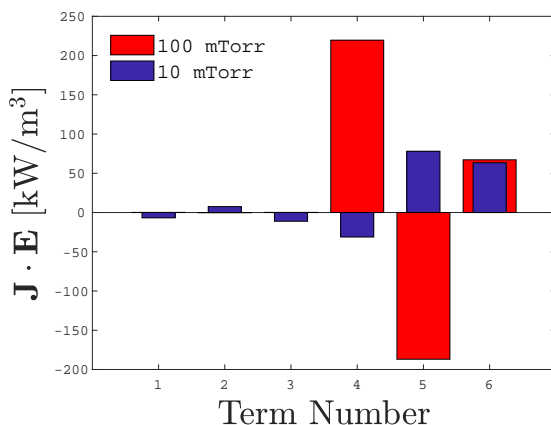

Figure 7.4. The space-time averaged electron power absorption profile terms calculated using the Boltmann equation at 10 mTorr (blue bars) and 100 mTorr (red bars) for a parallel plate capacitively coupled oxygen discharge for 45 mm of gap separation driven by a 400 V voltage source at a driving frequency of 13.56 MHz.

The one-dimensional object-oriented particle-in-cell Monte Carlo collision code `oopd1` was applied to explore the properties of the electric field and the electron power absorption at different time-steps and time averaged over a full rf cycle within the plasma bulk in a capacitively coupled oxygen discharge at both 100 and 10 mTorr for a gap distance of 45 mm. The output from the simulations is analyzed using Boltzmann term analysis. At $t/\tau_{rf} = 0.50$, the main contributions to both the electric field and the electron power absorption come from the pressure gradient related terms and from the Ohmic heating term (Term VI). Figure 7.4 shows the space-time averaged electron power absorption profile terms calculated using the Boltzmann equation at 10 mTorr (blue bars) and 100 mTorr (red bars). We recognize a general pattern where the Ohmic term (pressure term) contribution in the space-time averaged total electron power absorption increases (decreases) when the total pressure decreases (increases). Moreover, we observe that the lower is the pressure, the lower is the contribution of the pressure terms in the absolute value. Finally, we see that each of the two pressure terms flips the sign when the pressure is increased from 10 to 100 mTorr.

Paper V: Electron power absorption dynamics in radio frequency driven capacitively coupled chlorine discharge

Boltzmann term analysis was applied on the output from particle-in-cell Monte Carlo collision simulations in order to explore the origins of the electric field within the electronegative core and electron power absorption mechanism of a capacitively coupled

chlorine discharge operated in the pressure range 1 – 50 Pa, while the driving voltage amplitude is kept fixed. The electron power absorption increases in amplitude and the power absorption to the ions decreases with increased pressure. Figure 7.5 shows the spatio temporal behaviour of the electron power absorption over the full gap length. At the lowest pressure, 1 Pa, the electron power absorption is due to both the pressure and the Ohmic terms. As the pressure is increased above 10 Pa, the Ohmic term becomes dominating and all the other contributions to the electron power absorption become negligible. Therefore, the discharge becomes more of a resistive load as the pressure is increased. Striations become apparent at 25 Pa and are most significant at 35 Pa but their importance decreases with further increase in pressure.
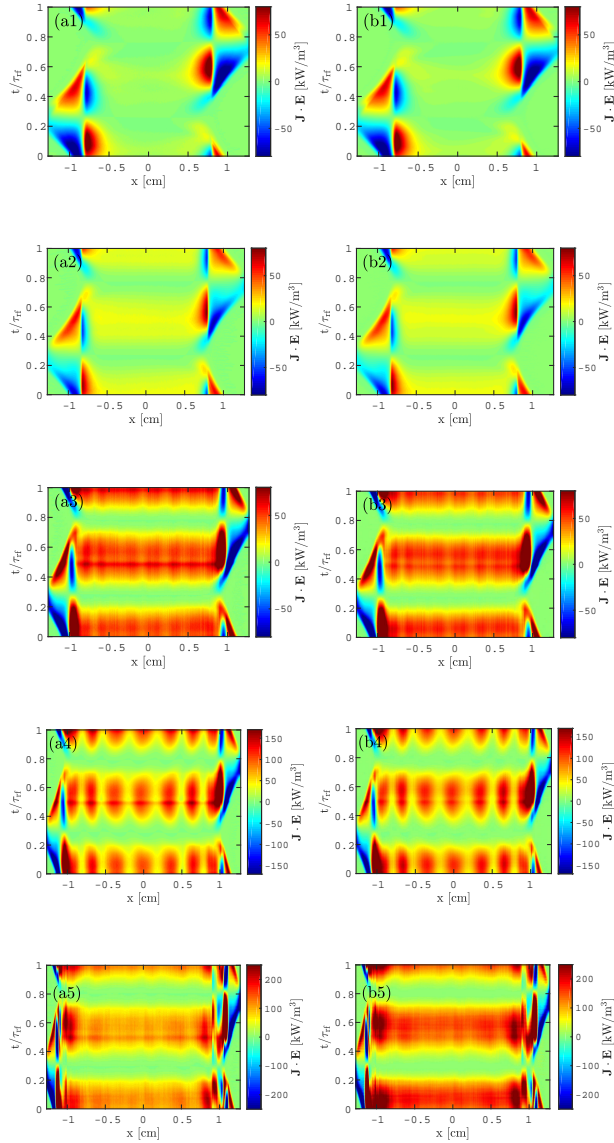
Figure 7.5. The spatio temporal behaviour of the electron power absorption over the full gap length for a parallel plate capacitively coupled chlorine discharge with 25.4 mm gap separation driven by a 222 V voltage source at driving frequency of 13.56 MHz. The left column (a) is the electron power absorption calculated using Eq. (4) in Paper IV and the right column (b) the result from the simulation. The rows represent the various pressures (1) 1 Pa, (2) 10 Pa, (3) 25 Pa, (4) 35 Pa and (5) 50 Pa.

8 Conclusions

In conclusion, the behaviour of capacitively coupled discharges in both oxygen and chlorine was explored via PIC/MCC simulations by tuning different parameters.

For capacitively coupled oxygen discharges, it has been demonstrated that the oxygen metastables dictate the electronegativity and, consequently, the electron power absorption mode. In fact as the overall pressure is increased (decreased), the electron density increases (decreases) and the effective electron temperature decreases (increases). The main source for O^- ion production are the dissociative attachment reactions, while the main source for O^- ion loss are the detachment reactions. At low pressure the effective electron temperature is high and there is efficient creation of O^- ions through dissociative attachment. As the pressure is increased the effective electron temperature decreases along with the creation of O^- ions. This means that the density of singlet metastable molecule $O_2(a^1\Delta_g)$ increases with increased pressure, while the O^- density decreases, along with the electronegativity. Moreover, at low pressure the capacitively coupled oxygen discharge operates in DA-mode and a Druyvesteyn-like EEPF has been observed. On the other hand, at high pressure, the capacitively coupled oxygen discharge operates in pure α-mode and a bi-Maxwellian like EEPF has been observed. In general, the higher is the pressure, the higher is the population of low energy electrons. When the surface quenching coefficient of the metastable $O_2(a^1\Delta_g)$ is increased (decreased), the $O_2(a^1\Delta_g)$ density decreases (increases). When the surface quenching coefficient of the metastable $O_2(a^1\Delta_g)$ is increased (decreased), both the detachment and the dissociative attachment reactions are less (more) efficient. Since at fixed low pressure dissociative attachment dominates over detachment and increasing the surface quenching coefficient means to undermine such a supremacy and the creation of O^- is less efficient. On the other hand, at fixed low pressure, decreasing the surface quenching coefficient leads to a balancing between the O^- creation and loss, leading to a very small change in O^- for the lowest quenching coefficient. At fixed high pressure, detachment dominates over dissociative attachment and increasing the surface quenching coefficient leads to less efficient creation of O^-. On the other hand, at fixed high pressure, decreasing the surface quenching coefficient leads to a more efficient O^- loss. At low pressure (1.33 Pa) the surface quenching coefficient has no influence on the electron heating mechanism and the discharge operates in hybrid DA- α-mode, where the former dominates on the latter. At 3.33 Pa electron heating exhibits a combination of DA-mode and α-mode and, for the highest (lowest) quenching coefficient, the DA-mode becomes more (less) important. At 6.66 Pa the discharge operates in pure α-mode for the lowest quenching coefficients. On the other hand, for the highest quenching coefficient some contribution from DA-mode is observed.

We have also studied how the secondary electron emission and the electron reflection

from the electrodes influence the heating mechanism and the EEPF in capacitively coupled oxygen discharges. We observed that adding secondary electron emission to the model increases the electron density as well as the the population of high energy electrons, at all pressures. On the other hand, adding electron reflection does not lead to any significant change in the EEPF, nor in the electron density. As regards to the time averaged electron power absorption, we have observed that adding secondary electron emission and fixed electron reflection does not lead to any significant change at the lowest pressure (1.33 Pa). On the other hand, at higher pressure (3.33 and 6.66 Pa), adding secondary electron emission and fixed electron reflection leads to an increase (decrease) in the time averaged electron power absorption within the sheath (bulk) region. On the other hand, at the lowest pressure (1.33 Pa) at fixed secondary electron emission yield, adding electron reflection increases the time averaged electron power absorption within the plasma bulk. At 3.33 Pa the situation is opposite and adding electron reflection decreases (increases) the time averaged electron power absorption within the bulk (sheath) region. Finally, at the highest pressure (6.66 Pa), adding electron reflection does not lead to any significant change in the time averaged electron power absortpion.

Then, we have explored the behaviour of a capacitively coupled oxygen discharge when the gap distance is varied at fixed pressure (6.66 Pa). For the shortest gap distance (25 mm), the electron heating occurs both within the bulk and in the sheath region, where the former dominates over the latter. At 30 mm the electron heating in the sheath region dominates over the bulk. For larger gap separation (35, 45 and 60 mm) no heating is observed in the bulk and the discharge operates in pure α-mode. The smaller is the discharge gap, the higher is the relative contribution of surface quenching of the singlet metastable molecules, which results in lower singlet metastable molecule density and thus lower reaction rate for detachment and higher electronegativity. Therefore, the observed transition is related to the high electronegativity and the high electric field within the electronegative core when the electrode separation is small.

We have also explored the the properties of the electric field and the electron power absorption at different time-steps and time averaged over a full rf cycle within the plasma bulk in a capacitively coupled oxygen discharge at 13.33 and 1.33 Pa for a gap distance of 45 mm, by applying the Boltzmann term analysis to the simulation outputs. We have shown that at $t/\tau_{\mathrm{rf}} = 0.50$, the main contributions to both the electric field and the electron power absorption come from the pressure gradient related terms and from the Ohmic heating term. We have recognized a general pattern where the Ohmic term (pressure term) contribution in the space-time averaged total electron power absorption increases (decreases) when the total pressure decreases (increases). Moreover, we have observed that the lower is the pressure, the lower is the contribution of the pressure terms in absolute value. Finally, we have seen that each of the two pressure terms flips the sign when pressure is increased from 1.33 to 13.33 Pa.

Finally, we have explored the properties of the electric field and the electron power absorption at different time-steps and time averaged over a full rf cycle within the plasma bulk in a capacitively coupled chlorine discharge in the pressure range 1 – 50 Pa while the driving voltage amplitude was kept fixed, by applying the Boltzmann term analysis to the simulation outputs. We have found that at 1 Pa the electron power absorption is due to both the pressure and the Ohmic terms. As the pressure is increased above 10

Pa, the Ohmic term becomes dominating and the contributions of all the other terms to the electron power absorption become negligible. Therefore, the discharge becomes more of a resistive load as the pressure is increased. Striations become apparent at 25 Pa and are most significant at 35 Pa but their importance decreases with further increase in pressure.

Paper I

The role of surface quenching of the singlet delta molecule in a capacitively coupled oxygen discharge

A. Proto and J.T. Gudmundsson

The role of surface quenching of the singlet delta molecule in a capacitively coupled oxygen discharge

A Proto[1] and **J T Gudmundsson[1,2]**

[1] Science Institute, University of Iceland, Dunhaga 3, IS-107 Reykjavik, Iceland
[2] Department of Space and Plasma Physics, School of Electrical Engineering and Computer Science, KTH–Royal Institute of Technology, SE-100 44, Stockholm, Sweden

E-mail: tumi@hi.is

Abstract

We use the one-dimensional object-oriented particle-in-cell Monte Carlo collision code `oopd1` to explore the influence of the surface quenching of the singlet delta metastable molecule $O_2(a^1\Delta_g)$ on the electron heating mechanism, and the electron energy probability function (EEPF), in a single frequency capacitively coupled oxygen discharge. When operating at low pressure (10 mTorr) varying the surface quenching coefficient in the range 0.000 01–0.1 has no influence on the electron heating mechanism and electron heating is dominated by drift-ambipolar (DA) heating in the plasma bulk and electron cooling is observed in the sheath regions. As the pressure is increased to 25 mTorr the electron heating becomes a combination of DA-mode and α–mode heating, and the role of the DA-mode decreases with decreasing surface quenching coefficient. At 50 mTorr, electron heating in the sheath region dominates. However, for the highest quenching coefficient there is some contribution from the DA-mode in the plasma bulk, but this contribution decreases to almost zero and pure α–mode electron heating is observed for a surface quenching coefficient of 0.001 or smaller.

Keywords: oxygen discharge, particle-in-cell, surface quenching, electron heating mechanism

1. Introduction

Low pressure radio frequency (rf) driven capacitively coupled plasma (CCP) discharges have been applied in integrated circuit manufacturing for a few decades. Currently the CCPs consist of two parallel electrodes, typically with a radius of a few tens of cm, separated by a few cm, and driven by a radio-frequency power supply. In the capacitively coupled discharges a plasma forms between the electrodes, from which it is separated by space charge sheaths. The energy transport mechanism and particle interactions in the plasma-surface interface region play a significant role in the discharge operation. Atomic species recombine to form molecules and metastable species are quenched on the electrode surfaces. Both of these processes influence the discharge operation and can have determining influence on the electronegativity of the discharge and the electron heating mechanisms and thus on the electron kinetics. In turn the electron kinetics dictate the ionization and dissociation processes that maintain the discharge and create the radicals that are desired for materials processing.

When operated at low pressure the electron heating mechanism in a CCP is referred to as being collisionless and is associated with the electron dynamics in the sheath region, a rapid movement of the electrode sheaths or stochastic electron heating [1, 2]. When the electrons interact with the moving sheaths, they can be either cooled (collapsing sheath) or heated (expanding sheath). Energetic electrons can also bounce back and forth between the two sheaths. When they hit the sheath edge during its expansion phase, energy is transferred to the electrons. This electron heating process is referred to as electron bounce resonance heating (BRH) and can occur for certain combinations of driving frequency and electrode gap [3–7]. The sheath motion and thus the stochastic heating can also be enhanced by self-excited non-linear plasma series resonance (PSR) oscillations [8–11].

141

A Proto and J T Gudmundsson

Collisionless electron heating via sheath oscillations is commonly referred to as the α-mode [12]. When the discharge is operated at high applied voltages and pressures secondary electron emission can contribute to or even dominate the ionization, and the operating mode is then referred to as γ-mode [12]. In electronegative discharges, large electron density gradients can develop within the rf period which can cause the generation of ambipolar fields along with drift fields, that can accelerate the electrons, a heating mechanism referred to as the drift-ambipolar (DA) mode [13, 14].

The oxygen discharge has been applied in plasma materials processing for decades and its applications include processes such as oxidation or anodization of silicon [15–17], ashing of photoresist [18, 19], and surface modification of polymer films [20–22]. The oxygen discharge is weakly electronegative and the electronegativity depends on the control parameters including pressure and power [23]. At low operating pressure the negative O^--ion is the dominant negative ion and it is created almost solely by electron impact dissociative attachment, where the singlet metastables play a significant role [24, 25]. Previously, we have demonstrated how these singlet metastable molecular states influence the electron heating mechanism and thus the electron kinetics in the capacitively coupled oxygen discharge operated at a single frequency of 13.56 MHz [26–29] as well as the ion energy distribution in both single and dual frequency discharges [30]. We have demonstrated that at low pressure (10 mTorr), the electron heating is mainly within the plasma bulk (the electronegative core), and at higher pressures (50–500 mTorr) the electron heating occurs mainly in the sheath region [27, 28]. When operating at low pressure the electron heating within the discharge is due to combined drift-ambipolar-mode (DA-mode) and α-mode and at higher pressures the discharge is operated in the α-mode [31, 32].

Recent fluid model and PIC/MCC simulation studies have indicated that there are significant changes in the electronegativity and the electron heating mechanism as the quenching coefficient for the $O_2(a^1\Delta_g)$ on the electrode surfaces is varied [33–35]. Derzsi *et al* [34], using a PIC/MCC simulation, demonstrate that the $O_2(a^1\Delta_g)$ density decreases exponentially with increasing quenching coefficient γ_{wqa} in the range $10^{-4} \leqslant \gamma_{wqa} \leqslant 5 \times 10^{-2}$. In these PIC/MCC simulation studies [34, 35] the $O_2(a^1\Delta_g)$ density is taken as a fraction of the ground state oxygen molecule $O_2(X^3\Sigma_g^-)$. Similarly, using a 1D fluid model, Greb *et al* [33] demonstrated that the electronegativity depends strongly on the $O_2(a^1\Delta_g)$ surface quenching coefficient and argued that increased quenching coefficient leads to decreased $O_2(a^1\Delta_g)$ density, decreased detachment by the $O_2(a^1\Delta_g)$ state, and thus higher negative ion density. This is due to the very effective annihilation of the O^--ions in the plasma bulk via detachment by the singlet metastable molecules $O_2(a^1\Delta_g)$. More recently Gibson and Gans [36] explored the particle dynamics in an oxygen CCP while keeping the $O_2(a^1\Delta_g)$ as either 16% or 0.5% of the ground state density, to create a weekly and highly, electronegative oxygen discharge, respectively. Using a 1D fluid model they demonstrated that oxygen discharges can operate in distinctly different modes dependent upon the

$O_2(a^1\Delta_g)$ density within the discharge. Less is known about the role of the quenching of $O_2(b^1\Sigma_g^+)$ on the electrodes.

Here we study how the surface quenching coefficients for the singlet metastable molecules $O_2(a^1\Delta_g)$ influence the electron heating processes, the electron energy probability function (EEPF), the effective electron temperature, in the single frequency voltage driven capacitively coupled oxygen discharge by means of numerical simulation, for a fixed discharge voltage, while the discharge pressure is varied from 10 to 50 mTorr. The simulation parameters and the cases explored are defined in section 2, where we give an overview of the known surface quenching coefficients for the singlet metastable molecules on various surfaces and determine the partial pressures of the neutral background species using a global model. The results of the PIC/MCC simulations, the various electron heating modes observed for the various combinations of surface quenching coefficients and operating pressures, are discussed in section 3. Finally, concluding remarks are given in section 4.

2. The simulation

The one-dimensional object-oriented particle-in-cell Monte Carlo collision (PIC/MCC) code oopd1 [37, 38] is applied to a capacitively coupled oxygen discharge. In 1d-3v PIC codes, like oopd1, the model system has one spatial dimension and three velocity components. In our earlier work, we added oxygen atoms in the ground state $O(^3P)$ and ions of the oxygen atom O^+ and the relevant reactions to the oopd1discharge model [39]. Later we added the singlet metastable molecule $O_2(a^1\Delta_g)$, the metastable oxygen atom $O(^1D)$ [26], and the singlet metastable molecule $O_2(b^1\Sigma_g^+)$ [28], along with energy dependent secondary electron emission coefficients for oxygen ions and neutrals as they bombard the electrodes [28]. For this current work the discharge model contains nine species: electrons, the ground state neutrals $O(^3P)$ and $O_2(X^3\Sigma_g^-)$, the negative ions O^-, the positive ions O^+ and O_2^+, and the metastables $O(^1D)$, $O_2(a^1\Delta_g)$ and $O_2(b^1\Sigma_g^+)$. The full oxygen reaction set and the cross sections used have been discussed in our earlier works and will not be repeated here [26, 28, 39]. However, as the role of the singlet metastable oxygen molecule $O_2(a^1\Delta_g)$ is being explored two important reactions are mentioned here (see further discussion in [26]). It is known from global model studies [24] that dissociative attachment of the oxygen molecule is almost the sole source of O^--ions in the discharge and the metastable oxygen molecules play a major role. In particular dissociative attachment from the metastable oxygen molecule $O_2(a^1\Delta_g)$ can be the dominant path for the creation of negative ion O^- through

$$e + O_2(a^1\Delta_g) \longrightarrow \begin{cases} O(^3P) + O^- \\ O(^1D) + O^- \end{cases}$$
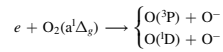
Lower pressure, and thus higher effective electron temperature, promotes the creation of the negative ion O^-. The metastable molecule $O_2(a^1\Delta_g)$ also contributes significantly to the loss of

A Proto and J T Gudmundsson

the negative ion O^--ion through the detachment process

$$O^- + O_2(a^1\Delta_g) \longrightarrow \text{products}$$
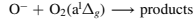
while detachment by the oxygen molecule in the ground state is negligible. Here we use the rate coefficient measured at 400 K of 1.5×10^{-16} m^3/s by Midey *et al* [40] to estimate the cross section by assuming a Maxwellian velocity distribution of the particles. The cross section is allowed to fall as $1/\sqrt{\mathcal{E}}$ to 184 meV and then take a fixed value of 5.75×10^{-20} m^2. Also we assume that the detachment by the metastable molecule $O_2(a^1\Delta_g)$ leads to the formation of $O(^3P) + O_2(X^3\Sigma_g^-) + e$, instead of $O_3 + e$ and $O + O_2^-$. Increased discharge pressure thus promotes the loss of the negative ion O^-.

We assume a symmetric capacitively coupled discharge where one of the electrodes is driven by an rf voltage

$$V(t) = V_0 \sin(2\pi f t) \tag{1}$$

while the other is grounded. Here V_0 is the voltage amplitude, f the driving frequency, and t is the time. For this current study we assume the discharge to be operated with voltage amplitude of $V_0 = 222$ V with an electrode separation of 4.5 cm and a capacitor of 1 F in series with the voltage source, while the surface quenching coefficient for the singlet delta metastable $O_2(a^1\Delta_g)$ and discharge pressure is varied. These are the same parameters as assumed in our earlier work using oopd1 [26, 28, 29, 32, 39] and by Lichtenberg *et al* [41] using the xpdp1 code. The discharge electrode separation is assumed to be small compared to the electrode diameter so that the discharge can be treated as one dimensional. We assume 10.25 cm diameter electrodes in order to determine the absorbed power and set the discharge volume for the global model calculations, discussed in section 2.3. The time step Δt and the grid spacing Δx resolve the electron plasma frequency and the electron Debye length of the low-energy electrons, respectively, according to $\omega_{pe} \Delta t < 0.2$, where ω_{pe} is the electron plasma frequency, and the simulation grid is uniform and consists of 1000 cells. The electron time step is 3.68×10^{-11} s. The simulation was run for 5.5×10^6 time steps or 2750 rf cycles. It takes roughly 1700 rf cycles to reach equilibrium for all particles and the time averaged plasma parameters shown, such as the densities, the electron heating rate, and the effective electron temperature, are averages over 1000 rf cycles. All particle interactions are treated by the Monte Carlo method with a null-collision scheme [42]. For the heavy particles we use a sub-cycling and the heavy particles are advanced every 16 electron time steps and we assume that the initial density profiles are parabolic [43].

The kinetics of the charged particles (electrons, O_2^+-ions, O^+-ions and O^--ions) was followed for all energies. Since the neutral gas density is much higher than the densities of charged species, the neutral species at thermal energies (below a certain cut-off energy) are treated as a background with fixed density and temperature and maintained uniformly in space. These neutral background species are assumed to have a Maxwellian velocity distribution at the gas temperature (here $T_n = 26$ mV). The kinetics of the neutrals are followed when their energy exceeds a preset energy threshold

Table 1. The parameters of the simulation, the particle weight, and the energy threshold above which dynamics of the neutral particles are followed.

Species	particle weight	energy threshold [meV]
$O_2(X^3\Sigma_g^-)$	5×10^7	500
$O_2(a^1\Delta_g)$	5×10^6	100
$O_2(b^1\Sigma_g)$	5×10^6	100
$O(^3P)$	5×10^7	500
$O(^1D)$	5×10^7	50
O_2^+	10^7	–
O^+	10^6	–
O^-	5×10^7	–
e	1×10^7	–

value. The energy threshold values used here for the various neutral species are listed in table 1. Due to recombination of atomic oxygen and quenching of metastable atoms and molecules on the electrode surfaces there is a drop in the high energy (energy above the threshold value) atomic oxygen density and increase in the high energy oxygen molecule densities next to the electrodes as shown in our earlier work [28]. Thus assuming uniformity of the background gas is thus somewhat unrealistic.

The ratio of the number of physical particles to computational particles, the particle weight, is also listed in table 1 for all the neutral species. Note that in oopd1 the particles can have different weights [44, 45] and the collisions among particles with different weights is implemented in oopd1 following the method suggested by Miller and Combi [46].

In our earlier studies we have used fixed partial pressure for each of the neutral species as we have varied the pressure [27], the driving voltage amplitude [31], and the driving frequency [32]. Here we take a different approach and calculate the partial pressure for each combination of pressure and surface quenching coefficient using a global (volume averaged) model as discussed in section 2.3. The two electrodes are assumed to be identical, and the surface coefficients, surface recombination and surface quenching, are kept the same at both electrodes. We neglect the reflection of electrons from the electrodes.

2.1. Wall recombination coefficients

As a neutral species hits the electrode it returns as a thermal particle with a given probability and atoms can recombine to form a thermal molecule with the given probability. The wall recombination coefficient for the neutral atoms in ground state $O(^3P)$ is taken to be 0.5 as measured by Booth and Sadeghi [47] for a pure oxygen discharge in a stainless steel reactor at 2 mTorr. As the oxygen atom $O(^3P)$ hits the electrode we assume that half of the atoms are reflected as $O(^3P)$ at room temperature and the other half recombines to form the

3

143

A Proto and J T Gudmundsson

Table 2. Overeiw of the measured wall quenching coefficients for the singlet metastables $O_2(a^1\Delta_g)$ and $O_2(b^1\Sigma_g)$ that can be found in the literature. All of the values listed were measured at room temperature.

Surface	$O_2(a^1\Delta_g)$ γ_{wqa}	References	$O_2(b^1\Sigma_g)$ γ_{wqb}	References
Pyrex	$(3.1 \pm 0.2) \times 10^{-5}$	[54]	2×10^{-3}	[55]
	1.3×10^{-5}	[56]	2.2×10^{-3}	[57]
	2.1×10^{-5}	[58]	1×10^{-2}	[59]
	4.3×10^{-5}	[60]		
Teflon	$<10^{-3}$	[49]	4.5×10^{-3}	[55]
Fe	7×10^{-3}	[49]		
	4.4×10^{-3}	[61]		
Cu	1.4×10^{-2}	[49]	1.0×10^{-2}	[55]
	8.5×10^{-4}	[61]		
	2.9×10^{-4}	[54]		
	$1.15 - 1.43 \times 10^{-3}$	[48]		
Ni	2.7×10^{-3}	[61]	2.6×10^{-2}	[55]
	1.1×10^{-2}	[49]		
	$(3.1 \pm 0.2) \times 10^{-4}$	[54]		
	$0.6 - 1.0 \times 10^{-3}$	[48]		
Monel (Cu/Ni)	$(2.8 \pm 0.2) \times 10^{-4}$	[54]		
	1.2×10^{-2}	[49]		
Al	$<10^{-3}$	[49]		
	5.9×10^{-5}	[61]		
Pt	1×10^{-2}	[49]		
	4.0×10^{-4}	[61]		
Ti	6.5×10^{-5}	[61]		
	$<10^{-3}$	[49]		
Ag	1.1×10^{-2}	[61]		
Si	7.3×10^{-4}	[61]		
Graphite	3×10^{-3}	[49]		

ground state oxygen molecule $O_2(X^3\Sigma_g^-)$ at room temperature. Note that this is a rough assumption as it is known that the wall recombination coefficient drops significantly with increased pressure [24]. This could lead to underestimation of the atomic oxygen density. However, the atomic oxygen density is low and is expected to decrease with increased pressure so this is not expected to have a significant influence on the results reported here. Similarly, as the metastable atom $O(^1D)$ hits the electrode we assume that half of the atoms are quenched to form $O(^3P)$ and the other half recombines to form the ground state oxygen molecule $O_2(X^3\Sigma_g^-)$ at room temperature.

2.2. Wall quenching coefficients

It is difficult to determine an actual value for the surface quenching coefficients of the singlet metastables on the electrode surfaces either experimentally or theoretically. In general we would expect that the quenching probability for any excited species hitting the electrodes to depend not only on the species itself, but also on the surface material, the surface temperature, and the actual surface condition, such as surface roughness and contamination, which can vary substantially. Indeed it has been pointed out by Du *et al* [48] that the quenching probability of $O_2(a^1\Delta_g)$ increases with both the duration of the exposure to and the concentration of $O_2(a^1\Delta_g)$. The values for the measured wall quenching

coefficient, found in the literature, for $O_2(a^1\Delta_g)$ and $O_2(b^1\Sigma_g^+)$ on various surfaces are listed in table 2. All of the values listed in table 2 were measured at room temperature. We note that the listed values span a few orders of magnitude and depend on the surface material. Furthermore, we note that the measured values also vary by orders of magnitude for the same materials. We also note that the quenching probability for $O_2(b^1\Sigma_g^+)$ is in general significantly higher than for $O_2(a^1\Delta_g)$. In our earlier studies [25, 27–29, 32] we have used a quenching coefficients for the singlet metastable $O_2(a^1\Delta_g)$ on the electrode surface of $\gamma_{wqa} = 0.007$, estimated by Sharpless and Slanger for iron [49]. As the measured wall quenching probability for $O_2(a^1\Delta_g)$ on aluminum is lower than for iron as seen in table 2, we would expect that aluminum electrodes would therefore lead to higher singlet metastable densities and lower electronegativity. In these studies we assumed the quenching coefficient for $O_2(b^1\Sigma_g^+)$ to be $\gamma_{wqb} = 0.1$, an assumed value, based on the suggestion that the quenching coefficient for the $b^1\Sigma_g^+$ state is about two orders of magnitude larger than for the $a^1\Delta_g$ state [50]. We will use this value for the surface quenching coefficient of $O_2(b^1\Sigma_g^+)$ in this current study. We are aware that this may be overestimation based on the values listed in table 2. We have seen in global model studies that wall quenching can be the main loss mechanism for the singlet metastable state $O_2(b^1\Sigma_g^+)$ [25]. Gordiets *et al* [51] and Kutasi *et al* [52] use

wall quenching coefficient for $O_2(a^1\Delta_g)$ of 2×10^{-5} and for $O_2(b^1\Sigma_g^+)$ of 2×10^{-2} for a quartz tube in their models of flowing N_2/O_2 dc glow discharge and Ar/O_2 surface-wave microwave discharge, respectively. By comparing the 1D fluid simulations to phase and space resolved optical emission (PROES) measurements Greb *et al* [53] determine the wall quenching coefficient for $O_2(a^1\Delta_g)$ to be 1×10^{-5} for stainless steel and 3×10^{-3} for teflon. A comparison of PIC/MCC simulation with experimental findings using PROES for a CCP with aluminum electrodes and electrode spacing of 2.5 cm suggests a wall quenching coefficient of 0.006 [35]. Due to the fact that the measured surface quenching coefficients for $O_2(a^1\Delta_g)$ vary a few orders of magnitude from roughly 10^{-5} to a few times 10^{-2} we allow the surface quenching coefficients for $O_2(a^1\Delta_g)$ to vary in the range 0.000 01–0.1 as we explore the how it influences the electron heating processes. The lowest value of 0.000 01 corresponds to pyrex or aluminum and values of 0.01 correspond to Pt or Ag electrodes.

2.3. Global model–partial pressures

To determine the partial pressures of the background thermal neutral species we applied a global (volume averaged) model of the oxygen discharge. The global model used is discussed in detail by Thorsteinsson and Gudmundsson [62] but 32 additional reactions have been added to improve the treatment of $O_2(b^1\Sigma_g^+)$, O_3, and O_2^- [63], and in order to make the oxygen reaction set as detailed as the one discussed by Toneli *et al* [25]. We explored the partial pressures at 10, 25 and 50 mTorr and the total absorbed power was found to be 1.8 W after iteration between the oopd1 simulations and the global model. We assume a cylindrical discharge of diameter 10.25 cm and length 4.5 cm. We vary the surface quenching coefficient for the singlet metastable molecule $O_2(a^1\Delta_g)$ in the range $\gamma_{wqa} = 0.000 01 - 0.1$ while the surface quenching coefficient for the singlet metastable molecule $O_2(b^1\Sigma_g)$ is kept constant $\gamma_{wqb} = 0.1$. The fractional densities found by the global model calculations involving the neutrals $O_2(X^3\Sigma_g^-)$, $O(^3P)$, $O_2(a^1\Delta_g)$ and $O_2(b^1\Sigma_g)$ are listed in table 3. These values are used as input for the simulation in the particle-in-cell Monte Carlo collision (PIC/MCC) code oopd1 as the partial pressure of the neutral background gas. Note that not all the neutrals considered in the global model calculations are shown in the table. We see that the partial pressure of the singlet metastable molecule $O_2(a^1\Delta_g)$ increases with decreasing surface quenching coefficient and takes its highest value at 25 mTorr for the lowest surface quenching coefficient. The partial pressure of $O_2(b^1\Sigma_g)$ is always much smaller, maybe due to too large surface quenching coefficient.
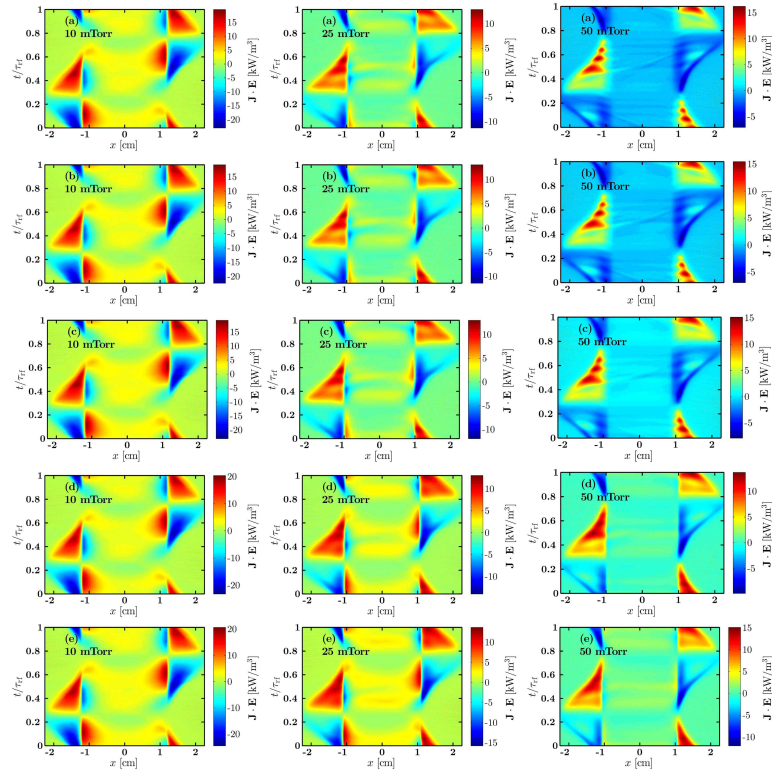
3. Results and discussion

Figures 1 show the spatio temporal behaviour of the electron power absorption as the surface quenching coefficient for the singlet metastable molecule $O_2(a^1\Delta_g)$ is varied in the range 0.000 01–0.1, for pressures of 10 mTorr (left column),

Table 3. The partial pressures of the thermal neutrals at 10, 25 and 50 mTorr for different wall quenching coefficients of the singlet metastable molecule $O_2(a^1\Delta_g)$ calculated by a global (volume averaged) model.

| γ_{wqa}	$O_2(X^3\Sigma_g^-)$	$O_2(a^1\Delta_g)$	$O_2(b^1\Sigma_g)$	$O(^3P)$
10 mTorr				
10^{-1}	0.992 6	0.002 2	0.001 5	0.001 5
10^{-2}	0.982 5	0.012 4	0.001 6	0.000 9
10^{-3}	0.971 7	0.024 0	0.001 8	0.000 7
10^{-4}	0.968 4	0.026 5	0.001 8	0.001 5
10^{-5}	0.968 1	0.026 8	0.001 8	0.001 5
25 mTorr				
10^{-1}	0.991 8	0.001 8	0.001 2	0.000 6
10^{-2}	0.984 7	0.010 5	0.001 5	0.000 7
10^{-3}	0.966 7	0.029 0	0.001 9	0.000 7
10^{-4}	0.960 7	0.035 0	0.001 9	0.000 7
10^{-5}	0.960 0	0.035 7	0.002 0	0.000 7
50 mTorr				
10^{-1}	0.989 5	0.001 3	0.001	0.000 3
10^{-2}	0.988 3	0.005 4	0.001 5	0.000 4
10^{-3}	0.979 1	0.016 1	0.002 0	0.000 4
10^{-4}	0.973 9	0.021 5	0.002 2	0.000 4
10^{-5}	0.973 2	0.022 3	0.002 2	0.000 4

25 mTorr (center column) and 50 mTorr (right column). The electron power absorption is calculated as $\mathbf{J}_e \cdot \mathbf{E}$, where $\mathbf{J}_e$ and $\mathbf{E}$ are the spatially and temporally varying electron current density and electric field, respectively. For each of the figures the abscissa covers the whole inter-electrode gap, from the powered electrode on the left hand side to the grounded electrode on the right hand side. Similarly the ordinate covers the full rf cycle. As displayed in figure 1 left column, for low pressure (10 mTorr), the change in the quenching coefficient γ_{wqa} does not alter the heating mechanism, which is a combination of a drift ambipolar (DA) heating in the bulk plasma and stochastic heating due to the sheath oscillation (α-mode). As the operating pressure is raised to 25 mTorr (see figure 1 center column) varying the quenching coefficients clearly has an influence on the heating mechanism. For a high quenching coefficient the electron heating is a combination of DA- and α-mode, as seen in figure 1 center column (e), similar to what is seen at 10 mTorr independent of the quenching coefficient (figure 1 left column (a)–(e)). As the quenching coefficient is lowered the bulk heating decreases and stochastic heating in the sheath region becomes more prominent, as seen in figures 1 center column (d)–(a). At 50 mTorr we still see some bulk heating for the highest quenching coefficients (figures 1 right column (e)–(d)) but for low quenching coefficients there is no electron heating observed in the plasma bulk (figures 1 right column (c)–(a)) and pure $\alpha-$ mode is observed. Figure 2 shows the time averaged electron heating profile between the electrodes $\langle \mathbf{J}_e \cdot \mathbf{E} \rangle$. We see in figure 2 (a) that at 10 mTorr almost all the electron heating occurs in the plasma bulk (the electronegative core) and the electron heating profile is almost independent of the surface quenching

Figure 1. The spatio-temporal behaviour of the electron power absorption at 10 mTorr (left column), 25 mTorr (center column) and 50 mTorr (right column) for surface quenching coefficient for the singlet metastable molecule $O_2(a^1\Delta_g)$ as (a) $\gamma_{wqa} = 0.000\,01$, (b) $\gamma_{wqa} = 0.000\,1$, (c) $\gamma_{wqa} = 0.001$, (d) $\gamma_{wqa} = 0.01$ and (e) $\gamma_{wqa} = 0.1$ for a parallel plate capacitively coupled oxygen discharge with electrode separation of 4.5 cm driven by a 222 V voltage source at driving frequency of 13.56 MHz.
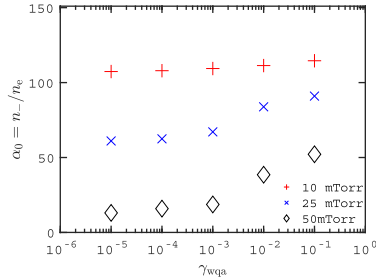
coefficient for the singlet metastable molecule $O_2(a^1\Delta_g)$. In the sheath regions the time averaged $\langle \mathbf{J}_e \cdot \mathbf{E} \rangle$ value indicates electron cooling. This can occur in the sheath regions as the DA-heating in the bulk maintains the discharge. At 25 mTorr for high surface quenching coefficient the electron heating in the plasma bulk region dominates as seen in figure 2(b). As the surface quenching coefficient for the singlet metastable molecule $O_2(a^1\Delta_g)$ decreases the electron heating in the bulk region decreases and the heating in the sheath regions increases. For surface quenching coefficient in the range

0.001–0.000 01 the time averaged heating profile remains roughly the same, electron heating occurs both in the bulk and in the sheath regions, and a combination of DA- and $\alpha-$ mode is observed. When operating at 50 mTorr electron heating in the sheath region dominates as seen in figure 2(c). Only for the highest surface quenching coefficients 0.1 and 0.01 there is some electron heating observed in the bulk region. For surface quenching coefficients <0.001 there is almost no electron heating in the bulk region at 50 mTorr. Furthermore, at the higher pressures 25 mTorr and 50 mTorr,
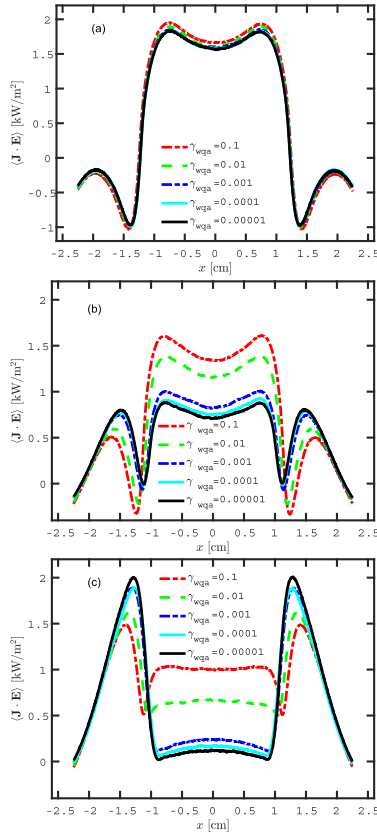
6

146

Figure 2. The time averaged electron heating profile for a parallel plate capacitively coupled oxygen discharge at (a) 10 mTorr, (b) 25 mTorr, and (c) 50 mTorr, with a gap separation of 4.5 cm driven by a 222 V voltage source at driving frequency of 13.56 MHz.

the more the quenching coefficient is raised, the more the power absorbtion in the bulk is increased. Also, when the power absorbtion in the bulk increases, the power absorbtion in the sheath regions decreases. High frequency oscillations in the electron power absorption density adjacent to the expanding sheath edge are seen at 25 and 50 mTorr and become more clear as the pressure is increased and the surface

Figure 3. The electronegativity in the discharge center (α_0) as a function of the quenching coefficient of the singlet metastable molecule $O_2(a^1\Delta_g)$ for a parallel plate capacitively coupled oxygen discharge with a gap separation of 4.5 cm driven by a 222 V voltage source at driving frequency of 13.56 MHz.

quenching coefficient is decreased. These oscillations are a beam-plasma instability at the electron plasma frequency, due to an electron-electron two-stream instability between the bulk electrons and electrons accelerated by the moving sheath [11, 64].

In order to explore the observed transition further, we plot the time averaged center electronegativity as a function of the surface quenching coefficient for the singlet metastable molecule $O_2(a^1\Delta_g)$ in figure 3. At 10 mTorr the discharge is the most electronegative and the least electronegative at 50 mTorr. At 10 mTorr the electronegativity does not vary much when the surface quenching coefficient is varied. The electronegativity is high, in the range 107–114, as the surface quenching coefficient is decreased from 0.1 to 0.000 01. At 25 and 50 mTorr an increase in the electronegativity is observed with increasing surface quenching coefficient. At 25 mTorr the electronegativity increases from 61 to 90, and at 50 mTorr the electronegativity increases from 13 to 52 as the surface quenching coefficient is increased. This is related to the fact that, when the surface quenching coefficient is increased, the number of singlet delta metastable molecules $O_2(a^1\Delta_g)$ decreases, the negative ion density increases, and the electronegativity increases. This also means, as has been pointed out by others [33–35], that the surface quenching coefficient dictates the electronegativity of the oxygen discharge. We note that the electronegativity in this current study is somewhat larger than we have reported in our earlier works [28, 32], particularly at the higher pressures. This is due to the fact that the density of the singlet metastable molecule $O_2(a^1\Delta_g)$ is somewhat lower in this current study and the density of the the singlet metastable molecule $O_2(b^1\Sigma_g)$ is significantly lower than assumed in the earlier studies. These are the results of the improved global model calculations as discussed in section 2.3. A few measurements of the electronegativity in capacitively coupled oxygen discharges have been reported. Berezhnoj *et al* [65] report a value of around 10 in a symmetric capacitively coupled oxygen discharge

A Proto and J T Gudmundsson

with stainless steel electrodes operated at 45 mTorr with electrode spacing of 6 cm. At 50 mTorr we find electronegativity of 13 for $\gamma_{wqa} = 10^{-5}$ and 18.7 for $\gamma_{wqa} = 10^{-3}$. Similarly, Katsch *et al* [66] estimated the electronegativity in the discharge center of a capacitively coupled oxygen discharge, with aluminum electrodes with 2.54 cm separation, to be roughly 2 at 103 mTorr and 150 V and to fall below unity at 280 V. We would expect the electronegativity to decrease for aluminum electrodes and higher pressure. For higher pressures Küllig *et al* [67] reported electronegativity of 5–6 at 225 mTorr in an asymmetric capacitively coupled discharge with stainless steel electrodes and Kaga *et al* [68] measured center electronegativity of 7.4–11.6 at 100 mTorr and 10.8–18.6 at 500 mTorr with aluminum electrodes with spacing of 6 cm.

The time averaged electron density profile is shown in figure 4. The center electron density at 10 mTorr is 8.6×10^{13} m^{-3} and is roughly independent of the surface quenching coefficient as seen in figure 4(a). The electron density profile is flat within the plasma bulk with a peak close to the sheath edge. At 25 mTorr the center electron density is 1.25×10^{14} m^{-3} for $\gamma_{wqa} = 0.1$ and increases slightly with decreasing quenching coefficient or to 1.57×10^{14} m^{-3} for $\gamma_{wqa} = 0.000\,01$. The electron density profile is flat within the plasma bulk and an increase in the density is observed close to the sheath edge. At 50 mTorr the electron density is 2.4×10^{14} m^{-3} for $\gamma_{wqa} = 0.1$ and increases with decreasing quenching coefficient to 7.7×10^{14} m^{-3} for $\gamma_{wqa} = 0.000\,01$. The electron density profile is flat within the plasma bulk and here no increase (or a peak) is observed at the sheath edge. Kechkar *et al* [69] explored experimentally slightly asymmetric capacitively couple oxygen discarge operated at 13.56 MHz, and report electron density in the range 10^{15}–7×10^{16} m^{-3} for a discharge operated at 100 mTorr while the power is varied in the range 30–600 W. When operating low power of 30 W, in what they refer to as the $\alpha-$ mode, the electron density is in the range 6×10^{14}–1.6×10^{15} m^{-3}, increasing with increasing pressure from 10–50 mTorr. These values measured at low power of 30 W and in the pressure range 10–50 mTorr are very similar to the simulated electron density values reported here. Also Katsch *et al* [66] report eletron density of 3×10^{14} m^{-3} at 150 V and 1.4×10^{15} at 280 V when operating oxygen discharge at 100 mTorr and Berezhnoj *et al* [65] report electron density of 1.1×10^{14} m^{-3} in a symmetric capacitively coupled oxygen discharge with stainless steel electrodes operated at 45 mTorr with electrode spacing of 6 cm, and current density of $J = 0.31$ mA cm^{-2}.

Figure 5 shows the electric field profile in the plasma bulk for the various quenching coefficients at a fixed time slice $t/\tau_{rf} = 0.5$. Note that these curves are not time averaged. At 10 mTorr there is a strong electric field gardient in the bulk region and the electric field strength and profile is independent of the surface quenching coefficient as seen in figure 5(a). The electric field is almost flat and takes its lowest absolute value in the center of the electronegative core, while it assumes strong values as the sheath region is approached. The shape of the electric field profile is similar to the one predicted by the simple model of Schulze *et al* [13]. The resulting electric field is a
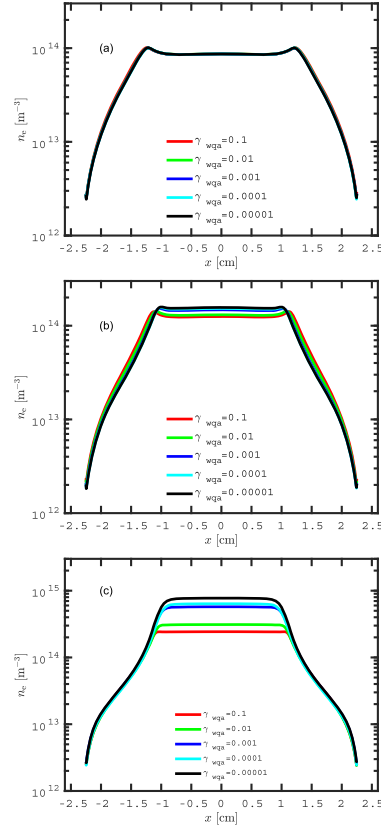
Figure 4. The electron density profile for a parallel plate capacitively coupled oxygen discharge at (a) 10 mTorr, (b) 25 mTorr, and (c) 50 mTorr, with a gap separation of 4.5 cm driven by a 222 V voltage source at driving frequency of 13.56 MHz.

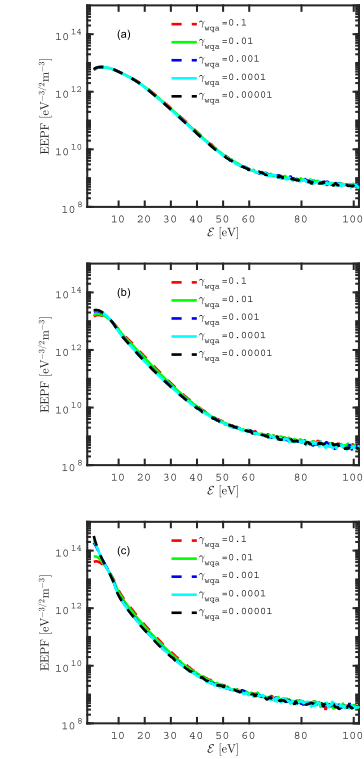combination of a drift field and an ambipolar field. The drift electric field is due to low bulk conductivity or low electron density. We have seen in figure 4 that the electron density is very low indeed. The peak in the electric field at the sheath edge is mainly caused by a local maximum of the electron density at the sheath edge and the corresponding high value of $\partial n_e/\partial x$ on
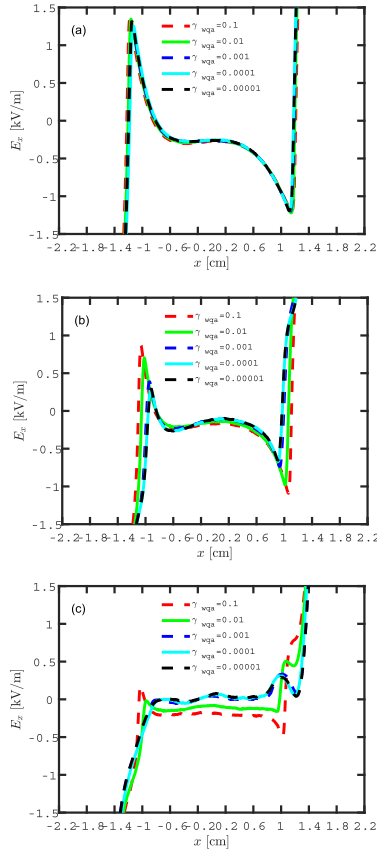
Figure 5. The electric field $t/\tau_{rf} = 0.5$ in the bulk region for a parallel plate capacitively coupled oxygen discharge at (a) 10 mTorr, (b) 25 mTorr, and (c) 50 mTorr with a gap separation of 4.5 cm driven by a 222 V voltage source at driving frequency of 13.56 MHz.

Figure 6. The electron energy probability function (EEPF) in the discharge center for a parallel plate capacitively coupled oxygen discharge at (a) 10 mTorr, (b) 25 mTorr, and (c) 50 mTorr with a gap separation of 4.5 cm driven by a 222 V voltage source at driving frequencies of 13.56 MHz.

the plasma bulk side of this maximum. At this location diffusion directs the electrons into the plasma bulk, while positive ions flow continuously toward the electrode. This generates an ambipolar field, that couples electron and positive ion motion and accelerates electrons towards the electrode. At 25 mTorr

and 50 mTorr (figures 5(b) and (c)) important changes are observed. For both the pressures considered, the higher the quenching coefficient, the higher is the electric field peak in the sheath region. There is clearly a transition from DA-α-mode to $\alpha-$ mode when increasing the operating pressure from 25 mTorr to 50 mTorr. At 50 mTorr and low quenching coefficient the electric field is flat and no peaks are observed on the plasma bulk side of the sheath edge. Transitions between the DA-mode and the α-mode have been demonstrated by both simulations and experiments on CF$_4$ discharges [13, 70] where

by increasing the operating pressure at a fixed applied voltage, a transition from the α-mode to the DA-mode is induced. Note that the CF$_4$ discharge is weakly electronegative at 75 mTorr while it is strongly electronegative at 600 mTorr [14]. Also by increasing the voltage at a fixed pressure, a transition from the DA-mode to the α-mode is observed in a CF$_4$ discharge [13]. Oxygen behaves in the opposite way, by increasing the pressure at a given voltage a transition from the DA-α-mode to the α-mode is observed in the oxygen discharge [31]. This is a similar to the transition reported by Derzsi *et al* [35] which observe an operation mode transition from DA-α-mode to α-mode in an oxygen discharge as harmonics are added to the voltage waveforms for 10 and 15 MHz driving frequency, which also coincides with a strong decrease in the electronegativity.

The evolution of the electron energy probability function (EEPF) in the discharge center with surface quenching coefficient γ_{wqa} is shown in figure 6. At the lower pressures 10 mTorr and 25 mTorr (figures 6(a) and (b)) the EEPF curves outward for every quenching coefficient value. This is due to the significant contribution of the DA-mode to the bulk electron heating as clearly seen in figures 2(a) and (b) for 10 and 25 mTorr, respecitvely. At the higher pressure of 50 mTorr the EEPF still curves outward for the highest quenching coefficients (as there is DA-heating present) but it transitions to curve inward (bi-Maxwellian) for the lowest quenching coefficients. The bi-Maxwellian shape of the EEPF in CCPs is commonly associated with predominant sheath heating (α-mode). The low energy electron population represents electrons confined in the bulk plasma by an ambipolar potential, which are only weakly heated by the rf field, while the high energy population participates in the sheath heating. So the population of low energy electrons is high, as the bulk heating mechanism is weak. At 50 mTorr the electon probability function shows the highest value for low surface quenching, i.e. it has transitioned to become a bi-Maxwellian, that is when the sheath heating mechanism predominates, as was seen in figure 1 right column (a)–(c), where the bulk heating is almost absent.

4. Conclusion

The one-dimensional object-oriented particle-in-cell Monte Carlo collision code oopd1 was applied to explore the evolution of the electron heating mechanism and the EEPF in a capacitively coupled oxygen discharge while the wall quenching probability of the single metastable molecule O$_2$(a$^1\Delta_g$) is varied. We find that at low pressure (10 mTorr) the surface quenching coefficient has no influence on the electron heating mechanism and electron heating is dominated by drift-ambipolar heating in the plasma bulk and electron cooling is observed in the sheath region. At 25 mTorr the electron heating exhibits a combination of DA-mode and $\alpha-$ mode. For the highest quenching coefficient the DA-mode dominates, but the role of the DA-mode decreases with decreasing quenching coefficient. At the highest pressure explored, 50 mTorr, electron heating in the sheath region dominates. However, for the highest quenching coefficient there is some contribution from the DA-mode in the

plasma bulk, but this contribution decreases to almost zero, and thus a pure $\alpha-$ mode is observed for quenching coefficient of 0.001 or smaller. We have demonstrated that the surface quenching coefficient of the singlet metastable molecule O$_2$(a$^1\Delta_g$), and thus the electrode material, more or less dictates the electronegativity within the discharge and the electron heating mechanism, except at very low operating pressure ($\sim$10 mTorr). However, the quenching coefficients, even for the most common electrodes, are not very well known.

ORCID iDs

A Proto ⬤ https://orcid.org/0000-0003-2288-935X
J T Gudmundsson ⬤ https://orcid.org/0000-0002-8153-3209

References

[1] Lieberman M A and Godyak V 1998 *IEEE Trans. Plasma Sci.* **26** 955
[2] Gozadinos G, Vender D, Turner M M and Lieberman M A 2001 *Plasma Sources Sci. Technol.* **10** 117
[3] Wood B P 1991 *PhD Thesis* University of California, Berkeley
[4] Wood B P, Lieberman M A and Lichtenberg A J 1995 *IEEE Trans. Plasma Sci.* **23** 89
[5] Liu Y-X, Zhang Q-Z, Jiang W, Hou L-J, Jiang X-Z, Lu W-Q and Wang Y-N 2011 *Phys. Rev. Lett.* **107** 055002
[6] Liu Y-X, Zhang Q-Z, Liu J, Song Y-H, Bogaerts A and Wang Y-N 2012 *Appl. Phys. Lett.* **101** 114101
[7] Wilczek S, Trieschmann J, Schulze J, Schüngel E, Brinkmann R P, Derzsi A, Korolov I, Donkó Z and Mussenbrock T 2015 *Plasma Sources Sci. Technol.* **24** 024002
[8] Czarnetzki U, Mussenbrock T and Brinkmann R 2006 *Phys. Plasmas* **13** 123503
[9] Donkó Z, Schulze J, Czarnetzki U and Luggenhölscher D 2009 *Appl. Phys. Lett.* **94** 131501
[10] Schüngel E, Brandt S, Donkó Z, Korolov I, Derzsi A and Schulze J 2015 *Plasma Sources Sci. Technol.* **24** 044009
[11] Wilczek S *et al* 2016 *Phys. Plasmas* **23** 063514
[12] Belenguer P and Boeuf J 1990 *Phys. Rev.* A **41** 4447
[13] Schulze J, Derzsi A, Dittmann K, Hemke T, Meichsner J and Donkó Z 2011 *Phys. Rev. Lett.* **107** 275001
[14] Derzsi A, Schüngel E, Donkó Z and Schulze J 2015 *Open Chemistry* **13** 346
[15] Pulfrey D L, Hathorn F G M and Young L 1973 *J. Electrochem. Soc.* **120** 1529
[16] Kawai Y, Konishi N, Watanabe J and Ohmi T 1994 *Appl. Phys. Lett.* **64** 2223
[17] Hess D W 1999 *IBM J. Res. Dev.* **43** 127

A Proto and J T Gudmundsson

[18] Tolliver D L 1984 (*VLSI Electronics: Microstructure Science* vol 8) ed N G Einspruch and D M Brown (Orlando, FL: Academic) pp 1–24
[19] Hartney M A, Hess D W and Soane D S 1989 *J. Vac. Sci. Technol.* B **7** 1
[20] Vesel A and Mozetic M 2012 *Vacuum* **86** 634
[21] Chashmejahanbin M R, Salimi A and Ershad Langroudi A 2014 *Int. J. Adhes. Adhes.* **49** 44
[22] Vesel A and Mozetic M 2017 *J. Phys. D: Appl. Phys.* **50** 293001
[23] Gudmundsson J T, Kouznetsov I G, Patel K K and Lieberman M A 2001 *J. Phys. D: Appl. Phys.* **34** 1100
[24] Gudmundsson J T and Thorsteinsson E G 2007 *Plasma Sources Sci. Technol.* **16** 399
[25] Toneli D A, Pessoa R S, Roberto M and Gudmundsson J T 2015 *J. Phys. D: Appl. Phys.* **48** 325202
[26] Gudmundsson J T and Lieberman M A 2015 *Plasma Sources Sci. Technol.* **24** 035016
[27] Gudmundsson J T and Ventéjou B 2015 *J. Appl. Phys.* **118** 153302
[28] Hannesdottir H and Gudmundsson J T 2016 *Plasma Sources Sci. Technol.* **25** 055002
[29] Gudmundsson J T and Hannesdottir H 2017 *AIP Conf. Proc.* **1811** 120001
[30] Hannesdottir H and Gudmundsson J T 2017 *J. Phys. D: Appl. Phys.* **50** 175201
[31] Gudmundsson J T and Snorrason D I 2017 *J. Appl. Phys.* **122** 193302
[32] Gudmundsson J T, Snorrason D I and Hannesdottir H 2018 *Plasma Sources Sci. Technol.* **27** 025009
[33] Greb A, Gibson A R, Niemi K, O'Connell D and Gans T 2015 *Plasma Sources Sci. Technol.* **24** 044003
[34] Derzsi A, Lafleur T, Booth J-P, Korolov I and Donkó Z 2016 *Plasma Sources Sci. Technol.* **25** 015004
[35] Derzsi A, Bruneau B, Gibson A, Johnson E, O'Connell D, Gans T, Booth J-P and Donkó Z 2017 *Plasma Sources Sci. Technol.* **26** 034002
[36] Gibson A R and Gans T 2017 *Plasma Sources Sci. Technol.* **26** 115007
[37] Hammel J and Verboncoeur J P 2003 *Bull. Am. Phys. Soc.* **48** 66
[38] Verboncoeur J P, Langdon A B and Gladd N T 1995 *Comput. Phys. Commun.* **87** 199
[39] Gudmundsson J T, Kawamura E and Lieberman M A 2013 *Plasma Sources Sci. Technol.* **22** 035011
[40] Midey A, Dotan I and Viggiano A A 2008 *J. Phys. Chem. A* **113** 3040
[41] Lichtenberg A J, Vahedi V, Lieberman M A and Rognlien T 1994 *J. Appl. Phys.* **75** 2339
[42] Birdsall C 1991 *IEEE Trans. Plasma Sci.* **19** 65
[43] Kawamura E, Birdsall C K and Vahedi V 2000 *Plasma Sources Sci. Technol.* **9** 413
[44] Nguyen C 2006 *Master's Thesis* University of California, Berkeley
[45] Lim C-H 2007 *PhD Thesis* University of California, Berkeley
[46] Miller R H and Combi M R 1994 *Geophys. Res. Lett.* **21** 1735
[47] Booth J P and Sadeghi N 1991 *J. Appl. Phys.* **70** 611
[48] Du S, Leng J, Yang H, Sha G and Zhang C 2011 *Chin. J. Chem. Phys.* **24** 256
[49] Sharpless R L and Slanger T G 1989 *J. Chem. Phys.* **91** 7947
[50] O'Brien R J and Myers G H 1970 *J. Chem. Phys.* **53** 3832
[51] Gordiets B, Ferreira C, Guerra V, Loureiro J, Nahorny J, Pagnon D, Touzeau M and Vialle M 1995 *IEEE Trans. Plasma Sci.* **23** 750
[52] Kutasi K, Guerra V and Sá P 2010 *J. Phys. D: Appl. Phys.* **43** 175201
[53] Greb A, Niemi K, O'Connell D and Gans T 2013 *Appl. Phys. Lett.* **103** 244101
[54] Crannage R P, Dorko E A, Johnson D E and Whitefield P D 1993 *Chem. Phys.* **169** 267
[55] Perram G, Determan D, Dorian J, Lowe B and Thompson T L 1992 *Chem. Phys.* **162** 427
[56] Steer R P, Ackerman R A and Pitts J N 1969 *J. Chem. Phys.* **51** 843
[57] Arnold S J and Ogryzlo E A 1967 *Can. J. Phys.* **45** 2053
[58] Clark I D and Wayne R P 1969 *Chem. Phys. Lett.* **3** 93
[59] Izod T P J and Wayne R P 1968 *Proc. of the Royal Society of London. Series A, Mathematical and Physical Sciences* **308** 81
[60] Leiss A, Schurath U, Becker K H and Fink E H 1978 *J. Photochem.* **8** 211
[61] Ryskin M E and Shub B R 1981 *React. Kinet. Catal. Lett.* **17** 41
[62] Thorsteinsson E G and Gudmundsson J T 2010 *Plasma Sources Sci.Technol.* **19** 055008
[63] Jonsson R D B 2018 *BS project, University of Iceland, Reykjavik* http://hdl.handle.net/1946/29537
[64] O'Connell D, Gans T, Vendera D, Czarnetzki U and Boswell R 2007 *Phys. Plasmas* **14** 034505
[65] Berezhnoj S V, Shin C B, Buddemeier U and Kaganovich I 2000 *Appl. Phys. Lett.* **77** 800
[66] Katsch H M, Sturm T, Quandt E and Döbele H F 2000 *Plasma Sources Sci. Technol.* **9** 323
[67] Küllig C, Dittmann K and Meichsner J 2010 *Plasma Sources Sci. Technol.* **19** 065011
[68] Kaga K, Kimura T and Ohe K 2001 *Japan. J. Appl. Phys.* **40** 330
[69] Kechkar S, Swift P, Kelly S, Kumar S, Daniels S and Turner M 2017 *Plasma Sources Sci. Technol.* **25** 065009
[70] Liu G-H, Liu Y-X, Wen D-Q and Wang Y-N 2015 *Plasma Sources Sci. Technol.* **24** 034006

151

Paper II

The Influence of Secondary Electron Emission and Electron Reflection on a Capacitively Coupled Oxygen Discharge

A. Proto and J.T. Gudmundsson

Atoms, **6**(4) (2018) 65.

The Influence of Secondary Electron Emission and Electron Reflection on a Capacitively Coupled Oxygen Discharge

Andrea Proto [1] and **Jon Tomas Gudmundsson** [1,2,*]

[1]   Science Institute, University of Iceland, Dunhaga 3, IS-107 Reykjavik, Iceland; proto.andrea@yahoo.com
[2]   Department of Space and Plasma Physics, School of Electrical Engineering and Computer Science,
      KTH Royal Institute of Technology, SE-100 44 Stockholm, Sweden
*   Correspondence: tumi@hi.is; Tel.: +354-525-4946

Abstract: The one-dimensional object-oriented particle-in-cell Monte Carlo collision code oopd1 is applied to explore the role of secondary electron emission and electron reflection on the properties of the capacitively-coupled oxygen discharge. At low pressure (10 mTorr), drift-ambipolar heating of the electrons dominates within the plasma bulk, while at higher pressure (50 mTorr), stochastic electron heating in the sheath region dominates. Electron reflection has negligible influence on the electron energy probability function and only a slight influence on the electron heating profile and electron density. Including ion-induced secondary electron emission in the discharge model introduces a high energy tail to the electron energy probability function, enhances the electron density, lowers the electronegativity, and increases the effective electron temperature in the plasma bulk.

Keywords: capacitively-coupled discharge; oxygen; particle-in-cell/Monte Carlo collision; electron heating; secondary electron emission

1. Introduction

Low pressure radio frequency (rf)-driven capacitively-coupled discharges have a range of material processing applications such as plasma etching and plasma enhanced chemical vapor deposition within the microelectronics industry. These discharges have been explored extensively over the past few decades. However, a few issues remain to be fully understood, including the electron heating mechanism, in particular when driven by multiple frequencies [1], and the role of surfaces regarding recombination and quenching of various species and phenomena such as secondary electron emission and electron reflection [2,3]. The modern capacitively-coupled discharge consists of two parallel electrodes separated by a few cm and is driven by a radio-frequency power generator. The plasma forms when rf voltage is applied between the electrodes. The electrons that gain enough energy from the resulting electric field produce positive ions, negative ions, and electrons through electron impact ionization of neutral atoms and molecules and electron impact dissociative attachment of molecules, which forms the plasma. The plasma is separated from the electrodes by space charge sheaths. Multiple frequencies are commonly applied in order to achieve separate control of ion flux and ion energy, as the ion flux dictates the throughput of the process and the ion energy determines the etching and deposition parameters on the wafer surface.

The particle-in-cell (PIC) method, when combined with Monte Carlo (MC) treatment of collision processes, is a self-consistent kinetic approach that has become a predominant numerical approach to investigate the properties of the low pressure capacitively-coupled discharge. This approach is commonly referred to as particle-in-cell Monte Carlo collision (PIC/MCC) method. The basic idea of the PIC method is to allow typically a few hundred thousand computer-simulated particles (superparticles) to represent a significantly higher number of real particles (density in the range of 10^{14}–10^{18} m^{-3}) [4–6]. In a PIC simulation, the motion of each particle is simulated and the various macro-quantities are calculated from the position and velocity of these particles. The particle interaction is handled through a macro-force acting on the particles, which is calculated from the field equations at points on a computational grid. This method allows us to follow the spatio-temporal evolution of the various plasma parameters such as particle density, particle energy, particle fluxes, and particle heating rates.

The kinetics of the capacitively-coupled oxygen discharge have been studied for over two decades starting with the seminal work of Vahedi and Surendra [7] using the 1D xpdp1 PIC/MCC code. Since then, a number of PIC/MCC studies have been reported on oxygen and Ar/O$_2$ discharges using the xpdx1 series of codes, in both symmetrical and asymmetrical geometry, performed over a range of pressures and compared to experimental findings [8] and to analytical density profiles [9], showing good agreement, to explore the formation of the ion energy distribution function in an O$_2$/Ar mixture in an asymmetric capacitively-coupled discharge [10], and the influence of the secondary electron emission on the density profiles and the electron energy distribution function (EEDF) [11]. Other 1D PIC/MCC codes have been developed to explore the oxygen discharge. A 1D PIC/MCC model developed in Greifswald, that includes the metastable oxygen molecule O$_2(a^1\Delta_g)$ as a fraction of the ground state molecule, was used to determine the ion energy distribution function (IEDF) in oxygen CCP [12,13]. Furthermore, they found by comparison with experiments that one sixth of the oxygen molecules are in the metastable singlet delta. A 1D PIC/MCC code, developed in Dalian [14,15], was applied to explore the electrical asymmetry effect in a dual-frequency capacitively-coupled oxygen discharge. Similar to Bronold et al. [12], this work assumed a constant density for the singlet metastable molecule O$_2(a^1\Delta_g)$. More recently, a 1D PIC/MCC code that was developed in Budapest was used to explore the heating mechanism in a capacitively-coupled oxygen discharge driven by tailored waveforms (composed of N harmonics in addition to a fundamental frequency f_1) [16,17]. Furthermore, a PIC/MCC fluid hybrid model was applied to explore the electron power absorption and the influence of pressure on the energetics and particle densities [18,19]. In all of these works, only electrons, the positive ion O$_2^+$, and the negative ion O$^-$ were treated kinetically, and the positive ion O$^+$ was neglected. Furthermore, none of the metastable states were treated kinetically. The one-dimensional object-oriented plasma device one (oopd1) code allows having the simulated particles of different weights, which allows for tracking both charged and neutral particles in the simulation. Earlier, we benchmarked the basic reaction set for the oxygen discharge in oopd1 to the xpdp1 code [20].

In recent years, the oxygen reaction set in the oopd1 code was improved significantly [20–22]. Using this improved discharge model, we showed that the singlet metastable molecular states have a significant influence on the electron heating mechanism in the capacitively-coupled oxygen discharge [21–24] as well as the ion energy distribution [25]. We demonstrated that, when operating at low pressure (10 mTorr), the electron heating is mainly located within the plasma bulk (the electronegative core), while, when operating at higher pressures (50–500 mTorr), the electron heating appears almost solely within the sheath regions [22,23]. Furthermore, when operating at low pressure, the electron heating within the discharge is due to a hybrid drift-ambipolar-mode (DA-mode) and α-mode, and while operating at higher pressures, the discharge is operated in a pure α-mode [26,27]. We have also shown that detachment by the singlet molecular metastable states is the process that has the most influence on the electron heating process in the higher pressure regime, while it has almost negligible influence at lower pressures [22–24].

Secondary electron emission and electron reflection from the electrodes have often been neglected in PIC/MCC simulations. When it is included, it is common to assume the secondary electron emission to have a constant value (independent of the discharge conditions such as the energy of the bombarding ions), while only the ion-induced secondary electron emission is taken into account, and thus, the contributions of other species are neglected [2,3]. The effects of including a constant secondary electron emission yield are increased electron density, enhancement of the density profiles and the electron energy distribution functions (EEDFs), decreased sheath width, and the electron heating rate profiles changing significantly in both argon [28] and oxygen [11] discharges. Furthermore, it has been demonstrated that an asymmetry can be introduced by having electrodes with different secondary electron emission properties in a capacitively-coupled discharge [29], which was later extended to also include the electrical asymmetry effect in a dual-frequency capacitively-coupled discharge driven by two consecutive harmonics with different electrode materials [30]. In these studies, the secondary electron emission yield was set to be a constant. A few recent studies have emphasized using realistic secondary electron emission yields for both fast neutrals and ions bombarding the electrodes [2,3,22,28,31–33].

In an earlier study, we explored the role of including an energy-dependent secondary electron emission yield for both O^+ and O_2^+-ions and O and O_2 neutrals in an oxygen discharge [22]. We noted that this had a significant influence on the discharge properties, including increased electron and ion densities and decreased sheath width. Here, we study systematically how the secondary electron emission and the electron reflection from the electrodes influence the charged particle profiles, the electron heating processes, the electron energy probability function (EEPF), and the effective electron temperature, in a single frequency voltage-driven capacitively-coupled oxygen discharge by means of numerical simulation, for a fixed discharge voltage, while the discharge pressure is varied from 10–50 mTorr. The simulation parameters and the cases explored are defined in Section 2, and the simulation results found by including and excluding the ion-induced secondary electron emission and electron reflection are compared in Section 3. We give a summary and concluding remarks in Section 4.

2. The Simulation

The one-dimensional (1d-3v) object-oriented particle-in-cell Monte Carlo collision (PIC/MCC) code oopd1 [34,35] is herein applied to a capacitively-coupled oxygen discharge. The oopd1 code, like the well-known xpdp1 code [7], is a general plasma device simulation tool capable of simulating various types of plasmas, including breakdown, accelerators, beams, as well as processing discharges [20].

The oxygen reaction set included in the oopd1 code is rather extensive. Like xpdp1, it includes the ground state oxygen molecule $O_2(X^3\Sigma_g^-)$, the negative ion O^-, the positive ion O_2^+, and electrons [7,20]. In addition, oxygen atoms in the ground state $O(^3P)$ and ions of the oxygen atom O^+ [20], the singlet metastable molecule $O_2(a^1\Delta_g)$, and the metastable oxygen atom $O(^1D)$ [21], and the singlet metastable molecule $O_2(b^1\Sigma_g^+)$ [22] were added along with the relevant reactions and cross-sections. The full oxygen reaction set was discussed in our earlier works where the cross-sections used were also given [20–22]. Furthermore, oopd1 has energy-dependent secondary electron emission coefficients for oxygen ions and neutrals as they bombard both clean and dirty metal electrodes [22]. Thus, for this current work, the discharge model contains nine species: electrons, the ground state neutrals $O(^3P)$ and $O_2(X^3\Sigma_g^-)$, the negative ions O^-, the positive ions O^+ and O_2^+, and the metastables $O(^1D)$, $O_2(a^1\Delta_g)$, and $O_2(b^1\Sigma_g^+)$. We herein use the secondary electron emission yield for a dirty surface as given in our earlier work [22].

We assume a geometrically-symmetric capacitively-coupled discharge where one of the electrodes is driven by an rf voltage at a single frequency:

$$V(t) = V_0 \sin(2\pi f t) \tag{1}$$

while the other electrode is grounded. Here, V_0 is the voltage amplitude, f the driving frequency, and t the time. The discharge operating parameters assumed are the voltage amplitude of $V_0 = 222$ V, an electrode separation of 4.5 cm, and a capacitor of 1 F connected in series with the voltage source. The driving frequency is assumed to be 13.56 MHz. These are the parameters used in our earlier works using oopd1 [20–22,24,27] and in the work of Lichtenberg et al. [9] using the xpdp1 code. The discharge electrode separation is assumed to be small compared to the electrode diameter so that the discharge can be treated as one dimensional. We assume the electrode diameter to be 10.25 cm, which is needed in order to determine the absorbed power, and set the discharge volume for the global model calculations applied to determine the partial pressure of the neutral species. The time step Δt and the grid spacing Δx are set to resolve the electron plasma frequency and the electron Debye length of the low-energy electrons, respectively, according to $\omega_{pe}\Delta t < 0.2$, where ω_{pe} is the electron plasma frequency, and the simulation grid is taken to be uniform and consists of 1000 cells. The electron time step is set to 3.68×10^{-11} s. The simulation was run for 5.5×10^6 time steps, which corresponds to 2750 rf cycles. It takes roughly 1700 rf cycles to reach equilibrium for all particles, and the time averaged plasma parameters shown, such as the densities, the electron heating rate, and the effective electron temperature, are averages over 1000 rf cycles. All particle interactions are treated by the Monte Carlo method with a null-collision scheme [4]. For the heavy particles, we use sub-cycling, and the heavy particles are advanced every 16 electron time steps [36]. Furthermore, we assume that the initial density profiles are parabolic [36].

The kinetics of the charged particles (electrons, O_2^+-ions, O^+-ions, and O^--ions) was followed for all energies. Since the neutral gas density is much higher than the densities of charged species, the neutral species at thermal energies (below a certain cut-off energy) are treated as a background with fixed density and temperature and maintained uniformly in space. These neutral background species are assumed to have a Maxwellian velocity distribution at the gas temperature (here, $T_n = 26$ mV). The kinetics of the neutrals are followed when their energy exceeds a preset energy threshold value. The energy threshold values and the particle weights used here for the various neutral species included in the simulation are listed in Table 1. The partial pressures of the background thermal neutral species were calculated using a global (volume averaged) model of the oxygen discharge, as discussed in Proto and Gudmundsson [37]. The fractional densities for the neutrals $O_2(X^3\Sigma_g^-)$, $O(^3P)$, $O_2(a^1\Delta_g)$, and $O_2(b^1\Sigma_g)$, estimated using the global model calculations at 10, 25, and 50 mTorr, are listed in Table 2. These values are used as input for the PIC/MCC simulation as the partial pressures of the neutral background gas. Note that not all the neutrals considered in the global model calculations are shown in Table 2. Due to recombination of atomic oxygen and quenching of metastable atoms and molecules on the electrode surfaces, discussed below, there is a drop in the high energy (energy above the threshold value) atomic oxygen density and an increase in the high energy oxygen molecule densities next to the electrodes, as shown in our earlier work [22]. Thus, assuming uniformity of the background gas is thus somewhat an unrealistic assumption.

Table 1. The parameters of the simulation, the particle weight, and the energy threshold above which kinetics of the neutral particles are followed.

Species	Particle Weight	Energy Threshold (meV)
$O_2(X^3\Sigma_g^-)$	5×10^7	500
$O_2(a^1\Delta_g)$	5×10^6	100
$O_2(b^1\Sigma_g)$	5×10^6	100
$O(^3P)$	5×10^7	500
$O(^1D)$	5×10^7	50
O_2^+	10^7	-
O^+	10^6	-
O^-	5×10^7	-
e	1×10^7	-

The electrode surfaces have significant influence on the discharge properties. There are a few parameters regarding the surface interaction of the neutral species that have to be set in the discharge model. For a neutral species that hits the electrode, we assume it returns as a thermal particle with a given probability. Similarly atoms can recombine on the electrode surfaces to form a thermal molecule with a given probability. As the oxygen atom O(^{3}P) hits the electrode, we assume that half of the atoms are reflected as O(^{3}P) at room temperature, and the other half recombines to form the ground state oxygen molecule O$_2$(X$^3\Sigma_g^-$) at room temperature. Thus, for a neutral oxygen atom in the ground state O(^{3}P), we use a wall recombination coefficient of 0.5, as measured by Booth and Sadeghi [38], for a pure oxygen discharge in a stainless steel reactor at 2 mTorr. Similarly, as the metastable oxygen atom O(^{1}D) hits the electrode, we assume that half of the atoms are quenched to form O(^{3}P) and that the other half recombines to form the ground state oxygen molecule O$_2$(X$^3\Sigma_g^-$) at room temperature. For the surface quenching coefficients of the singlet metastables molecules on the electrode surfaces, we assume for the singlet metastable O$_2$(a$^1\Delta_g$) a value of $\gamma_{wqa} = 0.0001$, and for the singlet metastable O$_2$(b$^1\Sigma_g^+$), we assume a value of $\gamma_{wqb} = 0.1$, based on the suggestion by O'Brien and Myers [39] that the surface quenching coefficient for the b$^1\Sigma_g^+$ state is significantly larger than for the a$^1\Delta_g$ state. We explored the influence of the surface quenching coefficients of the singlet metastable molecule O$_2$(a$^1\Delta_g$) on the discharge properties in an earlier work [37]. There, we demonstrated that the influence of γ_{wqa} on the discharge properties and the electron heating mechanism can be significant indeed. The partial pressures listed in Table 2 were calculated by a global model using these surface quenching and recombination parameters as discussed in our earlier study [37].

Table 2. The partial pressures of the thermal neutrals at 10, 25, and 50 mTorr for the wall quenching coefficient for the singlet metastable molecule O$_2$(a$^1\Delta_g$) of $\gamma_{wqa} = 0.0001$ calculated by a global (volume averaged) model.

Pressure	O$_2$(X$^3\Sigma_g^-$)	O$_2$(a$^1\Delta_g$)	O$_2$(b$^1\Sigma_g^+$)	O(^{3}P)
10 mTorr	0.9684	0.0265	0.0018	0.0015
25 mTorr	0.9607	0.0350	0.0019	0.0007
50 mTorr	0.9739	0.0215	0.0022	0.0004

In the simulations, we either neglect electron reflection from the electrode or assume that electrons are reflected from the electrodes with a probability of 0.2, which is the number of elastically-reflected electrons per incoming electron, independent of their energy and angle of incidence. This value is based on the summary of values presented by Kollath [40] for various materials. This value has been used by others in PIC/MCC simulations of capacitively-coupled discharges [2,3]. However, in reality, the reflection of electrons is known to depend on the electrode material, incident electron energy and the angle of incidence [40,41]. Furthermore, for all the cases explored here, we neglect secondary electron emission due to electron impact of the electrodes. The four cases explored for each pressure are listed in Table 3.

Table 3. The four cases explored for each pressure.

| Case	γ_{see}	Electron Reflection
1	$\gamma_{see}(\mathcal{E})$ [22]	none
2	$\gamma_{see}(\mathcal{E})$ [22]	20%
3	$\gamma_{see} = 0.0$	none
4	$\gamma_{see} = 0.0$	20%

3. Results and Discussion

The choice of the surface quenching coefficient for the singlet metastable $O_2(a^1\Delta_g)$ of γ_{wqa} = 0.0001 was based on our earlier study of the time averaged electron heating profile between the electrodes $\langle \mathbf{J}_e \cdot \mathbf{E} \rangle$ [37]. In this study, we found that at 10 mTorr, almost all the electron heating occurred within the plasma bulk (the electronegative core), and the electron heating profile was almost independent of the surface quenching coefficient for the singlet metastable molecule $O_2(a^1\Delta_g)$, while the DA-heating mode dominated the time averaged electron heating over one rf cycle. At 25 mTorr, the time averaged electron heating occurred both in the bulk (the electronegative core) and in the sheath regions, and a hybrid DA- and α-mode heating was observed. When operating at 50 mTorr, electron heating in the sheath region dominated, and the discharge was operated in a pure α-mode. Thus, this choice of pressure values and $\gamma_{wqa} = 0.0001$ gave us three distinct operating regimes to analyze further.

The electron energy probability function (EEPF) in the discharge center is shown in Figure 1, for the various combinations of pressures, including and excluding secondary electron emission and electron reflection from the electrodes, for a total of four cases for each pressure, as shown in Table 3. Figure 1a shows the electron probability function (EEPF) at 10 mTorr. At low electron energy, the EEPF curved outwards, and a high energy tail was apparent when secondary electron emission was excluded from the simulation. We see that adding secondary electron emission to the discharge model enhanced the EEPF. When including the ion-induced energy-dependent secondary electron emission yield, more electrons were created at the electrodes, which were subsequently accelerated to the plasma bulk across the sheath. Thus, more high energy electrons were created in the discharge, and the EEPF exhibits a high energy tail when secondary electrons were emitted from the electrodes. This high energy tail extended up to roughly 240 eV. At 10 mTorr, both cases (including and excluding electron reflection) including secondary electron emission overlapped, and both cases (including and excluding electron reflection) neglecting the secondary electron emission overlapped. Thus, including electron reflection from the electrodes had negligible effects on the EEPF. Figure 1b shows the EEPF at 25 mTorr. We see that the shape changed for all four cases as the pressure increased. The electron reflection had a negligible effect on the EEPF. This can be seen from the overlap of the green dashed line on the black one, when secondary electron emission was excluded, and from the overlap of the red line on the blue one, where secondary electron emission was included. Furthermore, an overall reduction of the high energy part of the curve, compared to the 10 mTorr case, was observed when secondary electron emission was neglected. This means that, when the pressure was raised and the secondary electron emission was neglected, there were fewer hot electrons within the bulk. Figure 1c shows the EEPF at 50 mTorr. Here, the transition, which already started at 25 mTorr, was fully accomplished and the shape of the EEPF now curved inwards or was bi-Maxwellian for all four cases. As before including secondary electron emission led to a high energy tail. Furthermore, now, the black dashed line with the green one and the blue dashed line with the red one overlapped almost perfectly, which indicates that the electron reflection from the electrodes had negligible effects.

Figure 2 shows the profile of the time averaged power absorption by the electrons over an rf cycle $\langle \mathbf{J}_e \cdot \mathbf{E} \rangle$. A predominance of the electron heating within plasma bulk was observed in all four cases at 10 mTorr. We see that, when including the ion-induced secondary electron emission, the difference between including and excluding the electron reflection at the electrodes was very small within the plasma bulk. The same occurred when the secondary electron emission was excluded. A maximum in the power absorption in the bulk and a minimum in the sheath region were observed when the secondary electron emission was excluded and the electron reflection was included in the simulation (black line in Figure 2a). On the contrary, a maximum in the power absorption in the sheath edge and a minimum in the bulk were seen when the secondary electron emission was included and the electron reflection was excluded (red line in Figure 2a). At the transition pressure of 25 mTorr, the situation was drastically changed. A combination of the electron heating in the plasma bulk and in the sheath region was observed in all four cases. Indeed Figure 2b shows that there was a maximum in the power

absorption in the bulk and a minimum in the sheath edge when both secondary electron emission and electron reflection were excluded (green line in Figure 2b), while a minimum in the bulk and a maximum in the sheath edge were observed when the secondary electron emission and the electron reflection were included (blue line in Figure 2b). At 50 mTorr, the transition was fully accomplished and the electron heating was almost solely in the sheath region or stochastic electron heating. This is clearly seen in Figure 2c when averaged over the rf cycle. Indeed, the electron reflection did not play much of a role. The maximum in the power absorption was observed when secondary electron emission was included in the simulation and the sheath was slightly narrower.
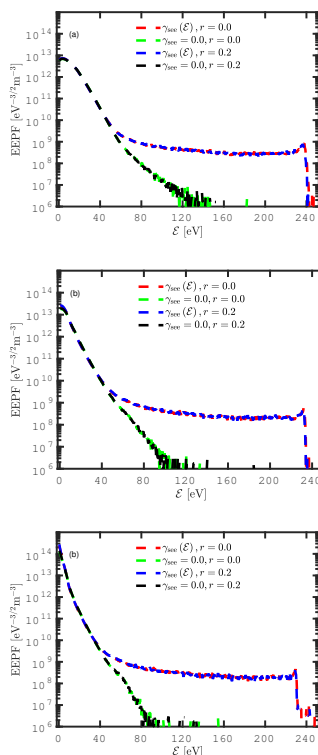
Figure 1. The electron energy probability function (EEPF) in the discharge center for a parallel plate capacitively-coupled oxygen discharge at (**a**) 10 mTorr, (**b**) 25 mTorr, and (**c**) 50 mTorr with a surface quenching coefficient for the singlet metastable molecule $O_2(a^1\Delta_g)$ as $\gamma_{wqa} = 0.0001$ and a gap separation of 4.5 cm driven by a 222 V voltage source at a driving frequency of 13.56 MHz.
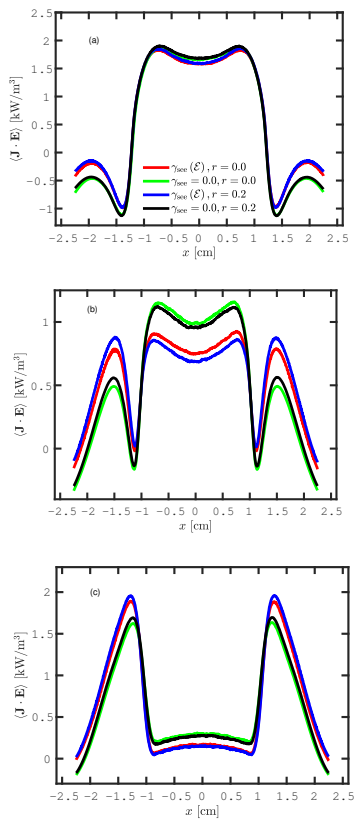
Figure 2. The time averaged electron heating profile for a parallel plate capacitively-coupled oxygen discharge at (**a**) 10 mTorr, (**b**) 25 mTorr, and (**c**) 50 mTorr with a surface quenching coefficient for the singlet metastable molecule $O_2(a^1\Delta_g)$ as $\gamma_{wqa} = 0.0001$ and a gap separation of 4.5 cm driven by a 222 V voltage source at a driving frequency of 13.56 MHz.

In order to explore the observed transition further, we plot the center electron density as a function of pressure in Figure 3a. The electron density increased with increased pressure. At 10 mTorr, all four cases exhibited a similar electron density, and the electron density was slightly enhanced when the electron reflection was included in the simulation. At 25 mTorr, we see that including both

the secondary electron emission and the electron reflection gave the highest center electron density, while excluding both processes led to the lowest center electron density. The differences in electron density between including and excluding both secondary electron emission and electron reflection were bigger than at 10 mTorr. At 50 mTorr, we see that including the ion induced secondary electron emission increased the center electron density and that including electron reflection increased the electron density even further.

Further insights about the observed transition are shown in the plot of the center electronegativity as a function of pressure in Figure 3b. At 10 mTorr, the discharge was the most strongly electronegative. The electronegativity decreased from ~110 at 10 mTorr to ~20 at 50 mTorr. The electronegativity was higher (lower) when electron reflection was excluded (included) in the simulation; however, all four cases were very close to each other. The maximum (minimum) value of the electronegativity was reached when both secondary electron emission and electron reflection were excluded (included). At 25 mTorr, we observe that the gap between including and excluding both secondary electron emission and electron reflection was bigger than at 10 mTorr. We observe that, when secondary electron emission was included, excluding the electron reflection enhanced the electronegativity. The same occurred when secondary electron emission was included. Indeed, in this case, excluding both secondary electron emission and electron reflection gave the highest electronegativity. At 50 mTorr, the electronegativity was drastically reduced. We observed that electronegativity was lowest when secondary electron emission was included in the simulation and that electron reflection did not play much of a role. On the other hand, the electronegativity was highest when secondary electron emission and electron reflection were excluded from the simulation.
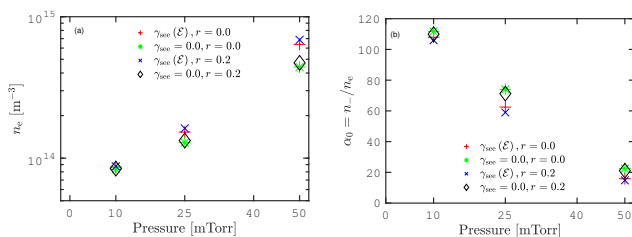
Figure 3. The (**a**) electron density and the (**b**) electronegativity in the discharge center as a function of pressure for a parallel plate capacitively-coupled oxygen discharge with a surface quenching coefficient for the singlet metastable molecule $O_2(a^1\Delta_g)$ as $\gamma_{wqa} = 0.0001$ and a gap separation of 4.5 cm driven by a 222 V voltage source at a driving frequency of 13.56 MHz.

Figure 4 shows the spatio-temporal behavior of the electron power absorption $\mathbf{J}_e \cdot \mathbf{E}$, where $\mathbf{J}_e$ and $\mathbf{E}$ are the spatially and temporally-varying electron current density and electric field, respectively. The figures show the electron power absorption for the various combinations of pressures, including and excluding secondary electron emission, while excluding electron reflection from the electrodes. For each of the figures, the abscissa covers the whole inter-electrode gap, from the powered electrode on the left-hand size to the grounded electrode on the right-hand size. Similarly, the ordinate covers the full rf cycle. Note that each of the six figures may have different magnitude scales, represented by the color scales on the right-hand side of each figure. Therefore, there can be differences in the six figures, not only qualitative, but also quantitative. Figure 4a,b shows the spatio-temporal behavior of the electron power absorption including and excluding $\gamma_{see}(\mathcal{E})$ at 10 mTorr, respectively. Figure 4c shows the difference between including and excluding the ion-induced

secondary electron emission from the electrodes. In Figure 4a,b, the most significant heating is observed in the sheath region, during the sheath expansion, and the most significant cooling is observed during the sheath collapse. Here, significant energy gain (red and yellow areas) and small energy loss (dark blue areas) were evident within the plasma bulk region. We observe electron heating during the sheath collapse on the bulk side of the edge of the collapsing sheath (next to the instantaneous anode), while there was cooling (electrons loose energy) on the electrode side (the lower left-hand corner and upper center on the right-hand side). This kind of electron heating structure was observed experimentally in a capacitively-coupled SF_6/N_2 discharge [42] and SiH_4 discharge [43] using spatiotemporal optical emission spectroscopy. This heating mechanism was explored further using the relaxation continuum model [44], where electron heating due to three processes was identified: sheath expansion (α-mode), high electric field within the bulk, and ionization due to formation of a double layer on the instantaneous anode side, which resulted in acceleration of electrons. Indeed, in electronegative discharges, this electron heating within the plasma bulk can be the dominating electron heating mechanism [42,44]. This heating mechanism, which is due to electrons that are accelerated by strong drift and ambipolar electric fields within the plasma bulk and at the sheath edges in strongly electronegative discharges, was later coined as drift ambipolar (DA) electron heating [45]. In highly electronegative discharges, these electrons are often found to dominate the ionization processes. As seen in Figure 3b, the electronegativity was high $\sim$110 at 10 mTorr, which is essential for the DA-heating to be effective. The electron heating occurred both within the bulk and in the sheath regions, and a hybrid DA- and α-mode heating was observed. By looking at the time averaged electron heating profile in Figure 2a, we see that there was electron cooling in the sheath region and all the electron heating occurred in the bulk region averaged over one rf cycle. Figure 4c shows that there were no significant differences in the power absorption between the two cases, and in fact, there was a slightly higher electron heating within the discharge when secondary electron emission was excluded. Figure 4d,e shows the spatio-temporal behavior of the electron power absorption for $\gamma_{see}(\mathcal{E})$ and $\gamma_{see} = 0.0$, respectively, at 25 mTorr. Figure 4f shows the difference between including and excluding secondary electron emission from the electrodes. At 25 mTorr, a transition process was observed. Indeed, Figure 4e shows that the heating and the cooling in the sheath regions were reduced, while Figure 4d shows that a significant contribution to the electron heating in the bulk region was observed. Therefore, a hybrid DA- and α-mode heating was observed, where the DA-heating was more important when secondary electron emission was excluded (Figure 4e) than when it was included (Figure 4d). This is clearly seen in the difference plot shown in Figure 4f when cooling was seen as the difference. We see in Figure 2b that in this case, the time averaged power absorption was observed both in the plasma bulk, as well as in the sheath regions. Figure 4g,h shows the spatio-temporal behavior of the electron power absorption for $\gamma_{see}(\mathcal{E})$ and $\gamma_{see} = 0.0$ at 50 mTorr, respectively. Figure 4i shows the difference between including secondary electron emission (Figure 4g) and excluding secondary electron emission (Figure 4h). Here, the electron heating rate in the sheath regions reduced again, and there was almost no heating in the plasma bulk, as seen in Figure 4g,h; a pure α-mode was observed for both plots. This is clearly seen in Figure 2a when averaged over the rf cycle. As seen from the difference plot shown in Figure 4i, the electron heating in the sheath region was quantitatively more important for $\gamma_{see}(E)$ than for $\gamma_{see} = 0.0$. There was clearly higher electron heating at sheath expansion when secondary electron emission was included. However, including ion-induced secondary electron emission from the electrodes decreased the overall electron power absorption.
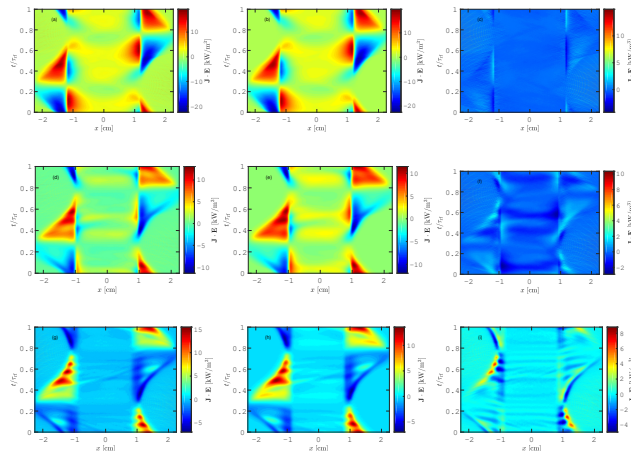
Figure 4. The spatio-temporal behavior of the electron power absorption for a parallel plate capacitively-coupled oxygen discharge at 10 mTorr for (**a**) $\gamma_{\text{see}}(\mathcal{E})$ and (**b**) $\gamma_{\text{see}} = 0.0$, (**c**) the difference between $\gamma_{\text{see}}(\mathcal{E})$ and $\gamma_{\text{see}} = 0.0$, at 25 mTorr, for (**d**) $\gamma_{\text{see}}(\mathcal{E})$ and (**e**) $\gamma_{\text{see}} = 0.0$, (**f**) the difference between $\gamma_{\text{see}}(\mathcal{E})$ and $\gamma_{\text{see}} = 0.0$, at 50 mTorr for, (**g**) $\gamma_{\text{see}}(\mathcal{E})$ and (**h**) $\gamma_{\text{see}} = 0.0$, and (**i**) the difference between $\gamma_{\text{see}}(\mathcal{E})$ and $\gamma_{\text{see}} = 0.0$ with a surface quenching coefficient for the singlet metastable molecule $O_2(a^1\Delta_g)$ as $\gamma_{\text{wqa}} = 0.0001$, $r = 0.0$, and a gap separation of 4.5 cm driven by a 222 V voltage source at a driving frequency of 13.56 MHz.

Figure 5 shows the spatio-temporal behavior of the effective electron temperature. It shows the effective electron temperature as a function of position between the electrodes within one rf cycle, for the various combinations of pressures including and excluding secondary electron emission from the electrodes. At 10 mTorr, the effective electron temperature was high within the plasma bulk, and no important difference was observed in the spatio-temporal behavior of the effective electron temperature between $\gamma_{\text{see}}(\mathcal{E})$ and $\gamma_{\text{see}} = 0.0$, as seen in Figure 5a,b, respectively. A peak in the effective electron temperature was observed within the bulk region on the instantaneous anode side and agrees with the region of peak electron heating seen in Figure 4a,b. The difference in the effective electron temperature calculated excluding and including the secondary electron emission is seen in Figure 5c. We see that the effective electron temperature within the plasma bulk was slightly higher when secondary electron emission was included. The peaks in the effective electron temperature were higher when secondary electron emission was included. We also observe that the effective electron temperature had a peak within the plasma bulk at the instantaneous anode side and at the sheath expansion at 25 mTorr for both $\gamma_{\text{see}}(\mathcal{E})$ and $\gamma_{\text{see}} = 0.0$, as seen in Figure 5d,e, respectively. This is clearly seen in the difference plot in Figure 5f. The electron effective temperature was higher for $\gamma_{\text{see}}(\mathcal{E})$ than for $\gamma_{\text{see}} = 0.0$ in the bulk region. In particular, the peak in the bulk region on the instantaneous anode side increased when secondary electron emission was included. At 50 mTorr, we observe a peak in the effective electron temperature during the sheath expansion. We also see that there was an increase in the effective electron temperature within the bulk when secondary electron emission was

included. For $\gamma_{see} = 0.0$, the effective electron temperature in the bulk and in the sheath region was lower than when secondary electron emission was included, as seen in Figure 5g,h. This behavior is clearly manifest in the difference plot shown in Figure 5i. At all pressures, we found that including secondary electron emission in the discharge model increased the electron energy.
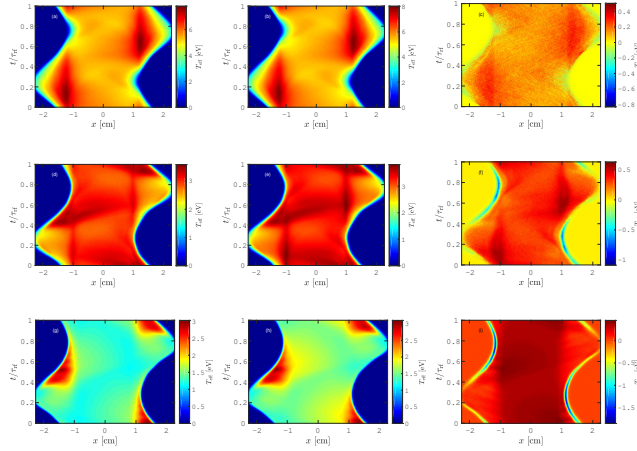
Figure 5. The spatio-temporal behavior of the effective electron temperature for a parallel plate capacitively-coupled oxygen discharge at 10 mTorr for (**a**) $\gamma_{see}(\mathcal{E})$ and (**b**) $\gamma_{see} = 0.0$, (**c**) the difference between $\gamma_{see} = 0.0$ and $\gamma_{see}(\mathcal{E})$, at 25 mTorr, for (**d**) $\gamma_{see}(\mathcal{E})$, and (**e**) $\gamma_{see} = 0.0$, (**f**) the difference between $\gamma_{see} = 0.0$ and $\gamma_{see}(\mathcal{E})$, at 50 mTorr for, (**g**) $\gamma_{see}(\mathcal{E})$ and (**h**) $\gamma_{see} = 0.0$, and (**i**) the difference between $\gamma_{see} = 0.0$ and $\gamma_{see}(\mathcal{E})$ with a surface quenching coefficient for the singlet metastable molecule $O_2(a^1\Delta_g)$ as $\gamma_{wqa} = 0.0001$, $r = 0.0$, and a gap separation of 4.5 cm driven by a 222 V voltage source at a driving frequency of 13.56 MHz.

4. Conclusions

The one-dimensional object-oriented PIC/MCC code oopd1 was applied to explore the evolution of the EEPF and of the electron heating mechanism in a capacitively-coupled oxygen discharge while including and excluding the ion-induced secondary electron emission and electron reflection. Adding secondary electron emission enhances the EEPF with a high energy tail for all the pressures. At 10 mTorr, the EEPF curves outwards. The electron heating at 10 mTorr is a hybrid DA- and α-mode heating, and no significant difference is observed including and excluding secondary electron emission from the electrodes. Averaged over one rf cycle, a predominance of the electron heating in the plasma bulk was observed for all the cases. At 25 mTorr, the shape of the EEPF starts to develop an inward curving behavior and a hybrid DA- and α-mode heating is observed. The role of sheath heating increases when secondary electron emission from the electrodes is included in the simulation. At 50 mTorr, the transition, which had already started at 25 mTorr, is fully accomplished, and the shape of the EEPF is now bi-Maxwellian, while no electron heating is observed in the plasma bulk.

Author Contributions: Conceptualization, J.T.G. and A.P.; Formal Analysis, A.P. and J.T.G.; Investigation, A.P. and J.T.G.; Resources, J.T.G.; Data Curation, A.P.; Writing—Original Draft Preparation, J.T.G. and A.P.; Writing—Review & Editing, J.T.G. and A.P.; Supervision, J.T.G.; Project Administration, J.T.G.; Funding Acquisition, J.T.G.

Conflicts of Interest: The authors declare no conflict of interest.

References

1. Donkó, Z.; Schulze, J.; Czarnetzki, U.; Derzsi, A.; Hartmann, P.; Korolov, I.; Schüngel, E. Fundamental investigations of capacitive radio frequency plasmas: Simulations and experiments. *Plasma Phys. Control. Fusion* **2012**, *54*, 124003. [CrossRef]
2. Derzsi, A.; Korolov, I.; Schüngel, E.; Donkó, Z.; Schulze, J. Effects of fast atoms and energy-dependent secondary electron emission yields in PIC/MCC simulations of capacitively coupled plasmas. *Plasma Sources Sci. Technol.* **2015**, *24*, 034002. [CrossRef]
3. Daksha, M.; Derzsi, A.; Wilczek, S.; Trieschmann, J.; Mussenbrock, T.; Awakowicz, P.; Donkó, Z.; Schulze, J. The effect of realistic heavy particle induced secondary electron emission coeffcients on the electron power absorption dynamics in single- and dual-frequency capacitively coupled plasma. *Plasma Sources Sci. Technol.* **2017**, *26*, 085006. [CrossRef]
4. Birdsall, C.K. Particle-in-cell charged-particle simulations, plus Monte Carlo collisions with neutral atoms, PIC-MCC. *IEEE Trans. Plasma Sci.* **1991**, *19*, 65–85. [CrossRef]
5. Verboncoeur, J.P. Particle simulation of plasmas: Review and advances. *Plasma Phys. Control. Fusion* **2005**, *47*, A231–A260. [CrossRef]
6. Tskhakaya, D.; Matyash, K.; Schneider, R.; Taccogna, F. The Particle-In-Cell Method. *Contrib. Plasma Phys.* **2007**, *47*, 563–594. [CrossRef]
7. Vahedi, V.; Surendra, M. A Monte Carlo collision model for the particle-in-cell method: Applications to argon and oxygen discharges. *Comput. Phys. Commun.* **1995**, *87*, 179–198. [CrossRef]
8. Lee, S.H.; Iza, F.; Lee, J.K. Particle-in-cell Monte Carlo and fluid simulations of argon-oxygen plasma: Comparisons with experiments and validations. *Phys. Plasmas* **2006**, *13*, 057102. [CrossRef]
9. Lichtenberg, A.J.; Vahedi, V.; Lieberman, M.A.; Rognlien, T. Modeling electronegative plasma discharges. *J. Appl. Phys.* **1994**, *75*, 2339–2347. [CrossRef]
10. Babaeva, N.Y.; Lee, J.K.; Shon, J.W.; Hudson, E.A. Oxygen ion energy distribution: Role of ionization, resonant, and nonresonant charge-exchange collisions. *J. Vac. Sci. Technol. A* **2005**, *23*, 699–704. [CrossRef]
11. Roberto, M.; Verboncoeur, J.; Verdonck, P.; Cizzoto, E. Effects of the Secondary Electron Emission Coefficent on the Generation of Charged Particles in RF Oxygen Discharge. *ECS Trans.* **2006**, *4*, 563–571.
12. Bronold, F.X.; Matyash, K.; Schneider, D.T.R.; Fehske, H. Radio-frequency discharges in oxygen: I. Particle-based modelling. *J. Phys. D Appl. Phys.* **2007**, *40*, 6583–6592. [CrossRef]
13. Matyash, K.; Schneider, R.; Dittmann, K.; Meichsner, J.; Bronold, F.X.; Tskhakaya, D. Radio-frequency discharges in oxygen: III. Comparison of modelling and experiment. *J. Phys. D Appl. Phys.* **2007**, *40*, 6601–6607. [CrossRef]
14. Schüngel, E.; Zhang, Q.Z.; Iwashita, S.; Schulze, J.; Hou, L.J.; Wang, Y.N.; Czarnetzki, U. Control of plasma properties in capacitively coupled oxygen discharges via the electrical asymmetry effect. *J. Phys. D Appl. Phys.* **2011**, *44*, 285205. [CrossRef]
15. Zhang, Q.Z.; Jiang, W.; Hou, L.J.; Wang, Y.N. Numerical simulations of electrical asymmetry effect on electronegative plasmas in capacitively coupled rf discharge. *J. Appl. Phys.* **2011**, *109*, 013308. [CrossRef]
16. Derzsi, A.; Lafleur, T.; Booth, J.P.; Korolov, I.; Donkó, Z. Experimental and simulation study of a capacitively coupled oxygen discharge driven by tailored voltage waveforms. *Plasma Sources Sci. Technol.* **2016**, *25*, 015004. [CrossRef]
17. Derzsi, A.; Bruneau, B.; Gibson, A.; Johnson, E.; O'Connell, D.; Gans, T.; Booth, J.P.; Donkó, Z. Power coupling mode transitions induced by tailored voltage waveforms in capacitive oxygen discharges. *Plasma Sources Sci. Technol.* **2017**, *26*, 034002. [CrossRef]

18. Bera, K.; Rauf, S.; Collins, K. PIC-MCC/Fluid Hybrid Model for Low Pressure Capacitively Coupled O$_2$ Plasma. *AIP Conf. Proc.* **2011**, *1333*, 1027–1032.

19. Bera, K.; Rauf, S.; Collins, K. Plasma Dynamics in Low-Pressure Capacitively Coupled Oxygen Plasma Using PIC–MCC/Fluid Hybrid Model. *IEEE Trans. Plasma Sci.* **2011**, *39*, 2576–2577. [CrossRef]

20. Gudmundsson, J.T.; Kawamura, E.; Lieberman, M.A. A benchmark study of a capacitively coupled oxygen discharge of the oopd1 particle-in-cell Monte Carlo code. *Plasma Sources Sci. Technol.* **2013**, *22*, 035011. [CrossRef]

21. Gudmundsson, J.T.; Lieberman, M.A. On the role of metastables in capacitively coupled oxygen discharges. *Plasma Sources Sci. Technol.* **2015**, *24*, 035016. [CrossRef]

22. Hannesdottir, H.; Gudmundsson, J.T. The role of the metastable O$_2$(b$^1\Sigma_g^+$) and energy-dependent secondary electron emission yields in capacitively coupled oxygen discharges. *Plasma Sources Sci. Technol.* **2016**, *25*, 055002. [CrossRef]

23. Gudmundsson, J.T.; Ventéjou, B. The pressure dependence of the discharge properties in a capacitively coupled oxygen discharge. *J. Appl. Phys.* **2015**, *118*, 153302. [CrossRef]

24. Gudmundsson, J.T.; Hannesdottir, H. On the role of metastable states in low pressure oxygen discharges. *AIP Conf. Proc.* **2017**, *1811*, 120001.

25. Hannesdottir, H.; Gudmundsson, J.T. On singlet metastable states, ion flux and ion energy in single and dual frequency capacitively coupled oxygen discharges. *J. Phys. D Appl. Phys.* **2017**, *50*, 175201. [CrossRef]

26. Gudmundsson, J.T.; Snorrason, D.I. On electron heating in a low pressure capacitively coupled oxygen discharge. *J. Appl. Phys.* **2017**, *122*, 193302. [CrossRef]

27. Gudmundsson, J.T.; Snorrason, D.I.; Hannesdottir, H. The frequency dependence of the discharge properties in a capacitively coupled oxygen discharge. *Plasma Sources Sci. Technol.* **2018**, *27*, 025009. [CrossRef]

28. Bojarov, A.; Radmilović-Radjenović, M.; Petrović, Z.L. The influence of the ion induced secondary electron emission on the characteristics of rf plasmas. *Publ. Astron. Obs. Belgrade* **2010**, *89*, 131–134.

29. Lafleur, T.; Chabert, P.; Booth, J.P. Secondary electron induced asymmetry in capacitively coupled plasmas. *J. Phys. D Appl. Phys.* **2013**, *46*, 135201. [CrossRef]

30. Korolov, I.; Derzsi, A.; Donkó, Z.; Schulze, J. The influence of the secondary electron induced asymmetry on the electrical asymmetry effect in capacitively coupled plasmas. *Appl. Phys. Lett.* **2013**, *103*, 064102. [CrossRef]

31. Radmilović-Radjenović, M.; Petrović, Z.L. Influence of the surface conditions on rf plasma characteristics. *Eur. Phys. J. D* **2009**, *54*, 445–449. [CrossRef]

32. Bojarov, A.; Radmilović-Radjenović, M.; Petrović, Z.L. Modeling the effects of the secondary electron emission in a dual-frequency capacitively coupled plasma reactor. In Proceedings of the 20th Europhysics Sectional Conference on Atomic and Molecular Physics of Ionized Gases (ESCAMPIG XX), Novi Sad, Serbia, 13–17 July 2010; p. P2.38.

33. Bojarov, A.; Radmilović-Radjenović, M.; Petrović, Z.L. Particle in cell simulation of the electrical asymmetric effect with a realistic model of the ion induced secondary electron emission. In Proceedings of the 27th Summer School and International Symposium on the Physics of Ionized Gases, Belgrade, Serbia, 26–29 August 2014; pp. 407–410.

34. Hammel, J.; Verboncoeur, J.P. DC Discharge Studies Using PIC-MCC. *Bull. Am. Phys. Soc.* **2003**, *48*, 66.

35. Verboncoeur, J.P.; Langdon, A.B.; Gladd, N.T. An object-oriented electromagnetic PIC code. *Comput. Phys. Commun.* **1995**, *87*, 199–211. [CrossRef]

36. Kawamura, E.; Birdsall, C.K.; Vahedi, V. Physical and numerical methods of speeding up particle codes and paralleling as applied to RF discharges. *Plasma Sources Sci. Technol.* **2000**, *9*, 413–428. [CrossRef]

37. Proto, A.; Gudmundsson, J.T. The role of surface quenching of the singlet delta molecule in a capacitively coupled oxygen discharge. *Plasma Sources Sci. Technol.* **2018**, *27*, 074002. [CrossRef]

38. Booth, J.P.; Sadeghi, N. Oxygen and fluorine kinetics in electron cyclotron resonance plasmas by time-resolved actinometry. *J. Appl. Phys.* **1991**, *70*, 611–620. [CrossRef]

39. O'Brien, R.J.; Myers, G.H. Direct flow measurement of O$_2$(b$^1\Sigma_g^+$) quenching rates. *J. Chem. Phys.* **1970**, *53*, 3832–3835. [CrossRef]

40. Kollath, R. Sekundärelektronen-Emission fester Körper bei Bestrahlung mit Elektronen. In *Elektronen-Emission Gasentladungen I*; Flügge, S., Ed.; Handbuch der Physik; Springer: Berlin, Germany, 1956; Volume 21, pp. 232–303.

41. Braginsky, O.; Kovalev, A.; Lopaev, D.; Proshina, O.; Rakhimova, T.; Vasilieva, A.; Voloshin, D.; Zyryanov, S. Experimental and theoretical study of dynamic effects in low-frequency capacitively coupled discharges. *J. Phys. D Appl. Phys.* **2012**, *45*, 015201. [CrossRef]
42. Petrović, Z.L.; Tochikubo, F.; Kakuta, S.; Makabe, T. Spatiotemporal optical emission spectroscopy of rf discharges in SF_6. *J. Appl. Phys.* **1993**, *73*, 2163–2172. [CrossRef]
43. Makabe, T.; Tochikubo, F.; Nishimura, M. Influence of negative ions in rf glow discharges in SiH_4 at 13.56 MHz. *Phys. Rev. A* **1990**, *42*, 3674–3677. [CrossRef] [PubMed]
44. Nakano, N.; Shimura, N.; Petrović, Z.L.; Makabe, T. Simulations of rf glow discharges in SF_6 by the relaxation continuum model: Physical structure and function of the narrow-gap reactive-ion etcher. *Phys. Rev. E* **1994**, *49*, 4455–4465. [CrossRef]
45. Schulze, J.; Derzsi, A.; Dittmann, K.; Hemke, T.; Meichsner, J.; Donkó, Z. Ionization by drift and ambipolar electric fields in electronegative capacitive radio frequency plasmas. *Phys. Rev. Lett.* **2011**, *107*, 275001. [CrossRef] [PubMed]

Paper III

Electron heating mode transitions in a low pressure capacitively coupled oxygen discharge

J.T. Gudmundsson and A. Proto

Electron heating mode transitions in a low pressure capacitively coupled oxygen discharge

J T Gudmundsson[1,2] and A Proto[1]

[1] Science Institute, University of Iceland, Dunhaga 3, IS-107 Reykjavik, Iceland
[2] Department of Space and Plasma Physics, School of Electrical Engineering and Computer Science, KTH Royal Institute of Technology, SE-100 44, Stockholm, Sweden

E-mail: tumi@hi.is

Abstract

Using particle-in-cell Monte Carlo collision simulations we have demonstrated an electron heating mode transition from drift-ambipolar (DA) mode to α-mode in the capacitively coupled oxygen discharge as the operating pressure and/or electrode separation are increased. Here we explore further the transition as pressure and electrode separation are varied. At fixed electrode spacing of 45 mm when operating at low pressure (10 mTorr) the electron heating is a combination of DA- and α-mode heating while at higher pressures (>30 mTorr) electron heating in the sheath regions dominates. When varying the electrode spacing from 25 to 60 mm at fixed operating pressure at the higher pressures (50 mTorr) the electron heating is a combination of DA- and α-mode heating for small electrode spacing and it transitions to pure α-mode heating as the electrode spacing is increased. We relate the transition to increased electronegativity and generation of drift and ambipolar electric field within the electronegative core when the discharge pressure is low or electrode spacing is small.

Keywords: cpacitively coupled discharge, particle-in-cell Monte Carlo collision, oxygen, electron heating, detachment

1. Introduction

The low pressure radio frequency (rf) driven capacitively coupled discharges have a wide range of applications. Modern capacitively coupled discharges consist of two parallel electrodes, typically few tens of cm in radius and separated by a few cm. In the capacitively coupled discharge a plasma forms between the electrodes when a rf field is applied between the electrodes. A number of operating modes exist in the capacitively coupled discharge including bulk electron heating during sheath expansion (α-mode) [1–3], secondary electron emission from the electrodes (γ- mode) [1, 2, 4], the drift-ambipolar (DA)-mode [5], and striation mode [6, 7]. The oxygen discharge has been applied in materials processing applications for over five decades. The initial application of the oxygen discharge was ashing of photoresist [8] where its role has remained significant over the years [9, 10]. Other applications include surface modification of polymer films

[11, 12], and oxidation or anodization of silicon [13, 14]. The electron heating mechanism and the electron kinetics dictate the ionization and dissociation processes that maintain the discharge and create the radicals that are desired for materials processing.

There have been a number of studies of the capacitively coupled oxygen discharge over the years starting with the seminal work of Vahedi and Surendra [15] using the 1D `xpdp1` particle-in-cell Monte Carlo collision (PIC/MCC) code. This includes a number of PIC/MCC studies using the `xpdx1` series of codes [16–18]. In addition few 1D PIC/MCC codes have been developed to explore the oxygen discharge, including a code developed in Greifswald [19, 20], and a code developed in Dalian [21, 22] that both include the metastable oxygen molecule $O_2(a^1\Delta_g)$ as a fraction of the ground state molecule. More recently, a 1D PIC/MCC code that was developed in Budapest has been used to explore the heating mechanism in an capacitively coupled oxygen

J T Gudmundsson and A Proto

discharge driven by tailored waveforms (composed of N harmonics in addition to a fundamental frequency f_1) [23–25]. Donkó *et al* [25] benchmarked the Budapest code to an extensive set of experimental data and performed a limited sensitivity analysis regarding some of the parameters such as surface quenching of metastables and a few selected cross sections. In all of these works only electrons, the positive ion O_2^+, and the negative ion O^- are treated kinetically and the positive ion O^+ is neglected. Also none of the metastable states are treated kinetically. The one-dimensional object-oriented plasma device one (oopd1) code allows having the simulated particles of different weights so that both charged and neutral particles can be tracked in the simulation. Earlier the basic reaction set for the oxygen discharge in oopd1 was benchmarked to the xpdp1 code [26].

Recently we have applied the oopd1 code to explore the electron heating mechanism in the capacitively coupled oxygen discharge while varying the various external parameters and operating conditions such as discharge pressure [27–29], driving voltage amplitude [30], driving frequency [31], the secondary electron emission [28, 32], and the surface quenching of the metastable states [33]. We have observed that, when operating at low oxygen pressure (10 mTorr), the time averaged electron heating appears mainly within the plasma bulk (the electronegative core) and when operating at higher pressures (50–500 mTorr) electron heating is observed almost solely within the sheath regions [27, 28]. Thus when the oxygen discharge is operated at low pressure, the electron heating within the discharge is a hybrid drift-ambipolar-mode (DA-mode) and α-mode and, while operating at higher pressures, the electron power absorption is due to stochastic heating during sheath expansion and a pure α-mode is observed [30, 31]. We have also demonstrated that the driving frequency plays a role in determining the electron heating mode. At low driving frequency and low operating pressure (5 and 10 mTorr) a combination of stochastic (α-mode) and DA-mode heating in the bulk plasma (the electronegative core) is observed and the DA-mode dominates the time averaged electron heating. As the driving frequency or pressure are increased the heating mode transitions into a pure α-mode, where sheath heating dominates [31]. We have also demonstrated that the singlet metastable molecular states have a significant influence on the electron heating mechanism in the capacitively coupled oxygen discharge and in particular it is the associate deteachment by the singlet delta metastable state that has a determining influence on the discharge properties [34]. In fact the associate detachment by the singlet molecular metastable states has significant influence on the electron heating process in the higher pressure regime, while it has negligible effect at lower pressures [27–29]. It has to be emphasized that the transition in the electron heating mode with increased operating pressure and increased driving frequency is only observed when the singlet metastable states are properly included in the discharge model. When the singlet metastable states are neglected in the simulation the electronegativity is high and there is significant electron heating in the electronegative core up to 100 mTorr [27, 34]. The dominating negative ion in the oxygen discharge at low operating pressure is the O^- ion. This negative ion is created almost solely through electron impact dissociative attachment of the oxygen molecule and the metastable oxygen molecules have a significant contribution. The loss of the negative ion O^- is dominated by heavy particle detachment where the metastable oxygen molecules play a significant role and ion–ion recombination plays somewhat smaller role. The dissociative attachment is an electron impact reaction and its reaction rate increases with decreasing discharge pressure and higher effective electron temperature, while the role of the heavy particle detachment decreases with decreasing pressure. In the capacitively coupled discharge the electron density is low but it increases with increasing discharge pressure. The increased electron density along with higher discharge pressure increases the number of metastable oxygen molecules and thus the reaction rate of the detachment process. Thus the discharge electronegativity is high at low pressure and decreaes with increasing discharge pressure. It turns out that it is the discharge electronegativity that determines the electron heating dynamics in the capacitively coupled oxygen discharge [31]. The electronegativity is set by the singlet metastable molecules $O_2(a^1\Delta_g)$ and $O_2(b^1\Sigma_g)$ through the detachment process and thus their presence dictate the overall discharge properties [27–29, 34]. The surface quenching of the singlet metastable states on the electrode surfaces can thus have a significant influence on the electron heating mode [33].

Recently, You *et al* [35] explored a geometrically symmetric capacitively coupled oxygen discharge both experimentally and by PIC/MCC simulations using the Budapest code. Experimentally they find at fixed operating pressure of 20 mTorr that the central electron density increases with increased electrode spacing in the range 30–90 mm. They applied the PIC/MCC simulations to to show that the electron density increases due to a mode transition from the DA-mode to the α-mode as the electrode spacing is increased.

Here we give an overview of our recent findings and present the full reaction set included in the current version of the oopd1 code and apply it to explore the electron heating mode transition in an oxygen discharge, including the variation in the electronegativity and electric field within the electronegative core, as the operating pressure and the electrode separation is varied. We use more realistic values for the partial pressures of the metastable states than used in our earlier studies. Furthermore, we allow the partial pressures to vary with discharge pressure and electrode separation.

2. The oxygen reaction set

We use the one-dimensional (1D-3v) object-oriented PIC/MCC code oopd1 [36, 37] to simulate a capacitively coupled oxygen discharge. Like the well known xpdp1 code [15], the oopd1 code, is a general simulation tool capable of simulating various types of plasma devices and plasma phenomena, including particle beams, electrical breakdown, particle accelerators, as well as processing discharges [26].

The oxygen reaction set included in the oopd1 code is rather extensive. The current discharge model for oxygen

2

J T Gudmundsson and A Proto

included in `oopd1` contains nine species: electrons, the ground state neutrals $O(^3P)$ and $O_2(X^3\Sigma_g^-)$, the negative ions O^-, the positive ions O^+ and O_2^+, and the metastables $O(^1D)$, $O_2(a^1\Delta_g)$ and $O_2(b^1\Sigma_g^+)$. The full oxygen reaction set has been discussed in our earlier works where the cross sections used are also given [26, 28, 34]. The basic reaction set included the ground state oxygen molecule $O_2(X^3\Sigma_g^-)$, the negative ion O^-, the positive ion O_2^+, and electrons [15, 26]. In addition it includes oxygen atoms in the ground state $O(^3P)$ and ions of the oxygen atom O^+ [26]. Later the singlet metastable molecule $O_2(a^1\Delta_g)$ and the metastable oxygen atom $O(^1D)$ were added [34], and then the singlet metastable molecule $O_2(b^1\Sigma_g^+)$ [28], along with the relevant reactions and cross sections. The full reaction included in the `oopd1` code is listed in table 1 for the basic reaction set and in table 2 for reactions involving the metastable oxygen atom $O(^1D)$ and the singlet metastable molecules $O_2(a^1\Delta_g)$ and $O_2(b^1\Sigma_g^+)$.

Energy-dependent secondary electron emission coefficients for oxygen ions and neutrals as they bombard both clean and dirty metal electrodes have been incorporated into the discharge model [28]. We here use the secondary electron emission yield for a dirty surface. We assume that electrons are reflected from the electrodes with a probability of 0.2, which is the number of elastically reflected electrons per incoming electron, independently of their energy and angle of incidence. This value is based on the summary of values presented by Kollath [68] for various materials. This value has been used by others in PIC/MCC simulations of capacitively coupled discharges [69, 70]. Note that in reality the reflection of electrons is known to depend on the electrode material, incident electron energy and the angle of incidence [68, 71]. Furthermore, for all the cases explored here, we neglect secondary electron emission due to electron impact of the electrodes.

For neutral atoms and molecules that hit the electrode we assume that it returns as a thermal particle with a given probability. Also atoms can recombine on the electrode surfaces to form a thermal molecule with a given probability. As the ground state oxygen atom $O(^3P)$ hits the electrode we assume that half of the atoms are reflected as $O(^3P)$ at room temperature and the other half recombines to form the ground state oxygen molecule $O_2(X^3\Sigma_g^-)$ at room temperature. Thus for a neutral oxygen atom in the ground state $O(^3P)$ we use a wall recombination coefficient of 0.5 as measured for a pure oxygen discharge in a stainless steel reactor at 2 mTorr [72]. This is a rough assumption as it is known that the wall recombination coefficient drops significantly with increased operating pressure [73]. Also as the metastable oxygen atom $O(^1D)$ hits the electrode we assume that half of the atoms are quenched to form $O(^3P)$ and the other half recombines to form the ground state oxygen molecule $O_2(X^3\Sigma_g^-)$ at room temperature. For the surface quenching coefficients of the singlet metastable molecules on the electrode surfaces we assume for the singlet metastable $O_2(a^1\Delta_g)$ a value of $\gamma_{wqa} = 0.007$, based on measurements for iron [74], while for the singlet metastable $O_2(b^1\Sigma_g^+)$ we assume a value of $\gamma_{wqb} = 0.1$, based on the suggestion that the surface quenching coefficient for

the $b^1\Sigma_g^+$ state is significantly larger than for the $a^1\Delta_g$ state [75]. We have explored the influence of the surface quenching coefficients for the singlet metastable molecule $O_2(a^1\Delta_g)$ on the electron heating mechanism of an oxygen discharge earlier [33] and demonstrated that the influence of γ_{wqa} on the discharge properties can be significant indeed. There we also list the known surface quenching coefficients for various electrode materials.

A comparison has been made of the simulation results to the experimental work of Kechkar *et al* [76–78] on a slightly asymmetric discharge, as the diameter of the driven electrode was 205 mm and the grounded electrode was 295 mm [28]. When both the singlet metastable molecules $O_2(a^1\Delta_g)$ and $O_2(b^1\Sigma_g^+)$ and energy-dependent secondary electron emission yield are included in the discharge model, we found the results of the simulation agree very well with the measured electron density in the entire pressure range up to 600 mTorr. Similarly, the simulated and measured effective electron temperature in the discharge center ($T_{eff} = (2/3)\langle\mathcal{E}\rangle$ is the average electron energy) in the pressure range up to 200 mTorr agree very well. The center effective electron temperature decreases as the pressure is increased, from around 7 eV at 10 mTorr to less than 1 eV for operating pressure in the range 50–200 mTorr. Note that the addition of the single metastable molecules and secondary electron emission to the oxygen discharge model has a significant influence to lower the effective electron temperature [28, 29].

3. The simulation setup

For this current study we assume a geometrically symmetric capacitively coupled discharge where one of the electrodes is driven by an rf voltage at a single frequency

$$V(t) = V_0 \sin(2\pi f t) \qquad (1)$$

while the other electrode is grounded. Here, V_0 is the voltage amplitude, f the driving frequency and t is the time. For this study the driving frequency is assumed to be 13.56 MHz. We assume a capacitor of 0.1 μF connected in series with the voltage source. The discharge electrode separation is assumed to be small compared to the electrode diameter so that the discharge can be treated as one-dimensional. We assume the electrode diameter to be 10.25 cm, which is needed in order to determine the absorbed power and set the discharge volume for the global model calculations applied to determine the partial pressure of the neutral species. To resolve the electron plasma frequency the time step Δt is determined from $\omega_{pe}\Delta t < 0.2$, where ω_{pe} is the electron plasma frequency and the electron time step is set 3.68×10^{-11} s. The simulation was run for 5.5×10^6 time steps which corresponds to 2750 rf cycles. It takes roughly 1700 rf cycles to reach equilibrium for all particles. The time averaged plasma parameters shown, such as the particle densities and the electron heating rate, are averages over 1000 rf cycles. The grid spacing Δx is set to resolve the electron Debye length of the low-energy electrons and the simulation grid is taken to be

3

J T Gudmundsson and A Proto

Table 1. The basic reaction set for oxygen used in the `oopd1` code.

Reaction	Process	References for cross section
Electron impact O$_2$		
e + O$_2$ $\longrightarrow$ O$_2$ + e	Elastic scattering	[38]
e + O$_2$($r=0$) $\longrightarrow$ e + O$_2$($r>0$)	Rotational excitation	[39]
e + O$_2$($v=0$) $\longrightarrow$ e + O$_2$($v>0$)	Vibrational excitation	[39]
e + O$_2$ $\longrightarrow$ e + O$_2$(a$^1\Delta_g$)	Metastable excitation (0.98 eV)	[39]
e + O$_2$ $\longrightarrow$ e + O$_2$(b$^1\Sigma_g^+$)	Metastable excitation (1.63 eV)	[39]
e + O$_2$ $\longrightarrow$ e + O$_2$(A$^3\Sigma_u^+$,A$'^3\Delta_u$,c$^1\Sigma_u^-$)	Metastable excitation (4.05 eV)	[38, 40, 41]
e + O$_2$ $\longrightarrow$ O(^{3}P) + O(^{3}P) + e	Dissociation (6.12 eV)	[39]
e + O$_2$ $\longrightarrow$ O(^{3}P) + O(^{1}D) + e	Dissociation (8.4 eV)	[39]
e + O$_2$ $\longrightarrow$ O(^{1}D) + O(^{1}D) + e	Dissociation (9.97 eV)	[39]
e + O$_2$ $\longrightarrow$ O$_2^+$ + 2e	Electron impact ionization (12.06 eV)	[42]
e + O$_2$ $\longrightarrow$ e + O + O(3p^3P)	Dissociative excitation (14.7 eV)	[39]
e + O$_2$ $\longrightarrow$ O + O$^-$	Dissociative attachment	[43]
e + O$_2$ $\longrightarrow$ O$^+$ + O$^-$ + e	Polar dissociation	[43]
e + O$_2$ $\longrightarrow$ O$^+$ + O + 2e	Dissociative ionization	[42]
Electron impact O		
e + O $\longrightarrow$ O + e	Elastic scattering	[44, 45]
e + O(^{3}P) $\longrightarrow$ O(^{1}D) + e	Excitation to ^{1}D (1.96 eV)	[46]
e + O(^{3}P) $\longrightarrow$ O(^{1}S) + e	Excitation to ^{1}S (4.18 eV)	[46]
e + O(^{3}P) $\longrightarrow$ O(^{3}P^0) + e	Excitation to ^{3}P^0 (15.65 eV)	[46]
e + O(^{3}P) $\longrightarrow$ O(^{5}S^0) + e	Excitation to ^{5}S^0 (9.14 eV)	[46]
e + O(^{3}P) $\longrightarrow$ O(^{3}S^0) + e	Excitation to ^{3}S^0 (9.51 eV)	[46]
e + O $\longrightarrow$ O$^+$ + 2e	Ionization (13.62 eV)	[47]
Detachment		
e + O$^-$ $\longrightarrow$ O + 2e	Electron impact detachment	[48]
O$^-$ + O$_2$ $\longrightarrow$ O + O$_2$ +e	Detachment by oxygen molecule	[49]
O$^-$ + O $\longrightarrow$ O$_2$ + e	Detachment by oxygen atom	[50]
Recombination		
e + O$_2^+$ $\longrightarrow$ O(^{3}P) + O(^{1}D)	Dissociative recombination	[51, 52]
O$^-$ + O$_2^+$ $\longrightarrow$ O + O$_2$	Mutual neutralization	[53, 54]
O$^+$ + O$^-$ $\longrightarrow$ O + O	Mutual neutralization	[53, 55]
Charge exchange and scattering		
O$_2^+$ + O$_2$ $\longrightarrow$ O$_2$ + O$_2^+$	Charge exchange	[56–58]
O$^+$ + O$_2$ $\longrightarrow$ O + O$_2^+$	Charge exchange	[59]
O$^+$ + O $\longrightarrow$ O + O$^+$	Charge exchange	[60]
O$_2^+$ + O $\longrightarrow$ O$_2$ + O$^+$	Charge exchange (1.56 eV)	[61, 62]
O$_2^+$ + O$_2$ $\longrightarrow$ O$^+$ + O + O$_2$	Fragmentation by energetic O$_2^+$	[26]
O$^-$ + O$_2$ $\longrightarrow$ O$^-$ + O$_2$	Scattering	[63]
O + O$_2$ $\longrightarrow$ O + O$_2$	Scattering	[64]
O$_2^+$ + O$_2$ $\longrightarrow$ O$_2^+$ + O$_2$	Scattering	[26]
O$^+$ + O$_2$ $\longrightarrow$ O$^+$ + O$_2$	Scattering	[26]
O$_2$ + O$_2$ $\longrightarrow$ O$_2$ + O$_2$	Scattering	[64]
O + O $\longrightarrow$ O + O	Scattering	[26]

uniform and consists of 1000 cells. For the heavy particles we use sub-cycling and the heavy particles are advanced every 16 electron time steps [79]. All particle interactions are treated by the Monte Carlo method with a null-collision scheme [80]. Furthermore, we assume parabolic initial density profile [79].

The kinetics of the charged particles (electrons, O$_2^+$-ions, O$^+$-ions and O$^-$-ions) was followed for all energies. Since the neutral gas density is much higher than the densities of charged species, the neutral species at thermal energies (below a certain cut-off energy) are treated as a background with fixed density and temperature and maintained uniformly in space. These neutral background species are assumed to have a Maxwellian velocity distribution at the gas temperature (here $T_n = 26$ meV). The kinetics of the neutrals are followed when their energy exceeds a preset energy threshold value. The energy threshold values and the particle weights used here for the various neutral species included in the simulation are listed in table 3.

The partial pressures of the background thermal neutral species were calculated using a global (volume averaged) model of the oxygen discharge as discussed in Proto and Gudmundsson [33]. These values are used as input for the

Table 2. The reactions involving the metastable atom O(^{1}D) and the singlet metastable molecules O$_2$(a$^1\Delta_g$) and O$_2$(b$^1\Sigma_g^+$).

Reaction	Process	References for cross section
The metastable O(^{1}D) atom		
e + O(^{1}D) $\longrightarrow$ O$^+$ + e + e	Ionization	Threshold reduced
e + O(^{1}D) $\longrightarrow$ O(^{3}P) + e	Deexcitation	Detailed Balancing
O(^{1}D) + O$_2$(X$^3\Sigma_g^-$) $\rightarrow$ O(^{1}D) + O$_2$(X$^3\Sigma_g^-$)	Scattering	[64]
The metastable O$_2$(a$^1\Delta_g$) molecule		
e + O$_2$(a$^1\Delta_g$) $\longrightarrow$ O$_2^+$ + e + e	Ionization	Threshold reduced
e + O$_2$(a$^1\Delta_g$) $\longrightarrow$ O(^{3}P) + O$^-$	Dissociative attachment	[65]
e + O$_2$(a$^1\Delta_g$) $\longrightarrow$ O$_2$(X$^3\Sigma_g^-$) + e	Deexcitation	Detailed balancing
e + O$_2$(a$^1\Delta_g$) $\longrightarrow$ O$_2$(A$^3\Sigma_u^+$,A$^3\Delta_u$,c$^1\Sigma_u^-$) + e	Metastable excitation (3.07 eV)	Threshold reduced
e + O$_2$(a$^1\Delta_g$) $\longrightarrow$ O(^{3}P) + O(^{3}P) + e	Dissociation (5.14 eV)	Threshold reduced
e + O$_2$(a$^1\Delta_g$) $\longrightarrow$ O(^{3}P) + O(^{1}D) + e	Dissociation (7.42 eV)	Threshold reduced
e + O$_2$(a$^1\Delta_g$) $\longrightarrow$ O(^{1}D) + O(^{1}D) + e	Dissociation (8.99 eV)	Threshold reduced
e + O$_2$(a$^1\Delta_g$) $\longrightarrow$ O(^{3}P) + O$^+$ + 2e	Dissociative ionization	Threshold reduced
O$^-$ + O$_2$(a$^1\Delta_g$) $\longrightarrow$ products	Detachment	[34]
O$_2$(a$^1\Delta_g$) + O$_2$(X$^3\Sigma_g^-$) $\rightarrow$ O$_2$(a$^1\Delta_g$) + O$_2$(X$^3\Sigma_g^-$)	Scattering	[64]
O$_2^+$ + O$_2$(a$^1\Delta_g$) $\rightarrow$ O$_2$(X$^3\Sigma_g^-$) + O$_2^+$	Charge exchange	[56–58]
O$^+$ + O$_2$(a$^1\Delta_g$) $\rightarrow$ O$_2^+$ + O(^{3}P)	Charge exchange	[59]
The metastable O$_2$(b$^1\Sigma_g^+$) molecule		
e + O$_2$(b$^1\Sigma_g^+$) $\rightarrow$ O$_2^+$ + e + e	Ionization	Threshold reduced
e + O$_2$(b$^1\Sigma_g^+$) $\rightarrow$ O(^{3}P) + O$^-$	Dissociative attachment	[65]
e + O$_2$(b$^1\Sigma_g^+$) $\rightarrow$ O$_2$(X$^3\Sigma_g^-$) + e	Deexcitation	Detailed balancing
e + O$_2$(b$^1\Sigma_g^+$) $\rightarrow$ O$_2$(A$^3\Sigma_u^+$,A$^3\Delta_u$,c$^1\Sigma_u^-$) + e	Metastable excitation (2.42 eV)	Threshold reduced
e + O$_2$(b$^1\Sigma_g^+$) $\rightarrow$ O(^{3}P) + O(^{3}P) + e	Dissociation (4.49 eV)	Threshold reduced
e + O$_2$(b$^1\Sigma_g^+$) $\rightarrow$ O(^{3}P) + O(^{1}D) + e	Dissociation (6.77 eV)	Threshold reduced
e + O$_2$(b$^1\Sigma_g^+$) $\rightarrow$ O(^{1}D) + O(^{1}D) + e	Dissociation (8.34 eV)	Threshold reduced
e + O$_2$(b$^1\Sigma_g^+$) $\rightarrow$ O(^{3}P) + O$^+$ + 2e	Dissociative ionization	Threshold reduced
O$^-$ + O$_2$(b$^1\Sigma_g^+$) $\rightarrow$ O(^{3}P) + O$_2$(X$^3\Sigma_g^-$)+ e	Detachment	Rate coefficient from [66]
O(^{1}D) +O$_2$(X $^3\Sigma_g^-$) $\rightarrow$ O(^{3}P) + O$_2$(b$^1\Sigma_g^+$)	Energy—transfer	Rate coefficient from [67]
O$_2$(b$^1\Sigma_g^+$) + O$_2$(X$^3\Sigma_g^-$) $\rightarrow$ O$_2$(X$^3\Sigma_g^-$) + O$_2$(X$^3\Sigma_g^-$)	Quenching	Rate coefficient from [67]
O$_2$(b$^1\Sigma_g^+$) + O$_2$(X$^3\Sigma_g^-$) $\rightarrow$ O$_2$(b$^1\Sigma_g^+$) + O$_2$(X$^3\Sigma_g^-$)	Scattering	Same as for the ground state in [64]
O$_2^+$ + O$_2$(b$^1\Sigma_g^+$) $\rightarrow$ O$_2$(X$^3\Sigma_g^-$) + O$_2^+$	Charge exchange	Same as for the ground state in [56–58]
O$^+$ + O$_2$(b$^1\Sigma_g^+$) $\rightarrow$ O$_2^+$ + O(^{3}P)	Charge exchange	Same as for the ground state in [59]

Table 3. The parameters of the simulation, the particle weight, and the energy threshold above which kinetics of the neutral particles are followed.

Species	Particle weight (range)	Energy threshold (meV)	Recombination coefficient	Quenching coefficient
O$_2$(X$^3\Sigma_g^-$)	5×10^7	500		
O$_2$(a$^1\Delta_g$)	5×10^6	100		0.007 [74]
O$_2$(b$^1\Sigma_g^+$)	5×10^6	100		0.1
O(^{3}P)	5×10^7	500	0.5 [72]	
O(^{1}D)	5×10^7	50	0.5	0.5
O$_2^+$	$10^7 - 10^8$	—	—	
O$^+$	$10^6 - 10^7$	—	—	
O$^-$	$5 \times 10^7 - 10^8$	—	—	
e	$10^7 - 10^8$	—	—	

J T Gudmundsson and A Proto

Table 4. The relative partial pressures of the thermal neutrals at 10, 20, 30, 50 and 100 mTorr calculated by a global (volume averaged) model for 1.8 W power.

	$O_2(X^3\Sigma_g^-)$	$O_2(a^1\Delta_g)$	$O_2(b^1\Sigma_g)$	$O(^3P)$
10 mTorr	0.9802	0.0148	0.0017	0.0008
20 mTorr	0.9810	0.0146	0.0016	0.0015
30 mTorr	0.9835	0.0112	0.0016	0.0020
50 mTorr	0.9875	0.0067	0.0016	0.0037
100 mTorr	0.9877	0.0017	0.0009	0.0095

PIC/MCC simulation as the partial pressures of the neutral background gas. Due to recombination of atomic oxygen and quenching of metastable atoms and molecules on the electrode surfaces, discussed earlier, there is a drop in the high energy (energy above the threshold value) atomic oxygen density and increase in the high energy oxygen molecule densities next to the electrodes as shown in our earlier work [28]. Thus assuming uniformity of the background gas is thus somewhat unrealistic assumption.

4. Results and discussion

We explore the electron heating mode transition in a capacitively coupled oxygen discharge as the pressure is varied at fixed electrode separation as discussed in section 4.1 and as the electrode separation is varied at fixed operating pressure which is discussed in section 4.2.

4.1. Pressure dependence

First we explore how the electron heating mechanism depends on the operating pressure. The electrode separation is assumed to be 45 mm and the voltage amplitude 400 V. The operating pressure is varied and the simulation performed for pressure values of 10, 20, 30, 50, and 100 mTorr. The relative partial pressures of the background thermal neutrals calculated using the global model are given in table 4 for discharge power of 1.8 W. Note that not all the neutrals considered in the global model calculations are shown in table 4. We see that the $O_2(a^1\Delta_g)$ density is roughly 1.5 % of the total discharge pressure at 10 mTorr while it is only 0.17 % at 100 mTorr. The contribution of $O_2(b^1\Sigma_g)$ is always almost one order magnitude smaller. The partial pressures are much lower than used in our earlier studies of the pressure dependence of the electron heating mechanism in capacitively coupled oxygen discharges [27, 28]. However these partial pressures are in line with recently measured partial pressures of the singlet metastable molecules in dc oxygen discharge [81] and inductively coupled oxygen discharge at low power [82].

The spatio-temporal behavior of the electron power absorption for a parallel plate capacitively coupled oxygen discharge driven by a 400 V voltage source at driving frequency of 13.56 MHz operated at various pressure is shown in figure 1. At 10 mTorr a significant electron power
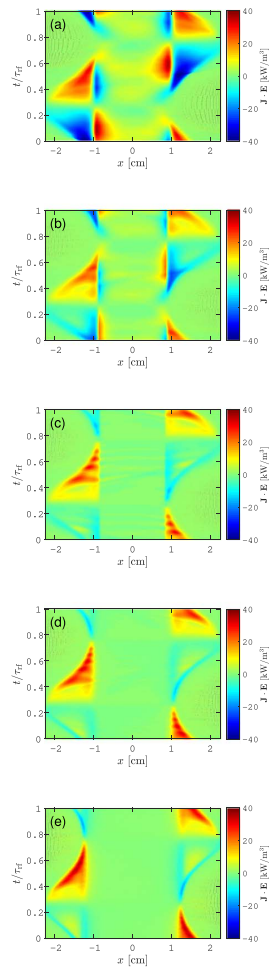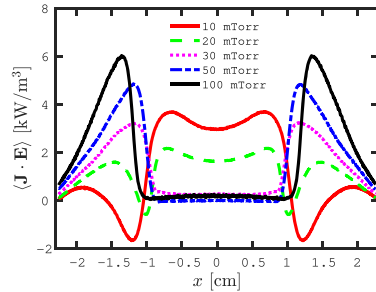

Figure 1. The spatio-temporal behavior of the electron power absorption for 45 mm gap distance for a parallel plate capacitively coupled oxygen discharge at (a) 10 mTorr, (b) 20 mTorr, (c) 30 mTorr, (d) 50 mTorr, and (e) 100 mTorr driven by a 400 V voltage source at driving frequency of 13.56 MHz.

absorption (red and yellow areas) and some electron cooling (dark blue areas) are evident in the plasma bulk region as seen in figure 1(a). The electron power absorption appears during the sheath collapse on the bulk side of the sheath edge, while there is electron cooling on the electrode side (the lower left hand corner and upper center on the right hand side). We refer to this bulk electron heating as Ohmic heating in our earlier study of the pressure dependence of the electron heating mode in a capacitively coupled oxygen discharge [27]. Furthermore, in this earlier study only the singlet metastable molecule $O_2(a^1\Delta_g)$ was included in the discharge model while the singlet metastable $O_2(b^1\Sigma_g)$ and secondary electron emission caused by ion and neutral bombardment of the electrodes was neglected. This Ohmic heating is due to acceleration of electrons due to strong drift and ambipolar electric fields within the electronegative core and the electron heating mode is referred to as DA-mode [5]. There is also apparent significant electron power absorption in the sheath region during sheath expansion and cooling during sheath collapse. Thus the electron heating within the discharge is a hybrid DA-mode and α-mode. At 20 mTorr, as seen in figure 1(b), the electron power absorption within the bulk region has decreased somewhat, and there is apparent power absorption during during sheath expansion and cooling during sheath collapse. At 30 and 50 mTorr the electron power absorption within the bulk has drastically decreased and electron heating is almost only observed within the sheath regions during the sheath expansion phase as seen in figures 1(c) and (d). Furthermore, the electron cooling during sheath collapse has decreased substantially. Similar behavior is observed at 100 mTorr and the electron power absorption is only observed in the sheath region during sheath expansion, as seen in figure 1(e). Here in the pressure range 30–100 mTorr the electron heating within the discharge is due to stochastic electron heating during sheath expansion and a pure α-mode is observed.

We note that at 30 and 50 mTorr (figures 1(c) and (d), respectively) high frequency oscillations in the electron heating rate are clearly seen adjacent to the expanding sheath edge. This kind of oscillations were first reported by Vender and Boswell [83]. Due to the sheath collapse there is a build up of an electric field that is large enough to accelerate bulk electrons toward the powered electrode. As the rf sheath expands again, these electrons are accelerated back into the bulk plasma with high kinetic energy. This leads to an electron–electron two-stream instability between the bulk electrons and the electrons accelerated by the moving sheath which is the cause of the oscillations observed [84]. The origins of the electric fields and the kinetics of multiple electron beams and the interactions of cold and hot electrons have been explored by Wilczek *et al* [85]. These oscillations have been confirmed experimentally using phase resolved optical emission spectroscopy [84, 86].

Figure 2 shows the time averaged electron power absorption $\langle \mathbf{J}_e \cdot \mathbf{E} \rangle$ profile between the electrodes as the pressure is varied where $\mathbf{J}_e$ is the electron current density and $\mathbf{E}$ is the electric field. At 10 mTorr the time averaged power absorption is almost entirely within the plasma bulk and the discharge is operated in DA-mode. The strong electron power

Figure 2. The time averaged electron power absorption for a parallel plate capacitively coupled oxygen discharge for 45 mm gap distance driven by a 400 V voltage source at driving frequency of 13.56 MHz as the pressure is varied.

absorption observed during the sheath expansion is cancelled out by the strong cooling during the sheath collapse as seen in figure 1(a). At 20 mTorr we have electron heating both in the plasma bulk and in the sheath region. Here a transition between the DA-mode and the α-mode occurs. At 30 mTorr the transition has been accomplished and the electron heating is almost solely in the sheath region and the discharge is operated in α-mode. At 50 mTorr the peak in the electron heating in the sheath region increases and approaches its maximum value when the pressure is 100 mTorr.

In our earlier discussion, we explored the evolution of the electron energy probability function (EEPF) with pressure [27, 28]. The EEPF is related to the electron energy distribution function (EEDF) through $g_p(\mathcal{E}) = \mathcal{E}^{-1/2}g_e(\mathcal{E})$ where $g_p(\mathcal{E})$ is the EEPF, $g_e(\mathcal{E})$ is the EEDF and $\mathcal{E}$ is the electron energy. We demonstrated that at low operating pressure ($<$20 mTorr) the EEPF curves outward, as the population of low-energy electrons is relatively low. As the operating pressure is increased the number of low-energy electrons increases and the number of higher energy electrons ($>$10 eV) decreases. Thus, the EEPF curves inward or becomes bi-Maxwellian as the pressure is increased. This bi-Maxwellian shape is commonly associated with predominantly stochastic sheath heating [87, 88]. For the oxygen discharge operated at the higher pressure ($>$30 mTorr) the electron heating occurs mainly in the sheath region as seen in figure 2. Note that these results seem to contradict what is commonly found for the capacitively coupled argon discharge as it is well known for a capacitively coupled argon discharge that the EEPF evolves from being bi-Maxwellian at low pressure and transition to curve outwards at high operating pressure as has been demonstrated experimentally [87, 89] and confirmed by particle-in-cell simulations [88, 90]. The explanation is that the oxygen discharge becomes highly electronegative when operating at pressures below 40 mTorr and drift and ambipolar electric fields develop within the electronegative core as
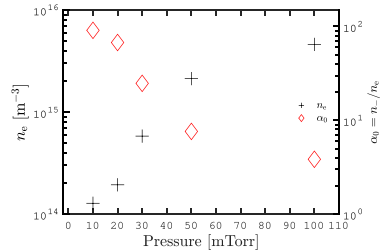
7

J T Gudmundsson and A Proto

Figure 3. The electron density in the discharge center (left *y* axis) and the electronegativity in the discharge center (right *y* axis) as a function of pressure for a parallel plate capacitively coupled oxygen discharge for 45 mm gap distance driven by a 400 V voltage source at driving frequency of 13.56 MHz.

discussed below. Thus at low pressure the electron heating mode is the DA-mode which results in outward curving EEPF.

In order to explore the observed transition further we plot the center electron density and the center electronegativity as a function of pressure in figure 3. The electron density increases while the electronegativity decreases with increased pressure. At low pressure the effective electron temperature is high [27, 28] and effective production of the negative ions through electron impact dissociative attachment, while due to low density of the singlet metastable molecules the detachment processes are not very efficient. At 10 mTorr the discharge is the most strongly electronegative. The electronegativity (electron density) slightly decreased (increased) from 10 to 20 mTorr. With increased pressure the effective electron temperature decreases and the number of metastable molecules increases. At 30 mTorr the electronegativity (electron density) has drastically reduced (enhanced). At 50 mTorr an analogous decrease (increase) in the electronegativity (electron density) is observed. Finally, at 100 mTorr, the electronegativity (electron density) approaches its lowest (highest) value.

As discussed previously, the DA-mode is a consequence of high electric field within the electronegative core. This electric field is a combination of a drift field and an ambipolar field. The drift electric field is due to low bulk conductivity or low electron density. Figure 4 shows the electric field profile in the plasma bulk for various time slices $t/\tau_{rf} = 0.25$ (red dash dotted line), $t/\tau_{rf} = 0.50$ (green dashed line), $t/\tau_{rf} = 0.75$ (violet dotted line), and fully time averaged (blue solid line) at 10, 20, 30, 50 and 100 mTorr with a gap separation of 45 mm. At 10 mTorr for all the time slices a strong electric field gradient and electric field strength are observed within the plasma bulk and the electric field shapes at the time slices $t/\tau_{rf} = 0.25$ and $t/\tau_{rf} = 0.75$ are almost specular along the bisector going from the lower left hand corner up to the upper right hand corner, as seen in figure 4(a). The electric field takes its lowest absolute value in the center of the electronegative core, while it assumes higher
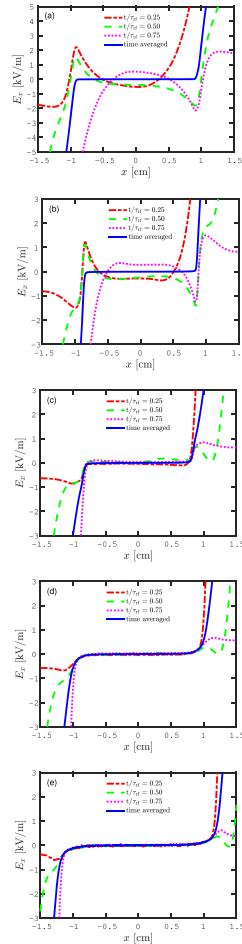
Figure 4. The electric field within the bulk region for various time slices $t/\tau_{rf} = 0.25$ (red dash dotted line), $t/\tau_{rf} = 0.50$ (green dashed line), $t/\tau_{rf} = 0.75$ (violet dotted line), and fully time averaged (blue solid line), for a parallel plate capacitively coupled oxygen discharge at (a) 10 mTorr, (b) 20 mTorr, (c) 30 mTorr, (d) 50 mTorr, and (e) 100 mTorr with a gap separation of 45 mm driven by a 400 V voltage source at driving frequency of 13.56 MHz.

J T Gudmundsson and A Proto

Table 5. The relative partial pressures of the thermal neutrals assuming electrode gaps 25, 30 35, 45 and 60 mm for 50 mTorr pressure calculated by a global (volume averaged) model for 5 W power.

|	$O_2(X^3\Sigma_g^-)$	$O_2(a^1\Delta_g)$	$O_2(b^1\Sigma_g)$	$O(^3P)$
25 mm	0.9970	0.0203	0.0023	0.0045
30 mm	0.9688	0.0215	0.0027	0.0047
35 mm	0.9681	0.0219	0.0030	0.0044
45 mm	0.9683	0.0212	0.0036	0.0044
60 mm	0.9711	0.0177	0.0044	0.0047

absolute values as the sheath region is approached. The peak in the electric field at the sheath edge is mainly caused by a local maximum of the electron density at the sheath edge and the corresponding high value of the electron density gradient on the plasma bulk side of this maximum. At this location diffusion directs the electrons into the plasma bulk, while positive ions flow continuously toward the electrode. This generates an ambipolar field, that couples electron and positive ion motion and accelerate electrons toward the electrode. The time averaged electric field is zero within the plasma bulk. At 20 mTorr the electric field shapes at the time slices $t/\tau_{\rm rf} = 0.25$ and $t/\tau_{\rm rf} = 0.75$ are almost specular specular along the bisector going from the lower left hand corner up to the upper right hand corner, as observed at 10 mTorr. Furthermore, the electric field gradient within the plasma bulk has decreased and the shape is flatter than in the 10 mTorr case for all the three time slices, as seen in figure 4(b). At 30 mTorr the time averaged electric field and the electric field at the time slices profiles $t/\tau_{\rm rf} = 0.25$, $t/\tau_{\rm rf} = 0.50$ and $t/\tau_{\rm rf} = 0.75$ do almost overlap and the electric field is low. At 50 mTorr the electric field within the plasma bulk is roughly zero for all the four cases considered and the electric field profile is flat and electronegative core is wider than at 30 mTorr, as seen in figure 4(d). At 100 mTorr the electric field is zero and the electronegative core is the widest, as shown in 4(e).

4.2. Dependency on electrode spacing

Here we explore how the electron heating mechanism depends on the electrode separation. We vary the electrode separation from 25 to 60 mm while we keep the voltage amplitude at 400 V and the discharge pressure at 50 mTorr. Table 5 shows the relative partial pressure of the most important neutrals. Note that not all the neutrals considered in the global model calculations are shown in table 5 for discharge power of 5 W. The spatio-temporal behavior of the electron power absorption at 50 mTorr for a parallel plate capacitively coupled oxygen discharge driven by a 400 V voltage source at driving frequency of 13.56 MHz is shown in figure 5. For 25 mm electrode spacing a significant electron power absorption (red and yellow areas) and small energy loss (dark blue areas) are evident in the plasma bulk region as seen in figure 5(a). The electron heating appears during the sheath collapse on the bulk side of the sheath edge, while there is cooling (electrons loose energy) on the electrode side

(the lower left hand corner and upper center on the right hand side). There is also apparent significant electron power absorption in the sheath region during sheath expansion and significant power loss during sheath collapse. It is worth to note that the electron power absorption in the plasma bulk is much higher than at 10 mTorr for 45 mm gap distance shown in figure 1(a). For 30 mm electrode spacing, seen in figure 5(b), the electron power absorption within the bulk region has decreased somewhat, and there is strong power absorption during during sheath expansion while the cooling during sheath collapse has decreased. Similarly to the previous case, the electron power absorption within the plasma bulk is much higher than at 20 mTorr for 45 mm gap distance shown in figure 1(b). For 35 mm electrode spacing, the electron power absorption is observed almost solely within the sheath regions and there is almost no electron power absorption within the plasma bulk as seen in figure 5(c). Furthermore, the electron cooling during sheath collapse has decreased substantially. Similar behavior is observed for electrode spacing of 45 and 60 mm seen in figures 5(d) and (e). High frequency oscillations in the electron heating rate, indicating electron–electron two-stream instability, are seen adjacent to the expanding sheath edge in figures 5(d) and (e) for gap sizes 45 and 65 mm, respectively.

Figure 6 shows the time averaged electron power absorption $\langle \mathbf{J}_{\rm e} \cdot \mathbf{E} \rangle$ profile between the electrodes for a parallel plate capacitively coupled oxygen discharge at 50 mTorr driven by a 400 V voltage source at driving frequency of 13.56 MHz as the gap separation is varied. When the electrode separation is 25 mm the electron heating is almost entirely within the plasma bulk and the discharge is operated in the DA-mode. When the electrode separation is 30 mm a combination of the time averaged electron heating in the plasma bulk and in the sheath region is observed and the discharge operates in both DA-mode and α-mode. We see that for electrode separation 35–60 mm the electron heating is almost solely in the sheath region and the discharge is operated in pure α-mode. The peak in the electron power absorbed in the sheath region (within the bulk) has its lowest (highest) value when the gap distance is 25 mm, and it increases (decreases) when the gap distance is enhanced until 45 mm, where a maximum (minimum) in the power absorbed in the sheath region is observed. Then a slight decrease in the absorbed power in the sheath region with respect to the maximum value is observed at 60 mm. The value of the time averaged absorbed power within the bulk is approximately zero for electrode separation in the range 35–60 mm. In order to explore the observed electron heating mode transition further we plot the center electron density and the center electronegativity as a function of the gap separation in figure 7. The electron density increases while the electronegativity decreases with increased gap separation. At 25 mm gap separation the discharge is the most strongly electronegative. The electronegativity (electron density) slightly decreased (increased) when varying the gap size from 25 to 30 mm. When the gap separation is 35 mm the electronegativity (electron density) has drastically reduced (enhanced). Finally at 45 and 60 mm the electronegativity
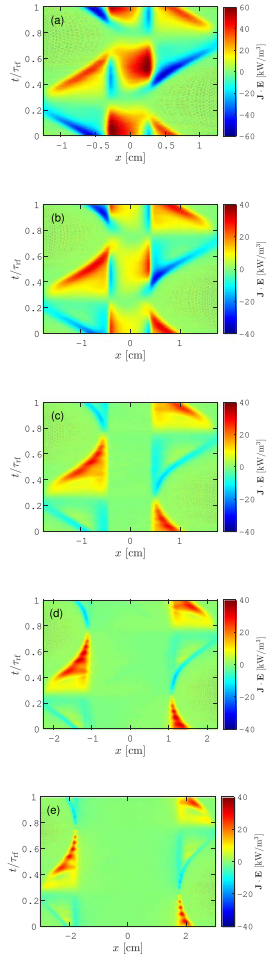
9

J T Gudmundsson and A Proto

Figure 5. The spatio-temporal behavior of the electron power absorption at 50 mTorr for a parallel plate capacitively coupled oxygen discharge with electrode separation of (a) 25 mm, (b) 30 mm, (c) 35 mm, (d) 45 mm and (e) 60 mm driven by a 400 V voltage source at driving frequency of 13.56 MHz.
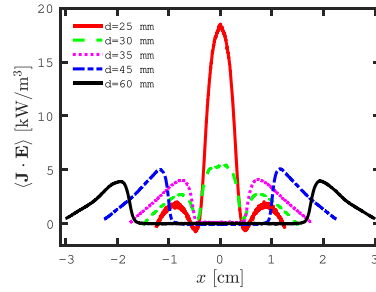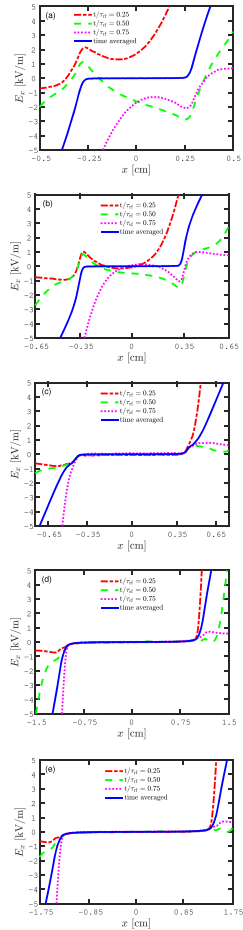

Figure 6. The time averaged electron power absorption for a parallel plate capacitively coupled oxygen discharge at 50 mTorr driven by a 400 V voltage source at driving frequency of 13.56 MHz as the gap separation is varied.
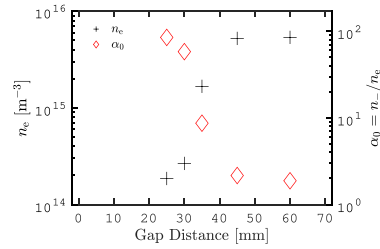
Figure 7. The electron density in the discharge center (left y axis) and the electronegativity in the discharge center (right y axis) as a function of the gap separation for a parallel plate capacitively coupled oxygen discharge at 50 mTorr driven by a 400 V voltage source at driving frequency of 13.56 MHz.

(electron density) approaches its lowest (highest) values. This is consistent with the findings of You *et al* [35], who find that the electron density is found to depend on the electrode separation, observed both experimentally and through PIC/MCC simulation. For a small gap size they observe first a weak increase in the electron density with increased electrode separation, then a strong increase (a jump) around certain gap length followed by a weak increase with further increasing electrode separation. The smaller the electrode separation the larger is the relative contribution of the electrodes to quenching of the metastables. As the metastable density decreases the role of the detachment processes decrease and the negative ion density increases and the electron density decreases which shows up as increased electronegativity.

The DA-mode is accompanied with generation of an electric field within the electronegative core. Figure 8 shows

10

Figure 8. The electric field within the bulk region for various time slices $t/\tau_{rf} = 0.25$ (red dash dotted line), $t/\tau_{rf} = 0.50$ (green dashed line), $t/\tau_{rf} = 0.75$ (violet dotted line), and fully time averaged (blue solid line), for a parallel plate capacitively coupled oxygen discharge at 50 mTorr for (a) 25 mm, (b) 30 mm, (c) 35 mm, (d) 45 mm, and (e) 60 mm gap separation driven by a 400 V voltage source at driving frequency of 13.56 MHz.

the electric field profile in the plasma bulk for various time slices $t/\tau_{rf} = 0.25$ (red dash dotted line), $t/\tau_{rf} = 0.50$ (green dashed line), $t/\tau_{rf} = 0.75$ (violet dotted line), and fully time averaged (blue solid line) at 50 mTorr for 25, 30, 35, 45 and 60 mm gap separation. At 25 mm gap separation the electric field shapes at the time slices $t/\tau_{rf} = 0.25$ and $t/\tau_{rf} = 0.75$ are almost specular along the bisector going from the lower left hand corner up to the upper right hand corner. Furthermore, a strong electric field gradient and electric field strength are observed, as seen in figure 8(a). The electric field takes its lowest absolute value in the center of the electronegative core, while it assumes strong values as the sheath region is approached. The time averaged electric field is flat and zero within the plasma bulk. At 30 mm the electric field gradient within the plasma bulk has decreased and the shape is flatter than in the 25 mm case for all the four cases considered, as seen in figure 8(b), but there is still a significant electric field apparent within the plasma bulk. At 35 mm the electric field do overlap almost perfectly and the electric field profile is flat within the plasma bulk a for the three time slices and the time averaged electric field, as observed in figure 8(c). At 45 mm the shape of the electric field in the plasma bulk is flat for all the four cases considered and the electric field profile is flat and zero along a bigger interval within the gap separation, as seen in figure 8(d). At 100 mTorr the electric profile indicates the widest electronegative core within the gap separation, as shown in figure 8(e).

5. Conclusion

The one-dimensional object-oriented particle-in-cell Monte Carlo collision code oopd1 was applied to explore the evolution of the electron heating mechanism in a capacitively coupled oxygen discharge while the pressure and the gap distance are varied. Keeping the electrode separation fixed at 45 mm and varying the pressure we find that at low pressure (10 mTorr) electron heating occurs both within the bulk and in the sheath regions, and a hybrid DA- and α-mode heating was observed. At 20 mTorr the electron heating in the sheath region dominates and the electron cooling in the sheath region has decreased. At higher pressures (30, 50 and 100 mTorr) the electron heating exhibits an almost pure α-mode and the electron cooling during sheath collapse has decreased substantially. These findings are related to higher electronegativity and generation of electric field when operating at low pressure. At low pressure the effective electron temperature is high and there is efficient creation of negative ions through dissociative attachment. As the pressure is increased the effective electron temperature decreases along with the creation of negative ions. Furthermore, the density of the singlet metastable molecules increases with increased pressure and increased electron density and thus the role of detachment increases. Keeping the pressure fixed while varying the gap distance we find that at 25 mm the electron heating occurs both within the bulk and in the sheath region, where the former dominates over the latter. At 30 mm the

electron heating in the sheath region dominates over the bulk. For larger gap separation (35, 45 and 60 mm) no heating is observed in the bulk and the discharge operates in pure α-mode. The smaller the discharge gap, the higher the relative contribution of surface quenching of the singlet metastable molecules, which results in lower singlet metastable molecule density and thus lower reaction rate for detachment and higher electronegativty. Thus the observed transition is related to high electronegativity and high electric field within the electronegative core when the electrode separation is small.

Acknowledgments

ORCID iDs

J T Gudmundsson ● https://orcid.org/0000-0002-8153-3209
A Proto ● https://orcid.org/0000-0003-2288-935X

References

[1] Godyak V A, Piejak R B and Alexandrovich B M 1992 *Phys. Rev. Lett.* **68** 40
[2] Belenguer P and Boeuf J 1990 *Phys. Rev. A* **41** 4447
[3] Lieberman M and Godyak V 1998 *IEEE Trans. Plasma Sci.* **26** 955
[4] Godyak V A and Khanneh A S 1986 *IEEE Trans. Plasma Sci.* **14** 112
[5] Schulze J, Derzsi A, Dittmann K, Hemke T, Meichsner J and Donkó Z 2011 *Phys. Rev. Lett.* **107** 275001
[6] Liu Y-X, Schüngel E, Korolov I, Donkó Z, Wang Y-N and Schulze J 2016 *Phys. Rev. Lett.* **116** 255002
[7] Liu Y-X, Korolov I, Schüngel E, Wang Y-N, Donkó Z and Schulze J 2017 *Plasma Sources Sci. Technol.* **26** 055024
[8] Irving S 1968 *Proc. Kodak Photoresist Seminar (Los Angeles, California, May 20–21)* (Rochester, New York: Eastman, Kodak) pp 26–9
[9] Tolliver D L 1984 *VLSI Electronics: Microstructure Science* ed N G Einspruch and D M Brown vol 8 (Orlando: Academic) pp 1–24
[10] Hartney M A, Hess D W and Soane D S 1989 *J. Vac. Sci. Technol. B* **7** 1
[11] Chashmejahanbin M R, Salimi A and Ershad Langroudi A 2014 *Int. J. Adhes. Adhes.* **49** 44
[12] Vesel A and Mozetic M 2017 *J. Phys. D: Appl. Phys.* **50** 293001
[13] Kawai Y, Konishi N, Watanabe J and Ohmi T 1994 *Appl. Phys. Lett.* **64** 2223
[14] Hess D W 1999 *IBM J. Res. Dev.* **43** 127
[15] Vahedi V and Surendra M 1995 *Comput. Phys. Commun.* **87** 179
[16] Lee S H, Iza F and Lee J K 2006 *Phys. Plasmas* **13** 057102
[17] Lichtenberg A J, Vahedi V, Lieberman M A and Rognlien T 1994 *J. Appl. Phys.* **75** 2339
[18] Babaeva N Y, Lee J K, Shon J W and Hudson E A 2005 *J. Vac. Sci. Technol. A* **23** 699
[19] Bronold F X, Matyash K, Schneider D T R and Fehske H 2007 *J. Phys. D: Appl. Phys.* **40** 6583
[20] Matyash K, Schneider R, Dittmann K, Meichsner J, Bronold F X and Tskhakaya D 2007 *J. Phys. D: Appl. Phys.* **40** 6601
[21] Schüngel E, Zhang Q-Z, Iwashita S, Schulze J, Hou L-J, Wang Y-N and Czarnetzki U 2011 *J. Phys. D: Appl. Phys.* **44** 285205
[22] Zhang Q-Z, Jiang W, Hou L-J and Wang Y-N 2011 *J. Appl. Phys.* **109** 013308
[23] Derzsi A, Lafleur T, Booth J-P, Korolov I and Donkó Z 2016 *Plasma Sources Sci. Technol.* **25** 015004
[24] Derzsi A, Bruneau B, Gibson A, Johnson E, O'Connell D, Gans T, Booth J-P and Donkó Z 2017 *Plasma Sources Sci. Technol.* **26** 034002
[25] Donkó Z *et al* 2018 *Plasma Phys. Control. Fusion* **60** 014010
[26] Gudmundsson J T, Kawamura E and Lieberman M A 2013 *Plasma Sources Sci. Technol.* **22** 035011
[27] Gudmundsson J T and Ventéjou B 2015 *J. Appl. Phys.* **118** 153302
[28] Hannesdottir H and Gudmundsson J T 2016 *Plasma Sources Sci. Technol.* **25** 055002
[29] Gudmundsson J T and Hannesdottir H 2017 *AIP Conf. Proc.* **1811** 120001
[30] Gudmundsson J T and Snorrason D I 2017 *J. Appl. Phys.* **122** 193302
[31] Gudmundsson J T, Snorrason D I and Hannesdottir H 2018 *Plasma Sources Sci. Technol.* **27** 025009
[32] Proto A and Gudmundsson J T 2018 *Atoms* **6** 65
[33] Proto A and Gudmundsson J T 2018 *Plasma Sources Sci. Technol.* **27** 074002
[34] Gudmundsson J T and Lieberman M A 2015 *Plasma Sources Sci. Technol.* **24** 035016
[35] You K-H, Schulze J, Derzsi A, Donkó Z, Yeom H J, Kim J H, Seong D-J and Lee H-C 2019 *Phys. Plasmas* **26** 013503
[36] Hammel J and Verboncoeur J P 2003 *Bull. Am. Phys. Soc.* **48** 66
[37] Verboncoeur J P, Langdon A B and Gladd N T 1995 *Comput. Phys. Commun.* **87** 199
[38] Itikawa Y 2009 *J. Phys. Chem. Ref. Data* **38** 1
[39] Phelps A V 1985 *Tech. Rep. JILA Information Center Report 28* University of Colorado at Boulder http://jilawww. colorado.edu/~avp/collision_data/electronneutral/ electron.txt
[40] Shyn T W and Sweeney C J 2000 *Phys. Rev. A* **62** 022711
[41] Green M A, Teubner P J O, Brunger M J, Cartwright D C and Campbell L 2001 *J. Phys. B: At. Mol. Opt. Phys.* **34** L157
[42] Krishnakumar E and Srivastava S K 1992 *Int. J. Mass Spectrom. Ion Process* **113** 1
[43] Rapp D and Briglia D 1965 *J. Chem. Phys.* **43** 1480
[44] Thomas L D and Nesbet R K 1975 *Phys. Rev. A* **12** 1729
[45] Itikawa Y and Ichimura A 1990 *J. Phys. Chem. Ref. Data* **19** 637
[46] Laher R R and Gilmore F R 1990 *J. Phys. Chem. Ref. Data* **19** 277
[47] Kim Y-K and Desclaux J-P 2002 *Phys. Rev. A* **66** 012708
[48] Vejby-Christensen L, Kella D, Mathur D, Pedersen H B, Schmidt H T and Andersen L H 1996 *Phys. Rev. A* **53** 2371
[49] Comer J and Schulz G J 1974 *J. Phys. B: At. Mol. Phys.* **7** L249
[50] Belostotsky S G, Economou D J, Lopaev D V and Rakhimova T V 2005 *Plasma Sources Sci. Technol.* **14** 532
[51] Mul P M and McGowan J W 1979 *J. Phys. B: At. Mol. Phys.* **12** 1591
[52] Peverall R *et al* 2001 *J. Chem. Phys.* **114** 6679
[53] Olson R E 1972 *J. Chem. Phys.* **56** 2979
[54] Padgett R and Peart B 1998 *J. Phys. B: At. Mol. Opt. Phys.* **31** L995
[55] Hayton D A and Peart B 1993 *J. Phys. B: At. Mol. Opt. Phys.* **26** 2879

180

[56] Ellis H W, Pai R Y, McDaniel E W, Mason E A and Viehland L A 1976 *At. Data Nucl. Data Tables* **17** 177
[57] Baer T, Murray P T and Squires L 1978 *J. Chem. Phys.* **68** 4901
[58] Wilcox J B and Moran T F 1981 *J. Phys. Chem.* **85** 989
[59] Lindsay B G and Stebbings R F 2005 *J. Geophys. Res.* **110** A12213
[60] Stebbings R F, Smith A C H and Ehrhard H 1964 *J. Geophys. Res.* **69** 2349
[61] Stebbings R F, Smith A C H and Gilbody H B 1963 *J. Chem. Phys.* **38** 2280
[62] Stebbings R F 1966 *Advances in Chemical Physics: Molecular Beams* ed J Ross vol 10 (New York: Wiley) pp 195–246
[63] Muschlitz E E 1959 *Proc. 4th Int. Conf. on Phenomena in Ionized Gases, (Uppsala, Sweden, August 17–21)* ed N R Nilsson (Amsterdam: North-Holland Publishing Co.) pp 52–6
[64] Brunetti B, Liuti G, Luzzatti E, Pirani F and Vecchiocattivi F 1981 *J. Chem. Phys.* **74** 6734
[65] Jaffke T, Meinke M, Hashemi R, Christophorou L G and Illenberger E 1992 *Chem. Phys. Lett.* **193** 62
[66] Aleksandrov N L 1978 *Sov. Phys.-Tech. Phys* **23** 806
[67] Baulch D L, Cox R A, Crutzen P J, Hampson R F, Kerr J A, Troe J and Watson R T 1982 *J. Phys. Chem. Ref. Data* **11** 327
[68] Kollath R 1956 *Elektronen-Emission Gasentladungen I* (*Handbuch der Physik* vol 21) ed S Flügge (Berlin: Springer) pp 232–303
[69] Derzsi A, Korolov I, Schüngel E, Donkó Z and Schulze J 2015 *Plasma Sources Sci. Technol.* **24** 034002
[70] Daksha M, Derzsi A, Wilczek S, Trieschmann J, Mussenbrock T, Awakowicz P, Donkó Z and Schulze J 2017 *Plasma Sources Sci. Technol.* **26** 085006
[71] Braginsky O, Kovalev A, Lopaev D, Proshina O, Rakhimova T, Vasilieva A, Voloshin D and Zyryanov S 2012 *J. Phys. D: Appl. Phys.* **45** 015201
[72] Booth J P and Sadeghi N 1991 *J. Appl. Phys.* **70** 611
[73] Gudmundsson J T and Thorsteinsson E G 2007 *Plasma Sources Sci. Technol.* **16** 399
[74] Sharpless R L and Slanger T G 1989 *J. Chem. Phys.* **91** 7947
[75] O'Brien R J and Myers G H 1970 *J. Chem. Phys.* **53** 3832
[76] Kechkar S 2015 *PhD Thesis* Dublin City University, Dublin
[77] Kechkar S 2016 Personal communications
[78] Kechkar S, Swift P, Kelly S, Kumar S, Daniels S and Turner M 2017 *Plasma Sources Sci. Technol.* **25** 065009
[79] Kawamura E, Birdsall C K and Vahedi V 2000 *Plasma Sources Sci. Technol.* **9** 413
[80] Birdsall C 1991 *IEEE Trans. Plasma Sci.* **19** 65
[81] Chatterjee A *et al* 2018 *Proc. 24th Europhysics Sectional Conf. on Atomic and Molecular Physics of Ionized Gases (ESCAMPIG XX) (Glasgow, Scotland)* pp 28–9
[82] Booth J P, Chatterjee A, Guaitella O, de Oliveira N, Nahon L and Western C M 2018 *Proc. 24th Europhysics Sectional Conf. on Atomic and Molecular Physics of Ionized Gases (ESCAMPIG XX) (Glasgow, Scotland)* pp 159–60
[83] Vender D and Boswell R W 1992 *J. Vac. Sci. Technol.* A **10** 1331
[84] O'Connell D, Gans T, Vender D, Czarnetzki U and Boswell R 2007 *Phys. Plasmas* **14** 034505
[85] Wilczek S *et al* 2016 *Phys. Plasmas* **23** 063514
[86] O'Connell D, Gans T, Meige A, Awakowicz P and Boswell R W 2008 *IEEE Trans. Plasma Sci.* **36** 1382
[87] Godyak V A and Piejak R B 1990 *Phys. Rev. Lett.* **65** 996
[88] Surendra M and Graves D B 1991 *Phys. Rev. Lett.* **66** 1469
[89] Lee M-H, Lee H-C and Chung C-W 2010 *Phys. Rev. E* **81** 046402
[90] Vahedi V, Birdsall C K, Lieberman M A, DiPeso G and Rognlien T D 1993 *Plasma Sources Sci. Technol.* **2** 273

13

181

Paper IV

Electron power absorption dynamics in a low pressure radio frequency driven capacitively coupled discharge in oxygen

A. Proto and J.T. Gudmundsson

Journal of Applied Physics, **128**(11) (2020) 113302

Electron power absorption dynamics in a low pressure radio frequency driven capacitively coupled discharge in oxygen 🔵

A. Proto[1] 🔵 and J. T. Gudmundsson[1,2,a)] 🔵

AFFILIATIONS

[1]Science Institute, University of Iceland, Dunhaga 3, IS-107 Reykjavik, Iceland
[2]Department of Space and Plasma Physics, School of Electrical Engineering and Computer Science,
KTH Royal Institute of Technology, SE-100 44 Stockholm, Sweden

[a)]Author to whom correspondence should be addressed: tumi@hi.is

ABSTRACT

We use the one-dimensional object-oriented particle-in-cell Monte Carlo collision code oopd1 to explore the properties and the origins of both the electric field and electron power absorption within the plasma bulk for a capacitively coupled oxygen discharge operated at 10 and 100 mTorr for a gap distance of 45 mm. The properties of the electric field at three different time slices as well as time averaged have been explored considering the moments of the Boltzmann equation. The electron power absorption is distinctly different at these operating pressures. The most relevant contributions to the electric field at different time steps come from the pressure terms, the ambipolar and the electron temperature gradient terms, along with the ohmic term. The same applies for the electron power absorption. At both 10 and 100 mTorr, the relative ohmic contribution to the electron power absorption remains roughly the same, while the ambipolar term contributes to power absorption and the temperature gradient term to electron cooling at 100 mTorr, and the opposite applies at 10 mTorr. At 100 mTorr, the discharge is weakly electronegative, and electron power absorption is mainly due to sheath expansion, while at 10 mTorr, it is strongly electronegative, and the electron power absorption occurs mainly within the electronegative core and the drift-ambipolar mode dominates. The agreement between the calculated values and the simulations is good for both the electric field and the electron power absorption within the plasma bulk and in the collapsed sheath region for all the cases considered.

Published under license by AIP Publishing. https://doi.org/10.1063/5.0019340

I. INTRODUCTION

The low pressure radio frequency (rf) driven capacitively coupled discharge has been applied in integrated circuit manufacturing for a few decades. The capacitively coupled discharge consists of two parallel electrodes, typically with a radius of a few tens of cm, separated by a few cm and driven by a power generator. These discharges have been explored extensively over the past few decades. The power transfer mechanism, which is commonly referred to as "electron heating" or "electron power absorption" in the literature,[1] is still a topic rather poorly understood. Although the electron power absorption mechanism is a topic widely studied and discussed over the past decades, a fully consistent and general mathematical–physical explanation of the several physical mechanisms involved in the power transfer mechanism is still lacking. This is, in particular, true for the electronegative capacitively coupled discharge.

It is widely accepted that the electron heating can be divided into two components: the ohmic heating (collisional) and the stochastic heating (collisionless), while several operating modes have been identified in the capacitively coupled discharge including the stochastic electron heating due to the sheath motion (α-mode),[2] secondary electron emission due to ion and neutral bombardment of the electrodes,[3] the drift-ambipolar (DA) mode,[4] non-linear electron resonance heating (NERH),[5–9] the electron bounce resonance effect,[10,11] and the generation of series resonance oscillations.[5,7] In a strongly electronegative discharge, the electrical conductivity tends to be low, and due to large ion inertia, high electric field is induced within the plasma bulk (electronegative core). Furthermore, ambipolar fields appear near the sheath edges.

The particle-in-cell (PIC) method, when combined with the Monte Carlo (MC) treatment of collision processes, is the

most frequently used numerical approach to investigate the properties and the operating modes of low pressure capacitively coupled-discharges. The combination of the particle-in-cell (PIC) method and the Monte Carlo collision (MCC) treatment of collision processes is commonly referred to as the PIC/MCC method. The PIC/MCC method is a self-consistent kinetic approach that has become a predominant numerical approach to investigate the properties of the low pressure capacitively coupled discharge.

The one-dimensional-object-oriented plasma device one (oopd1) code allows having the simulated particles of different weights so that in principle, both charged and neutral particles can be tracked during the simulation. Earlier, we benchmarked the basic reaction set for the oxygen discharge in the oopd1 code to the xpdp1 code.[12] In recent years, the oxygen reaction set in the oopd1 code has been improved significantly.[12–14] The oopd1 code has been applied to explore the electron power absorption in the capacitively coupled oxygen discharge while varying the various external parameters and operating conditions such as discharge pressure,[14–16] driving voltage amplitude,[17] driving frequency,[18] the secondary electron emission,[14,19] the surface quenching of the metastable states,[20] and the electrode gap distance.[21]

During the past decades, several attempts to describe correctly the behavior of the electron heating using the Boltzmann equation have been made. Surendra and Dalvie[22] were the first to set up a mathematical model to describe the electron power absorbed using the Boltzmann equation for both electrons and ions using the PIC results as input. In the years that followed, several authors used the formulation set by Surendra and Dalvie[22] to develop similar models inspired by their results.[23–29] Among these, Brinkmann[27] derived a unified description of electron power absorption in capacitively coupled discharges using a mathematical formulation where the electron density profile has been approximated by a smooth step function, finding that the total time averaged electron power absorption is the sum of four terms, each one corresponding to one of the heating mechanism known from separate previous theories, i.e. NERH, stochastic heating (hard wall model), ambipolar/pressure heating, and ohmic heating. Brinkmann also demonstrated that a time dependent temperature is necessary to obtain a non-zero time averaged electron power absorption. More recently, Schulze *et al.* used a simplified moment analysis of the Boltzmann equation (the Boltzmann term analysis) where the electron temperature gradient was both neglected and considered[30,31] in order to describe both the electric field and the electron power absorbed in an electropositive low pressure capacitively coupled argon discharge. They found that the time averaged ambipolar electron power absorption completely vanishes for a temporally independent electron temperature. This approach has recently been applied to explore the electron power absorption mechanisms in a capacitively coupled oxygen discharge by Vass *et al.*[32] Using the Boltzmann term analysis, they found that the ohmic contribution to the electron power absorption is small at different time steps at low pressure while it becomes important at higher pressures. Finally, they observed that at low pressure, the space-time averaged electron power absorbed was entirely given by the ohmic term and that the pressure term contribution increases as the pressure is increased. Here, we use the Boltzmann term analysis to investigate

the origins of both the electric field and the power absorbed by the electrons at different time steps within both the plasma bulk and the sheath collapsed region and the related time averaged quantities within the plasma bulk in a capacitively coupled oxygen discharge at 10 and 100 mTorr for a gap distance of 45 mm. The electron power absorption in the capacitively coupled oxygen discharge is distinctly different when the discharge is operated at 100 mTorr than when it is operated at 10 mTorr.[14,15,21] When operating at 100 mTorr with a gap size of 45 mm, the discharge is operated in an α-mode and stochastic electron heating dominates, while at 10 mTorr, the discharge is more electronegative and the DA-mode dominates. The main task of the current work is to perform a Boltzmann term analysis of a capacitively coupled oxygen discharge in order to shed light on the underlying physical mechanism behind the electric field and the electron power absorbed and to gain understanding of the electron power absorption in a capacitively coupled oxygen discharge operated at different pressures (10 and 100 mTorr), which represent the hybrid DA-α mode and the pure α mode, respectively. We will follow the framework of the Boltzmann term analysis given in the recent work of Schulze *et al.*[31] with some modifications since the physical conditions and gas considered are different. The current work is structured as follows. In Sec. II, we give a brief overview of the simulation setup. In Sec. III, we show the spatiotemporal profiles of both the total charge density and the quasineutrality deviation along with both the total charge density and the density profiles for all the species involved at different time steps and time averaged. Section IV discusses the model. In Subsection IV A, a simple fluid model based on the work of Schulze *et al.*[31] is employed to explore the behavior of both the electric field and the electron power absorbed at both 100 and 10 mTorr. The results from both the simulations and the calculations at both 10 and 100 mTorr are discussed and compared in Sec. V. Finally, Sec. VI summarizes our findings.

II. THE SIMULATION

The one-dimensional (1d-3v) object-oriented particle-in-cell Monte Carlo collision (PIC/MCC) code oopd1[12] is applied to a capacitively coupled oxygen discharge. In 1d-3v PIC codes, the model system has one spatial dimension and three velocity components. The oopd1 code, such as the well known xpdp1 code, is a general plasma device simulation tool capable of simulating various types of devices, where the plasma is the main actor, such as particle beams, electrical breakdown, particle accelerators as well as processing discharges.[12] The oxygen reaction set included in the oopd1 code is rather extensive, and nine different species are considered: electrons, the ground state neutrals $O(^3P)$ and $O_2(X^3\Sigma_g^-)$, the negative ions O^-, the positive ions O^+ and O_2^+, and the metastables O (^1D), $O_2(a^1\Delta_g)$, and $O_2(b^1\Sigma_g^+)$. The basic reaction set included $O_2(X^3\Sigma_g^-)$, O_2^+, and O^-. In our earlier work, we added oxygen atoms in the ground state $O(^3P)$ and ions of the oxygen atom O^+ to the oopd1 code.[12] In a later work, the singlet metastable molecule $O_2(a^1\Delta_g)$ and the metastable oxygen atom $O(^1D)$ were added,[13] as well as the singlet metastable molecule $O_2(b^1\Sigma_g^+)$.[14] The full oxygen reaction set together with the cross sections used has been discussed in our earlier works and will not be repeated here.[12–14,21] We assume a geometrically symmetric capacitively

coupled discharge where one of the electrodes is driven by an rf voltage at a single frequency,

$$V(t) = V_0 \sin(2\pi f t), \qquad (1)$$

while the other electrode is grounded. Here, V_0 is the voltage amplitude, f the driving frequency, and t the time. For this current study, we assume the discharge to be operated at the pressure of 10 mTorr and 100 mTorr with voltage amplitude $V_0 = 400$ V with an electrode separation of 4.5 cm. A capacitor of 0.1 μF is connected in series with the voltage source. The electrode diameter and the driving frequency are assumed to be 10.25 cm and 13.56 MHz, respectively. These are the same parameters as assumed in our previous work.[21] The time step Δt and the grid spacing Δx are set to resolve the electron plasma frequency and the electron Debye length of the low energy electrons, respectively, according to $\omega_{pe}\Delta t < 0.2$, where ω_{pe} is the electron plasma frequency and the simulation grid consists of 1000 equal cells. The electron time step is 3.68×10^{-11} s. The simulation was run for 5.5×10^6 time steps, which corresponds to 2750 rf cycles as it takes roughly 1700 rf cycles to reach equilibrium for all particles. Time averaged plasma parameters shown, such as the densities, the electron power absorption, and the effective electron temperature, are averaged over 1000 rf cycles. All particle interactions are treated by the Monte Carlo method with a null-collision scheme.[33] For the heavy particles, we apply sub-cycling, where the heavy particles are advanced every 16 electron time steps[34] and an initial parabolic density profile has been assumed.[34]

The kinetics of the charged particles (electrons, O_2^+ ions, O^+ ions, and O^- ions) was followed for all energies. Since the neutral gas density is much higher than the densities of charged species, the neutral species at thermal energies (below a certain cut-off energy) are treated as a background with a fixed density and temperature and maintained uniformly in space. The main challenge when PIC/MCC simulations are applied to simulate molecular gases has to due with the timescale difference between the processes of dissociation and the processes involving charged particles. Therefore, a global model[35] is used beforehand to determine the partial pressure of the various neutrals in the discharge as discussed in Proto and Gudmundsson,[20] i.e., the ground state neutral atoms $O(^3P)$ and the metastables $O(^1D)$, $O_2(a^1\Delta_g)$, and $O_2(b^1\Sigma_g^+)$ under certain control parameters including the discharge pressure, the absorbed power, the gap separation between the two electrodes, etc. The absorbed power determined by the PIC/MCC simulation is used as an input parameter in the global model calculations, iteratively. The partial pressure of the atoms and metastable species obtained from the global model calculation is then used as the partial pressure of these species in the neutral background gas in the simulation. Note that a global model is mainly developed to model high density low pressure discharges such as inductively coupled discharges rather than capacitively coupled discharges, and the proportion of the power absorbed by the electrons in the former is much larger than in the latter. Therefore, the global model may overestimate the atom and metastable density within the discharge, especially when operating at low pressure. The fractional densities for the neutrals $O_2(X^3\Sigma_g^-)$, $O_2(a^1\Delta_g)$, $O_2(b^1\Sigma_g)$, $O(^3P)$, and $O(^1D)$, estimated using the global model calculations,

TABLE I. The relative partial pressures of the thermal neutrals at 10 and 100 mTorr calculated by a global (volume averaged) model for 1.8 W power.

	$O_2(X^3\Sigma_g^-)$	$O_2(a^1\Delta_g)$	$O_2(b^1\Sigma_g)$	$O(^3P)$
10 mTorr	0.9801	0.0148	0.0016	0.0008
100 mTorr	0.9877	0.0017	0.0009	0.0095

are listed in Table I. These values have been used as input for the PIC/MCC simulation as the partial pressures of the neutral background gas. These neutral background species are assumed to have a Maxwellian velocity distribution at the gas temperature (here, $T_n = 26$ meV). The kinetics of the neutrals are followed when their energy exceeds a preset energy threshold value. The energy threshold values used here for the various neutral species are listed in Table II. The thresholds were chosen in order to keep the number of simulated particles within a suitable range, typically 10^4–10^5 particles. Particles with energy below this threshold energy are assumed to belong to the neutral background.

Note that the background neutrals are assumed to be uniform within the discharge. However, we are aware that the electrode surfaces have a significant influence on the neutral density profiles. The density profiles for fast neutrals indicate that the oxygen atom density decreases and the molecular metastable density increases in the electrode vicinity.[14] As an oxygen atom O (^3P) hits the electrode, it is assumed that half of the atoms are reflected as $O(^3P)$ at room temperature and the other half recombines to from the ground state oxygen molecule $O_2(X^3\Sigma_g^-)$ at room temperature. Similarly, as a metastable oxygen atom $O(^1D)$ hits the electrode, half of the atoms are quenched to form $O(^3P)$, and the other half is assumed to recombine to form the ground state oxygen molecule $O_2(X^3\Sigma_g^-)$ at room temperature. The surface quenching coefficients for the singlet metastable molecules on the electrode surfaces are assumed to have a value of $\gamma_{wqa} = 0.007$ and $\gamma_{wqb} = 0.1$ for $O_2(a^1\Delta_g)$ and $O_2(b^1\Sigma_g)$, respectively. The influence of the surface quenching coefficients of the singlet metastable molecule on the electron heating mechanism has been

TABLE II. The parameters of the simulation, the particle weight, the energy threshold above which kinetics of the neutral particles are followed, and the wall recombination and quenching coefficients for the neutral species on the electrode surfaces.

Species	Particle weight (range)	Energy threshold (meV)	Coefficient (recomb./quenching)
$O_2(X^3\Sigma_g^-)$	5×10^7	500	
$O_2(a^1\Delta_g)$	5×10^6	100	0.007
$O_2(b^1\Sigma_g)$	5×10^6	100	0.1
$O(^3P)$	5×10^7	500	0.5
$O(^1D)$	5×10^7	50	0.5/0.5
O_2^+	$10^7 - 10^8$	...	
O^+	$10^6 - 10^7$	...	
O^-	$5 \times 10^7 - 10^8$	...	
e	$10^7 - 10^8$	...	

185

explored in detail in an earlier work,[20] where it has been demonstrated that the influence of γ_{wqa} on the overall discharge properties can be rather significant. The surface quenching and recombination coefficients used in this current work are listed in Table II. Note that the oxygen reaction set used in this current study is significantly more extensive than the one used by Vass *et al.*[32] where the only metastable state included is the singlet metastable molecule $O_2(^1\Delta_g)$. To estimate the density of the singlet metastable molecule $O_2(^1\Delta_g)$, they assume a homogeneous spatial density where there is a balance between electron impact excitation and quenching at the electrodes.[36,37]

Secondary electron emission and electron reflection have been incorporated into the discharge model.[14] The energy dependent secondary electron emission yield for a dirty surface has been employed,[14] and the electrons are assumed to be elastically reflected from the electrodes independently of their energy and their angle of incidence with a probability of 0.2.[19] The secondary electron emission due to the electron impact on the electrodes has been neglected here as in all our previous works on the oxygen discharge.

III. RESULTS FROM THE SIMULATION

Through recent PIC/MCC simulations of a capacitively coupled oxygen discharge, it has been demonstrated that the singlet metastable molecular states have a significant influence on the electron power absorption mechanism[13–16] as well as the ion energy distribution.[38] At low (high) pressure and high (low) electronegativity, i.e., 10 mTorr (50–500 mTorr), the electron power absorption is mainly located within the plasma bulk (the sheath regions).[14,15] Furthermore, when operating at low pressure, the time averaged electron power absorption within the discharge is due to a hybrid drift-ambipolar mode, a (DA-mode), and an α-mode, and while operating at higher pressures, the electron power absorption is due

to stochastic heating and the discharge is operated in a pure α-mode.[17,18] It has also been demonstrated that detachment by singlet molecular metastable states is the process that has the most influence on the electron power absorption process in the higher pressure regime, while it has almost a negligible influence at lower pressures.[14–16] All the quantities returned by the simulations and involved in the calculations for both the electric field and the electron power absorption in the following sections are arrays extended along the x-axis, i.e., the discharge gap length. In particular, every single component of the electron temperature has been calculated as $T_{e,ii} = \frac{2}{e}\mathcal{E}_{e,ii} - \frac{m_e}{e}u_{e,i}^2$, where $\mathcal{E}_{e,ii}$ and $u_{e,ii}$, with $i = x, y, z$, are the mean electron energy density and the electron mean velocity, respectively. Since $\mathcal{E}_{e,i} = \frac{m_e}{2}\langle v_{e,i}^2\rangle$ by definition, the expression for the electron temperature given above is the same as the one shown by Wilczek *et al.*,[1] when the particle mean velocity is not negligible.

Figure 1 shows the density profiles for O_2^+ ions, O^+ ions, O^- ions, and electrons at 100 and 10 mTorr. At 100 mTorr, the center electronegativity is 3.55 and at 10 mTorr it is 93.64. The electronegative discharge consists of an electronegative core connected to electropositive edge plasma regions.[39,40] At 100 mTorr [Fig. 1(a)], both O^- ion and O_2^+ ion density profiles have a similar shape within the bulk region, while the O^- ion density decreases more steeply than the O_2^+ ion density profile approaching the sheath edges. We also see that the electron density profile is somewhat lower than both the O^- ion and the O_2^+ ion density profiles while it decreases sharply within both the sheath regions. At 10 mTorr [Fig. 1(b)], the situation is different. First of all, we see that O^- and the O_2^+ ion density profiles perfectly overlap within the bulk region and that the O^- ion density profile decreases more steeply than the O_2^+ density profile beyond the sheath edges. The time averaged value of both the O^- and the O_2^+ ion density profiles within the bulk region is slightly lower than in the 100 mTorr case. The electron density in the bulk plasma is
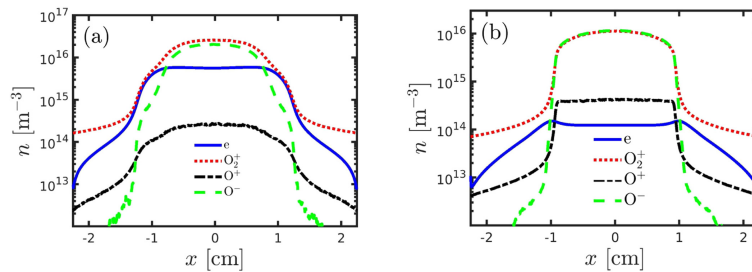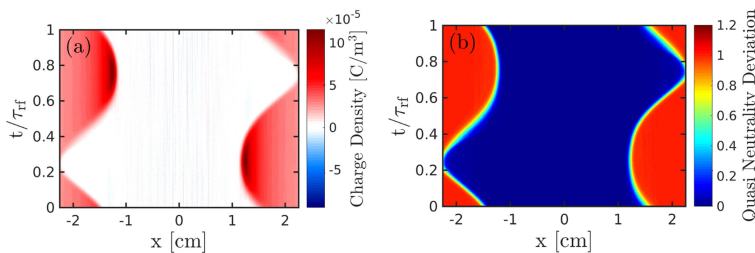

FIG. 1. The density profiles for charged particles at (a) 100 mTorr and at (b) 10 mTorr in a parallel plate capacitively coupled discharge with a gap separation of 45 mm driven by a 400 V voltage source at 13.56 MHz.

186

FIG. 2. The spatiotemporal behavior of the (a) total charge density and of the (b) quasineutrality deviation, defined by Eqs. (2) and (3), respectively, over the full gap length for a parallel plate capacitively coupled oxygen discharge at 100 mTorr for 45 mm of gap separation driven by a 400 V voltage source at a driving frequency of 13.56 MHz.

roughly two orders of magnitude lower than the O_2^+ and O^- densities. Moreover, we observe that the O^+ density is higher than the electron density within the bulk region, contrary to the 100 mTorr case. We also observe that the O^+ density profile is more flattened within the bulk region and that it decreases more steeply than for the 100 mTorr case. The electron density profile is flat and constant within the bulk region, and it has equal absolute maxima on both the sheath edges.

Figure 2(a) shows the spatiotemporal behavior of the total charge density at 100 mTorr over the full gap length for a full period defined as follows.

$$\text{Total Charge Density} = e\left(n_{O_2^+} + n_{O^+} - n_{O^-} - n_e\right). \quad (2)$$

First, we observe a net zero charge density within the bulk region and the fully collapsed sheath regions. Second, the right (left) sheath region is positively charged and reaches its maximum extension at $t/\tau_{rf} = 0.25$ ($t/\tau_{rf} = 0.75$). Moreover, the right (left) sheath positive net charge has a peak on the bulk side of the right (left) sheath edge and slowly decreases while approaching the right (left) electrode. Figure 2(b) shows the spatiotemporal behavior of the quasineutrality deviation at 100 mTorr over the full gap length defined as follows:

$$\text{Quasineutrality deviation} = \frac{\left(n_{O_2^+} + n_{O^+} - n_{O^-} - n_e\right)}{n_{O_2^+} + n_{O^+}}. \quad (3)$$

We observe that the quasineutrality deviation uniquely identifies the sheath region. Indeed, the quasineutrality deviation value is 1 within the expanded sheaths, while it is 0 within the plasma bulk and the sheath collapse regions and it has an intermediate value on the bulk-sheath time varying interface. Figure 3(a) shows the spatiotemporal behavior of the total charge density at 10 mTorr over

the full gap length for a full period defined by Eq. (2). First, we observe a net positive (negative) charged stripe that appears on the sheath side (on the bulk side) of both the sheath edges over the full rf cycle (on both the collapsing sheath edges). The positive charged stripe density strongly increases on the sheath side of the expanded sheath edge. This positive charged stripe was absent in the 100 mTorr case as shown in Fig. 2(a). Such a difference with respect to the 100 mTorr case is due to the fact that the electron mean free path is longer at low pressures so that they leave the positive ions behind while crossing the sheath edge during the sheath collapse. For example, at $t/\tau_{rf} = 0.25$, on very short time scales, a net negative ambipolar field builds up [Fig. 3(a)], which induces a recall force on the bulk electrons and a pushing force on the bulk positive ions toward the collapsing sheath edge. For this reason, an excess of positive charges on the immediate sheath side of both the collapsed sheath edges. It is worth noting that, once crossed the sheath side of the collapsed sheath edge, the electrons are free to accelerate toward the left electrode due to the flux compensation effect. On the other hand, a positive peak in the ambipolar field is observed on the bulk side of the collapsed sheath edge at 10 mTorr [Fig. 3(a)]. Such a peak is absent at 100 mTorr [Fig. 2(a)]. This can be explained considering that, at longer time scales, when the electrons are repelled from the sheath side of the collapsed sheath edge, the ambipolar field changes the sign and becomes positive on the bulk side of the collapsed sheath edge. Such a behavior is responsible for the negative charge excess observed on the bulk side of the collapsed sheath edge. Moreover, under the action of the ambipolar force, the electrons are confined within the bulk and the collapsed sheath region. The same reasoning can also be applied at both $t/\tau_{rf} = 0.50$ and $t/\tau_{rf} = 0.75$. We also observe that the sheath regions reach a larger extension at both $t/\tau_{rf} = 0.25$ and $t/\tau_{rf} = 0.75$ with respect to the 100 mTorr case, while the net positive charge present on the sheath side of both the sheath edges has a lower value when the sheath approaches its maximum extension. The net charge in the fully expanded sheath regions at 10 mTorr is
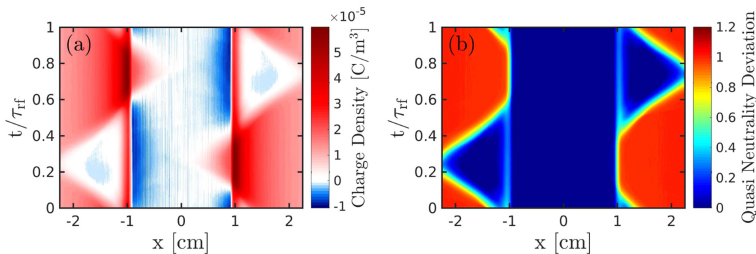
187

FIG. 3. The spatiotemporal behavior of the (a) total charge density and the (b) quasineutrality deviation, defined by Eqs. (2) and (3), respectively, over the full gap length for a parallel plate capacitively coupled oxygen discharge at 10 mTorr for 45 mm of gap separation driven by a 400 V voltage source at a driving frequency of 13.56 MHz.

globally lower than in the 100 mTorr case. Figure 3(b) shows the spatiotemporal behavior of the quasineutrality deviation at 10 mTorr over the full gap length defined as in Eq. (3). As in the 100 mTorr case shown in Fig. 2(b), the quasineutrality deviation uniquely identifies the sheath region. We observe a non-quasineutral stripe on both the sheath edges, which is related to the positive charged stripe observed in Fig. 3(a). At 100 mTorr, the sheath has a smooth contour over the full rf cycle [Fig. 2(b)], while at 10 mTorr, it ends abruptly on the non-quasineutral stripe on both the sheath edges. Figure 4(a) shows the total charge density profile at 100 mTorr defined by Eq. (2) at different time steps and time averaged over all the full gap length. We observe that the total charge density profile is flat and very close to zero over the full bulk width for all the cases considered. At $t/\tau_{\mathrm{rf}} = 0.25$

$(t/\tau_{\mathrm{rf}} = 0.75)$, the total charge density steeply increases while approaching the sheath edge of the right (left) bulk-sheath interface and sharply decreases toward the right (left) electrode. On the other hand, the total charge density is approximatively constant at $t/\tau_{\mathrm{rf}} = 0.25$ $(t/\tau_{\mathrm{rf}} = 0.75)$ and zero within the fully collapsed sheath region and slowly increases toward the right (left) electrode. The charge density profile at $t/\tau_{\mathrm{rf}} = 0.25$ is a mirror image of the charged density profile at $t/\tau_{\mathrm{rf}} = 0.75$. At $t/\tau_{\mathrm{rf}} = 0.50$, the total charge density slightly decreases once past both the sheath edges and steeply increases on the sheath side of both the sheath edges. Then, it slowly decreases while approaching both the electrodes overlapping with both the $t/\tau_{\mathrm{rf}} = 0.25$ and the $t/\tau_{\mathrm{rf}} = 0.75$ cases. In the time averaged case, the total charge density steeply increases once past both the sheath edges reaching a lower maximum with
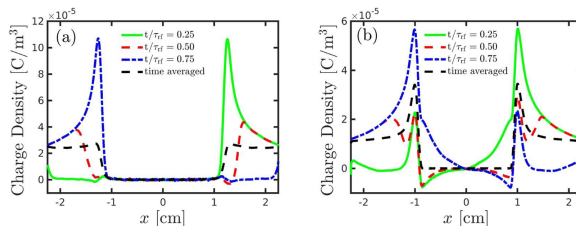

FIG. 4. The total charge density at (a) 100 mTorr and (b) 10 mTorr over the full gap length at $t/\tau_{\mathrm{rf}} = 0.25$ (green line), $t/\tau_{\mathrm{rf}} = 0.50$ (red dashed line), $t/\tau_{\mathrm{rf}} = 0.75$ (blue dotted dashed line), and time averaged (black dashed line) for a parallel plate capacitively coupled oxygen discharge for 45 mm of gap separation driven by a 400 V voltage source at a driving frequency of 13.56 MHz.

respect to all the other cases considered. We observe the time averaged case to be almost zero within the plasma bulk and to have an almost constant profile within the sheath regions while approaching both the electrodes.

Figure 4(b) shows the total charge density profile at 10 mTorr defined by Eq. (3) at different time steps and time averaged over the full gap length. The total charge density is zero within the discharge center ($x = 0$) for all the four cases considered even though there is always some charge density within the plasma bulk (either positive or negative), and the time average is zero. Also, the total charge density profile at $t/\tau_{rf} = 0.25$ ($t/\tau_{rf} = 0.75$) shows an additional local maximum on the left (right) sheath edge with respect to the 100 mTorr case [Fig. 4(a)]. The same applies to the $t/\tau_{rf} = 0.50$ and the time averaged case, with the presence of two almost equal local maxima on both the sheath edges, which are absent in the 100 mTorr case. At $t/\tau_{rf} = 0.25$, the total charge density profile sharply increases (decreases) while approaching the bulk side of the right (left) sheath edge, and it has an absolute maximum (minimum) on the sheath side (bulk side) of the right (left) sheath edge. Then, the total charge density profile sharply decreases (steeply increases) once past the right (left) sheath edge, reaching a positive value (a local maximum) toward the right electrode (on the sheath side of the left sheath edge). We also observe that the total charge density profile is approximately constant within the left sheath region.

IV. MODEL DESCRIPTION AND RESULTS

During the past years, several attempts have been made to describe correctly the behavior of the electric field using the Boltzmann equation. Surendra and Dalvie[22] used the first momentum Boltzmann equation to decompose the electric field into a sum of different terms, each one corresponding to different physical mechanisms. They were able to isolate all the single terms contributing to both the electric field and the electron power absorbed. Moreover, they found the electron pressure term to be important for the collisionless heating and that, for a constant electron temperature, the collisionless electron heating vanishes upon time average. Since then, several attempts have been made to explain the behavior of the electric field at different time steps and upon time average. In recent years, Surendra's framework has been employed to explain the behavior of the electric field within the bulk and in the sheath regions. In particular, Schulze and co-workers have used the zeroth momentum Boltzmann equation (stationary continuity equation), with a stationary density profile[30] and with a temporally dependent density profile together with a non-zero ionization rate,[31] combined with the first momentum Boltzmann equation, with and without the change in the momentum term[30,31] to derive a space- and time-resolved expression for the different electric field terms involved. The Surendra–Dalvie framework has improved our knowledge of the physical mechanisms behind the origins of the electric field within the bulk region and within the collapsed sheath region but has not given a general consensus on the origin of the electric field within the expanded sheath region.

The DA-mode is associated with the creation of electric field within the plasma bulk. The electric field within a plasma discharge is built up by several different phenomena, depending on the gas considered. The electronegative discharges present a bigger number of phenomena than the electropositive discharges, and the situation is much more complicated. For both electropositive and electronegative discharge sheaths form near the electrodes, a positive net charge within the sheath region builds up, leading to a potential profile that is positive within the bulk region and falls to zero near both electrodes.[41] However, a strong electric field within the bulk region has been observed, both experimentally and by simulations in electronegative discharges. The high value of the electric field has been related to the low dc conductivity within the bulk as discussed by Schulze et al.[4] Furthermore, strong peaks in the electric field at the sheath edges have been observed.[42] The observed peaks have been related to the corresponding local maxima of the electron density at the sheath edges, which are caused by the ambipolar field built up by a net charge separation between the positive charges as they are accelerated toward the electrode and the electrons, together with the negative ions, confined within the bulk region. This is completely different from the situation observed in the electropositive discharges, where the ambipolar field accelerates the electrons toward the discharge center.[4]

A. Simple fluid model

When operated at 100 mTorr (10 mTorr), the electronegativity is low (high) and the discharge operates in a pure α-mode (hybrid DA-mode and α-mode). Irrespective of the different discharge modes and conditions, a simple fluid model for an electronegative discharge is sufficient to describe the physics of such a system. In this subsection, the simple fluid model applied to a discharge operated at both 100 mTorr and 10 mTorr is discussed. The model describes the behavior of the electric field and of the electron power absorption within the bulk region. This model is based on the approach used by Schulze et al.,[31] with the only difference that here, both the ionization rate and the change of momentum terms are assumed to be negligible and are set equal to zero. The model is valid within the bulk region and in the collapsed sheath regions only since the electron density in the expanded sheath region is very small. Moreover, the quasineutrality condition has not been imposed, and the ideal gas law has been employed in the first momentum Boltzmann equation. At 100 mTorr, the pressure tensor (the temperature) is taken as (not) isotropic. Setting $p_e \equiv p_{e,\,xx} = p_{e,\,yy} = p_{e,\,zz}$, one finds $\mathrm{Tr}(p_{e,ij}) = 3p_{e,\,xx} = 3p_e = 3en_e T_e = en_e\left(T_{e,\,xx} + T_{e,\,yy} + T_{e,\,zz}\right)$ so that $T_e \equiv \left(T_{e,\,xx} + T_{e,\,yy} + T_{e,\,zz}\right)/3$; i.e., the electron temperature is direction averaged. Accordingly to the current setup and in order to make the physical system consistent, the ideal gas law has to be seen as an approximation. On the other hand at 10 mTorr, neither the pressure tensor nor the temperature is isotropic. Since $p_{e,\,xx} \neq p_{e,\,yy} \neq p_{e,\,zz}$ and $T_{e,\,xx} \neq T_{e,\,yy} \neq T_{e,\,zz}$, we are left with $p_e \equiv p_{e,\,xx} = en_{e,\,xx}T_{e,\,xx}, p_{e,\,yy} = en_{e,\,yy}T_{e,\,yy}$, and $p_{e,\,zz} = en_{e,\,zz}T_{e,\,zz}$. The zeroth and the first momentum Boltzmann equation for electrons in a plasma discharge in the absence of magnetic field are the continuity equation,

$$\frac{\partial n_e}{\partial t} + \frac{\partial}{\partial x}(un_e) = G - L, \tag{4}$$

189

where G and L are the reaction rates involving the creation and destruction of electrons, respectively, and the momentum balance equation,

$$\frac{\partial}{\partial t}[m_e n_e u_e] + \frac{\partial}{\partial x}[m_e n_e u_e^2] + \frac{\partial}{\partial x}[e n_e T_e] + e n_e E + \Pi_c = 0, \quad (5)$$

respectively. According to this setup, there is no need for keeping the continuity equation [Eq. (4)]. Now, according to Lieberman and Lichtenberg,[21] the momentum change term Π_c can be approximated by a Krook collisional operator as follows:

$$\Pi_c = \sum_\beta m_e n_e \nu_{e\beta}(u_e - u_\beta) - m_e(u_e - u_G)G + m_e(u_e - u_L)L, \quad (6)$$

where the summation is over all species; u_e and u_β are the mean velocities of the electrons and the species β, respectively; and $\nu_{e\beta}$ is the momentum transfer frequency for collisions between electrons and species β. Now, neglecting the reactions involving the creation and destructions of particles (e.g., ionization, recombination) and considering only the O_2 neutral species, with a negligible velocity compared to the electrons, the momentum change term becomes

$$\Pi_c = m_e \nu_e n_e u_e, \quad (7)$$

along with the continuity equation,

$$\frac{\partial n_e}{\partial t} + \frac{\partial}{\partial x}(u_e n_e) = 0. \quad (8)$$

Solving Eq. (8) with respect to the velocity gradient, one finds

$$\frac{\partial u_e}{\partial x} = -\frac{u_e}{n_e}\frac{\partial n_e}{\partial x} - \frac{1}{n_e}\frac{\partial n_e}{\partial t}. \quad (9)$$

Combining Eqs. (9), (7), and (5) together with the ideal gas law, one finds an expression for the electric field

$$E = \underbrace{-\frac{m_e}{e}\frac{\partial u_e}{\partial t}}_{I} + \underbrace{\frac{m_e u_e^2}{e}\frac{\partial n_e}{\partial x}}_{II} + \underbrace{\frac{m_e u_e}{e}\frac{\partial n_e}{\partial t}}_{III} - \underbrace{\frac{T_e}{n_e}\frac{\partial n_e}{\partial x}}_{IV} - \underbrace{\frac{\partial T_e}{\partial x}}_{V} - \underbrace{\frac{m_e u_e \nu_c}{e}}_{VI}. \quad (10)$$

Each electric field term in Eq. (10) has its own origin. The first and the third term (I and III) are electron inertia terms due to the temporal variation in the electron velocity and density, respectively. The second term (II) corresponds to an electric field due to the normalized electron density gradient. The fourth (IV) term corresponds to diffusion (ambipolar).[4,30] The fifth term (V) corresponds to the electron temperature gradient. Therefore, terms IV and V represent electron heating due to pressure effects, which is a collisionless mechanism.[23] The sixth term (VI) is due to electron collisions with atoms and molecules (drift field). Equation (10) has been applied to a given set of input parameters. The input parameters are the electron density and the electron temperature from the simulation. The collision term (Term VI) was taken from the reaction rate given by the simulation for an electron neutral elastic

collision. The electron collision frequency values at 100 and 10 mTorr are $\nu_c = 8.16 \times 10^7 \, \text{s}^{-1}$ and $\nu_c = 5.06 \times 10^7 \, \text{s}^{-1}$ within the discharge center, respectively. Multiplying the electric field coming from Eq. (10) times the electron current density $J_e = -e n_e u_e$, it is possible to find the electron absorbed power as follows:

$$J_e \cdot E = \underbrace{m_e u_e n_e \frac{\partial u_e}{\partial t}}_{I} - \underbrace{m_e u_e^3 \frac{\partial n_e}{\partial x}}_{II} - \underbrace{m_e u_e^2 \frac{\partial n_e}{\partial t}}_{III} + \underbrace{e u_e T_e \frac{\partial n_e}{\partial x}}_{IV}$$
$$+ \underbrace{e n_e u_e \frac{\partial T_e}{\partial x}}_{V} + \underbrace{m_e n_e \nu_c u_e^2}_{VI}. \quad (11)$$

Each electron power absorption term that constitutes Eq. (11) has its own origin, which is strictly related to the electric field given by Eq. (10). The first and the third term (I and III) are electron inertia power absorption terms. The second term (II) corresponds to the power absorption term related to the electron density gradient. The fourth (IV) term is related to the ambipolar field originating from the electron density gradient.[4,30] The fifth term (V) is related to the electron temperature gradient term for the electric field [Eq. (10)]. The fourth and fifth terms are usually known in the literature as pressure heating terms, respectively.[22,23,31] The sixth term (VI) is related to the collisions and represents ohmic heating. It is worth noting that the electron power absorption formula shown in Eq. (11) can be split as follows:[22]

$$(J_e \cdot E) = (J_e \cdot E)_{\text{Non ohmic}} + (J_e \cdot E)_{\text{ohmic}}, \quad (12)$$

where

$$(J_e \cdot E)_{\text{Non ohmic}} = \text{Term I} + \text{Term II} + \text{Term III} + \text{Term IV} + \text{Term V}, \quad (13)$$

$$(J_e \cdot E)_{\text{ohmic}} = \text{Term VI}. \quad (14)$$

In turn, the non-ohmic contribution can be split up as follows:[25]

$$(J_e \cdot E)_{\text{Non ohmic}} = (J_e \cdot E)_{\text{Inertia}} + (J_e \cdot E)_{\text{Pressure}}, \quad (15)$$

where

$$(J_e \cdot E)_{\text{Inertia}} = \text{Term I} + \text{Term II} + \text{Term III}, \quad (16)$$

$$(J_e \cdot E)_{\text{Pressure}} = \text{Term IV} + \text{Term V}. \quad (17)$$

This will be useful later when we identify the different contributions to the electron power absorption. We underline that the same split applied to the electron power absorption can be applied to the electric field formula shown in Eq. (10).

V. RESULTS AND DISCUSSION

The sheath location is determined by assuming that the density of negatively charged species has fallen to half the density of the positive charged species. In more detail, the sheath edge position, which is defined as $x_{sh}(t)$, is taken to be the position x,

where the condition $n_e(x,t)/n_i = 1/2$ is satisfied. This determines the location of the gray shadowed rectangles hiding the sheath regions in the various plots shown in this section. We hide the sheath regions directly adjacent to the electrodes as the electron density is very low. Figure 5 shows the electric field profile of the terms that constitute Eq. (10) and their summation compared with the results of simulations at $t/\tau_{rf} = 0.25$ from the left electrode to the right sheath edge, at $t/\tau_{rf} = 0.50$ from the left to the right sheath edge, and at $t/\tau_{rf} = 0.75$ from the left sheath edge to the right electrode. For all the three time slices, an almost perfect match between the overall term summation and the result from the simulations is observed.

At $t/\tau_{rf} = 0.25$ [Fig. 5(a)], we see that the contribution from Terms II and III is negligible. On the other hand, the main

contribution comes from Terms I, IV, V, and VI. Term I is almost zero within the bulk region up to the right sheath edge, while it decreases to negative values as it approaches the left sheath edge up to the left electrode. The electric field inertia term due to a temporally varying electron velocity becomes negative approaching the left electrode, indicating that the electron velocity gradient is positive near the left electrode [Eq. (10)]. Term IV is flat and zero within the bulk region and sharply increases (sharply decreases) while approaching the right (left) sheath edge. An absolute minimum in the Term IV profile is observed on the sheath side of the left sheath edge. Moreover, once past this minimum, the profile of Term IV is approximatively constant over the left sheath region and it decreases while approaching the left electrode. Term V is flat and zero over the full bulk gap length. A small local minimum
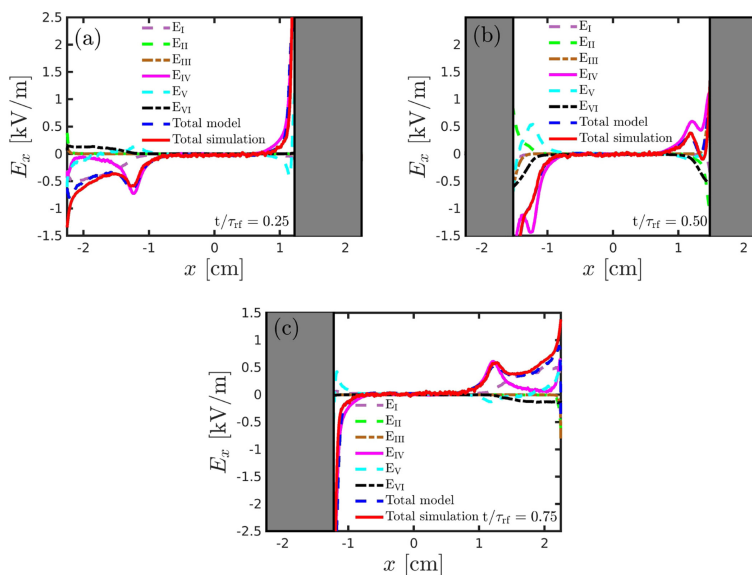

FIG. 5. The electric field profile of the terms that constitute Eq. (10) and their summation compared with the result of the simulations at (a) $t/\tau_{rf} = 0.25$ from the left electrode to the right sheath edge, at (b) $t/\tau_{rf} = 0.50$ from the left to the right sheath edge, and at (c) $t/\tau_{rf} = 0.75$ from the left sheath edge to the right electrode for a parallel plate capacitively coupled oxygen discharge at 100 mTorr for 45 mm of a gap separation driven by a 400 V voltage source at a driving frequency of 13.56 MHz.

(maximum) in the Term V profile is observed on the sheath side of the right (left) sheath edge. Then, it steeply increases (sharply decreases) while approaching the sheath side of the right sheath edge (the left electrode). Term VI is flat and zero within the bulk region up to the right sheath edge, while it slightly increases as it approaches the left sheath keeping an almost constant value while approaching the left electrode. Finally, Fig. 5(a) shows that the only important contributions to the electric field at $t/\tau_{rf} = 0.25$ come from the inertia term related to the temporal gradient of the electron velocity (Term I), from the pressure gradient related terms (Term IV and V), and from the ohmic heating term (Term VI). At $t/\tau_{rf} = 0.50$ [Fig. 5(b)], we see that the contribution from Terms I and III is negligible and Term II is small except near the sheath edges. Term IV is flat and zero within the bulk region and it sharply increases (steeply decreases) as it approaches the bulk side of the right (left) sheath edge. Term V is flat and zero within the bulk region and slightly decreases (sharply increases) as it approaches the sheath side of the right (left) sheath edge. Term VI is flat and zero within the bulk region up to both the sheath edges, and it sharply decreases as it approaches the bulk side of both the sheath edges. Figure 5(b) shows that the only important contributions to the electric field at $t/\tau_{rf} = 0.50$ come from the pressure gradient related terms (Term IV and V) and from the ohmic contribution (Term VI). At $t/\tau_{rf} = 0.75$ [Fig. 5(c)], we see almost a mirror image of Fig. 5(a). The contributions from Terms II and III are negligible and Term VI is small. The main contribution comes from Terms I, IV, and V. The only significant contributions to the electric field at $t/\tau_{rf} = 0.75$ come from the inertia term related to the temporal gradient of the electron velocity and from the pressure gradient related terms. Therefore, the most significant contribution to the electric field within the bulk plasma at 100 mTorr is due to the pressure gradient terms. An almost perfect match between the calculated electric field profile and the result from simulation can be observed for all the time steps considered as shown in Figs. 5(a)–5(c).
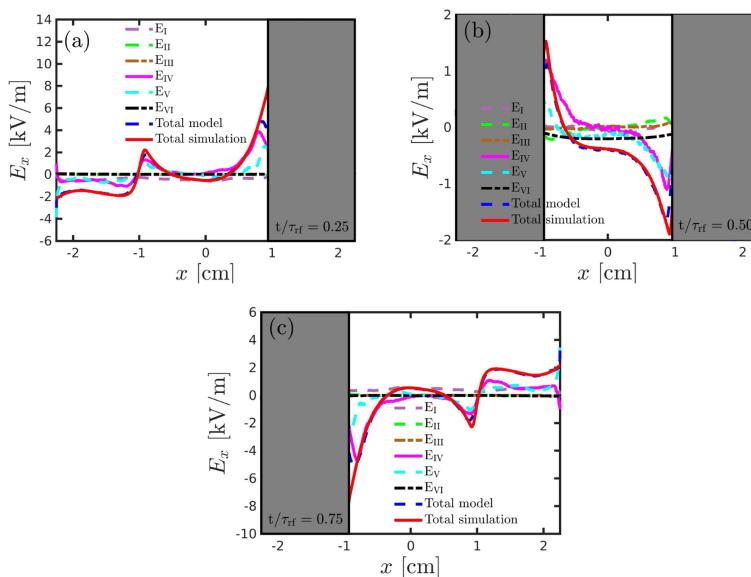
Figure 6 shows the electric field profile at 10 mTorr of the terms that constitute Eq. (10) and their summation compared with the result of the simulations at (a) $t/\tau_{rf} = 0.25$ from the left electrode to the right sheath edge, at (b) $t/\tau_{rf} = 0.50$ from the left to the right sheath edge, and at (c) $t/\tau_{rf} = 0.75$ from the left sheath edge to the right electrode. At $t/\tau_{rf} = 0.25$ [Fig. 6(a)], we see that the contribution from terms II and VI is negligible, while Term III is small. We observe that the main contribution to the electric field comes from terms IV and V. Term IV is zero within the discharge center and approximatively flat and zero within the inner bulk region and sharply increases while approaching the bulk side of both the sheath edges. A lower (higher) maximum on the bulk side of the left (right) sheath edge is observed. On the other hand, Term V has a similar behavior except that it increases less steeply while approaching the bulk side of the right sheath edge. The local maximum in Term V on the left sheath edge overlaps almost perfectly with the local maximum in Term IV, total term summation, and the result from the simulations placed in the same location as well as the respective profiles within the inner bulk region. Finally, Fig. 6(b) shows that the only important contributions to the electric field at $t/\tau_{rf} = 0.25$ come from the pressure gradient related terms (Terms IV and V). At $t/\tau_{rf} = 0.50$ [Fig. 6(b)], we see that the

contribution from Term I is negligible and Terms II, III, and VI are small. We also observe that the main contribution to the electric field comes from terms IV and V. Term IV is flat and zero within the inner core of the plasma bulk and decreases (increases) while approaching the bulk side of the right (left) sheath edge. Then, it increases again once past the right sheath edge building an absolute minimum. Finally, Fig. 6(b) shows that the only important contributions to the electric field at $t/\tau_{rf} = 0.50$ come from the pressure gradient related terms (Terms IV and V). Moreover, we observe that in the $t/\tau_{rf} = 0.50$ case, Terms II, IV, and V share the same importance in contribution to the electric field at both 10 and 100 mTorr, while the contribution from Term III (Term VI) is lacking at 100 mTorr (10 mTorr). At $t/\tau_{rf} = 0.75$ [Fig. 6(c)], we see a mirror image of the $t/\tau_{rf} = 0.25$ case. Terms II, III, and VI are negligible and Term I is small. The main contribution to the electric field comes from terms IV and V. The local minimum in Term V on the right sheath edge overlaps almost perfectly with the local minimum in Term IV, total term summation, and the result from the simulations placed in the same location as well as the respective profiles within the inner bulk region. To summarize, the only important contributions to the electric field at $t/\tau_{rf} = 0.75$ come from the pressure gradient related terms (Terms IV and V).

An almost perfect match between the calculated electric field profile and the result from simulation can be observed over the full gap length up to the bulk side of the expanding sheath edge for all the three time slices considered. Moreover, at $t/\tau_{rf} = 0.25$ and $t/\tau_{rf} = 0.75$, the calculated electric field sharply underestimates the electric field coming from the simulations while approaching the bulk side of the fully collapsed sheath edge, while at $t/\tau_{rf} = 0.50$, the difference is very small. We observe that the inertia term (Term I), for all the three time slices considered, is negligible compared to the 100 mTorr case (Fig. 5). Such a term is absent due to the presence of the negatively charged stripes placed on bulk side of the collapsing sheath edge, which prevents the electrons from crossing the collapsing sheath edge (see discussion in Sec. III). Moreover, due to the presence of the positively charged stripes placed on the sheath side over the full rf period, the electrons are prevented from increasing their own velocity. Since at 10 mTorr, there is a higher number of electrons within the collapsing sheath region than at 100 mTorr [Figs. 2(a) and 3(a), respectively], the displacement current is lower, and the temporal change in the electron velocity due to the time varying electric field is also lower.

Figure 7(a) shows the time averaged electric field profile at 100 mTorr for the three main contributing terms to the calculated electric field using Eq. (10) from the left to the right (time averaged) sheath edge: Terms IV (red line), V (blue dashed line), and VI (green dotted dashed line). We see that all the three terms considered are flat and zero within the bulk region. Term IV steeply increases (decreases) while approaching the right (left) sheath edge. On the other hand, Term V sharply increases (decreases) while approaching the sheath side of the left (right) edge. Finally, Fig. 7(a) shows that the only important contribution to the time averaged electric field comes from the pressure terms (Terms IV and V).

Figure 7(b) shows the time averaged electric field profile in a discharge operated at 10 mTorr for the three main contributing terms to the calculated electric field using Eq. (10) from the left to the right (time averaged) sheath edge: Terms IV (red line), V (blue

FIG. 6. The electric field profile of the terms that constitute Eq. (10) and their summation compared with the result of the simulations at (a) $t/\tau_{rf} = 0.25$ from the left electrode to the right sheath edge, at (b) $t/\tau_{rf} = 0.50$ from the left to the right sheath edge, and at (c) $t/\tau_{rf} = 0.75$ from the left sheath edge to the right electrode (c) for a parallel plate capacitively coupled oxygen discharge at 10 mTorr for 45 mm of gap separation driven by a 400 V voltage source at a driving frequency of 13.56 MHz.

dashed line), and VI (green dotted dashed line). We see that all the three terms considered are zero within the discharge center. Term IV sharply increases (decreases) while approaching the bulk side of the right (left) sheath edge. Term V steeply decreases (increases) while approaching the bulk side of the right (left) sheath edge, and it steeply increases (decreases) while crossing the right (left) sheath edge. Finally, Fig. 7(b) shows that the only important contribution to the time averaged electric field comes from the pressure terms (Terms IV and V), just like at 100 mTorr.

Figure 8(a) shows the time averaged electric field at 100 mTorr calculated using Eq. (10) (blue dashed line) and the result from simulations (red line) from the left to the right sheath edge. An almost perfect match is observed over the gap length considered. Figure 8(b) shows the time averaged electric field at 10 mTorr

calculated using Eq. (10) (blue dashed line) and the result from simulations (red line) from the left to the right sheath edge. We observe an almost perfect match within the inner bulk gap length. However, the calculated electric field overestimates (underestimates) the electric field from the simulation on the bulk side of both the sheath edges, resembling the observed slight difference between the calculated and simulated electric field at different time steps on the bulk side of the expanding sheath edge (Fig. 6).

Figure 9 shows the spatiotemporal behavior of the electron power absorption $\mathbf{J}_e \cdot \mathbf{E}$ at 100 mTorr. The figures show the electron power absorption calculated using Eq. (11) [Fig. 9(a)] and from the simulation over the full gap length [Fig. 9(b)]. The ordinate covers the full rf cycle. We see that almost all the electron power absorption occurs during the sheath expansion and that the electron
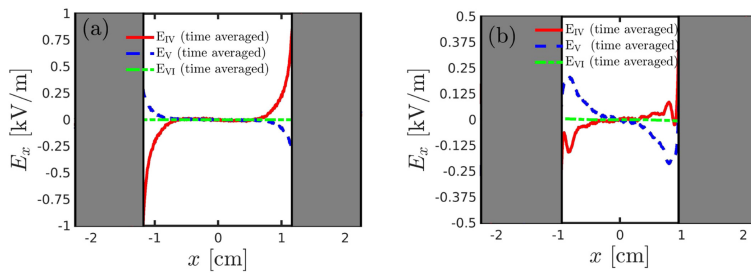
128, 113302-11

FIG. 7. The time averaged electric field profile at (a) 100 mTorr and at (b) 10 mTorr of Term IV (red line), Term V (blue dashed line), and Term VI (green dotted dashed line) from Eq. (10) from the left to the right sheath edge for a parallel plate capacitively coupled oxygen discharge for 45 mm of gap separation driven by a 400 V voltage source at a driving frequency of 13.56 MHz.

power absorption mode is a pure α-mode. The calculated electron power absorption almost perfectly matches the result from the simulation on both the sheath edges. We recall that the theoretical model does not take the sheath dynamics into account since it has been built for the bulk and collapsed sheath region only. Within the gap length, we see an almost perfect match between the electron power absorption coming from the theoretical model and the simulation.

Figure 10 shows the spatiotemporal behavior of the electron power absorption $\mathbf{J}_e \cdot \mathbf{E}$ at 10 mTorr, where $\mathbf{J}_e$ and $\mathbf{E}$ are the spatially and temporally varying electron current density and electric field, respectively. The figures show the electron power absorption for the theoretical model [Eq. (11); [Fig. 10(a)] and from the simulation results over the full gap length [Fig. 10(b)]. The ordinate covers the full rf cycle. First, we observe that at 10 mTorr, a significant power absorption (red and yellow areas) and some electron cooling (dark blue areas) are evident within the plasma bulk region. The electron power absorption appears during the sheath expansion (collapse) on the sheath side (on the bulk side) of the sheath edge, while there is electron cooling during the sheath
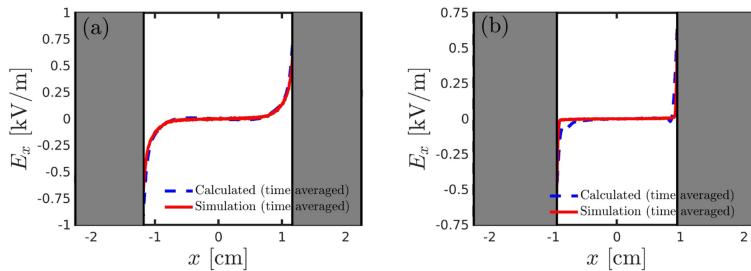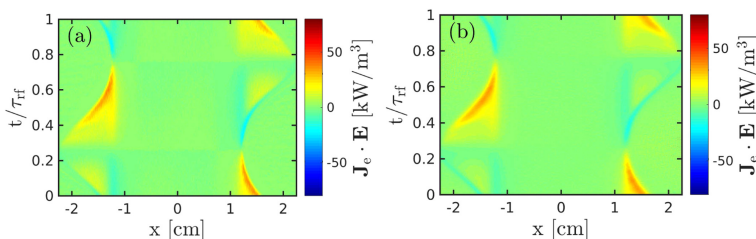

FIG. 8. The time averaged electric field profile calculated using Eq. (10) (blue dashed line) and the result from simulations (red line) from the left to the right sheath edge at (a) 100 mTorr and at (b) 10 mTorr for a parallel plate capacitively coupled oxygen discharge for 45 mm of gap separation driven by a 400 V voltage source at a driving frequency of 13.56 MHz.
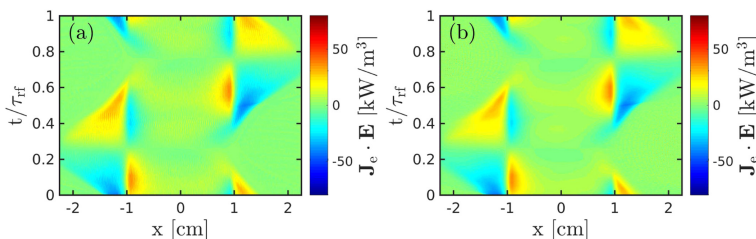
194

FIG. 9. The spatiotemporal behavior of the electron power absorption over the full gap length (a) calculated using Eq. (11) and (b) the result from simulations for a parallel plate capacitively coupled oxygen discharge at 100 mTorr for 45 mm of gap separation driven by a 400 V voltage source at a driving frequency of 13.56 MHz.

expansion (collapse) on the bulk side of the sheath edge (on the electrode side). Indeed, at 10 mTorr, the electron heating mechanism is a combination of a drift-ambipolar (DA) heating in the bulk plasma and stochastic heating due to the sheath oscillation (α-mode), as it has been shown in our previous works.[19–21] Second, we observe that the calculated electron power absorption resembles well the result from the simulation, which is slightly overestimated within the sheath region only.
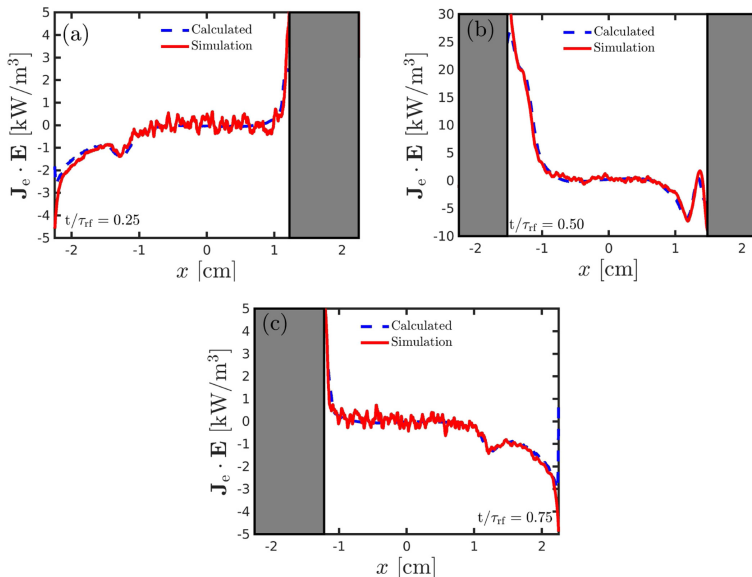
Figure 11 shows the electron power absorption profile at 100 mTorr calculated using Eq. (11) (blue dashed line) and the result from simulations (red line) at (a) $t/\tau_{rf} = 0.25$ from the left electrode to the right sheath edge, at (b) $t/\tau_{rf} = 0.50$ from the left to the right sheath edge, and at (c) $t/\tau_{rf} = 0.75$ from the left sheath edge to the right electrode. An almost perfect match is observed for all the time steps considered as shown in Figs. 11(a)–11(c).

Figure 12 shows the electron power absorption profile at 10 mTorr calculated using Eq. (11) (blue dashed line) and the result from simulations (red line) at $t/\tau_{rf} = 0.25$ from the left electrode to the right sheath edge (a), at $t/\tau_{rf} = 0.50$ from the left to the right sheath edge (b), and at $t/\tau_{rf} = 0.75$ from the left sheath edge to the right electrode (c). An almost perfect match is observed for all the time steps considered as shown in Figs. 12(a)–12(c).

Figure 13(a) shows the time averaged electron power absorption profile at 100 mTorr of Terms IV (red line), V (blue dashed line) and VI (green dotted dashed line) calculated using Eq. (11) from the left to the right sheath edge. All the three terms considered are flat and zero within the bulk gap length. We observe that Term IV (Term V) steeply increases (decreases) while approaching the sheath side of both the sheath edges. On the other hand, we observe that Term VI slightly increases while crossing both the

FIG. 10. The spatiotemporal behavior of the electron power absorption over the full gap length calculated (a) using Eq. (11) and (b) the result from simulation for a parallel plate capacitively coupled oxygen discharge at 10 mTorr for 45 mm of gap separation driven by a 400 V voltage source at a driving frequency of 13.56 MHz.

195

FIG. 11. The electron power absorption profile from Eq. (11) (blue dashed line) at (a) $t/\tau_{rf} = 0.25$ and the result from simulations (red line) from the left electrode to the right sheath edge, at (b) $t/\tau_{rf} = 0.50$ from the left to the right sheath edge, and at (c) $t/\tau_{rf} = 0.75$ from the left sheath edge to the right electrode for a parallel plate capacitively coupled oxygen discharge at 100 mTorr for 45 mm of gap separation driven by a 400 V voltage source at a driving frequency of 13.56 MHz.

sheath edges reaching small positive values on the sheath side of both the sheath edges. Finally, Fig. 13 shows that the main contributions to the time averaged electron power absorption at 100 mTorr comes from the pressure gradient related terms (Terms IV and V) and from ohmic term (Term VI).

Figure 13(b) shows the time averaged electron power absorption profile at 10 mTorr of Terms IV (red line), V (blue dashed line), and VI (green dotted dashed line) calculated using Eq. (11) from the left to the right sheath edge. We observe that all the three terms considered have a parabolic behavior over the bulk gap length. Moreover, Term V is higher (lower) on the bulk side of both the sheath edges (within the inner electronegative core) than Term VI, while Term IV is sharply lower over the full gap length. In more detail, we see that Term IV is almost flat and zero within

the discharge center up to the bulk side of both the sheath edges and that it slightly increases while approaching both the sheath edges building equal local maxima. Then, it steeply decreases while crossing both the sheath edges, building two almost equal local minima. On the other hand, Term V slightly increases while approaching the bulk side of both the sheath edges, building two almost equal local maxima, and it sharply decreases while approaching both the sheath edges. As regards Term VI, we see that it builds an absolute maximum at the discharge center and that it sharply decreases while approaching both the sheath edges.

Figure 14(a) shows the comparison between the time averaged electron power absorption calculated using Eq. (11) (blue dashed line) and the result from simulations (red line) over the full gap length at 100 mTorr. In Fig. 14(a), we see that the calculated time
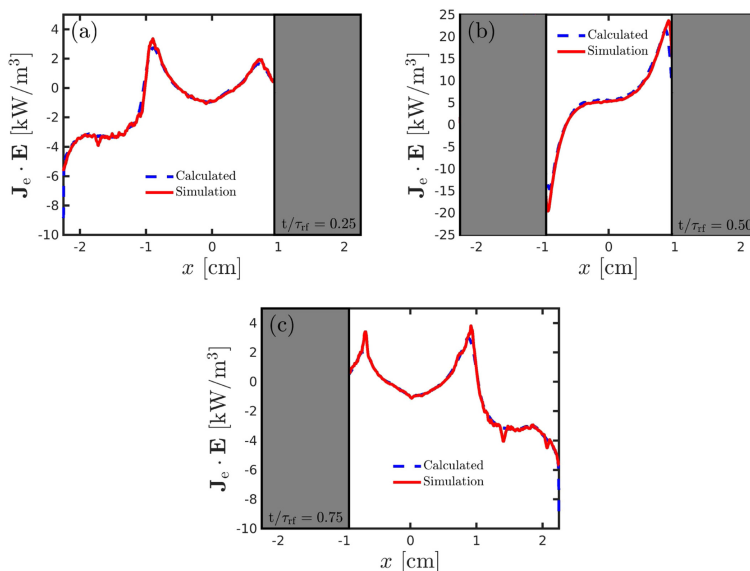
FIG. 12. The electron power absorption profile from Eq. (11) (blue dashed line) at (a) $t/\tau_{rf} = 0.25$ and the result from simulations (red line) from the left electrode to the right sheath edge, at (b) $t/\tau_{rf} = 0.50$ from the left to the right sheath edge, and at (c) $t/\tau_{rf} = 0.75$ from the left sheath edge to the right electrode for a parallel plate capacitively coupled oxygen discharge at 10 mTorr for 45 mm of gap separation driven by a 400 V voltage source at a driving frequency of 13.56 MHz.

averaged electron power absorption overlaps almost perfectly with the result from the simulation over the bulk gap length up to the sheath side of both the sheath edges. Moreover, it slightly understimates the result from the simulation within the inner core of both the sheath regions up to the respective electrodes.

Figure 14(b) shows a comparison between the time averaged electron power absorption calculated using Eq. (11) (blue dashed line) and the result from simulation (red line) over the full gap length at 10 mTorr. In Fig. 14(b), we see that the calculated time averaged electron power absorption calculated using Eq. (11) overlaps almost perfectly with the result from the simulation over the bulk gap length up to the sheath side of both the sheath edges. Moreover, the closer to the electrodes, the bigger is the difference between the calculation and the simulation.

Figure 15 shows a comparison between the space-time averaged electron power absorption within the plasma bulk at 10 mTorr calculated using Eq. (11) (blue bars) and at 100 mTorr calculated using Eq. (11) (red bars). The space average has been taken within the bulk region only using the time averaged sheath locations as already discussed at the beginning of Sec. V. The histogram has been constructed considering the calculated space-time averaged electron absorbed power and then building the following quantity:

$$(J_e \cdot E)_{X \text{ Term Percentage}} = \frac{100 \times (J_e \cdot E)_{X \text{ Term}}}{(J_e \cdot E)}, \quad (18)$$
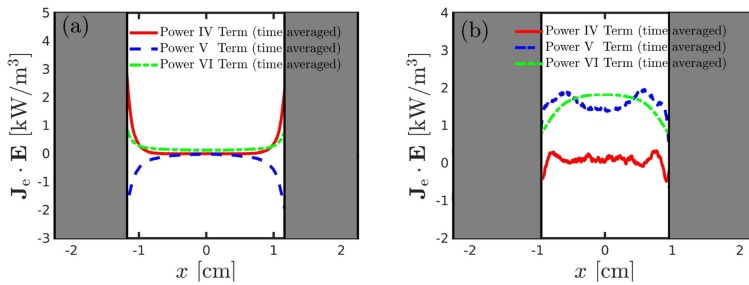
FIG. 13. The time averaged electron power absorption profile of Term IV (red line), Term V (blue dashed line), and Term VI (green dotted dashed line) from Eq. (11) from the left to the right (time averaged) sheath edge at (a) 100 mTorr and at (b) 10 mTorr for a parallel plate capacitively coupled oxygen discharge for 45 mm of gap separation driven by a 400 V voltage source at a driving frequency of 13.56 MHz.

where $(J_e \cdot E)_{X\,\mathrm{Term}}$ labels the space-time averaged electron power absorption related to the X term, where X refers to terms I, II, . . ., VI in Eq. (11). In Fig. 15, we observe that in the 100 mTorr case, the space-time averaged electron power absorption comes from the pressure terms (Terms IV and V) and the ohmic Term (Term VI). Moreover, we see that Term IV is positive, while Term V is negative, and they share almost the same magnitude in the absolute value, while Term VI is the smallest. Therefore, the ambipolar term

is a power absorption term, while the electron temperature gradient presents power loss (electron cooling). The main electron power absorption at 100 mTorr is due to the pressure gradient terms. At 10 mTorr, the situation has changed drastically. First of all, Terms IV and V flip their sign with respect to the 100 mTorr case and are sharply smaller in the absolute value compared to the 100 mTorr case. In this context, the ohmic term's magnitude (Term VI) has not significantly changed compared to the 100 mTorr case but now
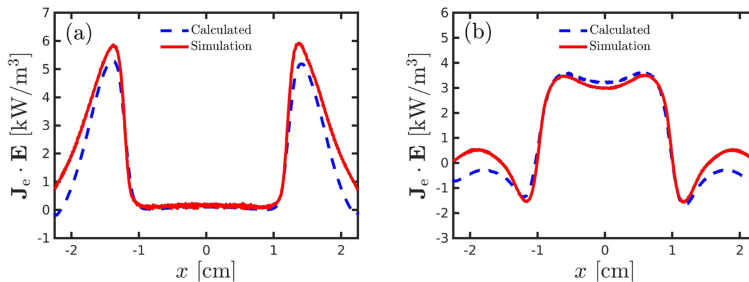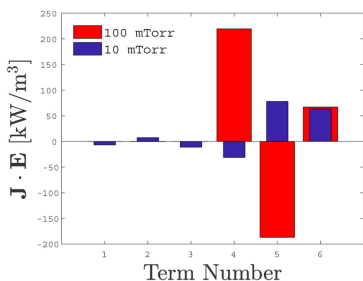

FIG. 14. The time averaged electron power absorption profile calculated using Eq. (11) (a) (blue dashed line) and the result from simulations (red line) over the full gap length at (a) 100 mTorr and at (b) 10 mTorr for a parallel plate capacitively coupled oxygen discharge for 45 mm of gap separation driven by a 400 V voltage source at a driving frequency of 13.56 MHz.

FIG. 15. The space-time averaged electron power absorption profile terms calculated using Eq. (11) at 10 mTorr (blue bars) and 100 mTorr (red bars) for a parallel plate capacitively coupled oxygen discharge for 45 mm of gap separation driven by a 400 V voltage source at a driving frequency of 13.56 MHz.

shares the same order of magnitude with respect to both Terms IV and V. Moreover, in Fig. 15, we recognize a general pattern where the ohmic term (pressure term) contribution in the space-time averaged total electron power absorption increases (decreases) when the total pressure decreases (increases). Such a behavior is expected and has also been observed by Vass *et al.*[32] The only difference is that Vass *et al.*[32] find the pressure term contribution in the space-time averaged electron power absorption to be negligible at low pressure. Like Vass *et al.*,[32] we find the ohmic power absorption to be important even at low pressure. Finally, at 10 mTorr, we observe the presence of small contributions coming from Terms I, II, and III, respectively. The inertia terms I and III provide electron cooling, while the electron density gradient term II contributes to electron power absorption.

VI. CONCLUSION

The one-dimensional object-oriented particle-in-cell Monte Carlo collision code oopd1 was applied to explore the properties of the electric field and the electron power absorption at different time steps and time averaged over a full rf cycle within the plasma bulk in a capacitively oxygen coupled discharge at both 100 and 10 mTorr for a gap distance of 45 mm. At both 100 and 10 mTorr, the fluid model presented by Schulze *et al.*[31] was applied.

At 100 mTorr at both $t/\tau_{rf} = 0.25$ and $t/\tau_{rf} = 0.75$, the main contributions to both the electric field and the electron power absorption are due to the electron inertia term related to the temporal gradient of the electron velocity (Term I), the gradient pressure related terms (Term IV and V), and the ohmic heating term. At $t/\tau_{rf} = 0.50$, the main contributions to both the electric field and the electron power absorption come from the pressure gradient related terms (Terms IV and V) and from the ohmic heating term

(Term VI). We have also shown that the pressure gradient related terms and the ohmic term contribute to the time averaged electron power absorption, while only the pressure gradient related terms contribute to the time averaged electric field.

At 10 mTorr at $t/\tau_{rf} = 0.25$ and $t/\tau_{rf} = 0.75$, the main contributions to both the electric field and the electron power absorption come from the pressure gradient related terms (Terms IV and V) only, while at $t/\tau_{rf} = 0.50$, a small additional but not negligible contribution from the drift field (Term VI) has been observed. Moreover, in the time averaged case, the main contributions to the electron power absorption come from both the drift field (Term VI) and the pressure gradient related terms (Terms IV and V). We have also shown that the pressure gradient related terms and the ohmic term contribute to the time averaged electron power absorption.

DATA AVAILABILITY

The data that support the findings of this study are available from the corresponding author upon reasonable request.

REFERENCES

[1]S. Wilczek, J. Schulze, R. P. Brinkmann, Z. Donkó, J. Trieschmann, and T. Mussenbrock, J. Appl. Phys. **127**, 181101 (2020).
[2]M. Lieberman and V. Godyak, IEEE Trans. Plasma Sci. **26**, 955 (1998).
[3]V. A. Godyak and A. S. Khanneh, IEEE Trans. Plasma Sci. **14**, 112 (1986).
[4]J. Schulze, A. Derzsi, K. Dittmann, T. Hemke, J. Meichsner, and Z. Donkó, Phys. Rev. Lett. **107**, 275001 (2011).
[5]T. Mussenbrock and R. P. Brinkmann, Appl. Phys. Lett. **88**, 151503 (2006).
[6]U. Czarnetzki, T. Mussenbrock, and R. Brinkmann, Phys. Plasmas **13**, 123503 (2006).
[7]T. Mussenbrock, R. P. Brinkmann, M. A. Lieberman, A. J. Lichtenberg, and E. Kawamura, Phys. Rev. Lett. **101**, 085004 (2008).
[8]M. A. Lieberman, A. J. Lichtenberg, E. Kawamura, T. Mussenbrock, and R. P. Brinkmann, Phys. Plasmas **15**, 063505 (2008).
[9]Z. Donkó, J. Schulze, U. Czarnetzki, and D. Luggenhölscher, Appl. Phys. Lett. **94**, 131501 (2009).
[10]G. Y. Park, S. J. You, F. Iza, and J. K. Lee, Phys. Rev. Lett. **98**, 085003 (2007).
[11]Y.-X. Liu, Q.-Z. Zhang, W. Jiang, L.-J. Hou, X.-Z. Jiang, W.-Q. Lu, and Y.-N. Wang, Phys. Rev. Lett. **107**, 055002 (2011).
[12]J. T. Gudmundsson, E. Kawamura, and M. A. Lieberman, Plasma Sources Sci. Technol. **22**, 035011 (2013).
[13]J. T. Gudmundsson and M. A. Lieberman, Plasma Sources Sci. Technol. **24**, 035016 (2015).
[14]H. Hannesdottir and J. T. Gudmundsson, Plasma Sources Sci. Technol. **25**, 055002 (2016).
[15]J. T. Gudmundsson and B. Ventéjou, J. Appl. Phys. **118**, 153302 (2015).
[16]J. T. Gudmundsson and H. Hannesdottir, AIP Conf. Proc. **1811**, 120001 (2017).
[17]J. T. Gudmundsson and D. I. Snorrason, J. Appl. Phys. **122**, 193302 (2017).
[18]J. T. Gudmundsson, D. I. Snorrason, and H. Hannesdottir, Plasma Sources Sci. Technol. **27**, 025009 (2018).
[19]A. Proto and J. T. Gudmundsson, Atoms **6**, 65 (2018).

[20]A. Proto and J. T. Gudmundsson, Plasma Sources Sci. Technol. **27**, 074002 (2018).

[21]J. T. Gudmundsson and A. Proto, Plasma Sources Sci. Technol. **28**, 045012 (2019).

[22]M. Surendra and M. Dalvie, Phys. Rev. E **48**, 3914 (1993).

[23]M. M. Turner, Phys. Rev. Lett. **75**, 1312 (1995).

[24]G. Gozadinos, M. M. Turner, and D. Vender, Phys. Rev. Lett. **87**, 135004 (2001).

[25]T. Lafleur, P. Chabert, and J. P. Booth, Plasma Sources Sci. Technol. **23**, 035010 (2014).

[26]Y. Liu, J.-P. Booth, and P. Chabert, Plasma Sources Sci. Technol. **27**, 025006 (2018).

[27]R. P. Brinkmann, Plasma Sources Sci. Technol. **25**, 014001 (2016).

[28]M. J. Grapperhaus and M. J. Kushner, J. Appl. Phys. **81**, 569 (1997).

[29]I. Kaganovich, V. Kolobov, and L. Tsendin, Appl. Phys. Lett. **69**, 3818 (1996).

[30]J. Schulze, Z. Donkó, D. L. B. G. Heil, T. Mussenbrock, R. P. Brinkmann, and U. Czarnetzki, J. Phys. D: Appl. Phys. **41**, 105214 (2008).

[31]J. Schulze, Z. Donkó, T. Lafleur, S. Wilczek, and R. P. Brinkmann, Plasma Sources Sci. Technol. **27**, 055010 (2018).

[32]M. Vass, S. Wilczek, T. Lafleur, R. P. Brinkmann, Z. Donkó, and J. Schulze, Plasma Sources Sci. Technol. **29**, 025019 (2020).

[33]C. Birdsall, IEEE Trans. Plasma Sci. **19**, 65 (1991).

[34]E. Kawamura, C. K. Birdsall, and V. Vahedi, Plasma Sources Sci. Technol. **9**, 413 (2000).

[35]E. G. Thorsteinsson and J. T. Gudmundsson, Plasma Sources Sci. Technol. **19**, 055008 (2010).

[36]A. Derzsi, T. Lafleur, J.-P. Booth, I. Korolov, and Z. Donkó, Plasma Sources Sci. Technol. **25**, 015004 (2016).

[37]L. Wang, D.-Q. Wen, Q.-Z. Zhang, Y.-H. Song, Y.-R. Zhang, and Y.-N. Wang, Plasma Sources Sci. Technol. **28**, 055007 (2019).

[38]H. Hannesdottir and J. T. Gudmundsson, J. Phys. D: Appl. Phys. **50**, 175201 (2017).

[39]A. J. Lichtenberg, V. Vahedi, M. A. Lieberman, and T. Rognlien, J. Appl. Phys. **75**, 2339 (1994).

[40]A. J. Lichtenberg, I. G. Kouznetsov, Y. T. Lee, M. A. Lieberman, I. D. Kaganovich, and L. D. Tsendin, Plasma Sources Sci. Technol. **6**, 437 (1997).

[41]M. A. Lieberman and A. J. Lichtenberg, *Principles of Plasma Discharges and Materials Processing*, 2nd ed. (John Wiley & Sons, New York, 2005).

[42]V. Georgieva, A. Bogaerts, and R. Gijbels, J. Appl. Phys. **93**, 2369 (2003).

200

Paper V

Electron power absorption dynamics in radio frequency driven capacitively coupled chlorine discharge

A. Proto and J.T. Gudmundsson

Electron power absorption in radio frequency driven capacitively coupled chlorine discharge

A. Proto[1] and J. T. Gudmundsson[1, 2, *]

[1]*Science Institute, University of Iceland, Dunhaga 3, IS-107 Reykjavik, Iceland*
[2]*Department of Space and Plasma Physics, School of Electrical Engineering and Computer Science,*
KTH Royal Institute of Technology, SE-100 44, Stockholm, Sweden
(Dated: June 7, 2021)

Particle-in-cell Monte Carlo collision simulations and Boltzmann term analysis are applied to study the origination and properties of the electric field and the electron power absorption within the electronegative core of a capacitively coupled discharge in chlorine as the pressure is varied from 1 to 50 Pa. The capacitively coupled chlorine discharge exhibits high electronegativity and high electric field develops within the electronegative core. It is found that the electron power absorption increases and the ion power absorption decreases as the pressure is increased. At 1 Pa the electron power absorption is due to both the pressure and Ohmic terms. At the higher pressures > 10 Pa the Ohmic term dominates and all the other contributions to the electron power absorption become negligible. Therefore, the discharge becomes increasingly Ohmic with increased pressure and eventually behaves as a resistive load.

I. INTRODUCTION

A capacitively coupled discharge is composed of two parallel metallic electrodes, one driven by an rf voltage or current source while the other electrode is grounded [1, 2]. A neutral gas pressure is maintained between the electrodes, typically in the range from 0.1 to 100 Pa. The applied voltage amplitude is typically few hundred volts while the driving frequency is in the range between hundreds of kHz and few hundred MHz. Such discharges are used in a wide range of applications and they are indispensable for deposition, etching, and sputtering, which are all vital processes in microelectronic and solar cell fabrication. The chlorine discharge is commonly applied for etching processes in integrated circuit fabrication, in particular to etch poly-silicon, aluminum, and compound semiconductors [3]. Chlorine based plasma discharges are often applied when highly anisotropic etching is desired, in particular for conductive materials such as for poly-silicon gate definition [4–6]. Due to its importance, the etching of silicon in chlorine discharges has been studied extensively for decades [4, 7–12].

The capacitively coupled chlorine discharge is known to exhibit high electronegativity [13, 14] and electric field is known to develop within the discharge electronegative core. In electronegative discharges, large electron density gradients are established as there appears a local maxima at the bulk-sheath interface and consequently ambipolar fields develop. Drift fields are also known to develop as the electron density is typically low and therefore, the bulk conductivity is low. Consequently, due to the drift and ambipolar fields, electron power absorption appears within the discharge electronegative core, as electrons are accelerated by these fields. In capacitively coupled

discharges this mode of operation has been called drift-ambipolar (DA) mode [15, 16]. Such electron power absorption structure has been observed experimentally in a capacitively coupled SF_6/N_2 [17] and SiH_4 [18] discharges using spatiotemporal optical emission spectroscopy, and in CF_4 discharges using phase resolved optical emission spectroscopy [19, 20]. Furthermore, this electron power absorption mechanism has been identified by relaxation continuum modeling [21]. In fact DA electron power absorption can be the dominating electron power absorption mechanism in highly electronegative discharges [17, 21]. The electronegative discharge can also exhibit striations, where under certain conditions the positive and negative ions can be driven to oscillations as their densities are modulated by the external driving potential, and therefore, induce electric field, that is superimposed onto the drift field [22–25].

Particle-in-cell/Monte Carlo collision (PIC/MCC) simulations have been applied to study the capacitively coupled chlorine discharge, including the impact of discharge pressure on a voltage driven single frequency (SF) discharge [13], the influence of the current amplitude, the frequency and the secondary electron emission in a current driven SF discharge [26], a 'classical' dual frequency (DF) discharge [26, 27], and a current driven DF discharge, while varying the high frequency (HF) and the low frequency (LF) source control parameters independently [28]. It has been demonstrated that the electron power absorption is dominated by the drift-ambipolar (DA) mode within the electronegative core [13, 14]. Furthermore, at higher operating pressures it has been shown that electron power absorption dominates over ion power absorption. The fractional power absorbed by the electrons, Cl_2^+ ions, and Cl^+ ions, varies with pressure [13, 14]. At low pressure ∼1 Pa the Cl_2^+ ion power absorption dominates, with roughly 69 % contribution, while the electrons absorb about 29 %. At 10 Pa 69 % of the power is absorbed by the electrons, while Cl_2^+ ions exhibit about 31 % contribution [14]. At pressure

*tumi@hi.is

of 50 Pa the electron power absorption has increased significantly to about 85 % of the overall power absorption. Power absorption due to the Cl$^+$ ions has much smaller or almost negligible contribution at all pressures [13, 14]. Note that the total electron power absorption increases with increasing pressure and is significantly higher at 50 Pa than at 1 Pa. In the more recent study PIC/MCC simulations were applied to study a capacitively coupled chlorine discharge that was driven by a tailored voltage waveform [14]. The voltage waveform was constructed from a fundamental frequency of 13.56 MHz and a second harmonic of 27.12 MHz. It was there demonstrated that a dc self-bias and therefore asymmetric response can be created. This can be used to control the ion energy independent of the ion flux onto the electrodes in the pressure range 1 – 10 Pa. However, the achievable control range for the ion energy bombarding the grounded electrode is found to be rather limited [14], significantly narrower range than achieved for electropositive discharge operated in the α-mode [29–31]. At 50 Pa, the highest operating pressure studied, the electrical asymmetry effect was found to be unsuited for ion energy control in the chlorine discharge. Operation in DA-mode therefore, appears to restrict the application of the electrical asymmetry effect, to independently control the ion energy and ion flux onto the electrodes, in capacitively coupled chlorine discharges.

There have been several attempts to use the Boltzmann equation to describe the electron power absorption process in capacitively coupled discharges [32–36]. Schulze et al. [35, 36] presented a streamlined moment analysis of the Boltzmann equation (referred to as Boltzmann term analysis). This approach was subsequently applied to study the power absorption processes for the electrons in capacitively coupled argon discharges [36–38] and oxygen discharges [39, 40]. Using Boltzmann term analysis, Ohmic power absorption is found to play a significant role even at low pressure in argon [37] and oxygen discharges [39, 40]. Note that the electron power absorption processes in oxygen discharges are distinctly different depending on the operating pressure, at low pressure < 2 Pa, the discharge is highly electronegative and DA-power absorption dominates, while at higher pressure > 4 Pa, the discharge is weakly electronegative and is operated in α-mode [41, 42]. In the oxygen discharge, the pressure terms dominate, the temperature gradient term contributes to electron cooling, and the ambipolar term to electron power absorption, when operating at the higher pressures > 10 Pa, and the opposite applies at low pressure ∼ 1 Pa [40].

Here, 1d-3v PIC/MCC simulations are applied to study the various contributions to the electric field and therefore, the power absorption by the electrons within the electronegative core of a capacitively coupled chlorine discharge. Section II is a brief overview of the method of the simulation and its set up. In Section III the density profiles of the charged particles and the spatio-temporal plots showing the total charge density are discussed. In Section IV a simple Boltzmann term analysis based on the method described by Schulze et al. [36] is employed to study the origins, and the behavior of the electric field as well as the electron power absorption mechanisms, in the operating pressure range 1 – 50 Pa, and the terms, contributing to creation of electric field and consequent electron power absorption, identified. Finally, a summary and conclusions are given in Section VI.

II. THE SIMULATION METHOD AND SETUP

Here, the one-dimensional object-oriented PIC/MCC code oopd1 [43] is applied to explore a capacitively coupled chlorine discharge. oopd1 is a 1d-3v PIC/MCC code and the model system has one spatial dimension and three velocity components. The Cl$_2$ molecule exhibits low (near zero) threshold for dissociative attachment and low dissociation energy (2.5 eV), while the electron affinity is high (2.45 eV). The PIC/MCC model for chlorine is constituted of the ground state molecule Cl$_2(X^1\sum_g^+, v = 0)$, the ground state atom Cl(^{2}P$_u$), the negative ion Cl$^-$(^{1}S$_g$), and the positive ions Cl$^+$(^{3}P$_g$) and Cl$_2^+$($^2\Pi_g$). The reactions taken into account in our PIC/MCC study and the cross sections are described in detail elsewhere [13]. All interactions between particles are treated through the null-collision scheme in the Monte Carlo method [44]. The dc self-bias is calculated in oopd1 to ensure that the fluxes of charged particles at both the electrodes, averaged over one period of the fundamental driving frequency, are equal [45, 46]. This is done iteratively.

In oopd1 the particle weights, the ratio of the number of real particles to computational particles, can be implemented separately for each species [43]. The charged particles are tracked for all energies, while only the neutral particles that exhibit kinetic energy exceeding a preset threshold value are tracked kinetically. The preset thresholds and particle weights were chosen to maintain the number of simulated particles within a suitable range, typically $10^4 - 10^5$ particles. Neutral particles with energy below this set threshold energy belong to the fixed background density. The species of the fixed background density have a Maxwellian energy distribution for a temperature of $T_n = 26$ mV. For both Cl$_2$ molecules and Cl atoms the set threshold energy is 500 meV for all the discharges studied here.

When modeling and simulating molecular gases, the dissociation processes, and the processes that involve charged particles, occur on widely different timescales. For a pure Cl$_2$ feedstock gas, the creation of Cl atoms is dominated by electron impact dissociation of Cl$_2$ molecules. Here we take a hybrid approach, where a global model [47, 48] is used to determine the dissociation fraction within the discharge, beforehand, for a given operating pressure, absorbed power and electrode separation, etc. In a volume averaged global model the plasma chemistry is described by a set of nonlinear first order dif-

TABLE I: The composition of the thermal background neutrals used in the PIC/MCC simulations. The partial pressure is determined by global (volume averaged) model calculations.

p [Pa]	Cl	Cl_2
1	0.0422	0.9578
10	0.0638	0.9362
25	0.0246	0.9754
35	0.0218	0.9782
50	0.1790	0.8210

ferential equations; a particle balance equation for each of the species included in the discharge model and an equation describing the conservation of energy. The species are assumed to be nearly spatially uniform and the power deposited uniformly into the volume. Furthermore, the acceleration of ions towards the surfaces is significantly smaller than that expected in a capacitively coupled discharge, so higher fraction of the absorbed power will be dissipated in electron heating in the global model calculation which may overestimate the Cl atom density somewhat, in particular at lower pressure. Global models neglect spatial variations in the plasma parameters as well as the kinetics of the discharge. The absorbed power calculated by the PIC/MCC simulation for a given pressure and gap size becomes an input parameter for the global model calculations, iteratively. This gives the partial pressures for Cl_2 molecules and Cl atoms that are used to set the composition of the neutral background gas in the PIC/MCC simulation and are listed in Table I. The calculated values are in agreement with the experimentally determined values, as the fraction of Cl atoms is found to be roughly few percent at 1.33 Pa for absorbed power below 10 W [49–51].

The fraction of Cl atoms that recombine to form Cl_2 molecules as they hit the electrodes is given by the surface recombination coefficient. This parameter determines the dissociation fraction and the negative ion density in a chlorine discharge [52]. The measured surface recombination coefficients span the range $0.01 - 0.85$ [53–56]. Therefore, we assume here that a Cl atom hits the electrode, it is assumed to return as a thermal Cl atom with 50 % probability or to recombine and form a thermal Cl_2 molecule with 50 % probability. This is the same assumption as made in our previous studies [13, 26, 27]. The electron reflection coefficient as well as the ion and neutral impact secondary electron emission yield from the electrodes are assumed to be zero. Therefore, secondary electrons and their influence on the discharge properties are neglected in this study.

The discharge is sustained between two electrodes of equal size where one of the electrodes is driven by an rf voltage

$$V(t) = V_0 \sin(2\pi f t) \qquad (1)$$

for single frequency operation, where f is the frequency, V_0 is the voltage amplitude, and t is time. For this present study the voltage amplitude is $V_0 = 222$ V the frequency $f = 13.56$ MHz and the electrode separation 25.4 mm. A capacitor of 1 μF is connected in series with the voltage source. The other electrode is grounded. The pressure is varied in the range from 1 to 50 Pa.

The sheath edge $x_{\mathrm{sh}}(t)$ is assumed to be located where the electron density has dropped to half the density of the positively charged species or $n_e(x,t)/n_i = 1/2$. This determines the location of the vertical dashed lines indicating the time averaged position of the sheath edge in the various plots shown below.

III.   RESULTS FROM THE SIMULATION

An electronegative discharge consists of an electronegative core with electrons and negative ions in Boltzmann equilibrium and electropositive edge plasma regions next to the electrodes [57, 58]. When operating at high pressure (> 10 Pa) and low power the electronegative core almost fills the entire gap between the electrodes, and the positive and negative ion densities can be assumed to exhibit parabolic profiles, while the electron density is significantly lower and uniform, except at the plasma sheath interface [57, 58].

The charged particle density profiles for Cl_2^+ ions, Cl^+ ions, Cl^- ions, and electrons at 1, 10, 25, 35 and 50 Pa, from the discharge center up to the right electrode, are shown in Figure 1. At all pressures the Cl_2^+ and Cl^- ion densities are similar within the plasma bulk, or the electronegative core, and their densities increase with increased pressure. That is the same pattern that has been observed in oxygen discharge operated at very low pressure (< 4 Pa) [40, 59] and for CF_4 discharge operated above few tens of Pa [60]. At 1 Pa (Figure 1 (a)) both the Cl^- ion and Cl_2^+ ion density profiles are very similar, but closer to the sheath edge the Cl^- ion density decreases faster than the Cl_2^+ ion density. The presence of negative ions is met by depletion in the electron density to maintain quasi-neutrality. Therefore, the electron density profile is roughly two orders of magnitude lower than both the Cl^- ion and the Cl_2^+ ion densities and rather uniform within the plasma bulk region. The electron density peaks at the edge of the electronegative core and then sharply decreases in the sheath regions, remaining lower than the Cl_2^+ ion density but becoming higher than the Cl^- ion density. The Cl_2^+ and Cl^- ion densities increase as the pressure is increased, as seen by comparing Figures 1 (a) – (e). Also the electron density increases with increasing pressure. The Cl^+ ion density is almost constant within the electronegative core and decreases sharply as the sheath edge is approached. We observe that the Cl^+ density decreases with increased pressure but increases again at 50 Pa where it is higher than at 35 Pa. The center electronegativity is in the range 104 – 144 and the spatially averaged electronegativity some-
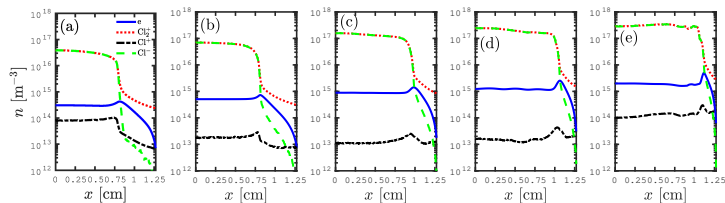
FIG. 1: The time averaged charged particle density profiles of a parallel plate capacitively coupled chlorine discharge at (a) 1 Pa, (b) 10 Pa, (c) 25 Pa, (d) 35 Pa, and (e) 50 Pa, from the discharge center up to the right electrode. The gap separation is 25.4 mm, the voltage amplitude 222 V and driving frequency 13.56 MHz.

what lower or in the range 69 – 95 [14]. Therefore, the electronegativity is high, indeed.

Figure 2 shows the spatio-temporal behavior of the total charge density ρ_{total} at various pressures between the electrodes spanning a full rf period. The total charge density is defined

$$\rho_{\text{total}} = e \left(n_{\text{Cl}_2^+} + n_{\text{Cl}^+} - n_{\text{Cl}^-} - n_{\text{e}} \right), \qquad (2)$$

where $n_{\text{Cl}_2^+}$ is the density of Cl_2^+ ions, n_{Cl^+} is the density of Cl^+ ions, n_{Cl^-} is the density of Cl^- ions and n_{e} is the electron density. For all pressures a net positively charged stripe is observed on the sheath side of both the sheath edges over the full rf-cycle. Also a net negative charged stripe appears on the bulk side of both the collapsing sheath edges for all pressures. Moreover, both the positive and negative charged stripes decrease in width with increased pressure. Finally, the sheath regions tighten as the pressure is increased. That is the same general pattern as has already been observed in oxygen discharges [40]. The spatio-temporal behavior of the total charge density at 1 Pa is shown in Figure 2 (a). Apart from the already mentioned positive and negative charged stripes, we observe vertical negative stripes within the bulk region. In fact the bulk region is neutral only for small space intervals. At 10 Pa (Figure 2 (b)) we observe almost the same situation encountered at 1 Pa, with a few differences. The charge density has increased everywhere and both the positive and negative charged stripes are narrower compared to the 1 Pa case (Figure 2 (a)). At 25 Pa (Figure 2 (c)) we observe that both the positive and negative charged stripes have become still narrower compared to the 1 and 10 Pa cases. The charge density has increased everywhere with respect to the 10 Pa case. At 35 Pa (Figure 2 (d)) we observe that both the positive and negative charged stripes are very weak, as well as the vertical negative lines within the bulk region. The charge density has increased within the sheath regions with respect to both the 10 Pa and the 25 Pa cases. At 50 Pa (Figure 2 (e)) we observe that both the positive

and negative charged stripes are even fainter (Figure 2 (d)).

IV. BOLTZMANN TERM ANALYSIS

The DA-electron power absorption is related to the development of electric field within the electronegative core. The appearance of electric field within the electronegative core, or the plasma bulk, constitutes contributions through various different phenomena, and depends on the gas considered and its pressure. The electron power absorption process is more complicated in the electronegative discharge. Surendra and Dalvie [32] proposed an approach based on the moments of the Boltzmann equation, where the electric field was decomposed into a sum of terms, each representing a particular physical mechanism. Furthermore, they determined that the electron pressure terms (or collisionless heating), are indeed important. Recently, the Surendra-Dalvie framework has been used to describe the behavior of the electric field within the plasma bulk of capacitively coupled discharges. Based on this framework, Boltzmann term analysis describes the electric field origins and behavior as well as the electron power absorption mechanisms within the electronegative core [36]. However, here we neglect both ionization and momentum change. Due to the very small electron density in the expanded sheath regions the electric field is only applicable within the discharge bulk region as well as in the collapsed sheath regions. Furthermore, the ideal gas law is employed and the quasi-neutrality condition has not been imposed. The pressure tensor and the temperature are not isotropic for all pressures explored here for chlorine. Therefore, since $p_{\text{e,xx}} \neq p_{\text{e,yy}} \neq p_{\text{e,zz}}$ and $T_{\text{e,xx}} \neq T_{\text{e,yy}} \neq T_{\text{e,zz}}$, we are left with $p_{\text{e}} \equiv p_{\text{e,xx}} = e n_{\text{e,xx}} T_{\text{e,xx}}, p_{\text{e,yy}} = e n_{\text{e,yy}} T_{\text{e,yy}}$, and $p_{\text{e,zz}} = e n_{\text{e,zz}} T_{\text{e,zz}}$. In this framework, the electric field is
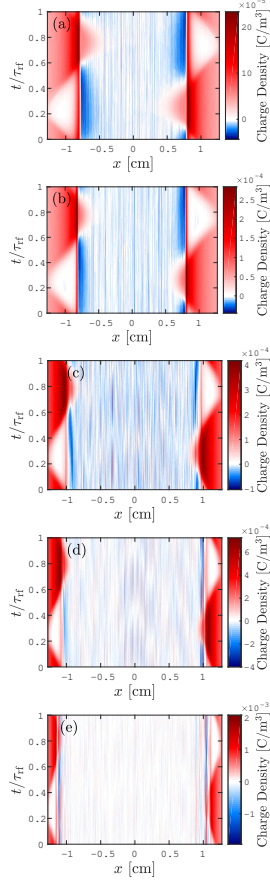
FIG. 2: The spatio-temporal behavior of the total charge density, defined by Eq. (2), at (a) 1 Pa, (b) 10 Pa, (c) 25 Pa, (d) 35 Pa and (e) 50 Pa, over the full gap length, for a capacitively coupled chlorine discharge. The gap separation is 25.4 mm, the voltage amplitude 222 V and the driving frequency 13.56 MHz.

composed of six terms [40]

$$E = -\underbrace{\frac{m_e}{e}\frac{\partial u_e}{\partial t}}_{\text{I}} + \underbrace{\frac{m_e}{e}\frac{u_e^2}{n_e}\frac{\partial n_e}{\partial x}}_{\text{II}} + \underbrace{\frac{m_e}{e}\frac{u_e}{n_e}\frac{\partial n_e}{\partial t}}_{\text{III}} - \underbrace{\frac{T_e}{n_e}\frac{\partial n_e}{\partial x}}_{\text{IV}}$$
$$- \underbrace{\frac{\partial T_e}{\partial x}}_{\text{V}} - \underbrace{\frac{m_e u_e \nu_c}{e}}_{\text{VI}}, \qquad (3)$$

where the first and the third term (I and III) represent electron inertia due to the time derivative of electron velocity and density, respectively, and term II represents the contribution from a normalized electron density gradient. Term IV is due to diffusion (ambipolar field) [15, 35] and term V represents the electron temperature gradient. Consequently, terms IV and V represent pressure effects, historically referred to as a collisionless mechanism [61]. The sixth term (VI) represents collisions between electrons and atoms or molecules (drift field). A given set of parameters are fed into Equation (3), including the electron density and temperature, which are taken from the results of the PIC/MCC simulations. Term VI was derived from the reaction rate for the electron neutral elastic collision. The quantities taken from the output of the simulations and used in the calculations using Eqs. (3) and discussed below, are stored as arrays that are extended spatially along the x−axis. In particular, the components that constitute the electron temperature are calculated using $T_{e,ii} = \frac{2}{e}\mathcal{E}_{e,ii} - \frac{m_e}{e}u_{e,i}^2$, where the mean electron energy density is $\mathcal{E}_{e,ii}$, and the electron mean velocity is $u_{e,ii}^2$, where $i = x, y, z$. By definition $\mathcal{E}_{e,i} = \frac{m_a}{2}\langle v_{e,i}^2 \rangle$, therefore the electron temperature is the same as suggested by Wilczek et al. [38], for non negligible particle mean velocity. Multiplying the electric field from Eq. (3) by the electron current density $J_e = -en_e u_e$ the electron absorbed power can be determined as follows

$$J_e \cdot E = \underbrace{m_e u_e n_e \frac{\partial u_e}{\partial t}}_{\text{I}} - \underbrace{m_e u_e^3 \frac{\partial n_e}{\partial x}}_{\text{II}} - \underbrace{m_e u_e^2 \frac{\partial n_e}{\partial t}}_{\text{III}}$$
$$+ \underbrace{e u_e T_e \frac{\partial n_e}{\partial x}}_{\text{IV}} + \underbrace{e n_e u_e \frac{\partial T_e}{\partial x}}_{\text{V}} + \underbrace{m_e n_e \nu_c u_e^2}_{\text{VI}} \qquad (4)$$

Each electron power absorption term that constitutes Eq. (4) is derived from the terms that constitute Eq. (3). Thus, terms I and III represent power absorption due to electron inertia, term II represents power absorption related to the electron density gradient, term IV represents the ambipolar field originating from the electron density gradient [15, 35], and term V represents the electron temperature gradient. The fourth and fifth terms therefore represent pressure or collisionless heating [32, 36, 38, 61]. The sixth term (VI) represents electron neutral collisions and therefore Ohmic heating.

V. RESULTS AND DISCUSSION

PIC/MCC simulations were used to study the creation of electric field and consequent power absorption by electrons within the electronegative core of a capacitively coupled discharge in chlorine as the pressure is varied in the range from 1 to 50 Pa. The chlorine discharge exhibits high electronegativity and high electric field is observed within the electronegative core.

Figure 3 shows the spatio-temporal behavior of the various electric field terms that constitute Eq. (3) at various pressures, 1, 25, and 50 Pa. Note that the color scale indicating the electric field strength for the various figures varies as the electric field varies over a wide range between the various terms and as the pressure is varied. At 1 Pa term I (inertia term) (Figure 3 (a1)) penetrates the bulk region and is slightly negative (positive) within the bulk region on the first (second) half of the rf cycle, while it is close to zero around the the middle of the rf cycle. We also observe that term I is positive on the left sheath edge and negative on the right sheath edge. Furthermore, within the expanded sheath regions term I is zero. At the higher pressures 25 Pa (Figure 3 (b1)) and 50 Pa (Figure 3 (c1)) it shows the same behavior but the magnitude in all regions decreases with increasing pressure. Term II (inertia term) (Figure 3 (a2)) is zero within both the bulk and the sheath regions. Like term I, term II is positive on the left sheath edge and negative on the right sheath edge. However, term II exhibits much higher amplitude on both the sheath edges than term I. Term II exhibits similar structure at the higher pressures 25 Pa (Figure 3 (b2)) and 50 Pa (Figure 3 (c2)) but exhibits increased amplitude with increasing pressure. The spatio-temporal behavior of Term III (inertia term) (Figure 3 (a3)) is similar to term II (Figure 3 (a2)), with the difference that term III is positive (negative) on the right (left) sheath edge, that is the behavior is opposite to terms I and II. Term III exhibits similar spatio-temporal structure at the higher pressures 25 Pa (Figure 3 (b3)) and 50 Pa (Figure 3 (c3)) but the amplitude decreases with increasing pressure. Terms I – III represent the electric field that balances a change in electron momentum or electron inertia. Term IV (ambipolar pressure term) (Figure 3 (a4), (b4) and c(4)) is zero within the bulk and the expanded sheath regions, while it is negative on the sheath side to the left of the collapsed sheath region and on the bulk side of the right collapsed sheath region, and positive on the bulk side of the left collapsed sheath region and on the sheath side of the right collapsed sheath region. Moreover, as already seen for Term III (Figure 3 (a3)), we observe that Term IV is positive (negative) on the right (left) sheath edge. There is also a small negative swelling on the bulk side of the left fully expanded sheath edge, and positive swelling on the bulk side of the right fully expanded sheath edge. Term IV maintains the same general structure as the pressure is increased as seen at 25 Pa (Figure 3 (b4)) and 50 Pa (Figure 3 (c4)) but the magnitude in-

creases slightly with increased pressure and the negative and positive charged stripes on both the bulk sides of the collapsed sheath regions are narrower. Note that terms II and IV are both proportional to $(1/n_e)(\partial n_e/\partial x)$ but have opposite signs. Recall that the electron density exhibits a maximum at the edge of electronegative core as seen in Figure 1. Therefore, these terms exhibit a maximum in the vicinity of the maximum sheath width as clearly seen in Figures 3 (a2) and (a4), (b2) and (b4), and (c2) and (c4). Term V (electron temperature gradient pressure term) (Figure 3 (a5)) behaves as term IV (Figure 3 (a4)), and exhibits a maximum around the position of the maximum sheath width. However, two important differences are observed: First, on the second half of the rf cycle we observe a negative stain starting from the sheath edges on both sides, up to the inner core of the plasma bulk. Second, non trivial stripes-like structures appear within the collapsed sheath regions. At 25 Pa and 50 Pa term V (Figure 3 (b5) and (c5)) has changed drastically from what was observed at 1 Pa (Figure 3 (a5)). The stripes placed within the collapsed sheath regions at 1 Pa have now completely disappeared. Also, Term V is now almost zero within the collapsed sheath regions. Term VI (Ohmic term) (Figures 3 (a6), (b6) and (c6)) is zero in the expanded sheath regions but it penetrates into the electronegative core. The Ohmic contribution is apparent within the plasma bulk and extends across the entire plasma bulk region. It is negative (positive) within the plasma bulk from $t/\tau = 0.25$ up to $t/\tau = 0.75$ (from $t/\tau = 0.75$ up to $t/\tau = 0.25$). The electric field magnitude due the the ohmic term increases with increasing pressure. Therefore, the dominating contribution to the electric field at 50 Pa is due to the Ohmic term. Note that the pressure terms have the highest peak magnitude of all the terms. However, they are active only around the sheath edge and their spatial extension decreases with increased pressure. At 1 Pa the electric field is due to the Ohmic term along with the pressure terms, while the inertia terms, show a higher peak magnitude compared to the Ohmic term at the sheath edges on both sides.

Figure 4 shows the time averaged profiles for the three dominating terms of Eq. (3): term IV (red line), term V (blue dashed line) and term VI (green dot dashed line). At 1 Pa (Figure 4 (a)) term IV appears to be almost uniform and zero within the bulk region and builds to a small local maximum (minimum) on the bulk side of the left (right) sheath edge. Then it decreases (increases) steeply while the left (right) sheath edge is crossed and increases (decreases) sharply as the left (right) electrode is approached. Term V is zero in the discharge center and increases (decreases) slightly as the bulk side of the left (right) sheath edge is approached, where it forms a local maximum (minimum), which almost overlaps the respective maximum (minimum) of term IV. It sharply decreases (increases) at the sheath edge and increases (decreases) slightly as the electrodes are approached. Term VI remains flat and zero spanning the full gap width. At 10 Pa (Figure 4 (b)) the situation is almost identi-

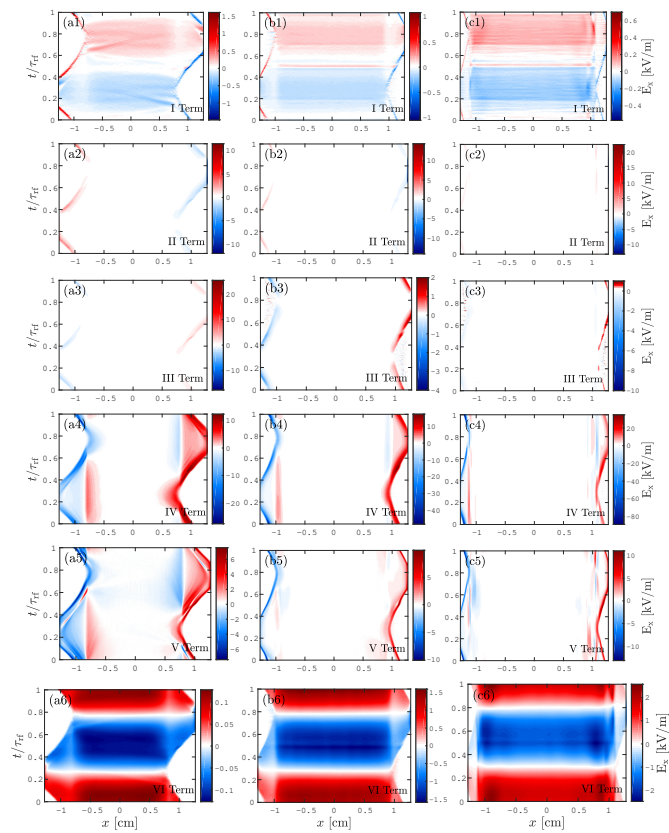FIG. 3: The spatio temporal behavior of the various terms that constitute the electric field given by Eq. (3) at (a) 1 Pa, (b) 25 Pa, and (c) 50 Pa for a capacitively coupled chlorine discharge. The gap separation is 25.4 mm, the voltage amplitude 222 V and driving frequency 13.56 MHz. The rows represent the various terms (1) Term I, (2) Term II, (3) Term III, (4) Term IV, (5) Term V and (6) Term VI.
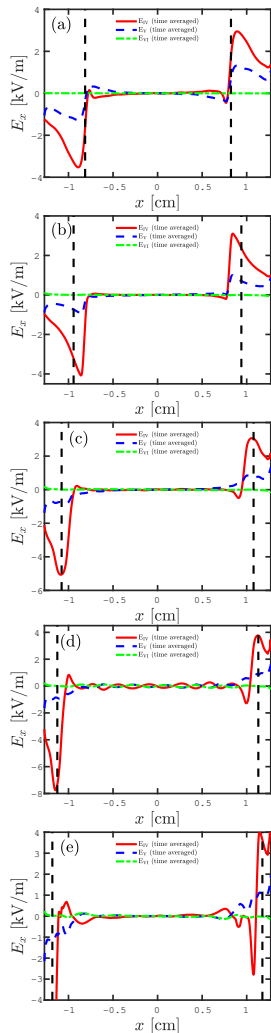
FIG. 4: The time averaged electric field due to term IV (red line), term V (blue dashed line), term VI (green dot dashed line) at (a) 1 Pa, (b) 10 Pa, (c) 25 Pa, (d) 35 Pa, and (e) 50 Pa calculated using Eq. (3) for a capacitively coupled chlorine discharge. The gap separation is 25.4 mm, the voltage amplitude 222 V and driving frequency 13.56 MHz. The vertical dashed lines indicate the time averaged position of the sheath edge.

cal compared to the 1 Pa case (Figure 4 (a)). Terms IV and V are totally flat and zero spanning most of the bulk width and the maximum (minimum) of term V is smaller (larger) compared to the 1 Pa case (Figure 4 (a)). Moreover, both the absolute maximum and the minimum of term IV are now located on the bulk sides close to the sheath edges, contrary to what we have observed at 1 Pa (Figure 4 (a)), where both the extrema are located on the sheath side of both the sheath edges. For the higher pressures of 25, 35, and 50 Pa (Figure 4 (c), (d) and (e)) the situation is similar to the 10 Pa case (Figure 4 (b)). The main difference lies in the fact that both the absolute maximum and minimum of term IV are now exactly placed on both the sheath edges. But at 35 Pa (Figure 4 (d)) all the terms IV, V and VI exhibit oscillating behavior within the bulk region. This is commonly associated in literature as being a hint of striation structures [22, 23]. Striations have been known to appear in electronegative discharges when two conditions are simultaneously fulfilled: high enough electronegativity and a driving frequency that is comparable to the ion plasma frequency. When these two conditions are fulfilled, the positively charged and negatively charged ions oscillate back and forth. Consequently the separation of the positive and negative charges leads to creation of electric field, that is superimposed onto the drift field. This field appears as a striated total field within the electronegative core. The appearance of the striations depends heavily on the ion-neutral collision frequency, and therefore the ion-neutral cross sections, and on the pressure [24]. Liu et al. [24] derived a critical ion density, beyond which the striations can be present. The ion density increases with pressure and at 25 Pa the critical ion density of 9.8×10^{16} m^{-3} is overcome. With further increase in pressure the oscillation amplitude decreases as it is proportional to inverse ion-neutral collision frequency, or inverse pressure. Note that in our current reaction set for chlorine the interactions between the heavy particles are based on cross sections that are estimated from rate coefficients using $\sigma = k_0/\sqrt{2e\mathcal{E}/\mu}$, where k_0 is the rate coefficient and μ is the reduced mass. The rate coefficients are often taken from measurements but some are estimated as discussed elsewhere [13]. In all cases the resulting cross section is of similar value as Langevin cross section and scales as $\propto 1/\sqrt{\mathcal{E}}$. Striations have been observed in capacitively coupled CF$_4$ [22–24] and oxygen [25] discharges. Keep in mind that secondary electron emission from the electrodes, due to ion and neutral impact, is neglected in our work. Secondary electron emission has been shown to disrupt the striations in capacitively coupled oxygen discharge and it has been demonstrated that the electron power absorption mode transitions to γ-mode as the secondary electron emission yield is increased [25]. The influence of the secondary electrons is expected to be particularly important at the higher pressures. Also note that at 50 Pa (Figure 4 (e)) term IV exhibits some significant structure in particular on the bulk side near the sheath edges.

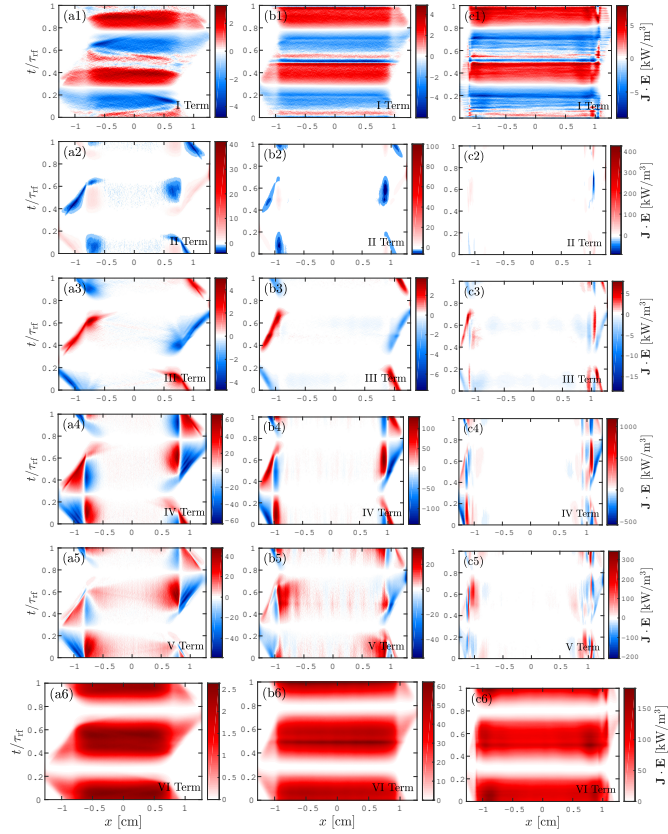FIG. 5: The spatio temporal behavior of the various terms that constitute the electron power absorption given Eq. (4) at (a) 1 Pa, (b) 25 Pa, and (c) 50 Pa for a capacitively coupled chlorine discharge. The gap separation is 25.4 mm, the voltage amplitude 222 V and driving frequency 13.56 MHz. The rows represent the various terms (1) Term I, (2) Term II, (3) Term III, (4) Term IV, (5) Term V, and (6) Term VI.

Figure 5 shows the spatio-temporal behavior of the electron power absorption terms that constitute Eq. (4) at various pressures, 1, 25, and 50 Pa. Note that the color scale indicating the electron power absorption by the various terms varies over a wide range between the various terms and as the pressure is varied. At 1 Pa Term I (inertia term) (Figure 5 (a1)) is negative (positive) within the collapsing (expanding) sheath regions, while it is positive (negative) within the plasma bulk from both $t/\tau = 0.25$ up to $t/\tau = 0.50$ and from $t/\tau = 0.75$ up to $t/\tau = 1$ (from both $t/\tau = 0$ up to $t/\tau = 0.25$ and from $t/\tau = 0.50$ up to $t/\tau = 0.75$). We also observe that term I is zero within the expanded sheath region. At 25 Pa and 50 Pa term I (Figure 5 (b1) and (c1)) shows similar spatio-temporal dependence, it is negative (positive) within the collapsing (expanding) sheath regions, while it is positive (negative) from both $t/\tau = 0.25$ up to $t/\tau = 0.50$ and from $t/\tau = 0.80$ up to $t/\tau = 1$ from both $t/\tau = 0$ up to $t/\tau = 0.25$ and from $t/\tau = 0.50$ up to $t/\tau = 0.80$) within the plasma bulk. Moreover, it exhibits horizontal stripes within the plasma bulk and the negative valued regions. The magnitude of the power increases slightly with increased pressure. At 50 Pa term I (Figure 5 (c1)) is similar to the 25 Pa case (Figure 5 (c2)). At 1 Pa Term II (inertia term) (Figure 5 (a2)) is positive on the bulk side of the expanding sheath edges as well as on the sheath side of the collapsing sheath edges and is negative on the bulk side of the collapsing sheath edges and on the sheath side of the expanding sheath edges. We observe that Term II is zero (negative) within the bulk from both $t/\tau = 0.20$ up to $t/\tau = 0.40$ and from $t/\tau = 0.60$ up to $t/\tau = 0.80$ (from both $t/\tau = 0.40$ up to $t/\tau = 0.60$ and from $t/\tau = 0.80$ up to $t/\tau = 0.20$) and within the expanded sheath regions. At 25 Pa and 50 Pa term II (Figure 5 (b2) and (c2)) is positive (negative) on the expanding (collapsing) sheath edges and is zero within both the plasma bulk as well as the sheath regions. These regions on the expanding (collapsing) sheath edges shrink as the pressure is increased. Term III (inertia term) (Figure 5 (a3)) is zero within the bulk region as well as in the expanded sheath regions while it is positive (negative) on the expanding (collapsing) sheath edges. For the collapsing sheath term III is negative on the sheath side. Small negative strains are observed within the bulk region around the middle of the rf cycle. At 25 Pa term III (inertia term) (Figure 5 (b3)) is almost identical to the 1 Pa case. At 50 Pa term III (inertia term) (Figure 5 (c3)) is weakly positive (negative) on the expanding (collapsing) sheath edges. Moreover, on the bulk side we observe small negative stains for both the collapsing sheath edges and within the bulk region, as has already been observed at 25 Pa (Figure 5 (b3)). Term III exhibits more structure around the sheath region at higher pressures than at the lower pressures. Term IV (ambipolar pressure term) (Figure 5 (a4), (b4) and (c4)) is positive (negative) on both the bulk side (sheath side) of the collapsing sheath edge as well as on the sheath side (bulk side) of the expanding sheath edge. Furthermore, term IV is zero within both

the electronegative core and the expanded sheath region. Finally, we observe a small positive (negative) swelling at the bulk side of the fully expanding (initially collapsing) sheath edge. With increasing pressure term IV exhibits the same basic spatial-temporal behavior except that the positive (negative) regions located on both the bulk side (sheath side) of the collapsing sheath and the sheath side (bulk side) of the expanding sheath become narrower. Also, the small positive (negative) swelling observed on the bulk side of the fully expanding (initially collapsing) sheath edge at 1 Pa have almost completely disappeared. Finally, the peak amplitude of term IV increases with increased pressure in particular between 25 and 50 Pa. There is more structure around the sheath edges at 50 Pa. Term V (electron temperature gradient pressure term) (Figure 5 (a5), (b5) and (c5)) exhibits similar spatio-temporal structure as term IV. The main difference lies in the amplitude of term V which is slightly lower everywhere. Moreover we observe negative strains crossing the bulk region around both the beginning and the middle of the rf cycle. At 25 Pa (Figure 5 (b5)) striations can be observed within the bulk region. Note that the peak amplitude is lower at 25 Pa than at 1 Pa, but it is significantly higher at 50 Pa. For all pressures there is apparent electron power loss in the vicinity of the position of the maximum sheath edge during sheath expansion. Vass et al. [39] relate this to energetic electrons that are moving to a region of lower electron temperature. Due to this a double layer is formed, with negative charges on the bulk side, which generates electric field which decelerates the electrons. This field penetrates into the electronegative core. Term VI (the Ohmic term) (Figure 5 (a6)) is zero within the expanded sheath regions and over the full gap length around both $t/\tau = 0.25$ and $t/\tau = 0.75$. Apart from the null stripes, term VI is strictly positive inside the plasma bulk region and slightly positive within the collapsed sheath regions as it depends on the mean electron velocity squared. The amplitude within the bulk region increases significantly with increased pressure (Figure 5 (b6) and (c6)) and it is up to two orders of magnitude higher at 50 Pa than at 1 Pa. The most significant contribution to electron power absorption at the higher pressures is due the Ohmic term which dominates within the bulk region.
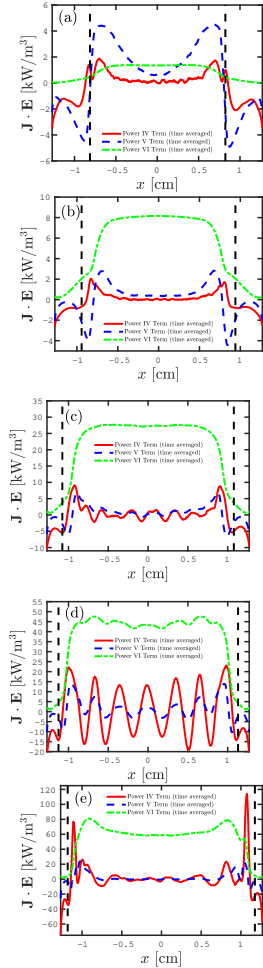
FIG. 6: The time averaged electron power absorption profile of term IV (red line), term V (blue dashed line), term VI (green dot dashed line) at (a) 1 Pa, (b) 10 Pa, (c) 25 Pa, (d) 35 Pa, and (e) 50 Pa calculated using Eq. (4) for a capacitively coupled chlorine discharge. The gap separation is 25.4 mm, the voltage amplitude 222 V and driving frequency 13.56 MHz. The vertical dashed lines indicate the time averaged position of the sheath edge.
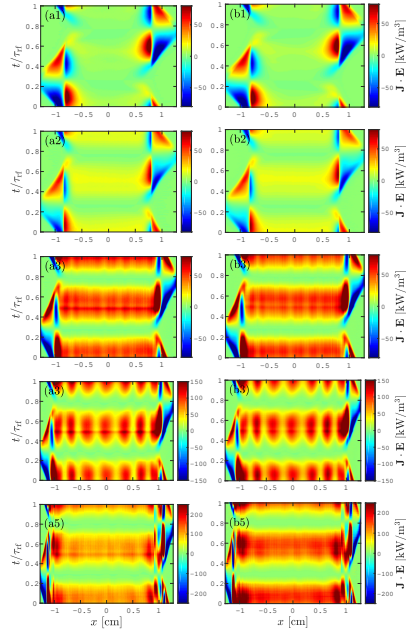
FIG. 7: The spatio temporal behavior of the total electron power absorption over the full gap length for a capacitively coupled chlorine discharge. The gap separation is 25.4 mm, the voltage amplitude 222 V and driving frequency 13.56 MHz. The left column (a) is the electron power absorption calculated using Eq. (4) and the right column (b) the result from the simulation. The rows represent the various pressures (1) 1 Pa, (2) 10 Pa, (3) 25 Pa, (4) 35 Pa, and (5) 50 Pa.

The time averaged profiles of the dominating electron power absorption contributors, term IV (red line), term V (blue dashed line) and term VI (green dot dashed line), calculated using Eq. (4), are shown in Figure 6 for the various operating pressures. At 1 Pa (Figure 6 (a)) term IV (ambipolar term) is zero and almost uniform within the inner plasma bulk. It increases sharply as both the sheath edges are approached, building two local maxima. At the sheath edges two almost equal local minima appear. Moving closer to the electrodes it decreases sharply again. At 10 Pa Term IV is still rather flat within

the electronegative core, and at 25 Pa oscillations appear that increase in amplitude as the pressure is increased to 35 Pa. The oscillations increase in amplitude approaching the sheath edge on the bulk side. These oscillations decrease in magnitude as the pressure is increased further to 50 Pa, due to increasing ion-neutral collision frequency. At 1 Pa Term V is close to zero at the discharge center and it steeply increases approaching the bulk side of the left and right sheath edges, where it builds two local maxima, which are higher compared to the maxima in Term IV (electron temperature gradient) placed at roughly the same location. Then it decreases steeply while crossing the sheath edges to both left and right and increases again sharply approaching both the electrodes. Term V shows similar behavior at 10 Pa but the amplitude decreases. At 25 Pa the amplitude at the bulk side of the sheath region increases again and oscillations set in. The oscillations exhibit increased amplitude at 35 Pa and decrease again as pressure is increased further to 50 Pa. Term VI is uniform and positive within the bulk region and it slowly decreases while approaching both the sheath edges, becoming zero at both the electrodes. The Ohmic heating (Term VI) increases in magnitude as the pressure is increased but retains its general shape. Oscillations are apparent at 35 Pa. At 50 Pa the Ohmic contribution exhibits a peak as approaching the sheath regions. Note that term VI is significantly larger in amplitude at 50 Pa than at 35 Pa. Ohmic heating increases both in absolute and relative terms with increasing pressure.

The spatio-temporal behavior of the total electron power absorption $\mathbf{J}_e \cdot \mathbf{E}$ is shown in Figure 7. The figures cover the full rf cycle and the full gap width, and results for various operating pressures are shown. The figures show $\mathbf{J}_e \cdot \mathbf{E}$ calculated using the theoretical model (a) and the results from the simulations (b). At 1 Pa (Figure 7 (a1) and Figure 7 (b1)) there is a significant absorption of power by the electrons (red and yellow areas) while some cooling of the electron (dark blue areas) are observed within the electronegative core. Furthermore, there is significant power absorption by the electrons during the sheath expansion on the sheath side of the sheath edge, while there is apparent electron cooling during the sheath expansion on the bulk side of the sheath edge. Also, there is significant electron power absorption during the sheath collapse which appears on the bulk side of the sheath edge, while there is apparent electron cooling during the sheath collapse on the electrode side. This indicates that at 1 Pa the dominant electron power absorption mechanism is hybrid of drift ambipolar heating (DA-mode) and stochastic heating due to the sheath oscillation or the pressure terms (α-mode). This is the same heating mechanism that has been observed for a capacitively coupled oxygen discharge operated at 1.33 Pa [40] and CF$_4$ discharge at 80 Pa [15]. Furthermore, we observe that there is a very good agreement between the calculated electron power absorption (Figure 7 (a1)) and the result from the simulation (Figure 7 (b1)). The power absorption at 10 Pa (Figures 7 (a2) and (b2)) shows a similar behavior. However, we observe a very much higher power absorption within the bulk region compared to the 1 Pa case (Figures 7 (a) and (b)). Again, at 10 Pa the electron power absorption is a hybrid of drift ambipolar heating (DA-mode) and stochastic heating (or sheath oscillation) (α-mode). As the pressure is increased to 25 Pa (Figure 7 (a3) and Figure 7 (b3)) the electron power absorption within the plasma bulk has increased. Moreover, we observe a very strong presence of striation structures within the plasma bulk, indicating that a transition is occurring. At 25 Pa the electron power absorption is a combination of striation mode, drift ambipolar heating (DA-mode) and stochastic heating (α-mode). At 35 Pa (Figure 7 (a4) and Figure 7 (b4)) we observe a stronger presence of striation structures within the plasma bulk compared to the 25 Pa case (Figure 7 (a3) and Figure 7 (b3)). At 50 Pa (Figure 7 (a5) and Figure 7 (b5)) the electron power absorption located on the sheath side (on the bulk side) of the expanding (collapsing) sheath edge has increased again. Moreover, we continue to observe the presence of striation structures like at 35 Pa. At 50 Pa the electron power absorption is constituted of striation, ambipolar heating (DA-mode) and stochastic heating (α-mode). Finally, at all pressures, the calculated electron power absorption (Figure 7 (a)) agrees well with the result from the simulation (Figure 7 (b)).

The time averaged total electron power absorption calculated using Eq. (4) (blue dashed line) is compared to the result from the simulation (red line), at various pressures is shown in Figure 8. At 1 Pa (Figure 8 (a)) the time averaged electron power absorption profile has a local minimum at the discharge center and it increases as the bulk side of the sheath edges are approached from left and right, building two almost equal absolute maxima. Moreover, the calculated time averaged total power absorption agrees very well with the simulation results, over the full gap length. Finally, the time averaged power absorption profile has a similar shape compared to what has been observed for oxygen discharge operated at 1.33 Pa [40, 41]. At 10 Pa (Figure 8 (b)) we observe that the profile is flat within the electronegative core. It then increases as the bulk side of the sheath edges are approached from both left and right, which appears as two almost equal absolute maxima on the bulk side. Closer to the sheath edge the electron power absorption decreases steeply, leading to two almost equal absolute minima. Then, the time averaged profile slightly increases to almost equal local maxima within both the sheath regions, and decreases again while approaching both the electrodes. At 25 Pa (Figure 8 (c)) the time averaged electron power absorption profile exhibits strong oscillations inside the plasma bulk region. The time averaged electron power absorption increases sharply as the bulk side of both the sheath edges are approached, building two almost equal absolute maxima. At 35 Pa (Figure 8 (d)) we observe that the time averaged power absorption profile exhibits

FIG. 8: The time averaged total electron power absorption at (a) 1 Pa, (b) 10 Pa, (c) 25 Pa, (d) 35 Pa, and (e) 50 Pa calculated using Eq. (4) for a capacitively coupled chlorine discharge. The gap separation is 25.4 mm, the voltage amplitude 222 V and driving frequency 13.56 MHz. The vertical dashed lines indicate the time averaged position of the sheath edge.
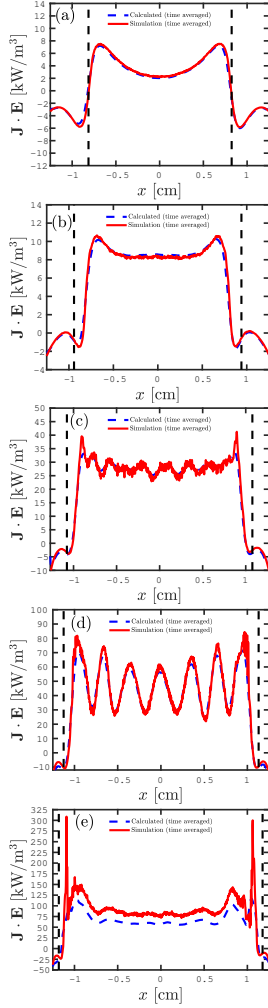
stronger oscillations within the plasma bulk compared to the 25 Pa case (Figure 8 (e)). We also see that the power absorption amplitude is higher closer to the sheath edges (bulk side), leading to two almost equal absolute maxima. The time averaged power absorption magnitude at 35 Pa is much higher compared to the 25 Pa case. Finally, we see that at 1, 10, 25 and 35 Pa the calculated electron power absorption overlaps the result from the simulation. At 50 Pa (Figure 8 (e)) we observe that the electron power absorption profile is almost flat within the bulk region. We also observe that the electron power absorption amplitude increases sharply closer to the bulk side of both the sheath edges, seen as two almost equal local maxima. The time averaged electron power absorption magnitude at 50 Pa is much higher compared to the 35 Pa case (Figure 8 (d)). Finally, the calculated time averaged electron power absorption underestimates the result from simulations within the plasma bulk, while it overlaps the result from the simulation within the sheath regions.

Figure 9 shows the amplitude of the individual contributions to the electron power absorption space averaged, calculated using Eq. (4), at two times within the rf period ($t/\tau = 0.25$ and $t/\tau = 0.50$) as well as time averaged. The space average is taken over the full gap length. At 1 Pa (Figure 9 (a)), the space-time averaged electron power absorption positive terms are term V (pressure term) and term VI (Ohmic Term), while term IV (ambipolar pressure term) is negative. We also observe very small contributions from term II (slightly positive) and term III (slightly negative) (inertia terms), respectively. Moreover, term I (inertia term) is negligible. Therefore, both the Ohmic and the electron temperature gradient terms are electron power absorption terms, while the ambipolar term presents power loss (electron cooling). Finally, term II (term III) (inertia term) provides electron heating (cooling). A net positive overall sum in the space-time average case (electron power absorption) is observed. At $t/\tau_{\rm rf} = 0.25$ the Ohmic term is zero, while term IV and term V (pressure terms) are both small and negative. Moreover, term I (inertia term) is negative and of the same magnitude as term V (pressure term), while term II (term III) (inertia term) is very small and slightly positive (negative). Therefore, at $t/\tau_{\rm rf} = 0.25$, term I and term III (inertia terms), term IV and term V (pressure terms) provide electron cooling, while term II (inertia term) is an electron power absorption term. Finally, we observe a net negative overall sum at $t/\tau_{\rm rf} = 0.25$ (electron power loss). At $t/\tau_{\rm rf} = 0.50$ term I (inertia term), term V (pressure term) as well as term VI (Ohmic term) are all positive. On the other hand term IV (ambipolar pressure term) is negative. Term II and term III (inertia terms) are negligible. Therefore, at $t/\tau_{\rm rf} = 0.50$ term IV provides electron cooling, while term I, term V along with term VI are electron power absorption terms. A net positive overall sum at $t/\tau_{\rm rf} = 0.50$ (electron power absorption) is observed. With increasing pressure the magnitude as well as the relative contribution of the Ohmic
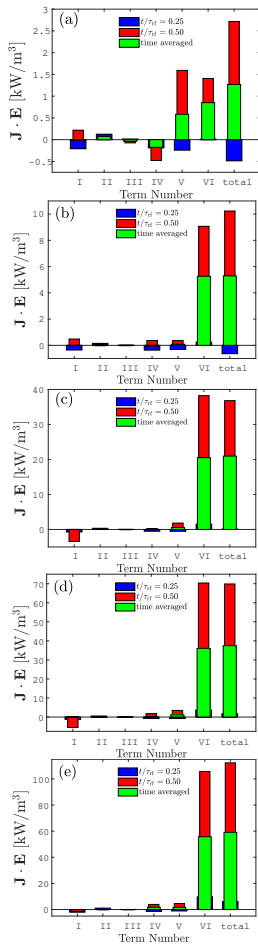
FIG. 9: The space averaged electron power absorption profile terms calculated using Eq. (4) at $t/\tau_{\rm rf} = 0.25$ (blue bar), $t/\tau_{\rm rf} = 0.50$ (red bar) and time averaged (green bar), at (a) 1 Pa, (b) 10 Pa, (c) 25 Pa, (d) 35 Pa, and (e) 50 Pa for a capacitively coupled chlorine discharge. The gap separation is 25.4 mm, the voltage amplitude 222 V and driving frequency 13.56 MHz.

term increases. At 10 Pa (Figure 9 (b)), term VI (Ohmic term) dominates the space and time averaged contribution. All the other terms are negligible in comparison. Therefore, term VI (Ohmic term) represents the dominating source for the space-time averaged electron power absorption. At $t/\tau_{\rm rf} = 0.25$ term I (inertia term), term IV and term V (pressure terms) are all negative, while term II and term III (inertia term), along with term VI (Ohmic term) are positive. Therefore, at $t/\tau_{\rm rf} = 0.25$, term I (inertia term), term IV and term V (pressure terms) provide electron cooling, while term II and term III (inertia term), along with term VI (Ohmic term) are electron power absorption terms. We observe a net negative overall sum at $t/\tau_{\rm rf} = 0.25$ (electron power loss). At $t/\tau_{\rm rf} = 0.50$ the main contribution to the electron power absorption comes from term VI (Ohmic term), which is positive. Smaller contributions come from both term IV and term V (pressure terms), along with term I (inertia term). Both term II and term III (inertia term) are negligible. Note that term IV (ambipolar pressure term) changes sign when the pressure is increased from 1 to 10 Pa. Finally, we observe a net positive overall sum at $t/\tau_{\rm rf} = 0.50$ (electron power absorption). When the pressure is 25, 35 and 50 Pa as shown in Figures 9 (c), (d) and (e) respectively, the electron power absorption averaged over space and time is dominated by term VI (Ohmic term). There is a very small added contribution from term V (pressure term). All the other terms are negligible. Therefore, term VI (Ohmic term) is almost the only significant process of electron power absorption. At $t/\tau_{\rm rf} = 0.25$ the electron power absorption is due to term VI (Ohmic term) (slightly positive) and term V (pressure term) (slightly negative). All the other terms are negligible. Therefore at $t/\tau_{\rm rf} = 0.25$ term V (pressure term) provides electron cooling, while term VI (Ohmic term) is an electron power absorption term. Finally, we observe that the total overall sum is zero, since term V and term VI cancel out. At $t/\tau_{\rm rf} = 0.50$ the Ohmic term dominates but there are smaller contributions from term I (inertia term), which is negative, and from term V (pressure term), which is slightly positive. All the other terms are negligible. Therefore at $t/\tau_{\rm rf} = 0.50$ term V (pressure term) and term VI (Ohmic term) are electron power absorption terms, while term I (inertia terms) provides electron cooling. Finally, we observe a net positive overall sum at $t/\tau_{\rm rf} = 0.50$ (electron power absorption). Note that the time averaged contribution of the electron temperature gradient term V to electron power absorption remains roughly at similar absolute value as pressure is varied, actually it has the highest absolute value at the highest pressure, as we can see in Figure 6. It is worth noting that the contribution of term VI (Ohmic term) to the overall electron power absorption increases with increasing pressure in the pressure range 1 Pa – 25 Pa. Then it remains almost constant at 35 Pa and 50 Pa.

These results confirm that the capacitively coupled chlorine discharge becomes more Ohmic or becomes more of a resistive load with increasing pressure. Earlier we

showed that more of the power is absorbed by the electrons and less by the ions as the pressure is increased [14]. This is in agreement with and confirms earlier reports, where the discharge current and electric field have been shown to be in phase at 66 Pa, and at 200 Pa the electric field leads the discharge current by $\sim 42°$ (inductive load) [7]. Similarly, the phase angle has been measured to increase from -73° to 10° as the pressure is increased from 13 – 213 Pa as the discharge transitions from being a capacitive load to become a resistive load for a chlorine discharge at 100 W with electrode spacing of 20 mm [62]. Furthermore, the capacitance of the sheath collapses almost entirely at the highest pressures. This was later confirmed by comparing the measured impedance to the impedance determined by PIC/MCC simulations [13]. Due to the Ohmic nature of the discharge a global model has been developed that describes a high pressure electronegative chlorine discharge, where the rf power is coupled via Ohmic power absorption and stochastic electron heating while ion power absorption due to acceleration across the sheaths is neglected [63].

VI. CONCLUSION

Boltzmann term analysis was applied on the output from particle-in-cell Monte Carlo collision simulations in order to study the origins of the electric field within the electronegative core and the electron power absorption mechanisms in a capacitively coupled chlorine discharge while the pressure is varied from 1 to 50 Pa, as the voltage amplitude is kept fixed. The electron power absorption increases in amplitude and the power absorption by the ions decreases with increased pressure. At the lowest pressure, 1 Pa, the electron power absorption is due to both the pressure and the Ohmic terms. As the pressure is increased > 10 Pa the Ohmic term becomes dominating and all the other contributions to the electron power absorption become negligible in comparison. Therefore, the discharge transitions into a resistive load as the discharge pressure is increased. The capacitively coupled chlorine discharge is highly electronegative and is operated in DA-mode. Striations become apparent at 25 Pa and are most significant at 35 Pa but their importance decreases with further increase in pressure. Recall, that in this study secondary electron emission, due to ion and neutral impact on the electrodes, and electron reflection from the electrodes, is neglected. Secondary electron emission is expected to have a significant influence on the discharge properties, including the electron power absorption mechanisms, in particular at the higher pressures explored. The secondary electron emsission therfore, as it increases the electron density, leads to an increased electrical conductivity and therefore it reduces the electric field within the electronegative core. Consequently, the secondary electron emission can disrupt the striations and is likely to lead to power absorption mode transition into γ-mode, that dominates at high pressure and high applied voltage, as has been demonstrated for capacitively coupled oxygen discharge [25]. The influence of secondary electron emsission on the discharge properties is certainly important and will be explored in a future study.

[1] P. Chabert and N. Braithwaite, *Physics of Radio-Frequency Plasmas* (Cambridge University Press, Cambridge, United Kingdom, 2011).

[2] M. A. Lieberman and A. J. Lichtenberg, *Principles of Plasma Discharges and Materials Processing* (John Wiley & Sons, New York, 2005), 2nd ed.

[3] V. M. Donnelly and A. Kornblit, Journal of Vacuum Science and Technology A **31**, 050825 (2013).

[4] J. P. Chang, A. P. Mahorowala, and H. H. Sawin, Journal of Vacuum Science and Technology A **16**, 217 (1998).

[5] W. C. Tian, J. W. Weigold, and S. W. Pang, Journal of Vacuum Science and Technology B **18**, 1890 (2000).

[6] Y. Zhang, C. Huard, S. Sriraman, J. Belen, A. Paterson, and M. J. Kushner, Journal of Vacuum Science and Technology A **35**, 021303 (2017).

[7] E. S. Aydil and D. J. Economou, Journal of The Electrochemical Society **139**, 1396 (1992).

[8] E. S. Aydil and D. J. Economou, Journal of The Electrochemical Society **139**, 1406 (1992).

[9] D. L. Flamm and V. M. Donnelly, Plasma Chemistry and Plasma Processing **1**, 317 (1981).

[10] J. P. Chang and H. H. Sawin, Journal of Vacuum Science and Technology **15**, 610 (1997).

[11] K. Ono, M. Tuda, H. Ootera, and T. Oomori, Pure and Applied Chemistry **66**, 1327 (1994).

[12] S. A. Vitale, H. Chae, and H. H. Sawin, Journal of Vacuum Science and Technology A **19**, 2197 (2001).

[13] S. Huang and J. T. Gudmundsson, Plasma Sources Science and Technology **22**, 055020 (2013).

[14] G. A. Skarphedinsson and J. T. Gudmundsson, Plasma Sources Science and Technology **29**, 084004 (2020).

[15] J. Schulze, A. Derzsi, K. Dittmann, T. Hemke, J. Meichsner, and Z. Donkó, Physical Review Letters **107**, 275001 (2011).

[16] A. Derzsi, E. Schüngel, Z. Donkó, and J. Schulze, Open Chemistry **13**, 346 (2015).

[17] Z. L. Petrović, F. Tochikubo, S. Kakuta, and T. Makabe, Journal of Applied Physics **73**, 2163 (1993).

[18] T. Makabe, F. Tochikubo, and M. Nishimura, Physical Review A **42**, 3674 (1990).

[19] S. Brandt, B. Berger, E. Schüngel, I. Korolov, A. Derzsi, B. Bruneau, E. Johnson, T. Lafleur, D. O'Connell, and

M. Koepke, Plasma Sources Science and Technology **25**, 045015 (2016).

[20] B. Bruneau, T. Lafleur, T. Gans, D. O'Connell, A. Greb, I. Korolov, A. Derzsi, Z. Donkó, S. Brandt, and E. Schüngel, Plasma Sources Science and Technology **25**, 01LT02 (2016).

[21] N. Nakano, N. Shimura, Z. L. Petrović, and T. Makabe, Physical Review E **49**, 4455 (1994).

[22] Y.-X. Liu, E. Schüngel, I. Korolov, Z. Donkó, Y.-N. Wang, and J. Schulze, Physical Review Letters **116**, 255002 (2016).

[23] Y.-X. Liu, I. Korolov, E. Schüngel, Y.-N. Wang, Z. Donkó, and J. Schulze, Physics of Plasmas **24**, 073512 (2017).

[24] Y.-X. Liu, I. Korolov, E. Schüngel, Y.-N. Wang, Z. Donkó, and J. Schulze, Plasma Sources Science and Technology **26**, 055024 (2017).

[25] L. Wang, D.-Q. Wen, Q.-Z. Zhang, Y.-H. Song, Y.-R. Zhang, and Y.-N. Wang, Plasma Sources Science and Technology **28**, 055007 (2019).

[26] S. Huang and J. T. Gudmundsson, Plasma Sources Science and Technology **23**, 025015 (2014).

[27] S. Huang and J. T. Gudmundsson, IEEE Transactions on Plasma Science **42**, 2854 (2014).

[28] S. Huang and J. T. Gudmundsson, Plasma Sources Science and Technology **24**, 015003 (2015).

[29] J. Schulze, E. Schüngel, and U. Czarnetzki, Journal of Physics D: Applied Physics **42**, 092005 (2009).

[30] Z. Donkó, J. Schulze, B. G. Heil, and U. Czarnetzki, Journal of Physics D: Applied Physics **42**, 025205 (2009).

[31] T. Lafleur, Plasma Sources Science and Technology **25**, 013001 (2016).

[32] M. Surendra and M. Dalvie, Physical Review E **48**, 3914 (1993).

[33] R. P. Brinkmann, Plasma Sources Science and Technology **25**, 014001 (2016).

[34] T. Lafleur, P. Chabert, and J. P. Booth, Plasma Sources Science and Technology **23**, 035010 (2014).

[35] J. Schulze, Z. Donkó, B. G. Heil, D. Luggenhölscher, T. Mussenbrock, R. P. Brinkmann, and U. Czarnetzki, Journal of Physics D: Applied Physics **41**, 105214 (2008).

[36] J. Schulze, Z. Donkó, T. Lafleur, S. Wilczek, and R. P. Brinkmann, Plasma Sources Science and Technology **27**, 055010 (2018).

[37] M. Vass, S. Wilczek, T. Lafleur, R. P. Brinkmann, Z. Donkó, and J. Schulze, Plasma Sources Science and Technology **29**, 085014 (2020).

[38] S. Wilczek, J. Schulze, R. P. Brinkmann, Z. Donkó, J. Trieschmann, and T. Mussenbrock, Journal of Applied Physics **127**, 181101 (2020).

[39] M. Vass, S. Wilczek, T. Lafleur, R. P. Brinkmann, Z. Donkó, and J. Schulze, Plasma Sources Science and Technology **29**, 025019 (2020).

[40] A. Proto and J. T. Gudmundsson, Journal of Applied

[41] Physics **128**, 113302 (2020).

[41] J. T. Gudmundsson and D. I. Snorrason, Journal of Applied Physics **122**, 193302 (2017).

[42] J. T. Gudmundsson and A. Proto, Plasma Sources Science and Technology **28**, 045012 (2019).

[43] J. T. Gudmundsson, E. Kawamura, and M. A. Lieberman, Plasma Sources Science and Technology **22**, 035011 (2013).

[44] C. Birdsall, IEEE Transactions on Plasma Science **19**, 65 (1991).

[45] S. Yonemura and K. Nanbu, IEEE Transactions on Plasma Science **31**, 479 (2003).

[46] H. Hannesdottir and J. T. Gudmundsson, Journal of Physics D: Applied Physics **50**, 175201 (2017).

[47] E. G. Thorsteinsson and J. T. Gudmundsson, Plasma Sources Science and Technology **19**, 015001 (2010).

[48] E. G. Thorsteinsson and J. T. Gudmundsson, Plasma Sources Science and Technology **19**, 055008 (2010).

[49] M. V. Malyshev and V. M. Donnelly, Journal of Applied Physics **88**, 6207 (2000).

[50] F. Neuilly, J.-P. Booth, and L. Vallier, Journal of Vacuum Science and Technology A **20**, 225 (2002).

[51] J. P. Booth, Y. Azamoum, N. Sirse, and P. Chabert, Journal of Physics D: Applied Physics **45**, 195201 (2012).

[52] C. Lee and M. A. Lieberman, Journal of Vacuum Science and Technology A **13**, 368 (1995).

[53] G. P. Kota, J. W. Coburn, and D. B. Graves, Journal of Vacuum Science and Technology A **16**, 270 (1998).

[54] L. Stafford, J. Margot, F. Vidal, M. Chaker, K. Giroux, J.-S. Poirier, A. Quintal-Léonard, and J. Saussac, Journal of Applied Physics **98**, 063301 (2005).

[55] L. Stafford, R. Khare, J. Guha, V. M. Donnelly, J.-S. Poirier, and J. Margot, Journal of Physics D: Applied Physics **42**, 055206 (2009).

[56] L. Stafford, J. Guha, R. Khare, S. Mattei, O. Boudreault, B. Clain, and V. M. Donnelly, Pure and Applied Chemistry **82**, 1301 (2010).

[57] A. J. Lichtenberg, V. Vahedi, M. A. Lieberman, and T. Rognlien, Journal of Applied Physics **75**, 2339 (1994).

[58] A. J. Lichtenberg, I. G. Kouznetsov, Y. T. Lee, M. A. Lieberman, I. D. Kaganovich, and L. D. Tsendin, Plasma Sources Science and Technology **6**, 437 (1997).

[59] J. T. Gudmundsson and B. Ventéjou, Journal of Applied Physics **118**, 153302 (2015).

[60] K. Denpoh and K. Nanbu, Japanese Journal of Applied Physics **39**, 2804 (2000).

[61] M. M. Turner, Physical Review Letters **75**, 1312 (1995).

[62] A. F. Bose, Ph.D. thesis, Swiss Federal Institute of Technology Zürich (1995).

[63] Y. T. Lee, M. A. Lieberman, A. J. Lichtenberg, F. Bose, H. Baltes, and R. Patrick, Journal of Vacuum Science and Technology A **15**, 113 (1997).

References

Aleksandrov, N. L. (1978). Electron detachment from O^- and O_2^- ions on excited molecules in an air discharge. *Soviet Physics-Technical Physics*, 23(7):806–808.

Ali, M. A. and Kim, Y.-K. (2005). Total ionization cross sections of Cl and Cl_2 by electron impact. *Surface and Interface Analysis*, 37(11):969–972.

Aliev, Y. M., Kaganovich, I. D., and Schlüter, H. (1997). Quasilinear theory of collisionless electron heating in radio frequency gas discharges. *Physics of Plasmas*, 4(7):2413–2421.

Allen, J. E. (2009). The plasma-sheath boundary: its history and Langmuir's definition of the sheath edge. *Plasma Sources Science and Technology*, 18(1):014014.

Annaratone, B. M., Ku, V. P. T., and Allen, J. E. (1995). Identification of plasma-sheath resonances in a parallel-plate plasma reactor. *Journal of Applied Physics*, 77(10):5455–5457.

Baalrud, S. D. and Hegna, C. C. (2011). Determining the Bohm criterion in plasmas with two ion species. *Physics of Plasmas*, 18(2):023505.

Baalrud, S. D., Hegna, C. C., and Callen, J. D. (2009). Instability-enhanced collisional friction can determine the Bohm criterion in multiple-ion-species plasmas. *Physical Review Letters*, 103(20):205002.

Babaeva, N. Y., Lee, J. K., Shon, J. W., and Hudson, E. A. (2005). Oxygen ion energy distribution: Role of ionization, resonant, and nonresonant charge-exchange collisions. *Journal of Vacuum Science and Technology A*, 23(4):699–704.

Baer, T., Murray, P. T., and Squires, L. (1978). Total cross sections for symmetric charge transfer reactions of O_2^+ in selected translational and internal energy states. *Journal of Chemical Physics*, 68(11):4901–4906.

Basner, R. and Becker, K. (2004). Experimental absolute electron impact ionization cross-sections of Cl_2. *New Journal of Physics*, 6(1):118.

Baulch, D. L., Cox, R. A., Crutzen, P. J., Hampson, R. F., Kerr, J. A., Troe, J., and Watson, R. T. (1982). Evaluated kinetic and photochemical data for atmospheric chemistry: Supplement I CODATA task group on chemical kinetics. *Journal of Physical and Chemical Reference Data*, 11(2):327–496.

Belenguer, P. and Boeuf, J. (1990). Transition between different regimes of rf glow discharges. *Physical Review A*, 41(8):4447–4459.

Belostotsky, S. G., Economou, D. J., Lopaev, D. V., and Rakhimova, T. V. (2005). Negative ion destruction by $O(^3P)$ atoms and $O_2(a^1\Delta_g)$ molecules in an oxygen plasma. *Plasma Sources Science and Technology*, 14(3):532–542.

Bera, K., Rauf, S., and Collins, K. (2011a). PIC-MCC/Fluid hybrid model for low pressure capacitively coupled O_2 plasma. *AIP Conference Proceedings*, 1333:1027–1032.

Bera, K., Rauf, S., and Collins, K. (2011b). Plasma dynamics in low-pressure capacitively coupled oxygen plasma using PIC–MCC/fluid hybrid model. *IEEE Transactions on Plasma Science*, 39(11):2576 –2577.

Birdsall, C. (1991). Particle-in-cell charged-particle simulations, plus Monte Carlo collisions with neutral atoms, PIC-MCC. *IEEE Transactions on Plasma Science*, 19(2):65–85.

Birdsall, C. K. and Fuss, D. (1969). Clouds-in-clouds, clouds-in-cells physics for many-body plasma simulation. *Journal of Computational Physics*, 3(4):494–511.

Birdsall, C. K. and Langdon, A. B. (1991). Particle simulation techniques. In Drobot, A. T., editor, *Computer Applications in Plasma Science and Engineering*, pages 7–41. Springer-Verlag, New York, New York.

Birdsall, C. K. and Langdon, A. B. (2004). *Plasma Physics via Computer Simulation*. Taylor & Francis, Boca Raton, Florida.

Bohm, D. (1949). Minimum ionic kinetic energy for a stable sheath. In Guthrie, A. and Wakerling, R. K., editors, *The characteristics of electrical discharges in magnetic fields*, number I, volume 5 in National nuclear energy series – Manhattan project technical section, chapter 3, pages 77–86. McGraw-Hill, New York.

Bojarov, A., Radmilović-Radjenović, M., and Petrović, Z. L. (13-17 July, 2010b). Modeling the effects of the secondary electron emission in a dual-frequency capacitively coupled plasma reactor. In *Proceedings of the 20th Europhysics Sectional Conference on Atomic and Molecular Physics of Ionized Gases (ESCAMPIG XX)*, page P2.38.

Bojarov, A., Radmilović-Radjenović, M., and Petrović, Z. L. (2010a). The influence of the ion induced secondary electron emission on the characteristics of rf plasmas. *Publications of the Astronomical Observatory of Belgrade*, 89:131–134.

Bojarov, A., Radmilović-Radjenović, M., and Petrović, Z. L. (2014). Particle in cell simulation of the electrical asymmetric effect with a realistic model of the ion induced secondary electron emission. In Marić, D., Milosavljević, A. R., and Mijatović, Z., editors, *Proceedings of the 27th Summer School and International Symposium on the Physics of Ionized Gases*, pages 407–410.

Bora, B., Bhuyan, H., Favre, M., Wyndham, E., and Chuaqui, H. (2012). Theoretical approach for plasma series resonance effect in geometrically symmetric dual radio frequency plasma. *Applied Physics Letters*, 100(9):094103.

Bora, B. and Soto, L. (2014). Influence of finite geometrical asymmetry of the electrodes in capacitively coupled radio frequency plasma. *Physics of Plasmas*, 21(8):083509.

Boris, J. P. (1970). Relativistic plasma simulation—optimization of a hybrid code. In Boris, J. P. and Shanny, R. A., editors, *Proceedings of the Fourth Conference on Numerical Simulation of Plasmas, November 2 – 3, 1979, Washington DC*, pages 3–67, Washington DC. Naval Research Laboratory.

Boswell, R. W. and Morey, I. J. (1988). Self-consistent simulation of a parallel-plate rf discharge. *Applied Physics Letters*, 52(1):21–23.

Boyd, R. L. F. and Thompson, J. B. (1959). The operation of Langmuir probes in electro-negative plasmas. *Proceedings of the Royal Society of London-Series A: Mathematical and Physical Sciences*, A252(1268):102–119.

Braithwaite, N. S. J. and Allen, J. E. (1988). Boundaries and probes in electronegative plasmas. *Journal of Physics D: Applied Physics*, 21(12):1733–1737.

Brinkmann, R. P. (2007). Beyond the step model: Approximate expressions for the field

in the plasma boundary sheath. *Journal of Applied Physics*, 102(9):093303.

Brinkmann, R. P. (2015). The electric field in capacitively coupled RF discharges: a smooth step model that includes thermal and dynamic effects. *Plasma Sources Science and Technology*, 24(6):065002.

Brinkmann, R. P. (2016). Electron heating in capacitively coupled RF plasmas: a unified scenario. *Plasma Sources Science and Technology*, 25(1):014001.

Bronold, F. X., Matyash, K., Schneider, D. T. R., and Fehske, H. (2007). Radio-frequency discharges in oxygen: I. Particle-based modelling. *Journal of Physics D: Applied Physics*, 40(21):6583–6592.

Brunetti, B., Liuti, G., Luzzatti, E., Pirani, F., and Vecchiocattivi, F. (1981). Study of the interactions of atomic and molecular oxygen with O_2 and N_2 by scattering data. *Journal of Chemical Physics*, 74(12):6734–6741.

Buneman, O. (1959). Dissipation of currents in ionized media. *Physical Review*, 115(3):503–517.

Buneman, O. (1967). Time-reversible difference procedures. *Journal of Computational Physics*, 1(4):517–525.

Burrow, P. D. (1973). Dissociative attachment from the $O_2(a^1\Delta_g)$ state. *Journal of Chemical Physics*, 59(9):4922 – 4931.

Calandra, P., O'Connor, C. S. S., and Price, S. D. (2000). Electron-impact ionization of the chlorine molecule. *Journal of Chemical Physics*, 112(24):10821–10830.

Chabert, P. and Braithwaite, N. (2011). *Physics of Radio-Frequency Plasmas*. Cambridge University Press, Cambridge.

Chabert, P., Tsankov, T. V., and Czarnetzki, U. (2021). Foundations of capacitive and inductive radio-frequency discharges. *Plasma Sources Science and Technology*, 30(2):024001.

Chanson, R., Rhallabi, A., Fernandez, M. C., Cardinaud, C., Bouchoule, S., Gatilova, L., and Talneau, A. (2012). Global model of Cl_2/Ar high-density plasma discharge and 2-D Monte-Carlo etching model of InP. *IEEE Transactions on Plasma Science*, 40(4):959–971.

Chashmejahanbin, M. R., Salimi, A., and Ershad Langroudi, A. (2014). The study of the coating adhesion on PP surface modified in different plasma/acrylic acid solution. *International Journal of Adhesion and Adhesives*, 49:44–50.

Child, C. D. (1911). Discharge from hot CaO. *Physical Review*, 32(5):492–511.

Christophorou, L. G. and Olthoff, J. K. (1999). Electron interactions with Cl_2. *Journal of Physical and Chemical Reference Data*, 28(1):131–169.

Church, M. J. and Smith, D. (1978). Ionic recombination of atomic and molecular ions in flowing afterglow plasmas. *Journal of Physics D: Applied Physics*, 11(16):2199–2206.

Comer, J. and Schulz, G. J. (1974). Measurements of electron detachment cross sections from O^-. *Journal of Physics B: Atomic, Molecular and Optical Physics*, 7(8):L249–L253.

Courant, R., Friedrichs, K., and Lewy, H. (1928). Über die partiellen differenzengleichungen der mathematischen physik. *Mathematische Annalen*, 100(1):32–74.

Czarnetzki, U. (2013). Analytical model for the radio-frequency sheath. *Physical Review E*, 88:063101.

Czarnetzki, U., Mussenbrock, T., and Brinkmann, R. (2006). Self-excitation of the

plasma series resonance in radio-frequency discharges: An analytical description. *Physics of Plasmas*, 13(12):123503.

Daksha, M., Derzsi, A., Wilczek, S., Trieschmann, J., Mussenbrock, T., Awakowicz, P., Donkó, Z., and Schulze, J. (2017). The effect of realistic heavy particle induced secondary electron emission coeffcients on the electron power absorption dynamics in single- and dual-frequency capacitively coupled plasma. *Plasma Sources Science and Technology*, 26(8):085006.

Dawson, J. (1962). One-dimensional plasma model. *Physics of Fluids*, 5(4):445–459.

Denpoh, K. (2012). Particle-in-cell/Monte Carlo collision simulations of striations in inductively coupled plasmas. *Japanese Journal of Applied Physics*, 51(10):106202.

Denpoh, K. and Nanbu, K. (1998). Self-consistent particle simulation of radio-frequency CF_4 discharge with implementation of all ion-neutral reactive collisions. *Journal of Vacuum Science and Technology A*, 16(3):1201–1206.

Denpoh, K. and Nanbu, K. (2000). Self-consistent particle simulation of radio frequency CF_4 discharge: Effect of gas pressure. *Japanese Journal of Applied Physics*, 39(5):2804–2808.

Derzsi, A., Bruneau, B., Gibson, A., Johnson, E., O'Connell, D., Gans, T., Booth, J.-P., and Donkó, Z. (2017). Power coupling mode transitions induced by tailored voltage waveforms in capacitive oxygen discharges. *Plasma Sources Science and Technology*, 26(3):034002.

Derzsi, A., Donkó, Z., and Schulze, J. (2013). Coupling effects of driving frequencies on the electron heating in electronegative capacitive dual-frequency plasmas. *Journal of Physics D: Applied Physics*, 46(48):482001.

Derzsi, A., Korolov, I., Schüngel, E., Donkó, Z., and Schulze, J. (2015a). Effects of fast atoms and energy-dependent secondary electron emission yields in PIC/MCC simulations of capacitively coupled plasmas. *Plasma Sources Science and Technology*, 24(3):034002.

Derzsi, A., Lafleur, T., Booth, J.-P., Korolov, I., and Donkó, Z. (2016). Experimental and simulation study of a capacitively coupled oxygen discharge driven by tailored voltage waveforms. *Plasma Sources Science and Technology*, 25(1):015004.

Derzsi, A., Schüngel, E., Donkó, Z., and Schulze, J. (2015b). Electron heating modes and frequency coupling effects in dual-frequency capacitive CF_4 plasmas. *Open Chemistry*, 13(1):346–361.

Donkó, Z., Schulze, J., Czarnetzki, U., and Luggenhölscher, D. (2009). Self-excited non-linear plasma series resonance oscillations in geometrically symmetric capacitively coupled radio frequency discharges. *Applied Physics Letters*, 94(13):131501.

Donkó, Z., Schulze, J., Heil, B. G., and Czarnetzki, U. (2009). PIC simulations of the separate control of ion flux and energy in CCRF discharges via the electrical asymmetry effect. *Journal of Physics D: Applied Physics*, 42(2):025205.

Donnelly, V. M. and Kornblit, A. (2013). Plasma etching: Yesterday, today, and tomorrow. *Journal of Vacuum Science and Technology A*, 31(5):050825.

Ellis, H. W., Pai, R. Y., McDaniel, E. W., Mason, E. A., and Viehland, L. A. (1976). Transport properties of gaseous ions over a wide energy range. *Atomic Data and Nuclear Data Tables*, 17(3):177–210.

Fermi, E. (1949). On the origin of the cosmic radiation. *Physical Review*, 75(8):1169–1174.

Fritioff, K., Sandström, J., Hanstorp, D., Ehlerding, A., Larsson, M., F. Collins, G., Pegg, D. J., Danared, H., Källberg, A., and Le Padellec, A. (2003). Electron-impact detachment from Cl^-. *Physical Review A*, 68(1):012712.

Ganas, P. S. (1988). Electron impact excitation cross sections for chlorine. *Journal of Applied Physics*, 63(2):277–279.

Gans, T., Schulz-von der Gathen, V., and Döbele, H. F. (2004). Spectroscopic measurements of phase-resolved electron energy distribution functions in RF-excited discharges. *Europhysics Letters*, 66(2):232–238.

Georgieva, V. (2006). *Computer modeling of low-pressure fluorocarbon-based discharges for etching purposes*. PhD thesis, University of Antwerp.

Georgieva, V., Bogaerts, A., and Gijbels, R. (2003). Particle-in-cell/Monte Carlo simulation of a capacitively coupled radio frequency Ar/CF_4 discharge: Effect of gas composition. *Journal of Applied Physics*, 93(5):2369–2379.

Godyak, V. A. (1972). Statistical heating of electrons at an oscillating plasma boundary. *Soviet Physis – Technical physics*, 16(7):1073–1076.

Godyak, V. A. (1986). *Soviet Radio Frequency Discharge Research*. Delphic Associates, Falls Church, VA.

Godyak, V. A. and Khanneh, A. S. (1986). Ion bombardment secondary electron maintenance of steady RF discharge. *IEEE Transactions on Plasma Science*, 14(2):112–123.

Godyak, V. A. and Piejak, R. B. (1990). Abnormally low electron energy and heating-mode transition in a low-pressure argon rf discharge at 13.56 MHz. *Physical Review Letters*, 65(8):996–999.

Godyak, V. A., Piejak, R. B., and Alexandrovich, B. M. (1992). Evolution of the electron-energy-distribution function during rf discharge transition to the high-voltage mode. *Physical Review Letters*, 68(1):40–43.

Godyak, V. A., Piejak, R. B., and Alexandrovich, B. M. (1994). Electrical characteristics and electron heating meachanism of an inductively coupled argon discharge. *Plasma Sources Science and Technology*, 3(2):169 – 176.

Gogolides, E. and Sawin, H. H. (1992). Continuum modeling of radio-frequency glow discharges. I. Theory and results for electropositive and electronegative gases. *Journal of Applied Physics*, 72(9):3971–3987.

Gogolides, E., Stathakopoulos, M., and Boudouvis, A. (1994). Modelling of radio frequency plasmas in tetrafluoromethane (CF_4): the gas phase physics and the role of negative ion detachment. *Journal of Applied Physics*, 27(9):1878–1886.

Goldstein, R. A., Huerta, M. A., and Nearing, J. C. (1979). Stationary striations in an argon plasma as a bifurcation phenomenon. *Physics of Fluids*, 22(2):231–240.

Golovitskii, A. P. (2000). Temperature dependence of an electron attachment to chlorine molecules. *Technical Physics*, 45(5):532–537.

Gote, M. and Ehrhardt, H. (1995). Rotational excitation of diatomic molecules at intermediate energies: Absolute differential state-to-state transition cross sections for electron scattering from N_2, Cl_2, CO and HCl. *Journal of Physics B: Atomic, Molecular and Optical Physics*, 28(17):3957–3986.

Gottscho, R. A. (1987). Glow-discharge sheath electric fields: Negative-ion, power, and frequency effects. *Physical Review A*, 36(5):2233–2242.

Gottscho, R. A. and Gaebe, C. E. (1986). Negative ion kinetics in rf glow discharges. *IEEE Transactions on Plasma Science*, 14(2):92–102.

Gozadinos, G. (2001). *Collisionless heating and particle dynamics in radio-frequency capacitive plasma sheaths*. PhD thesis, Dublin City University.

Gozadinos, G., Turner, M. M., and Vender, D. (2001). Collisionless electron heating by capacitive rf sheaths. *Physical Review Letters*, 87(13):135004.

Grapperhaus, M. J. and Kushner, M. J. (1997). A semianalytic radio frequency sheath model integrated into a two-dimensional hybrid model for plasma processing reactors. *Journal of Applied Physics*, 81(2):569–577.

Greb, A., Gibson, A. R., Niemi, K., O'Connell, D., and Gans, T. (2015). Influence of surface conditions on plasma dynamics and electron heating in a radio-frequency driven capacitively coupled oxygen plasma. *Plasma Sources Science and Technology*, 24(4):044003.

Green, M. A., Teubner, P. J. O., Brunger, M. J., Cartwright, D. C., and Campbell, L. (2001). Integral cross sections for electron impact excitation of the herzberg pseudocontinuum of molecular oxygen. *Journal of Physics B: Atomic, Molecular and Optical Physics*, 34(6):L157–L162.

Gregório, J. and Pitchford, L. C. (2012). Updated compilation of electron–Cl_2 scattering cross sections. *Plasma Sources Science and Technology*, 21(3):032002.

Gudmundsson, J. T. (2001). On the effect of the electron energy distribution on the plasma parameters of argon discharge: A global (volume averaged) model study. *Plasma Sources Science and Technology*, 10(1):76–81.

Gudmundsson, J. T. and Hannesdottir, H. (2017). On the role of metastable states in low pressure oxygen discharges. *AIP Conference Proceedings*, 1811:120001.

Gudmundsson, J. T., Kawamura, E., and Lieberman, M. A. (2013). A benchmark study of a capacitively coupled oxygen discharge of the oopd1 particle-in-cell Monte Carlo code. *Plasma Sources Science and Technology*, 22(3):035011.

Gudmundsson, J. T. and Lieberman, M. A. (2015). On the role of metastables in capacitively coupled oxygen discharges. *Plasma Sources Science and Technology*, 24(3):035016.

Gudmundsson, J. T. and Proto, A. (2019). Electron heating mode transitions in a low pressure capacitively coupled oxygen discharge. *Plasma Sources Science and Technology*, 28(4):045012.

Gudmundsson, J. T. and Snorrason, D. I. (2017). On electron heating in a low pressure capacitively coupled oxygen discharge. *Journal of Applied Physics*, 122(19):193302.

Gudmundsson, J. T., Snorrason, D. I., and Hannesdottir, H. (2018). The frequency dependence of the discharge properties in a capacitively coupled oxygen discharge. *Plasma Sources Science and Technology*, 27(2):025009.

Gudmundsson, J. T. and Ventéjou, B. (2015). The pressure dependence of the discharge properties in a capacitively coupled oxygen discharge. *Journal of Applied Physics*, 118(15):153302.

Hannesdottir, H. and Gudmundsson, J. T. (2016). The role of the metastable $O_2(b^1\Sigma_g^+)$ and energy-dependent secondary electron emission yields in capacitively coupled oxygen discharges. *Plasma Sources Science and Technology*, 25(5):055002.

Hannesdottir, H. and Gudmundsson, J. T. (2017). On singlet metastable states, ion flux and ion energy in single and dual frequency capacitively coupled oxygen discharges. *Journal of Physics D: Applied Physics*, 50(17):175201.

Hartney, M. A., Hess, D. W., and Soane, D. S. (1989). Oxygen plasma etching for resist

stripping and multilayer lithography. *Journal of Vacuum Science and Technology B*, 7(1):1–13.

Hayes, T. R., Wetzel, R. C., and Freund, R. S. (1987). Absolute electron-impact-ionization cross-section measurements of the halogen atoms. *Physical Review A*, 35(2):578–584.

Hayton, D. A. and Peart, B. (1993). Merged-beam measurements of the mutual neutralization of O^+/O^- and N^+/O^- ions. *Journal of Physics B: Atomic, Molecular and Optical Physics*, 26(17):2879–2885.

Heil, B. G., Czarnetzki, U., Brinkmann, R. P., and Mussenbrock, T. (2008). On the possibility of making a geometrically symmetric RF-CCP discharge electrically asymmetric. *Journal of Physics D: Applied Physics*, 41(16):165202.

Hess, D. W. (1999). Plasma-assisted oxidation, anodization, and nitridation of silicon. *IBM Journal of Research and Development*, 43(1-2):127–145.

Hockney, R. W. and Eastwood, J. W. (1988). *Computer simulation using particles*. Adam Hilger, Bristol.

Huang, S. and Gudmundsson, J. T. (2013). A particle-in-cell/Monte Carlo simulation of a capacitively coupled chlorine discharge. *Plasma Sources Science and Technology*, 22(5):055020.

Huang, S. and Gudmundsson, J. T. (2014a). A current driven capacitively coupled chlorine discharge. *Plasma Sources Science and Technology*, 23(2):025015.

Huang, S. and Gudmundsson, J. T. (2014b). Ion energy and angular distributions in a dual-frequency capacitively coupled chlorine discharge. *IEEE Transactions on Plasma Science*, 42(10):2854–2855.

Huang, S. and Gudmundsson, J. T. (2015). Dual-frequency capacitively coupled chlorine discharge. *Plasma Sources Science and Technology*, 24(1):015003.

Huq, M. S., Scott, D., White, N. R., Champion, R. L., and Doverspike, L. D. (1984). Measurements of absolute total cross sections for charge transfer and electron detachment of halide ions on chlorine. *Journal of Chemical Physics*, 80(8):3651–3655.

Irving, S. (Los Angeles, California, May 20 - 21, 1968). A dry photoresist removal method. In *Proceedings of Kodak Photoresist Seminar*, pages 26–29, Rochester, New York. Eastman, Kodak.

Itikawa, Y. (2009). Cross sections for electron collisions with oxygen molecules. *Journal of Physical and Chemical Reference Data*, 38(2):1–20.

Itikawa, Y. and Ichimura, A. (1990). Cross sections for collisions of electrons and photons with atomic oxygen. *Journal of Physical and Chemical Reference Data*, 19(3):637 – 651.

Jaffke, T., Meinke, M., Hashemi, R., Christophorou, L. G., and Illenberger, E. (1992). Dissociative electron attachment to singlet oxygen. *Chemical Physics Letters*, 193(1-3):62–68.

Kaganovich, I., Kolobov, V., and Tsendin, L. (1996). Stochastic electron heating in bounded radio-frequency plasmas. *Applied Physics Letters*, 69(25):3818–3820.

Kaganovich, I. D. (2002). Anomalous capacitive sheath with deep radio-frequency electric-field penetration. *Physical Review Letters*, 89(26):265006.

Kaganovich, I. D., Polomarov, O. V., and Theodosiou, C. E. (2006). Revisiting the anomalous RF field penetration into a warm plasma. *IEEE Transactions on Plasma Science*, 34(3):696 – 717.

225

Karmohapatro, S. B. (1965). Charge exchange of Cl^- ions with atomic chlorine. *Journal of the Physical Society of Japan*, 20(4):839–841.

Kawai, Y., Konishi, N., Watanabe, J., and Ohmi, T. (1994). Ultra-low-temperature growth of high-integrity gate oxide films by low-energy ion-assisted oxidation. *Applied Physics Letters*, 64(17):2223–2225.

Kawamura, E., Birdsall, C. K., and Vahedi, V. (2000). Physical and numerical methods of speeding up particle codes and paralleling as applied to rf discharges. *Plasma Sources Science and Technology*, 9(3):413–428.

Kawamura, E., Lieberman, M. A., and Lichtenberg, A. J. (2006). Stochastic heating in single and dual frequency capacitive discharges. *Physics of Plasmas*, 13(5):053506.

Kawano, S., Nanbu, K., and Kageyama, J. (2000). Systematic simulations of plasma structures in chlorine radio frequency discharges. *Journal of Physics D: Applied Physics*, 33(20):2637–2646.

Kim, G.-H., Efremov, A. M., Kim, D.-P., and Kim, C.-I. (2005). Inductively coupled Cl_2/N_2 plasma: Experimental investigation and modeling. *Microelectronic Engineering*, 81(1):96–105.

Kim, Y.-K. and Desclaux, J.-P. (2002). Ionization of carbon, nitrogen, and oxygen by electron impact. *Physical Review A*, 66(1):012708.

Klick, M. (1996). Nonlinearity of the radio-frequency sheath. *Journal of Applied Physics*, 79(7):3445–3452.

Kolobov, V. I. (2006). Striations in rare gas plasmas. *Journal of Physics D: Applied Physics*, 39(24):R487–R506.

Kolorenč, P. and Horáček, J. (2006). Dissociative electron attachment and vibrational excitation of the chlorine molecule. *Physical Review A*, 74(6):062703.

Korolov, I., Derzsi, A., Donkó, Z., and Schulze, J. (2013). The influence of the secondary electron induced asymmetry on the electrical asymmetry effect in capacitively coupled plasmas. *Applied Physics Letters*, 103(6):064102.

Krishnakumar, E. and Srivastava, S. K. (1992). Cross-sections for electron impact ionization of O_2. *International Journal of Mass Spectrometry and Ion Process*, 113:1–12.

Ku, V. P. T., Annaratone, B. M., and Allen, J. E. (1998a). Plasma-sheath resonances and energy absorption phenomena in capacitively coupled radio frequency plasmas. Part I. *Journal of Applied Physics*, 84(12):6536–6545.

Ku, V. P. T., Annaratone, B. M., and Allen, J. E. (1998b). Plasma-sheath resonances and energy absorption phenomena in capacitively coupled radio frequency plasmas. Part II. The Herlofson paradox. *Journal of Applied Physics*, 84(12):6546–6551.

Kurepa, M. V. and Belić, D. S. (1978). Electron-chlorine molecule total ionisation and electron attachment cross sections. *Journal of Physics B: Atomic, Molecular and Optical Physics*, 11(21):3719–3729.

Kutz, H. and Meyer, H.-D. (1995). Rotational excitation of N_2 and Cl_2 molecules by electron impact in the energy range 0.01–1000 eV: Investigation of excitation mechanisms. *Physical Review A*, 51(5):3819–3830.

Lafleur, Boswell, R. W., and Booth, J. P. (2012). Enhanced sheath heating in capacitively coupled discharges due to non-sinusoidal voltage waveforms. *Applied Physics Letters*, 100(19):194101.

Lafleur and Chabert, P. (2015). Is collisionless heating in capacitively coupled plasmas

really collisionless ? *Plasma Sources Science and Technology*, 24(4):044002.

Lafleur, Chabert, P., and Booth, J. P. (2013). Secondary electron induced asymmetry in capacitively coupled plasmas. *Journal of Physics D: Applied Physics*, 46(13):135201.

Lafleur, Chabert, P., and Booth, J. P. (2014a). Electron heating in capacitively coupled plasmas revisited. *Plasma Sources Science and Technology*, 23(3):035010.

Lafleur, T., Chabert, P., Turner, M. M., and Booth, J. P. (2014b). Equivalence of the hard-wall and kinetic-fluid models of collisionless electron heating in capacitively coupled discharges. *Plasma Sources Science and Technology*, 23(1):015016.

Laher, R. R. and Gilmore, F. R. (1990). Updated excitation and ionization cross sections for electron impact on atomic oxygen. *Journal of Physical and Chemical Reference Data*, 19(1):277 – 305.

Langdon, A. B. (1970). Effects of the spatial grid in simulation plasmas. *Journal of Computational Physics*, 6(2):247–267.

Lawton, S. A., Novick, S. E., Broida, H. P., and Phelps, A. V. (1977). Quenching of optically pumped $O_2(b^1\Sigma_g^+)$ by ground state O_2 molecules. *Journal of Chemical Physics*, 66(3):1381–1382.

Lawton, S. A. and Phelps, A. V. (1978). Excitation of the $b^1\Sigma_g^+$ state of O_2 by low energy electrons. *Journal of Chemical Physics*, 69(3):1055 – 1068.

Lee, C., Graves, D. B., Lieberman, M. A., and Hess, D. W. (1994). Global model of plasma chemistry in a high density oxygen discharge. *Journal of the Electrochemical Society*, 141(6):1546–1555.

Lee, C. and Lieberman, M. A. (1995). Global model of Ar, O_2, Cl_2 and Ar/O_2 high-density plasma discharges. *Journal of Vacuum Science and Technology A*, 13(2):368–380.

Lee, S. H., Iza, F., and Lee, J. K. (2006). Particle-in-cell monte carlo and fluid simulations of argon-oxygen plasma: Comparisons with experiments and validations. *Physics of Plasmas*, 13(5):057102.

Lichtenberg, A. J., Vahedi, V., Lieberman, M. A., and Rognlien, T. (1994). Modeling electronegative plasma discharges. *Journal of Applied Physics*, 75(5):2339 – 2347.

Lieberman, M. A. (1988). Analytical solution for capacitive rf sheath. *IEEE Transactions on Plasma Science*, 16(6):638–644.

Lieberman, M. A. and Godyak, V. A. (1998). From Fermi acceleration to collisionless discharge heating. *IEEE Transactions on Plasma Science*, 26(3):955 – 986.

Lieberman, M. A. and Lichtenberg, A. J. (2005). *Principles of Plasma Discharges and Materials Processing*. John Wiley & Sons, New York, 2 edition.

Lieberman, M. A., Lichtenberg, A. J., Kawamura, E., Mussenbrock, T., and Brinkmann, R. P. (2008). The effects of nonlinear series resonance on ohmic and stochastic heating in capacitive discharges. *Physics of Plasmas*, 15(6):063505.

Lim, C.-H. (2007). *The interaction of energetic charged particles with gas and boundaries in the particle simulation of plasmas*. PhD thesis, University of California at Berkeley.

Lindsay, B. G. and Stebbings, R. F. (2005). Charge transfer cross sections for energetic neutral atom data analysis. *Journal of Geophysical Research*, 110(A12):A12213.

Liu, Y., Booth, J.-P., and Chabert, P. (2018). Plasma non-uniformity in a symmetric radiofrequency capacitively-coupled reactor with dielectric side-wall: a two dimensional particle-in-cell/Monte Carlo collision simulation. *Plasma Sources Science and*

Technology, 27(2):025006.

Liu, Y.-X., Korolov, I., Schüngel, E., Wang, Y.-N., Donkó, Z., and Schulze, J. (2017). Striations in electronegative capacitively coupled radio-frequency plasmas: analysis of the pattern formation and the effect of the driving frequency. *Plasma Sources Science and Technology*, 26(5):055024.

Liu, Y.-X., Schüngel, E., Korolov, I., Donkó, Z., Wang, Y.-N., and Schulze, J. (2016). Experimental observation and computational analysis of striations in electronegative capacitively coupled radio-frequency plasmas. *Physical Review Letters*, 116(25):255002.

Liu, Y.-X., Zhang, Q.-Z., Jiang, W., Hou, L.-J., Jiang, X.-Z., Lu, W.-Q., and Wang, Y.-N. (2011). Collisionless bounce resonance heating in dual-frequency capacitively coupled plasmas. *Physical Review Letters*, 107(5):055002.

Liu, Y.-X., Zhang, Q.-Z., Liu, J., Song, Y.-H., Bogaerts, A., and Wang, Y.-N. (2012). Effect of bulk electric field reversal on the bounce resonance heating in dual-frequency capacitively coupled electronegative plasmas. *Applied Physics Letters*, 101(11):114101.

Liu, Y.-X., Zhang, Q.-Z., Liu, J., Song, Y.-H., Bogaerts, A., and Wang, Y.-N. (2013). Electron bounce resonance heating in dual-frequency capacitively coupled oxygen discharges. *Plasma Sources Science and Technology*, 22(2):025012.

Locht, R. and Schopman, J. (1974). The dissociative ionization in oxygen. *International Journal of Mass Spectrometry and Ion Physics*, 15(4):361–378.

Lymberopoulos, D. P. and Economou, D. J. (1995). Spatiotemporal electron dynamics in radio-frequency glow discharges: fluid versus dynamic Monte Carlo simulations. *Journal of Physics D: Applied Physics*, 28(4):727–737.

Mahony, C. M. O., Al Wazzan, R., and Graham, W. G. (1997). Sheath dynamics observed in a 13.56 MHz-driven plasma. *Applied Physics Letters*, 71(5):608–610.

Mantzaris, N. V., Boudouvis, A., and Gogolides, E. (1995). Radio-frequency plasmas in CF_4: Self-consistent modeling of the plasma physics and chemistry. *Journal of Applied Physics*, 77(12):6169–6180.

Martin, L. R., Cohen, R. B., and Schatz, J. F. (1976). Quenching of laser induced fluorescence of $O_2(b^1\Sigma_g^+)$ by O_2 and N_2. *Chemical Physics Letters*, 41(2):394–396.

Matyash, K., Schneider, R., Dittmann, K., Meichsner, J., Bronold, F. X., and Tskhakaya, D. (2007). Radio-frequency discharges in oxygen: III. Comparison of modelling and experiment. *Journal of Physics D: Applied Physics*, 40(21):6601–6607.

Meichsner, J., Schmidt, M., Schneider, R., and Wagner, H.-E., editors (2013). *Nonthermal Plasma Chemistry and Physics*. CRC Press, Boca Raton, Florida.

Moran, T. F. and Roberts, J. R. (1968). Collision-induced dissociation of low-kinetic-energy ions. *The Journal of Chemical Physics*, 49(8):3411–3421.

Mul, P. M. and McGowan, J. W. (1979). Merged electron-ion beam experiments. III. Temperature dependence of dissociative recombination for atmospheric ions NO^+, O_2^+ and N_2^+. *Journal of Physics B: Atomic, Molecular and Optical Physics*, 12(9):1591–1601.

Muschlitz, E. E. (August 17-21, 1959). Elastic and inelastic collisions of low-energy negative ions in gases. In Nilsson, N. R., editor, *Proceedings of the IV International Conference on Phenomena in Ionized Gases*, pages 52–56, Uppsala, Sweden. North-Holland Publishing Co., Amsterdam.

Mussenbrock, T. and Brinkmann, R. P. (2006). Nonlinear electron resonance heating in capacitive radio frequency discharges. *Applied Physics Letters*, 88(15):151503.

Mussenbrock, T., Brinkmann, R. P., Lieberman, M. A., Lichtenberg, A. J., and Kawamura, E. (2008). Enhancement of ohmic and stochastic heating by resonance effects in capacitive radio frequency discharges: A theoretical approach. *Physical Review Letter*, 101(8):085004.

Nanbu, K., Nakagome, T., and Kageyama, J. (1999a). Detailed structure of the afterglow of radio-frequency chlorine discharge. *Japanese Journal of Applied Physics*, 38(8):L951–L953.

Nanbu, K., Suetani, M., and Sasaki, H. (1999b). Direct simulation Monte Carlo (DSMC) modeling of silicon etching in radio-frequency chlorine discharge. *Computational Fluid Dynamics Journal*, 8(2):257–265.

O'Connell, D., Gans, T., Vender, D., Czarnetzki, U., and Boswell, R. (2007). Plasma ionization through wave-particle interaction in a capacitively coupled radio-frequency discharge. *Physics of Plasmas*, 14(3):034505.

Olson, R. E. (1972). Absorbing-sphere model for calculating ion-ion recombination total cross sections. *Journal of Chemical Physics*, 56(6):2979–2984.

Padgett, R. and Peart, B. (1998). Merged-beam measurements of the mutual neutralization of O_2^+/O^- and NO^+/O^- ions. *Journal of Physics B: Atomic, Molecular and Optical Physics*, 31(24):L995–L1000.

Park, G. Y., You, S. J., Iza, F., and Lee, J. K. (2007). Abnormal heating of low-energy electrons in low-pressure capacitively coupled discharges. *Physical Review Letters*, 98(8):085003.

Patel, K. K. (1998). Volume averaged modeling of high density discharges. Master's thesis, University of California at Berkeley.

Peverall, R., Rosén, S., Peterson, J. R., Larsson, M., Al-Khalili, A., Vikor, L., Semaniak, J., Bobbenkamp, R., Padellec, A. L., Maurellis, A. N., and van der Zande, W. J. (2001). Dissociative recombination and excitation of O_2^+: Cross sections, product yields and implications for studies of ionospheric airglows. *Journal of Chemical Physics*, 114(15):6679–6689.

Peyerimhoff, S. D. and Buenker, R. J. (1981). Electronically excited and ionized states of the chlorine molecule. *Chemical Physics*, 57(3):279–296.

Phelps, A. V. (1985). Technical Report JILA Information Center Report 28, University of Colorado at Boulder.

Phelps, A. V. and Petrović, Z. L. (1999). Cold-cathode discharges and breakdown in argon: surface and gas phase production of secondary electrons. *Plasma Sources Science and Technology*, 8(3):R21–R44.

Phelps, A. V., Pitchford, L. C., Pédoussat, C., and Donkó, Z. (1999). Use of secondary-electron yields determined from breakdown data in cathode-fall models for Ar. *Plasma Sources Science and Technology*, 8(4):B1–B2.

Popov, O. A. and Godyak, V. A. (1985). Power dissipated in low-pressure radio-frequency discharge plasmas. *Journal of Applied Physics*, 57(1):53–58.

Proshina, O. V., Rakhimova, T. V., Rakhimov, A. T., and Voloshin, D. G. (2010). Two modes of capacitively coupled rf discharge in CF_4. *Plasma Sources Science and Technology*, 19(6):065013.

Proto, A. and Gudmundsson, J. T. (2018a). The influence of secondary electron emission

and electron reflection on a capacitively coupled oxygen discharge. *Atoms*, 6(4):65.

Proto, A. and Gudmundsson, J. T. (2018b). The role of surface quenching of the singlet delta molecule in a capacitively coupled oxygen discharge. *Plasma Sources Science and Technology*, 27(7):074002.

Qiu, W. D., Bowers, K. J., and Birdsall, C. K. (2003). Electron series resonant discharges: comparison between simulation and experiment. *Plasma Sources Science and Technology*, 12(1):57–68.

Radmilović-Radjenović, M. and Petrović, Z. L. (2009). Influence of the surface conditions on rf plasma characteristics. *The European Physical Journal D*, 54(2):445–449.

Rapp, D. and Briglia, D. (1965). Total cross sections for ionization and attachment in gases by electron impact. II. Negative ion formation. *Journal of Chemical Physics*, 43(5):1480 – 1489.

Rapp, D. and Francis, W. E. (1962). Charge exchange between gaseous ions and atoms. *Journal of Chemical Physics*, 37(11):2631–2645.

Rescigno, T. N. (1994). Low-energy electron-collision processes in molecular chlorine. *Physical Review A*, 50(2):1382 – 1389.

Riemann, K.-U. (1991). The Bohm criterion and sheath formation. *Journal of Physics D: Applied Physics*, 24(4):493–518.

Roberto, M., Verboncoeur, J., Verdonck, P., and Cizzoto, E. (2006). Effects of the secondary electron emission coefficent on the generation of charged particles in RF oxygen discharge. *ECS Transactions*, 4(1):563–571.

Rogoff, G. L., Kramer, J. M., and Piejak, R. B. (1986). A model for the bulk plasma in an rf chlorne discharge. *IEEE Transactions on Plasma Science*, 14(2):103–111.

Ruf, M.-W., Barsotti, S., Braun, M., Hotop, H., and Fabrikant, I. (2004). Dissociative attachment and vibrational excitation in low-energy electron collisions with chlorine molecules. *Journal of Physics B: Atomic, Molecular and Optical Physics*, 37(1):41–62.

Salabaş, A. and Brinkmann, R. P. (2006). Non-neutral/quasi-neutral plasma edge definition for discharge models: A numerical example for dual frequency hydrogen capacitively coupled plasmas. *Japanese Journal of Applied Physics*, 45(6):5203–5206.

Salabas, A., Marques, L., Jolly, J., Gousset, G., and Alves, L. L. (2004). Systematic characterization of low-pressure capacitively coupled hydrogen discharges. *Journal of Applied Physics*, 95(9):4605–4620.

Sato, A. H. and Lieberman, M. A. (1990). Electron-beam probe measurements of electric fields in rf discharges. *Journal of Applied Physics*, 68(12):6117–6124.

Schulze, F. J. (2009). *Electron heating in capacitively coupled radio frequency discharges*. PhD thesis, Ruhr Universität Bochum.

Schulze, J., Derzsi, A., Dittmann, K., Hemke, T., Meichsner, J., and Donkó, Z. (2011a). Ionization by drift and ambipolar electric fields in electronegative capacitive radio frequency plasmas. *Physical Review Letters*, 107(27):275001.

Schulze, J., Derzsi, A., and Donkó, Z. (2011b). Electron heating and the electrical asymmetry effect in dual-frequency capacitive CF$_4$ discharges. *Plasma Sources Science and Technology*, 20(4):045008.

Schulze, J., Donkóó, Z., B G Heil1, D. L., Mussenbrock, T., Brinkmann, R. P., and Czarnetzki, U. (2008a). Electric field reversals in the sheath region of capacitively

coupled radio frequency discharges at different pressures. *Journal of Physics D: Applied Physics*, 41(10):105214.

Schulze, J., Donkó, Z., Lafleur, T., Wilczek, S., and Brinkmann, R. P. (2018). Spatio-temporal analysis of the electron power absorption in electropositive capacitive RF plasmas based on moments of the Boltzmann equation. *Plasma Sources Science and Technology*, 27(5):055010.

Schulze, J., Heil, B. G., Luggenhölscher, D., Mussenbrock, T., Brinkmann, R. P., and Czarnetzki, U. (2008b). Electron beams in asymmetric capacitively coupled radio frequency discharges at low pressures. *Journal of Physics D: Applied Physics*, 41(4):042003.

Schulze, J., Heil, B. G., Luggenhölscher, D., and Czarnetzki, U. (2008c). Electron beams in capacitively coupled radio-frequency discharges. *IEEE Transactions on Plasma Science*, 36(4):1400–1401.

Schulze, J., Kampschulte, T., , D. L., and Czarnetzki, U. (2007). Diagnostics of the plasma series resonance effect in radio-frequency discharges. *Journal of Physics: Conference Series*, 86:012010.

Schulze, J., Luggenhölscher, B. G. H. D., Brinkmann, R. P., and Czarnetzki, U. (2008d). Stochastic heating in asymmetric capacitively coupled RF discharges. *Journal of Physics D: Applied Physics*, 41(19):195212.

Schulze, J. and Mussenbrock, T. (2016). Electron heating in technological plasmas. *Plasma Sources Science and Technology*, 25(2):020401.

Schüngel, E., Brandt, S., Donkó, Z., Korolov, I., Derzsi, A., and Schulze, J. (2015). Electron heating via self-excited plasma series resonance in geometrically symmetric multi-frequency capacitive plasmas. *Plasma Sources Science and Technology*, 24(4):044009.

Schüngel, E., Zhang, Q.-Z., Iwashita, S., Schulze, J., Hou, L.-J., Wang, Y.-N., and Czarnetzki, U. (2011). Control of plasma properties in capacitively coupled oxygen discharges via the electrical asymmetry effect. *Journal of Physics D: Applied Physics*, 44(28):285205.

Semmler, E., Awakowicz, P., and von Keudell, A. (2007). Heating of a dual frequency capacitively coupled plasma via the plasma series resonance. *Plasma Sources Science and Technology*, 16(4):839–848.

Shibata, M., Nakano, N., and Makabe, T. (1995). O_2 rf discharge structure in parallel plates reactor at 13.56 MHz for material processing. *Journal of Applied Physics*, 77(12):6181–6187.

Shyn, T. W. and Sweeney, C. J. (2000). Measurement of absolute differential excitation cross sections of molecular oxygen by electron impact: Decomposition of the herzberg pseudocontinuum. *Physical Review A*, 62(2):022711.

Skarphedinsson, G. A. and Gudmundsson, J. T. (2020). Tailored voltage waveforms applied to a capacitively coupled chlorine discharge. *Plasma Sources Science and Technology*, 29(8):084004.

Skullerud, H. R. (1968). The stochastic computer simulation of ion motion in a gas subjected to a constant electric field. *Journal of Physics D: Applied Physics*, 1(11):1567–1568.

Španěl, P., Tichý, M., and Smith, D. (1993). The reactions of positive and negative halogen ions with Cl_2 and Br_2. *Journal of Chemical Physics*, 98(11):8660 – 8666.

Stebbings, R. F. (1966). Charge transfer. In Ross, J., editor, *Advances in Chemical Physics: Molecular Beams, Volume 10*, pages 195–246. John Wiley & Sons.

Stebbings, R. F., Smith, A. C. H., and Ehrhard, H. (1964). Charge transfer between oxygen atoms and O^+ and H^+ ions. *Journal of Geophysical Research*, 69(11):2349–2355.

Stebbings, R. F., Smith, A. C. H., and Gilbody, H. B. (1963). Charge transfer between some atmospheric ions and atomic oxygen. *Journal of Chemical Physics*, 38(9):2280–2284.

Subramonium, P. (2003). *Simulation of transients and transport in plasma processing reactors*. PhD thesis, University of Illinois at Urbana-Champaign.

Surendra, M. and Dalvie, M. (1993). Moment analysis of rf parallel-plate-discharge simulations using the particle-in-cell with Monte Carlo collisions technique. *Physical Review E*, 48(5):3914–3924.

Surendra, M. and Graves, D. B. (1991a). Electron acoustic waves in capacitively coupled, low-pressure rf glow discharges. *Physical Review Letters*, 66(11):1469–1472.

Surendra, M. and Graves, D. B. (1991b). Particle simulations of radio-frequency glow discharges. *IEEE Transactions on Plasma Science*, 19(2):144–157.

Taillet, J. (1969). Resonance-sustained radio frequency discharges. *American Journal of Physics*, 37(4):423–441.

Teichmann, T., Küllig, C., Dittmann, K., Matyash, K., Schneider, R., and Meichsner, J. (2013). Particle- In-Cell simulation of laser photodetachment in capacitively coupled radio frequency oxygen discharges. *Physics of Plasmas*, 20(11):113509.

Thomas, L. D. and Nesbet, R. K. (1975). Addendum: Low-energy electron scattering by atomic oxygen. *Physical Review A*, 12(4):1729 – 1730.

Thomson, J. J. (1912). Ionization by moving electrified particles. *Philosophical Magazine Series 6*, 23(136):449–457.

Thorsteinsson, E. G. and Gudmundsson, J. T. (2009). A global (volume averaged) model study of a nitrogen discharge: I. Steady state. *Plasma Sources Science and Technology*, 18(4):045001.

Thorsteinsson, E. G. and Gudmundsson, J. T. (2010a). A global (volume averaged) model of a chlorine discharge. *Plasma Sources Science and Technology*, 19(1):015001.

Thorsteinsson, E. G. and Gudmundsson, J. T. (2010b). The low pressure Cl_2/O_2 discharge and the role of ClO. *Plasma Sources Science and Technology*, 19(5):055008.

Tochikubo, F., Suzuki, A., Kakuta, S., Terazono, Y., and Makabe, T. (1990). Study of the structure in rf glow discharges in SiH_4/H_2 by spatiotemporal optical emission spectroscopy: Influence of negative ions. *Journal of Applied Physics*, 68(11):5532–5539.

Tolliver, D. L. (1984). The history of plasma processing. In Einspruch, N. G. and Brown, D. M., editors, *VLSI Electronics: Microstructure Science, vol. 8*, pages 1–24. Academic Press, Orlando.

Toneli, D. A., Pessoa, R. S., Roberto, M., and Gudmundsson, J. T. (2015). On the formation and annihilation of the singlet molecular metastables in an oxygen discharge. *Journal of Physics D: Applied Physics*, 48(32):325202.

Tong, D. (2012). Kinetic theory: University of Cambridge graduate course.

Tskhakaya, D., Matyash, K., Schneider, R., and Taccogna, F. (2007). The particle-in-cell

method. *Contributions to Plasma Physics*, 47(8-9):563–594.

Turner, M. M. (1995). Pressure heating of electrons in capacitively coupled rf discharges. *Physical Review Letters*, 75(7):1312–1315.

Turner, M. M. (2009). Collisionless heating in radio-frequency discharges: a review. *Journal of Physics D: Applied Physics*, 42(19):194008.

Turner, M. M. and Chabert, P. (2006). Collisionless heating in capacitive discharges enhanced by dual-frequency excitation. *Physical Review Letters*, 96(20):205001.

Vahedi, V., Birdsall, C. K., Lieberman, M. A., DiPeso, G., and Rognlien, T. D. (1993a). Capacitive rf discharges modelled by particle-in-cell Monte Carlo simulation. II. Comparisons with laboratory measurements of electron energy distribution functions. *Plasma Sources Science and Technology*, 2(4):273–278.

Vahedi, V. and DiPeso, G. (1997). Simultaneous potential and circuit solution for two-dimensional bounded plasma simulation codes. *Journal of Computational Physics*, 131(1):149–163.

Vahedi, V., DiPeso, G., Birdsall, C. K., Lieberman, M. A., and Ronhlien, T. D. (1993b). Capacitive RF discharges modelled by particle-in-cell Monte Carlo simulation. I. Analysis of numerical techniques. *Plasma Sources Science and Technology*, 2(4):261–272.

Vahedi, V. and Surendra, M. (1995). A Monte Carlo collision model for the particle-in-cell method: applications to argon and oxygen discharges. *Computer Physics Communications*, 87:179–198.

Vejby-Christensen, L., Kella, D., Mathur, D., Pedersen, H. B., Schmidt, H. T., and Andersen, L. H. (1996). Electron-impact detachment from negative ions. *Physical Review A*, 53(4):2371 – 2378.

Vender, D. (1990a). *Numerical studies of the low pressure RF plasma.* PhD thesis, Australian National University.

Vender, D. and Boswell, R. W. (1992). Electron–sheath interaction in capacitive radio-frequency plasmas. *Journal of Vacuum Science and Technology A*, 10(4):1331–1338.

Vender, D.; Boswell, R. (1990b). Numerical modeling of low-pressure RF plasmas. *IEEE Transactions on Plasma Science*, 18(4):725–732.

Verboncoeur, J. P. (2005). Particle simulation of plasmas: review and advances. *Plasma Physics and Controlled Fusion*, 47(5A):A231–A260.

Verboncoeur, J. P., Alves, M. V., Vahedi, V., and Birdsall, C. K. (1993). Simultaneous potential and circuit solution for 1D bounded plasma particle simulation codes. *Journal of Computational Physics*, 104(2):321–328.

Vesel, A. and Mozetic, M. (2017). New developments in surface functionalization of polymers using controlled plasma treatments. *Journal of Physics D: Applied Physics*, 50(29):293001.

von Keudell, A. and Schulz-von der Gathen, V. (2017). Foundations of low temperature plasma physics – an introduction. *Plasma Sources Science and Technology*, 26(11):113001.

Wang, Y., Zatsarinny, O., Bartschat, K., and Booth, J.-P. (2013). Fine-structure-resolved electron collisions from chlorine atoms in the $(3p^5)^2\mathrm{P}^o_{3/2}$ and $(3p^5)^2\mathrm{P}^o_{1/2}$ states. *Physical Review A*, 87(2):022703.

Wilcox, J. B. and Moran, T. F. (1981). Charge-transfer reactions of ground $\mathrm{O}_2^+(X^2\Pi_g,\nu)$ and excited $\mathrm{O}_2^+(A^4\Pi_u,\nu)$ state ions with neutral molecules. *Journal of Physical*

Chemistry, 85(8):989–994.

Wilczek, S., Schulze, J., Brinkmann, R. P., Donkó, Z., Trieschmann, J., and Mussenbrock, T. (2020). Electron dynamics in low pressure capacitively coupled radio frequency discharges. *Journal of Applied Physics*, 127(18):181101.

Wilczek, S., Trieschmann, J., Eremin, D., Brinkmann, R. P., Schulze, J., Schüngel, E., Derzsi, A., Korolov, I., Hartmann, P., Donkó, Z., and Mussenbrock, T. (2016). Kinetic interpretation of resonance phenomena in low pressure capacitively coupled radio frequency plasmas. *Physics of Plasmas*, 23(6):063514.

Wilczek, S., Trieschmann, J., Schulze, J., Schüngel, E., Brinkmann, R. P., Derzsi, A., Korolov, I., Donkó, Z., and Mussenbrock, T. (2015). The effect of the driving frequency on the confinement of beam electrons and plasma density in low-pressure capacitive discharges. *Plasma Sources Science and Technology*, 24(2):024002.

Wise, R. S., Lymberopoulos, D. P., and Economou, D. J. (1995). A two-region model of a radiofrequency low-pressure, high-density plasma. *Plasma Sources Science and Technology*, 4(3):317–331.

Wood, B. P. (1991). *Sheath heating in low-pressure capacitive radio frequency discharges*. PhD thesis, University of California at Berkeley.

Wood, B. P., Lieberman, M. A., and Lichtenberg, A. J. (1995). Stochastic electron heating in a capacitive RF discharge with non-Maxwellian and time-varying distributions. *IEEE Transactions on Plasma Science*, 23(1):89–96.

Yamazawa, Y. (2009). Effect of the resonant growth of harmonics on the electron density in capacitively coupled plasma. *Applied Physics Letters*, 95(19):191504.

Yan, M., Bogaerts, A., Goedheer, W. J., and Gijbels, R. (2000). Electron energy distribution function in capacitively coupled RF discharges: difference between electropositive Ar and electronegative SiH_4 discharges. *Plasma Sources Science and Technology*, 9(4):583–591.

You, S. J., Chung, C. W., and Chang, H. Y. (2005). Feature of electron energy distribution in a low-pressure capacitive discharge. *Applied Physics Letters*, 87(4):041501.

Young, R. A. and Black, G. (1967). Deactivation of $O(^1D)$. *Journal of Chemical Physics*, 47(7):2311–2318.

Zhang, M., Cai, X., Larson, A., and Orel, A. E. (2011a). Theoretical study of dissociative recombination of Cl_2^+. *Physical Review A*, 84:052707.

Zhang, Q.-Z., Jiang, W., Hou, L.-J., and Wang, Y.-N. (2011b). Numerical simulations of electrical asymmetry effect on electronegative plasmas in capacitively coupled rf discharge. *Journal of Applied Physics*, 109(1):013308.

Ziegler, D., Mussenbrock, T., and Brinkmann, R. P. (2008). Nonlinear dynamics of dual frequency capacitive discharges: a global model matched to an experiment. *Plasma Sources Science and Technology*, 17(4):045011.